Study on Local Cloud Coverage Using Ground-Based Measurement of Solar Radiation

Sweata Sijapati

Study on Local Cloud Coverage Using Ground-Based Measurement of Solar Radiation

Dissertation Submitted

to

the Faculty of Civil and Environmental Engineering

In Partial Fulfillment of the Requirements for the

Degree of Doctor at Ehime University

By

Sweata Sijapati

June 2016

Advisor: Professor Ryo Moriwaki

Dedicated to my parents

It’s your support and motivation that has made me stronger

CERTIFICATION

This is to certify that the dissertation entitled, "**Study on Local Cloud Coverage Using Ground-Based Measurement of Solar Radiation"** presented by Ms. Sijapati Sweata in partial fulfillment of the academic requirement of the degree of doctor has been examined and accepted by the evaluation committee at Graduate School of Science and Engineering of Ehime University.

…….

Ryo Moriwaki
Professor of Civil and Environmental Engineering
Thesis Advisor / Examiner 1

…….
……. of Civil and Environmental Engineering
Examiner 2

…….

……. of Civil and Environmental Engineering

Examiner 3

TABLE OF CONTENTS

LIST OF FIGURES

LIST OF TABLES

LIST OF ABBREVIATION

Ac	Altocumulus
AFWA	Air Force Weather Agency
As	Altostratus
AU	Astronomical Unit
AVHRR	Advanced Very High Resolution Radiometer
Cb	Cumulonimbus
CBL	Cloud Base Level
Ci	Cirrus
Cu	Cirrocumulus
FAA	Federal Aviation Administration
FNL	Final Operational Global Analysis data
FSL	Forecast Systems Laboratory
GIA	Geospatial Information Authority, Japan
GOES	Geostationary Operational Environmental Satellite
HIMAWARI	Japanese Geostationary Meteorological Satellite
IFS	Integrated Forecasting System
INSAT	Indian National Satellite
JMA	Japan Meteorological Agency
JST	Japan Standard Time
LCL	Lifted Condensation Level
LU/LC	Land use/Land Cover
ME	Mean Error

METROMEX	Metropolitan Meteorological Experiment
MLIT	Ministry of Land, Infrastructure, Transport and Tourism
MTSAT	Multi-functional Transport Satellite
NASA	National Aeronautics and Space Administration
NCAR	National Centre for Atmospheric Research
NCEP	National Centers for Environmental Prediction
NIP	Normal Incidence Pyrheliometer
Ns	Nimbostratus
NSEE	Normalized Standard Error of the Estimation
NOAA	National Oceanic and Atmospheric Administration
PSP	Precision Spectral Pyranometer
PTC	PVUSA Test Conditions
PV	Photovoltaic
RIC	Regional Instrument Centre
RMSE	Root Mean Square Error
Sc	Stratocumulus
St	Stratus
STC	Standard Test Conditions
TSI	Total Solar Irradiance
UDI	Urban Dry Island
USGS	United States Geological Survey
USM	Ultrasonic Motor
WMO	World Meteorological Organization
WRF	Weather Research and Forecasting Model

LIST OF SYMBOL

a and b	Correlation coefficient
α	Albedo
α_s	Thermopile constant
β	Inclination angle
c	Conversion factor
D	Diameter of the particle
δ	Declination angle of the sun
ΔV	Output voltage of the thermopile
d_n	Day number given in Nautical Almanac and ranges from 0 on 1st January to 364 on 31st December
E_o	Correction factor of the distance between the earth and the sun
ε_s , ε_d	Sensor and dome longwave emittances of pyranometer, respectively
Et	Equation of Time
f	Focal length
γ	Azimuth angle
h	Solar elevation angle
H_s	True solar time in minute
I	Global solar radiation on a horizontal surface
I_b	Direct beam solar radiation
$I_{\beta\gamma}$	Amount of solar radiation on a slope
I_d	Diffuse solar radiation
$I_{d\beta\gamma}$	Diffuse solar radiation on a slope
I_N	Normal beam radiation
I / I_o	Clearness index
I_o	Extra-terrestrial radiation on a plane perpendicular to the Sun's rays
I_{ON}	Extra-terrestrial normal solar radiation
$I_{r\beta\gamma}$	Reflected solar radiation on slope
I_{sc}	Solar constant

L	Longitude of the observation point
λ	Wavelength of radiation
ϕ	Local latitude
L_{irr}	Longwave irradiance
L_s	Longitude of the local standard time meridian
n	Refractive index
n	Day of the year that represents the mean daily radiation of the month
ω	Hour angle
P	Output ratio of the horizontal solar panel
$P_{\beta\gamma}$	Output ratio of the inclined solar panel
r	Distance from the earth to the sun in km
R	Radial distance or the distance between the center of the image and the image point
r_0	Mean distance from the earth to the sun in km
S	Shortwave irradiance
σ	Stenfan-Boltzman constant
τ	Longwave transmittance
Γ	Angle representing the earth's position in the elliptical orbit in radians
T_s , T_d	Sensor and dome temperature of pyranometer, respectively
θ	Angle between the optical axis and the incoming light beam
θ_z	Zenith angle

ACKNOWLEDGEMENT

The completion of the Ph.D. research has been the most transformative and hardworking experience of my life. My life as a Ph.D. candidate would not have been the same without the support and encouragement of the people who have been with me throughout my research period.

First and foremost, I, in no words, can express my sincere gratitude to my supervisor Prof. Dr. Ryo Moriwaki, School of Science and Engineering, Ehime University, for his guidance, wisdom, continuous support, encouragement and positive criticism. The contribution of my supervisors in intensifying my limited knowledge is unbound.

I owe my gratitude to Assistant professor Yoshifumi Fujimori, School of Science and Engineering, Ehime University for his guidance and support during my research and helping me out with the research papers.

I am truly indebted to my laboratory members, regrettably all the name which I cannot list here, for helping me with observation of the data used for the research. They have been a huge help from the initial phase of the research from the instrument installation to data collection every month. Without them I would have never been able to move forward with my research. They have also been of immense support during my stay in Japan especially when it comes to Japanese language skills and Japanese culture.

I will forever be indebted to Ehime University for providing me the financial support for both my Master's and Doctoral degree and making it possible for me to complete my research and make my dreams come true. I would also be always grateful to the International student support division for the continuous support and guidance and making my stay in Japan easier and comfortable.

I am grateful to Professor Masahiro Watanabe for his guidance during my Master's degree and further encouraging me to pursue my Ph.D. degree and making me believe that I will be able to succeed. Also, my heartfelt thanks to Associate Professor Dr. Netra Prakash Bhandary for his support and guidelines from the very beginning of my arrival at Ehime University and Professor Dr. Shinji Tsuzuki for providing the observation data of the photovoltaic network in the study area.

I also express my sincere gratitude to Mrs. Yukiko Fumoto and Mrs. Kazue Shigematsu for being the motherly figure during my entire stay in Japan. Its due to your support, love and care that has made me strong each day.

I will always be grateful to Lawan Thamsuhang Subba for his support, encouragement and positive criticism that has only helped be move forward in my life. I truly appreciate his readiness to help me and patience in listening to my thoughts and complainants.

Last but not the least, this acknowledgement would not be complete without a special mention to my family and friends back in Nepal for all their love, support and words of encouragement each time I felt down. My brother Sandeep Sijapati and sister Rakshya Khadka who have always been there by my side and guide me along the path when I felt discouraged and during my though days.

And most of all my loving parents, to whom I dedicate this work. Their moral support, love and encouragement has made me a stronger person. They have always believed in me and motivated me to live my dreams. They have always been my backbone and will always be the most important people in my life. I love them immensely.

June 2016

ABSTRACT

Clouds are basis of precipitation and its types plays an important role for the determination of the precipitation as well as the radiation reaching the earth's surface. Thus, the temporal and spatial variation of solar radiation and cloud is important to understand the concept of local climate such as torrential rainfall. In past, several studies regarding the radiative fluxes and cloud cover from satellite data have been widely used. However, there are limitation when it comes to spatial resolution. Hence, the main objective of the study is to develop a new technique to monitor the local cloud coverage using ground-based solar radiation monitoring network and to explore the potential of the method in Matsuyama plain. The first method includes the temporal and spatial analysis of solar radiation using pyranometer network and the second method include the spatially dense monitoring of solar radiation using photovoltaic (PV) network.

The amount of solar radiation varies with both time and latitude; thus we introduce the clear sky rate to estimate the percentage of solar radiation blocked due to the presence of cloud. Here in each month, the highest amount of solar radiation per minute was taken into account to create a time series data of a virtually sunny day. Then the time series data of the virtually sunny day were compared with the time series data of the target day and the CSR was determined. The clear sky rate is further used to perform the statistical analysis to study the cloud coverage and properties.

Initially, the one-hour time standard deviation of the clear sky rate for the 7 observation sites of the pyranometer network was considered for the analysis. The diurnal variation of the clear sky rate showed the presence of the cloud to be more in the morning and late afternoon with maximum value around mid-day. Similarly, the monthly average of the clear sky indicated the presence of the cloud to be more in winter as compared to other observation month especially through afternoon. Following the manner, the spatial variation of the solar radiation in the study area was considered. The clear sky rate at the inland area of the Matsuyama plain was found to be smallest compared to all other observation site. Further comparing the clear sky rate of the urban and rural area, the clear sky rate at the urban area was found to be smaller than the rural area. Thus, the temporal and spatial distribution of the solar radiation for the entire study period shows the tendency of cloud formation to be more in the urbanized and the inland area of the study area.

As, the pyranometer network sites were limited for the monitoring of the solar radiation distribution of the entire study area. The estimation of global solar radiation using photovoltaic system was proposed and examined on the basis of in-situ measurements. Solar panels were installed horizontally and at a tilt angle of 20^{o} due south. The estimated global radiation and the measured solar radiation were observed to be in high correlation. To estimate the global solar radiation using a tilted solar panel, it is necessary to convert the solar radiation on a slope to the global solar radiation on a horizontal plane. Thus, for this conversion the separation of the solar radiation into a direct beam solar radiation and diffuse solar radiation was conducted. The validity of the method proposed for the estimation of global solar radiation using solar panels at a tilt angle of 20^{o} was confirmed with high correlation irrespective of the season.

Further, the temporal and spatial variation of the estimated global solar radiation was studied using the photovoltaic network established within the study area. The estimation of the global solar radiation for all the observation site was confirmed with high correlation. The study was verified using the whole sky images taken by a camera mounted with a fisheye lens installed on the rooftop of Engineering building at Ehime University to monitor the distribution of clouds. Here along the observation time period, the spatial distribution of the solar radiation and the distribution of cloud studied from the whole-sky photographs were in agreement with each other. Thus, the potential of using the estimated global solar radiation to monitor the distribution of the solar radiation and the cloud coverage was studied with high efficiency.

To monitor the efficiency of the PV system as a solar radiometer, comparison of the pyranometer observation and the PV observation was conducted. Considering this, the temporal and the spatial variation of the one-hour average time standard deviation of the CSR using the PV observation dataset was calculated. The diurnal and monthly variation of the CSR from the pyranometer observation and the PV observation was found to be in high correlation with each other. Thus, all the above result confirms the accuracy and the good performance of the proposed method for the ground-based monitoring of the solar radiation in Matsuyama plain.

The cloud distribution and the sky condition over the study area was validated using the whole-sky camera installed at the Ehime University. The clear sky rate below 0.4 with smaller time standard deviation showed the cloud coverage to be larger. The maximum time standard deviation within the clear sky rates between 0.4 to 0.6 shows the dominance of the cumulus clouds and the observation value with minimum time standard deviation showed

the entire sky to be covered with the cloud during the observation period with the dominance of high raised clouds such as cirrostratus to cirrus. Both measured and the estimated global solar radiation indicted the similar cloud type and sky condition for the different ranges of the clear sky rates.

Hence, the ground-based measurement of the solar radiation was used to understand the temporal and the spatial distribution of the amount of solar radiation and the sky condition of the study areas. Further, the potential of using the photovoltaic system as a radiometer was studied with high efficiency. This study is applicable for all the megacities and urbanizing areas with increasing number of PV system for monitoring the effects of urbanization. The estimation of the global solar radiation can be beneficial for understanding the local climate studies such as torrential rainfall and to understand the effects of urbanization on the local climate.

CHAPTER 1

1. Introduction

This chapter introduces the background of the study and the basic concepts of the solar radiation and its importance. It also describes the methods or models used for the measurement of the radiation and its components used for the past years by many researchers around the different parts of the world including the study area.

1.1 Research Background

In recent years, the intensity and frequency of localized torrential rainfall in urban area might be increasing due to factors such as climatic change, unplanned land use patterns. Urban flood has large impacts, particularly in terms of direct and indirect economic losses. The impact of such floods on the lives and livelihoods of people, a function of their

Figure 1.1: The aerial view of the landslide damage caused after the localized torrential rainfall in Hiroshima, Western Japan, on August 20, 2014.

(Source: Jiji Press/AFP/Getty Images)

vulnerability, needs to be understood. Recently, on August 20, 2014 Hiroshima prefecture in the southwest Japan, received more than 200mm of rainfall within 3 hours, which was more than twice the monthly average for the area. The localized torrential heavy rainfall triggered 107 debris flows and claimed about 74 lives (Wang et al., 2015). Thus, the study of such torrential rainfall and local climate is of utmost importance for the prevention of the future disaster events. Houng and Pathirana (2013), studied the impact of the urbanization on the rainfall pattern which in turn has increased the risk of urban flooding and inundation effect in the urbanized city of Vietnam.

To consider the impact of such localized torrential rainfall, many studies have been conducted from past years till date. Scientist from the Argonne National Laboratory, University of Chicago, Illinois State Water Survey and University of Wyoming initiated a scientific program named METROMEX (METROpolitan Meteorological EXperiment) at St. Louis with an objective to study the effects of urban environment on the intensity, frequency and duration of rainfall and to identify the physical processes of the atmosphere and the causative agents which are responsible for producing the urban weather effects (Changnon and Huff, 1971). Results from METROMEX suggests that the urbanization effects lead to 5-25% increase in precipitation, particular 50-70km downward of the urban center during the summer month (Changnon et al., 1991). Sakakibana and Matsui (2005), shows a linear relationship between nocturnal heat island intensity and the logarithm of the city population in Japan. The frequency of heavy rainfall in Japan is higher during the summer season (Matsumoto and Takahashi 1999), making it prone to rainfall induced disasters such as shallow landslides due to its topographical and geological conditions (Saito et al., 2010). Fujibe (1988), suggested that increase in temperature caused by urbanization results in localized severe rainfall due to convergence of water vapor. Shimoju et al. (2010), have explained the change in the path of sea breeze due to urbanization, which leads to the localized heavy rainfall. Shepherd et al. (2010), in their case study for Houston suggested that the urban land cover growth could lead to temporal and spatial precipitation variability in the coastal urban microclimate which in turn is affected by the urban heat island effect (Burain and Shepherd, 2005).

Clouds are one of the most important forces that govern the earth's heat balance and hydrological cycle. Davies et al. (1975), explained the two effects of the cloud on the global radiation; attenuation of incoming radiation by the cloud absorption and downward reflection from the cloud bases of radiation reflected from the ground surface. Cloud reflects incoming solar radiation, thereby reducing the daytime temperature (Ackerman et al., 1998).

The cloud and its type in turn plays and important role by determining the amount radiation reaching the surface (Reno et al. 2012). Cess et al. (1995) studied the absorption of the solar radiation by the clouds which in turn can be increased due to the tropospheric aerosols. Further, the absorption of radiation was found be more for the observed dataset as compared to the theoretical models. Large scale cloud information is available from the several satellites but such data might be provided in a low resolution and may contain error. As per study of Goodman and Henderson-Seller (1988), satellite retrievals have known weaknesses in quantifying small and low latitude cloud features due to their limited spatial resolution. Moreover, it is difficult to determine the solar obstruction from the satellite sensor which is of utmost importance in radiation/cloud studies (Long et al., 2006). Automated method for the real time classification of the all-sky imager were conducted by Heinle et al. (2010), based on the 12 features of cloud listed by WMO. Martínez -Chico et al. (2011), classified the cloud according to the altitude by using ground-based measurement of the solar radiation and the images of the total sky imagers (TSI). Various type of classification such as block-based classification (Cheng and Yu, 2015), pixel based (Souza-Echer et al., 2006), K-nearest and neural network (Singh and Glennen, 2005), texture, class and shape features with K-nearest neighbour (Xia et al., 2015), feature extraction technique (Kliangsuawan and Heednacram, 2015) and many more. Hahn et al. (1990), have prepared a map based on the cloud coverage over the land based on the various cloud type and occurrence.

In addition, there are many studies done on convective clouds, which are the basis of the precipitation. According to Bornstein and Lin (2000), the urban heat island induced a convergence zone, which resulted in the convective rainfall in the urbanized area of Atlanta. Fujibe (2003), found a positive precipitation anomaly related to the urban effect over central and inland areas of Tokyo. Inoue and Kimura (2004), explained the frequency of low-level clouds to be higher over the urban areas than over the rural area. Williams et al. (2015), have documented the decrease in the fog formation and increase in the stratus cloud height due to the night time temperature as a result of urbanization in the coastal southern California.

Many studies related to the urban climate in the study area (Matsuyama plain) has been conducted in past years. Due to the difference in land use, the occurrence of heat island effect in the Matsuyama plain has been confirmed by Fujimori et al. (2010), using the dataset of thermo-hygrometers network in the area. Similarly, Moriwaki et al. (2013), on the basis of field measurement found the absolute humidity of the urban area to be smaller as compared to the rural absolute humidity, which in turn give rises to the urban dry island phenomenon (UDI). The seasonal change in the UDI, suggested the high UDI in summer

season (July to October) whereas the intensity starts decreasing and the lower intensity was observed in Winter season (March to December) as shown in Figure 1.2.

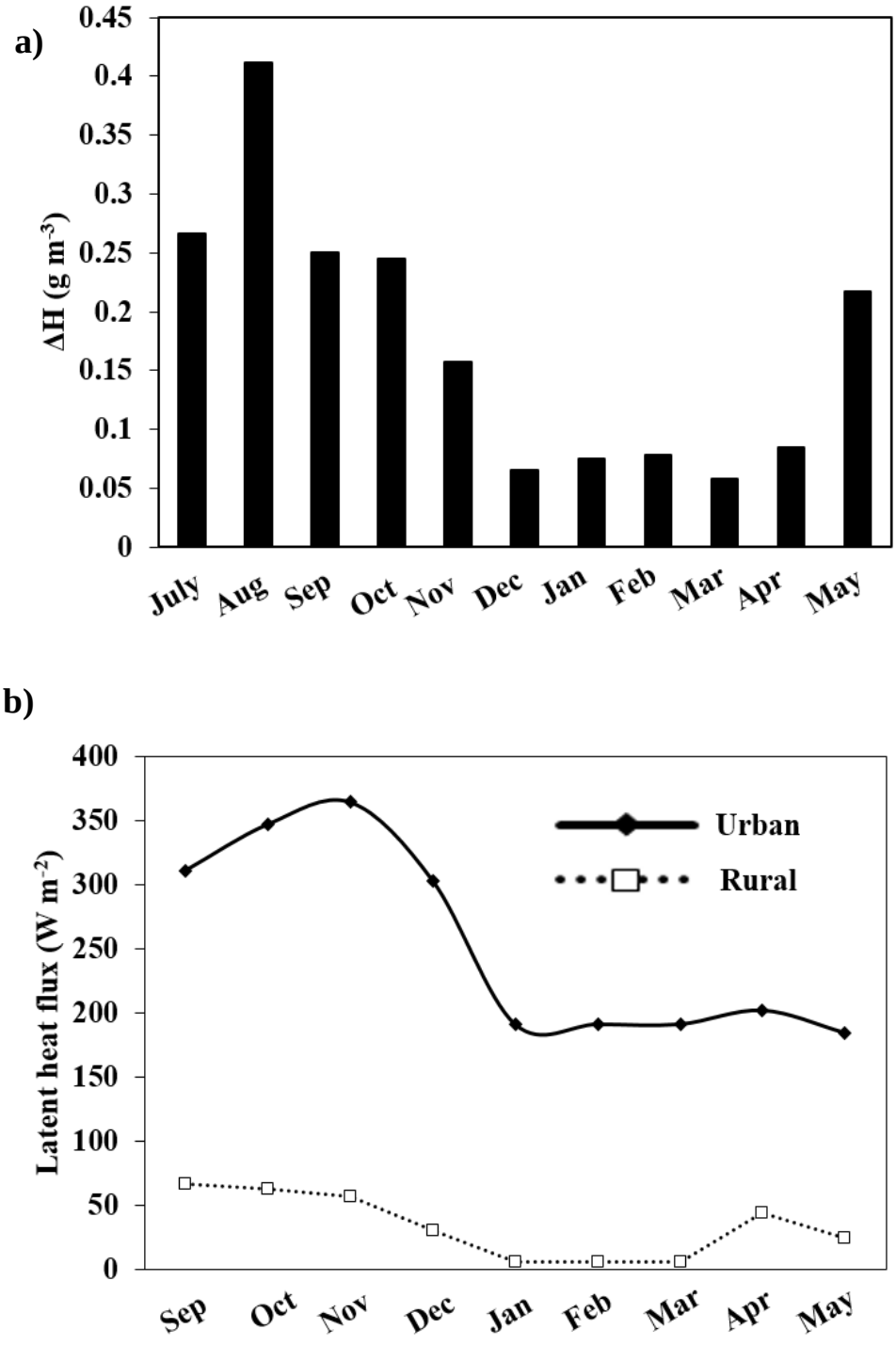

Figure 1.2: a) Seasonal change of daily averaged UDI intensity from July 2010 to May 2011 and b) Seasonal change of the noon latent heat flux of urban and rural area from September 2010 to May 2011 (Moriwaki et al. 2013)

They further studied the cloud base level (CBL) measurement using ceilometer, in the urban and rural area of the Matsuyama plain. Due to the dry island effect and the heat island effect, higher relative humidity was observed in the rural area than urban area. Especially, when the wind direction is from east- west, the CBL was higher in urban area as compared to the rural area (Figure 1.3). Similar results were also documented by Davies et al. (2004). On the other hand, if the wind direction was from north-south, the impact of urban dry island phenomenon on CBL was not noticeable. Also, in the Matsuyama plain the relative humidity in the urban area was found to be larger which in turn caused the increase in the Lifted Condensation Level (LCL). To clarify the effect of difference in land use on the cloud formation Morimoto et al. (2013), compared the elevation of the mixing layer developed using the observed dataset of sensible heat flux with the LCL, in which he confirmed the cloud formation to be greater in the urban area of the Matsuyama plain exceeding the LCL due to the significant supply of sensible heat as compared to the rural area as indicated in Figure 1.4.

The cloud optical thickness from the transmitted flux of solar irradiance has been studied for the ground based measurement of the solar irradiance using a pyranometer (Leontyeva and Stamnes, 1994). Thapa Chhetri et al. (2015), has confirmed that the reduction in solar radiation is closely associated to the thickness of the cloud. Therefore, the magnitude of the solar radiation becomes an index of the thickness of the cloud aloft. However, there are many difficulties in measuring the amount of solar radiation with high spatial resolution due to the limitation of the number of the meteorological observatories. The use of pyranometer has been widely used for the measurement of the solar radiation throughout the world. Duchon and O'Malley (1999), has suggested an analysis of the time series of irradiance from a pyranometer is an inexpensive and automated method used for the assessment of cloud type. Sakai and Umetani (2009), has studied the potential of small amorphous silicon solar cells as a device to monitor solar radiation. However, the solar panels mounted on the roof are usually of various types and installed at a fixed angle in much larger scale. The solar radiation reaching a titled surface includes reflection from the surrounding and the irradiance reaching the titled surface depend on the tilt angle (solid angle of the sky) and azimuth of the receiving surface, solar elevation angle, solar azimuth and cloud condition within the solid angle (Behr, 1997).

The accurate measurement of the solar radiation is necessary for understanding the local climate. Thus, it is necessary to understand the basic concept of the solar radiation and

have knowledge of the past studies and findings for the comprehensive monitoring and analysis of the radiation within an observation area.

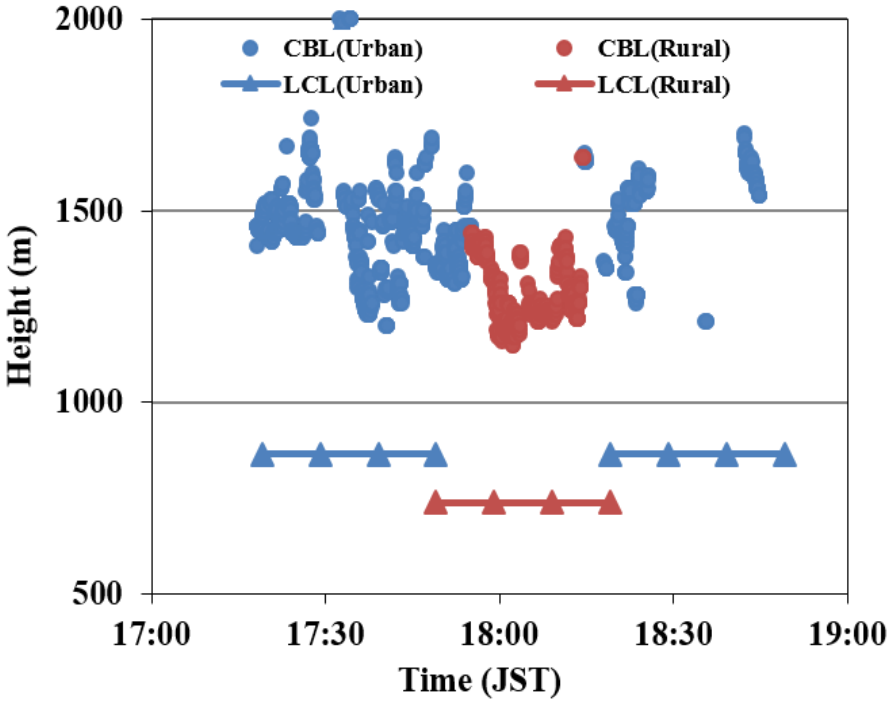

Figure 1.3: Observation of cloud base level (CBL), July 6, 2011 (Moriwaki et al. 2013)

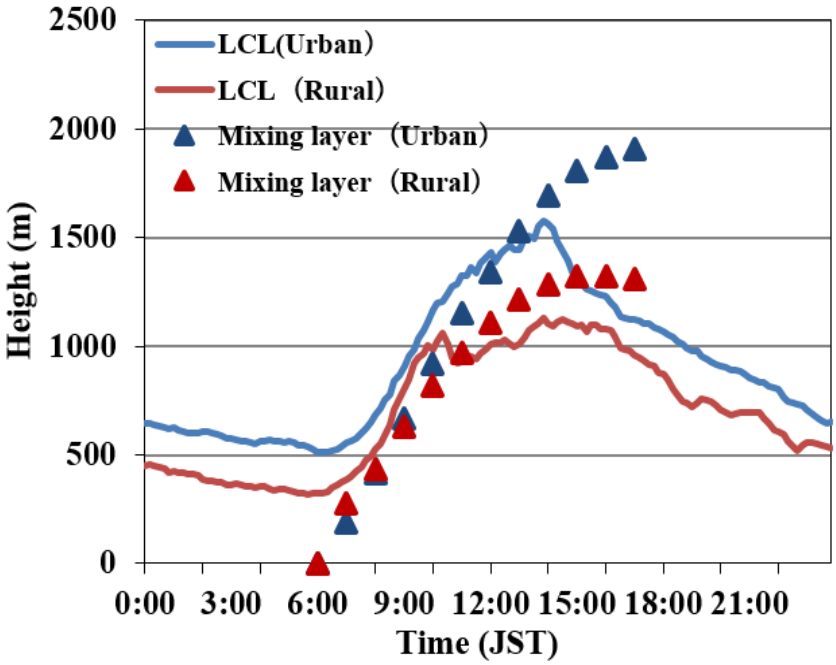

Figure 1.4: Comparison of the lifted condensation level (LCL) and the elevation of mixing layer, September 2010 (Morimoto et al. 2013)

1.2 Solar radiation

1.2.1 Measuring solar radiation

Solar radiation is a generally defined as energy emitted by the sun in the form of electromagnetic radiation. The total amount of solar radiation received at normal incidence at the top of the earth's atmosphere, at the mean sun-earth distance, is referred to as the Total Solar Irradiance (TSI) or extra-terrestrial solar irradiance (Coulson, 1975). The energy of extra-terrestrial solar radiation is distributed over a wide continuous spectrum ranging from ultraviolet to infrared rays. In this spectrum, solar radiation in short wavelengths (0.29 to 3.0 μm) accounts for about 97 percent of the total energy. Solar radiation is partly absorbed, scattered and reflected by molecules, aerosols, water vapor and clouds as it passes through the atmosphere. Approximately 25% of the incoming solar radiation is reflected back by the clouds in the atmosphere, other 10-12% of the incoming radiation either scattered or reflected by the surface of the land, by the atmosphere, by clouds and by the suspended material in the atmosphere further leaving about 65% to be absorbed by the atmosphere and the surface of the earth (Weisberg 1981). The incoming solar radiation arriving directly at the earth's surface is called direct beam solar radiation. The total amount of solar radiation falling on a horizontal surface (i.e. the direct solar beam plus diffuse solar radiation on a horizontal surface) is referred as global solar radiation. Direct solar radiation is observed from sunrise to sunset, while global solar radiation is observed in the twilight before sunrise and after sunset, despite its diminished intensity at these times. The SI unit for the measure of irradiance (radiative flux) is Watts per square meter (Wm^{-2}). Conversion between the currently used unit (SI) and the former unit (calories) can be performed using the following formulae:

$$\begin{aligned} &\textit{Solar irradiance}: 1\,\mathrm{kWm}^{-2} = 1.433\,\mathrm{calcm}^{-2}\mathrm{min}^{-1} \\ &\textit{Solar irrdiance}: 1\,\mathrm{MJm}^{-2} = 23.89\,\mathrm{calcm}^{-2} \end{aligned} \qquad (1.2)$$

According to RIC Japan Meteorological Agency (JMA), the total amount of global solar radiation per day is about 20 MJm^{-2} in the summer in Okinawa and about 5 MJm^{-2} in the winter along the Sea of Japan (Measurement of sunshine duration)

Solar radiation reaching the earth's surface varies significantly with location, atmospheric conditions including cloud cover, aerosol content, and ozone layer condition

and time of day earth/sun distance solar and ozone layer condition, and time of day, earth/sun distance, solar rotation and activity (Forgan, 2011). The World Meteorological Organization (WMO), defines sunshine hours the period during which direct solar irradiance exceeds a threshold value of 120 watts per square meter (Wm^{-2}) which is equivalent to the level of solar irradiance shortly after sunrise or shortly before sunset in cloud-free conditions.

Campbell-stoles sunshine recorder and Jordan sunshine recorder has been widely used for the measurement of the sunshine duration, whereas various other sunshine recorders such as rotating sunshine recorder, solar-cell-type sunshine recorder using photo-sensors as radiation has also been developed (Jarraud, 2008). At the mean distance between Earth and sun of 150 million kilometers, the flux of the solar radiation reaching the Earth's atmosphere is 1,367 W/m^2 (WMO, 1982) which is defined as the solar constant.

High quality ground-based measurements of solar radiation are always made using radiometers with a flat spectral response over a wide spectral bandwidth. This is usually achieved using a 'thermopile' detector with a black coating that absorbs the incoming radiation, heats up, and converts the temperature rise into a small electrical signal.

According to International Standard ISO 9060:1990 and the World Meteorological Organization (WMO) a pyranometer is the designated type of instrument for the measurement of hemispherical (global or diffuse) solar radiation integrated over the wavelength range from 0.3 μm to 3 μm (300 nm to 3000 nm).

Over the course of time researchers have developed number of correlation and method for the estimation of the daily or monthly global solar radiation on the basis of available meteoroidal parameters. The models which have been used to calculate solar radiation are usually based on the following factors (Besharat et al., 2013):

(1) Astronomical factors (solar constant, earth-sun distance, solar declination and hour angle).

(2) Geographical factors (latitude, longitude and elevation of the site).

(3) Geometrical factors (azimuth angle of the surface, tilt angle of the surface, sun elevation angle, sun azimuth angle).

(4) Physical factors (scattering of air molecules, water vapor content, scattering of dust and other atmospheric constituents such as O_2, N_2, CO_2, O, etc.).

(5) Meteorological factors (extra-terrestrial solar radiation, sunshine duration, temperature, precipitation, relative humidity, effects of cloudiness, soil temperature, evaporation, reflection of the surroundings, etc.).

1.2.2 Empirical models

The empirical models employ the atmospheric transmissivity and several meteorological variables for the study of the solar radiation. The empirical model can be mainly classified into four following categories based on the available meteorological parameters as follows:

(1) Sunshine-based models

One of the most commonly used parameter for the estimation of the solar radiation is the sunshine duration. A very high correlation between the daily sunshine and daily solar radiation has been explained by several researchers such as Ångström and Rodhe (1966), Drummond (1956) and others.

(2) Cloud-based models

Clouds are one of the most important forces that governs the earth's heat balance and hydrological cycle. the reduction in solar radiation is closely associated to the thickness of the cloud Long et al. (2006), Thapa Chettri et al. (2015) and so on. Large scale cloud information is available from satellites observations leading to the development of several model to estimate the solar radiation using the cloud information such as cloud cover, clouds types.

(3) Temperature-based models

Estimation of solar radiation using temperature is very common due to easy availability of the dataset. These model are especially beneficial to the area where the availability of the cloud information or other meteorological parameters are not available. The relationship between the ratio of the incoming solar radiation at the top of the atmosphere and the effect on the maximum and minimum daily temperature under clear sky condition has been explained by several researchers such as Bindi and Miglietta (1998), Jong and Steward (1993), Fortin et al. (2008) and others.

(4) Other meteorological parameter-based models

Several models based of other meteorological parameters such as relative humidity, precipitation, evaporation, pressure, wind speed and direction has been widely used for the

estimation of the solar radiation. For the accurate and reliable estimating of the global solar radiation various meteorological parameters are used in combination.

1.2.3 Physical factor based models

These models employ the algorithm to model the transfer of solar radiation through the atmosphere based on several laws of physics and mathematical relationships. Absorption of solar radiation by atmospheric molecules is a process that converts incoming energy to heat and is mainly due to water, oxygen, carbon dioxide, ozone (Spencer, 1971) and scattered by molecules, aerosols and cloud particles (Liou, 2002).

Physically- based models generally rely on estimates of atmospheric composition derived from numerical weather prediction models (Dee et al., 2011). Several numerical weather prediction model have been developed such as Weather Research and Forecasting Model (WRF), Integrated Forecasting System (IFS) used by ERA-interim, Ensemble forecasting and many more. Due to the complexity of the radiative transfer and high temporal and spatial variability of atmospheric composition these model requires numerous input parameters and physics, numeric, boundary layer information and others.

1.2.4 Satellite observation

Geostationary satellites are the most important source of satellite-derived solar radiation. Tarpley (1979), applied satellite technique to geostationary satellite (located at 37500 km above the Equator at 75^{o}W) to estimate the insolation at the surface and found a standard error in the satellite-derived daily insolation of 10% of the mean when compared against the pyranometer observation. Gautier et al. (1980), used geostationary satellite data with high spatial resolution (~2 km at 45^{o} latitude) to study the cloud variability and estimated the daily cumulative insolation in a large variety of cloud cases within 9% of the mean insolation measured by the pyranometer. Large scale cloud information is available from the several satellites but such data might be provided in a low resolution and may contain error. According per study of Goodman and Henderson-seller (1988), satellite retrievals have known weaknesses in quantifying small and low latitude cloud features due to their limited spatial resolution. Moreover, it is difficult to determine the solar obstruction from the satellite sensor which is of utmost importance in radiation/cloud studies (Long et

al., 2006). Several satellite observations from geostationary weather satellite, including the American Geostationary Operational Environmental Satellite (GOES), the European Meteosat missions, the Indian National Satellite (INSAT), Japanese Geostationary Meteorological Satellite (HIMAWARI) for the global measurement except polar regions are available whereas for polar region several polar orbiting satellite such as NOAA/AVHRR are available.

1.3 Importance of solar radiation

The sun is a sphere of intensely hot gaseous matter with a diameter of 1.39×10^9 m and is, on the average, 1.5×10^{11} m from the earth (Lutgens and Tarbuck, 1992). The sun has an effective blackbody temperature of 5777 K. The temperature in the central interior regions is variously estimated at 8×10^6 to 40×10^6 K and the density is estimated to be about 100 times that of water. The sun's structure and characteristics determine the nature of the energy it radiates into space. Solar energy represents more than 99.9% of the energy that heats the earth. However, the energy is not distributed equally over the earth's land-sea surface. The solar radiation is measured as the function of the wavelength is known as spectral irradiance

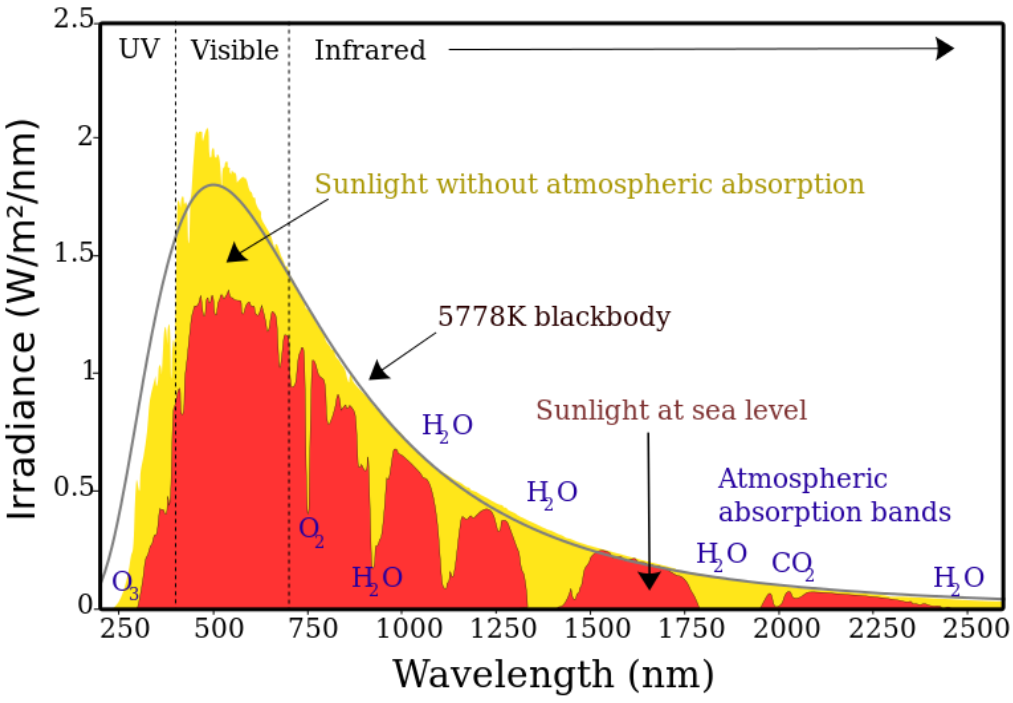

Figure 1.5: Spectral distribution of solar radiation above atmosphere and at surface

(Source:Nick84- http://commons.wikimedia.org/wiki/File:Solar_spectrum_ita.svg)

as indicated in Figure 1.5. The solar spectral irradiance is a measure of the brightness of the entire sun at a wavelength of light from the radio waves, infrared (IR) to visible and, through the ultraviolet (UV) to the smallest x-ray and gamma rays. These waves travel at the speed of light of about 300,000 kilometers per second. the measurement of the spectral irradiance is important because different wavelength of the sun is absorbed at different parts of the atmosphere (Lutgens and Tarbuck, 1992).

The earth's temperature, climate and chemistry depends on the absorption of the solar radiation which in turn plays an important role for the estimation of the global temperature and energy balance of the earth. Thus, the accurate measurement of the solar radiation is of utmost importance for many field of study such as climatology, meteorology, biodiversity, agriculture hydrology and many more.

1.4 Ground based measurement of radiation

As mentioned in the previous section there are different methods and model available for the measurement and estimation of the incoming solar radiation. Each models and method have their own advantages and some limitations. Satellite observation has been widely used for the measurement of the solar radiation but there might be some limitation when it comes to the temporal and spatial variability of the dataset (Long et al., 2006; Goodman and Henderson-Seller, 1988; and others). Watanabe et al. (2013), in their study of the cloud classification using the MTSAT data have pointed out that the 25 years' data (1980 – 2008) provided by International satellite cloud climatology project under NASA, is useful for the long-term radiation balance in the global scale but might have some limitation when it comes to smaller spatial resolution of 200-300 km at a temporal resolution of 3 hrs. Several researchers have compared the solar insolation from the geostationary (GOES) with pyranometer network (Gautier et al., 1980; Bland, 1996 and others) and reported the result to be better for a longer time integration with the accuracy of on daily insolation on the order of about 10% compared to the ground-based measurement.

Tarpley (1979), stated the importance of the temporal resolution of the data for the estimation of the solar radiation. A ground-based pyranometer provides continuous time solar data over the day compared to the satellite data which are instantaneous and taken at a fixed time interval representing solar radiation at particular time. Similarly, satellite estimation of the solar radiation represents an areal average, which might vary with the pixel

size of the sensor as well as the location. This might be considered as an advantage when a large domain with high spatial resolution is considered but might be considered as disadvantage compared to the point measurement made by the pyranometer specially when focusing on study of local climate of a smaller area (Diak et al., 1996).

The global horizontal irradiance falling on the earth's surface consists of diffuse horizontal radiation and direct beam radiation. Studies have suggested that the measurement of the total global radiation can be obtained by combining separate measurement of the direct beam solar radiation and the diffuse solar radiation to minimize the error (Michalsky et al., 1999; Ohmura et al., 1998). High quality ground-based measurement of solar radiation is made using the solar radiometers. Direct beam radiation is measured using a pyrheliometer and global solar radiation is measured using a pyranometer whereas for the diffuse radiation a shaded pyranometer can be used. The detail explanation on the types of radiometers are explained in Chapter 2.

1.5 Scope and objective of the study

Many studies have been conducted to study the impact of urbanization on climate change around the world using available meteorological data, satellite observation data and so on. However due to some limitation all these data might not be universally available. Moreover, these studies are mainly focused on the mega cities whereas least study are available for rapidly developing areas around the world. The effect of urbanization on the torrential rainfall and local climate has still not been elucidated. Therefore, it is necessary to perform a more detailed study on the generation of the localized rainfall, local climate. This research is mainly focused on studying the urban local climate of a small city of Japan which is rapidly being urbanized.

The main objective of the research is to study the local climate using the cloud coverage based on the ground-based solar radiation measurement in the Matsuyama plain. To fulfil the main objective of the thesis, the study is further categorized into two minor objectives described below:

1. To explore the potential for using the statistical analysis (standard deviation) of time series of one hour averaged pyranometer observation for temporal and spatial variation of the clouds types in the Matsuyama plain.

2. To explore the potential of a photovoltaic (PV) system to explore the temporal and spatial variation pattern of the solar radiation

The ground-based measurement includes a pyranometer network covering the study area. As establishing pyranometer network is not financially and practically applicable, the applicability of the photovoltaic network was studied for the estimation of the global solar radiation using photovoltaic system. As solar panels have already been installed in many houses, commercial buildings, schools, the estimation method proposed in this study is promising for the monitoring of the spatial and temporal variation of the solar radiation, which is beneficial for the local climate studies such as torrential rainfall, urban heat island phenomena. Further this study is applicable for all the megacities and urbanizing areas with increasing number of PV system for monitoring the effects of urbanization.

1.6 Outline of the thesis

The solar radiation is the main driving force for the Earth's weather and climate. The amount of solar radiation reaching the earth surface is in turn affected by the cloud coverage. Thus, the scientific research and technologies for the accurate determination of the terrestrial solar radiation distribution and the study of cloud and its characteristics can improve the long-term climate change. But the accurate assessment of the solar radiation is difficult due to spatial and temporal variability especially for the study of the local climate where the meteorological observations and radiation assessments are limited. In the light of the above problem, the study is aimed at the radiation assessment using the radiometer (pyranometer network) and further use of solar panel for the terrestrial solar radiation measurement.

The content of the thesis is basically divided into two major section including pyranometer network monitoring and dense panel network monitoring which further includes the comparison of the observation data between the two ground-based measurement techniques. To fulfil the overall objective of the study, the contents of each chapter of the thesis is briefly outlined below:

Chapter 2 describes the fundamental concepts of the solar radiation, the components of the solar radiation such as direct beam solar radiation diffuse solar radiation and the global solar radiation also including the concept of extra-terrestrial radiation. The chapter also introduces the radiometer and sky condition along with the cloud classification that influence the distribution and the measurement of the global solar radiation.

Chapter 3 describes the ground-based measurement of the solar radiation in the study area using the pyranometer network monitoring. The chapter further describes the concept of the clear sky rate and its temporal and spatial variation during the study period. The analyzed data are further validated using the whole-sky photography and meteorological modelling. The classification of the cloud based on the one-hour averaged time standard deviation of the clear sky rate is conducted using the whole-sky photography.

Chapter 4 describes the ground-based measurement of the solar radiation using the dense solar panel monitoring. The estimation of the global solar radiation from the solar radiation on a slope along with the calculation of the diffuse ratio is also conducted and was confirmed for all the sky condition (cloudy condition, partially cloudy and sunny weather condition). The estimated global solar radiation was further compared with the measured solar radiation on the slope for the validation of the estimation method.

Chapter 5 describes the comparison of the solar radiation of the pyranometer network monitoring and the estimated solar radiation using the solar panel monitoring. The observed dataset was further used for understanding the characteristics and the type of clouds using the whole-sky photography.

Chapter 6, the concluding chapter summarizes the overall outcome of the study and discusses the key outcome of the thesis. This chapter further provides the prospective for the future study and recommendation for the improvement of the accuracy of the solar radiation measurement and the cloud classification for the near future which can be beneficial for understanding the local climate of the study area and prevention/mitigation of the disaster events due to localized torrential rainfall.

The framework of the thesis is summarized in the Figure 1.6, which highlights from the beginning of the research, the data monitoring and analysis and finally the preparation of the thesis.

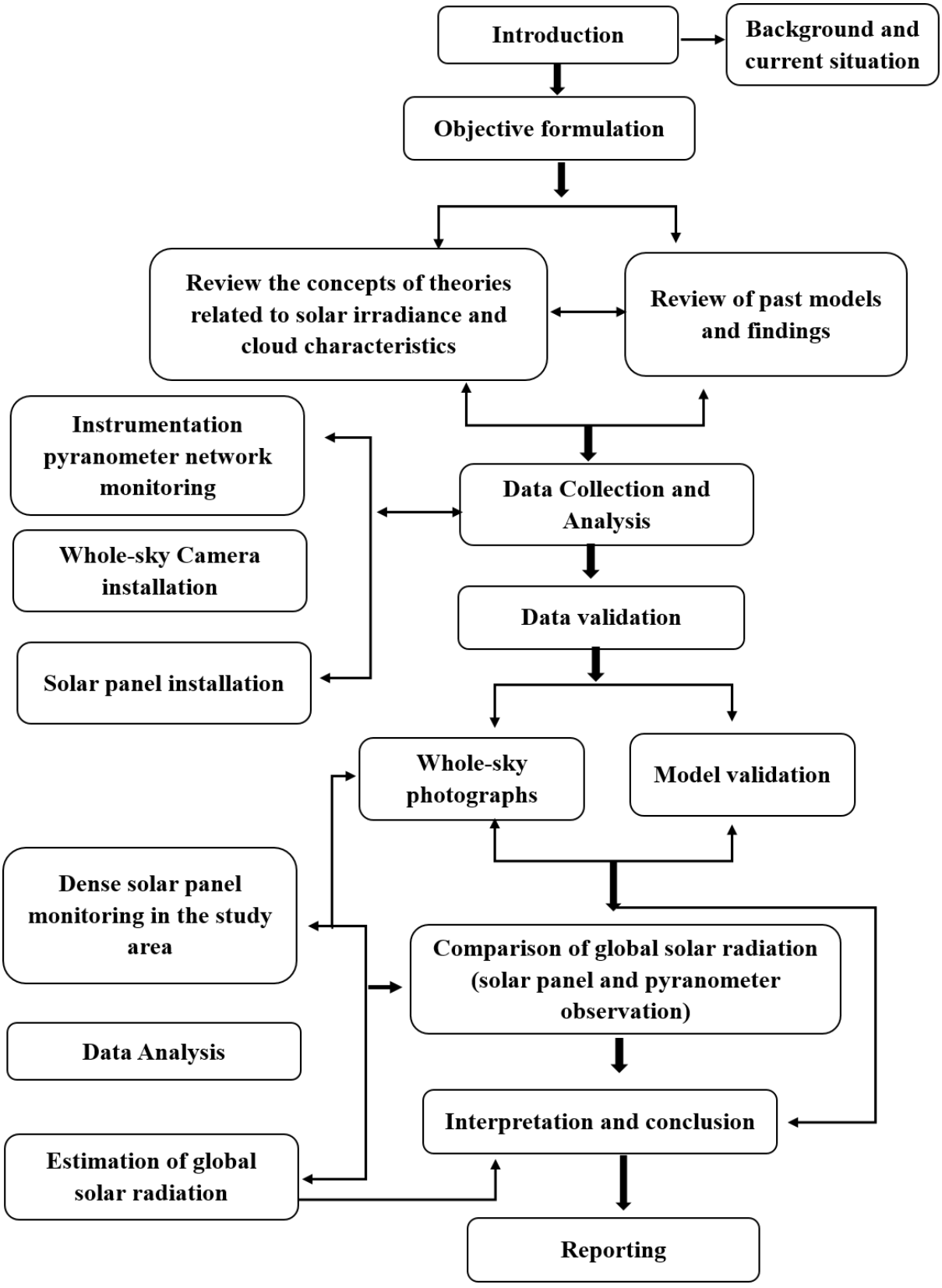

Figure 1.6: Framework of the overall study

1.7 Chapter summary

The chapter discussed about the solar radiation measurement that have been conducted for past many years along with the ground-based measurement which is one of the objective of this study. The purpose and interest behind the idea behind the measurement of the ground-based solar radiation for understanding the local climate of the Matsuyama was discussed. Finally, the outline of the overall thesis along with the framework of the study was presented.

CHAPTER 2

2. Fundamentals of solar radiations

The chapter 2 introduces the most important aspects of the solar radiation measurements; the measurement of the radiation at the top of the atmosphere (extra-terrestrial radiation) and the ground based measurement of the radiation. The components of the solar radiation, the instrument used for the measurement of the different components of the radiation are also discussed in detail.

2.1 Components of solar radiation

The solar radiation reaching the earth's surface is partly reflected and partly absorbed depending on the reflectivity of the surface. Both influence the extra-terrestrial spectrum by considering modifying the spectral energy passing through the atmosphere

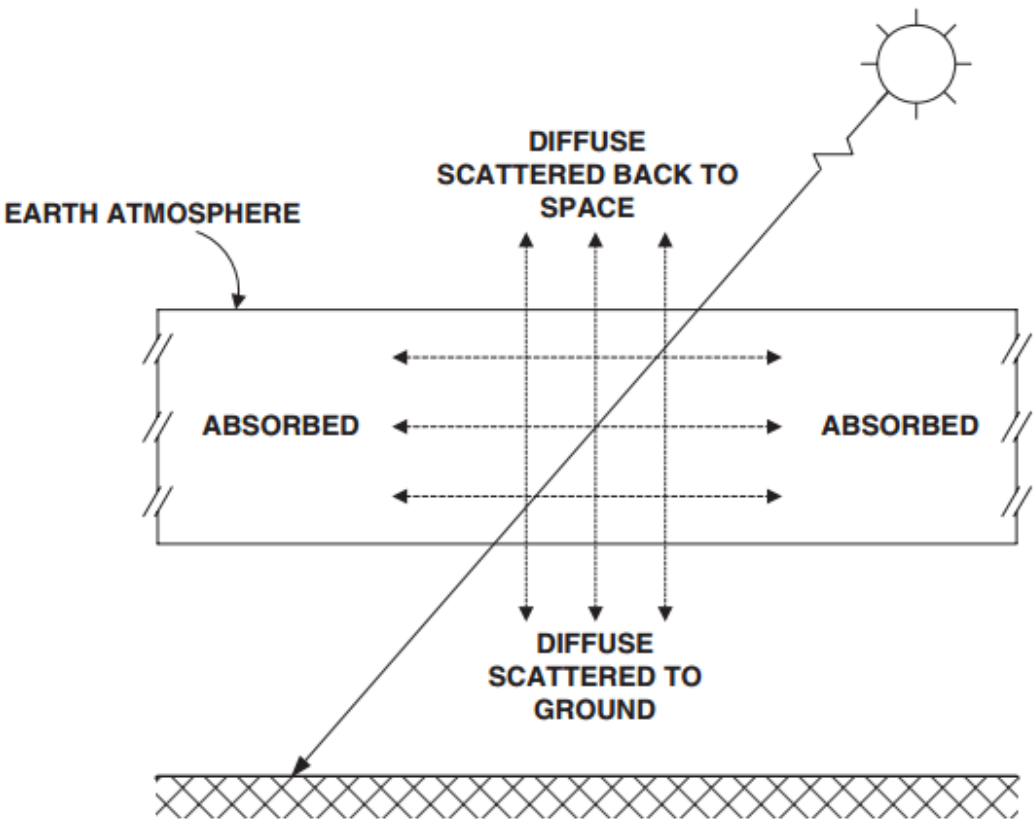

Figure 2.1: Components of solar radiation (Iqbal, 1983)

(Iqbal, 1983). The amount of energy reflected, scattered and absorbed depends on the amount of atmosphere that the incident radiation travels through as well as the levels of dust particles and water vapor present in the atmosphere (ITACA). The different components of the solar radiation are illustrated in the Figure 2.1.

2.1.1 Direct beam solar radiation

Direct beam solar radiation (also referred to as direct normal irradiance) is a measure of the rate of solar energy arriving at the Earth's surface from the Sun's direct beam, on a plane perpendicular to the beam, and is usually measured by a pyrheliometer mounted on a solar tracker (Drummond, 1956). The computation of the normal beam radiation is based on the precise measurement of the extra-terrestrial solar radiation and its spectral distribution and the attenuation characteristics of the atmospheric constituents as the function of the wavelength.

Spencer has provided function of the solar elevation h as the equation form of a higher degree polynomial of as the estimation of the normal beam solar radiation as indicates in Equation 2.1.

$$I_N = a_1 \sin \mathrm{h} + a_2 \sin^2 h + a_3 \sin^3 h + a_4 \sin^4 h + a_5 \sin^5 h \qquad (2.1)$$

Lambert's cosine law states that the energy flux density on a plane surface is directly proportional to the cosine of the incidence angle (Paulescu et al. 2013). Once the normal beam radiation I_N is calculated, the direct beam radiation on any tilted surface can be easily estimated by using the relation as follow.

$$I_b = I_N \cos \theta_z \qquad (2.2)$$

Where,

I_b is the direct beam solar radiation and

θ_z is the zenith angle

This is further illustrated by Equation 2.3.

$$\cos\theta_z = \sin\phi\sin\delta + \cos\phi\cos\delta\cos\omega \qquad (2.3)$$

Where,

ϕ is the local latitude

δ is the declination angle of the sun and

ω is the hour angle

The direct beam solar radiation measurement is difficult due to its major dependency on the aerosol present in the atmosphere (Gueymard, 2012)

2.1.2 Diffuse solar radiation

Diffuse solar irradiance is a measure of the rate of incoming solar energy on a horizontal plane at the Earth's surface resulting from scattering of the sun's beam due to atmospheric constituents. Diffuse solar irradiance is measured by a pyranometer, with its glass dome shaded from the Sun's beam. The shading is accomplished either by an occulting disc or a shading arm attached to a solar tracker. The proportion of diffuse in the total solar radiation depends upon the latitude and elevation of the place in question the solar altitude, the value of the sun's declination, the degree of atmospheric turbidity (i.e. the concentration of suspended particulate matter in the atmosphere locally), the amount of water vapor present and the cloudiness (Drummond, 1956).

In atmosphere the main factors that determine scattering or diffusion are air density fluctuations and aerosols particles (water droplets, dust particles etc.) (Halthore and Schwartz, 2000). The diffusion due to density fluctuation is commonly named as molecular scattering. The scattering in which the dimension of the scattering medium is notably smaller than the wavelength is called Rayleigh scattering whereas if the particle size of the order of wavelength of incident radiation is scattering is termed as Mei scattering. If the size of the

particle is $\pi D/\lambda$, where D is the diameter, λ the wavelength in micrometres and n the refractive index, it is considered that (Iqbal, 1983).

1. When $\pi D/\lambda < 0.6/n$, scattering is governed by Rayleigh's theory and in cloudless atmosphere applies to air molecules
2. When $\pi D/\lambda > 5$, scattering is chiefly a diffuse reflection process seldom occurring in the earth's atmosphere
3. When $\pi D/\lambda < 0.6/n < 5$, scattering is governed by Mei's theory and applies to scattering by larger particle such as aerosols.

Various models such as Erbs et al. model (1982), Lam and Li model (1996) and many more based on the empirical formula describe the diffuse fraction as the ratio of the diffuse solar radiation to the global solar radiation. The daily diffuse solar radiation on the titled panel can be estimated using Hay Anisotropic model (Duffie and Beckman, 1980). Bird and Riordan (1986), presented a simple model for the calculation of the direct and diffuse irradiance on the horizontal and the titled planes for the cloudless condition. Davies and Mckay (1989), compared the 12 models used for the estimation of the irradiance and presented that Erbs et al. model (1982), provided the best estimation for the hourly and daily irradiance.

The Erbs et al. model (1982), is further used in this study during the estimation of the global solar radiation using the dataset of solar panel monitoring. The detail of the model is explained in Chapter 4 of the thesis.

2.1.3 Global solar radiation

Global solar irradiance is a measure of the rate of total incoming solar energy on a horizontal plane at the Earth's surface. The global solar radiation is the sum of the direct beam solar radiation and the diffuse solar radiation by Equation 2.4 (New solar energy utilization handbook, Japan solar energy society).

$$I = I_b \cos\theta_z + I_d \qquad (2.4)$$

Where,

I is the global solar radiation on a horizontal surface

I_b is the direction bean radiation

I_d is the diffuse solar radiation and

θ_z is the solar zenith angle

Global solar radiation is typically measured with a pyranometer. The estimation of the global solar radiation on a horizontal surface from the data of sunshine hours, empirical formula was developed by many researchers. The basic procedure is to develop the correlation between the ratio of monthly mean daily global radiation (I) to the extra-terrestrial radiation (I_0) on a horizontal surface and the ratio of the monthly mean sunshine hours (n) to maximum possible sunshine hours (Lim, 1980)

The most commonly obtained form of linear empirical equation is as follows;

$$(I/I_0) = a + b(n/N) \qquad (2.5)$$

Here,

$$I_0 = \frac{24}{\pi} I_{sc}\left(1 + 0.033\cos\frac{360n}{365}\right)\left(\cos\phi\cos\delta\sin\omega_s + \omega_s\left(\frac{\pi}{180}\right)\sin\phi\sin\delta\right) \qquad (2.6)$$

Where,

δ is the declination angle of the sun

ϕ is the local latitude and ω is the hour angle

I_{sc} is the solar constant

n is the day of the year that represents the mean daily radiation of the month and

a and b are the correlation coefficient

Similarly, various empirical methods considered as simple have been developed for the estimation of the global solar radiation considering the clearness index.

2.2 Extra-terrestrial radiation

The amount of radiation emitted from the sun may be regarded as substantially constant, but the amount of energy reaching the ground may vary both spatially and temporarily. In order to understand the atmospheric processes, the cause of the temporal and spatial variation in the amount of the radiation reaching the earth must be understood.

During the 24-hour rotation of the earth, the temperature on a given area of the earth rises in the morning, reach their peak during the afternoon and starts decreasing towards evening. The daily change on the temperature is the direct result of solar energy being absorbed by the earth's surface and then radiated back into the air. It is evident that over 97% of the total solar energy lies between 300nm to 2500nm. The solar energy confined to this spectral region is often referred to as short-wave solar radiation, and the integrated energy (over the same region) is referred to as broadband or total solar radiation.

Similarly, the earth's revolution in its axis around the sun causes the seasonal variation. The earth is traveling at nearly 113,000 kilometers per hour in an elliptical orbit about the sun. The distance between the earth and sun average 150 kilometers however the earth's orbit is not perfectly circular, so the distance varies during the course of year. The inclination of the earth's axis is not perpendicular with respect to its orbital movement around the sun, but tilted at an angle of 23.5 degrees towards or away from the sun which is termed as inclination of the axis (Myers, 2013).

The intensity of solar radiation that reaches the top of the atmosphere is inversely proportional to the square of the distance between the sun and the earth. The mean sun-earth distance is called one astronomical unit i.e. $1\,\mathrm{AU} = 1.496 \times 10^{8}\ \mathrm{km}$ The minimum sun-earth distance is about 0.983 AU, and the maximum distance is about 1.017 AU. The earth is at its closest point to the sun (perihelion) on approximately 3rd January and farthest point (aphelion) on approximately 4th July, whereas the mean distance from the sun is on approximately 4th April and 5th October (Iqbal, 1983).

Since, the distance between the sun and the earth varies a little throughout the year, thus considering the correction factor of the distance becomes important for the determination of the extra-terrestrial radiation as given in Equation 2.7 below.

$$E_o = \left(\frac{r_0}{r}\right)^2 = 1.000110 + 0.034221\cos\Gamma + 0.001280\sin\Gamma + 0.000719\cos 2\Gamma + 0.000077\sin 2\Gamma \qquad (2.7)$$

Here,

r_0 is the mean distance from the earth to the sun in km (1 AU = 1.496x10^8 km)

r is the distance from the earth to the sun in km,

Γ is the angle representing the earth's position in the elliptical orbit in radians as expressed in equation below.

$$\Gamma = 2\pi(d_n - 1)/365 \qquad (2.8)$$

Here, the d_n is the day number given in Nautical Almanac and ranges from 0 on 1st January to 364 on 31st December. During the leap year the change in the angle of declination is negligible and thus, the month of February is treated always considered as 28 days. Here, the maximum error in $(r_o/r)^2$ is less than 0.0001.

The solar constant, a measure of flux density, is the amount of incoming solar electromagnetic radiation per unit area (Johnson, 1954) that would be incident on a plane perpendicular to the rays, at a distance of one astronomical unit (AU). Based on the measurement made until 1970, a standard bale of 1353 Wm^{-2} was adopted. Gueymard (2004), obtained a solar constant of 1366.1 Wm-2 from the 24 years of space-borne irradiance measurement. However, based on subsequent measurement (Fröhlich and Brusa, 1981), a revised value as indicated in Equation 2.9 is used.

$$I_{sc} = 1367\ \mathrm{Wm}^{-2} \qquad (2.9)$$

The solar constant I_{sc} can be used to calculate the extra-terrestrial solar radiation incident on a surface perpendicular to the sun's rays outside and the earth's atmosphere on any day of the year. The extra-terrestrial radiation is calculated using the following Equation 2.10.

$$I_{ON} = I_{SC} \times E_o \qquad (2.10)$$

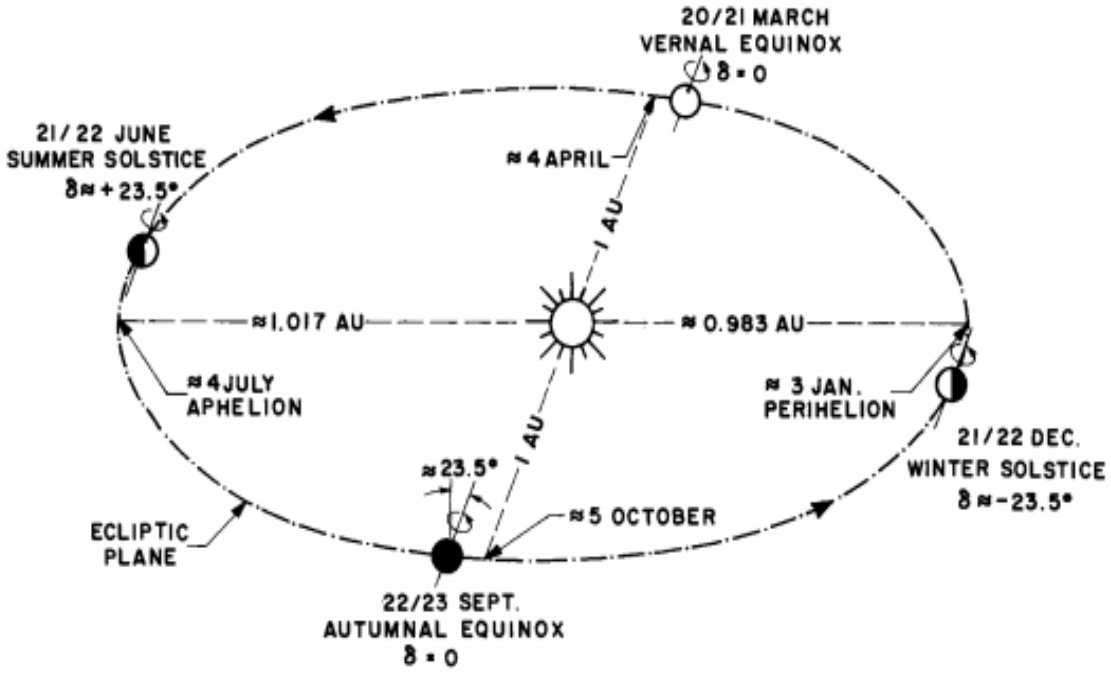

Figure 2.2: Motion of earth around the sun (Iqbal, 1983)

where,

I_{ON} is the extra-terrestrial normal solar radiation and

E_o is the correction factor of the distance between the earth and the sun.

- Solar declination

In absence of clouds, the sun moving across the sky during the day varies the insolation significantly by changing the direct beam's path length through the atmosphere and the projection angle of the sun on the horizontal surface. If the latitude, longitude, and local standard time (including the date) of the location are known the position of the sun (elevation and azimuth angle) can be computed. Astronomical data fluctuation in the intensity of the solar radiation of the earth's surface is largely dependent on the angle of incidence of the sun's ray in the earth's surface. For the estimation of the solar position and radiation intensity, the declination angle of the sun and equation of time are taken into consideration. The angle between the earth-sun line and the equatorial plane is called the declination angle which changes with the date and is independent of the location. The

declination angle is maximum at 23.45° on the summer/winter solstice and 0° on the equinoxes as indicated in the Figure 2.2.

In 24 hours, the maximum change in the declination angle is less than 0.5°, therefore the declination angle is assumed to be constant over a day with a maximum error of 0.5°. The declination angle of the sun is yielded by using the Fourier series as explained by Spencer and is illustrated in Equation 2.11.

$$\delta(\text{rad}) = (0.006918 - 0.399912\cos\Gamma + 0.070257\sin\Gamma - 0.006758\cos 2\Gamma + 0.000907\sin 2\Gamma - 0.002697\cos 3\Gamma + 0.00148\sin 3\Gamma)(180/\pi) \quad (2.11)$$

The other simple formula used for the calculation of the declination angle are

$$\delta = \sin^{-1}\left\{0.4\sin\left[\frac{360}{365}(d_n - 82)\right]\right\} \text{ in degrees} \quad (2.12)$$

$$\delta = 23.45\sin\left[\frac{360}{365}(d_n + 284)\right] \text{ in degrees} \quad (2.13)$$

Here, δ is the declination angle of the sun in radians. The series estimates the declination of the sun with a maximum error of 0.0006 radians equivalent to less than 3 seconds.

Solar time is based on the rotation of the earth about its polar axis ad its revolution around the sun. The solar day varies in length throughout the year. The equation of time Et in radians, is obtained from the Fourier series as illustrated in Equation 2.14

$$Et(\text{min}) = (0.000075 + 0.001868\cos\Gamma - 0.032077\sin\Gamma - 0.014615\cos 2\Gamma - 0.04089\sin 2\Gamma)(229.18) \quad (2.14)$$

The maximum error with this series is 0.0025 radians, equivalent to about 35 seconds of time. Since the equation of time is the difference between the mean solar time and true time, it can also be expressed by the following equation.

$$Equation\ of\ time\ (E_t) = True\ solar\ time - Mean\ solar\ time \quad (2.15)$$

By transforming Equation 2.15, the Equation 2.16 is obtained.

$$True\,solar\,time = Mean\,solar\,time + E_t \qquad (2.16)$$

$$True\,solar\,time = Local\,\text{standard}\,time + longitude\,correction + E_t \qquad (2.17)$$

The International Meridian Conference held in 1884, set the meridian that passes through the Greenwich astronomical observatory as the standard for longitude and determined that each country would use a time system that had a one-hour time difference at each 15° longitude interval.

$$True\,solar\ time\,(H_s) = \text{Local standard time} + 4(L - L_s) + E_t \qquad (2.18)$$

Where,

H_s is the true solar time in minute

L is the longitude of the observation point and

L_s is the longitude of the local standard time meridian.

The longitude of the local standard time meridian of Japan is 135^o East. L in case of east longitude is considered positive and west longitude negative, respectively. The net time correction factor (in minutes) accounts for the variation of the local solar time within a given time zone due to the longitudinal variation within the time zone and also incorporates the equation of time. The factor of 4 minutes comes from the fact that the earth rotates 1^o every 4 minutes.

The hour angle is an angular measure of the time and is equivalent to 15^o per hour. The hour angle (ω, in radian) converts the true solar time (TST) into the number of degrees which the sun moves across the sky. By definition, the hour Angle is 0° at solar noon (i.e. 12 o'clock). Since the Earth rotates 15° per hour, each hour away from solar noon corresponds to an angular motion of the sun in the sky of 15°. In the morning the hour angle is negative, in the afternoon the hour angle is positive as expressed in Equation 2.19.

$$\left.\begin{aligned}\omega(\text{rad}) &= 15(H_s - 12)\\ \omega(\text{rad}) &= 15(\text{H}_s + 12)\end{aligned}\right\} \qquad (2.19)$$

In the expression '-' sign is taken in degrees towards the west and '+' towards the east of the 0^o meridian (longitude, which passes through Greenwich in the United Kingdom. The altitude angle can be calculated by using the equation below

$$\sinh = \sin\phi\sin\delta + \cos\phi\cos\delta\cos\omega \qquad (2.20)$$

Similarly, the azimuth angle is expressed by the relation below

$$\sin\varphi = \cos\delta\sin\omega/\cosh \qquad (2.21)$$

Here,

h is the solar elevation angle in in degree

ϕ is the local latitude in degree and

δ is the declination angle of the sun.

The solar elevation is further expressed as

$$h = \sin^{-1}(\sinh) \qquad (2.22)$$

Thus from the above expression, the extra-terrestrial solar radiation can be computed as follows:

$$I_0 = I_{ON}\sinh \qquad (2.23)$$

2.3 Solar radiation measuring instrument (Radiometers)

Radiometry is the basic tool to attain solar radiation data. The pyrheliometer, mounted on a solar tracker, is used in the measurements of direct solar irradiance. The pyranometer is used for measurements of global solar irradiance. A common technique for the measurements of diffuse solar irradiance is a pyranometer equipped with a shadow band that shields off the direct sun beam. A radiometer absorbs solar radiation at its sensor, transforms it into heat and measures the resulting amount of heat to ascertain the level of solar radiation. Methods of measuring heat include taking out heat flux as a temperature change (using a water flow pyrheliometer, a silver-disk pyrheliometer or a bimetallic pyranograph) or as a thermos-electromotive force (using a thermoelectric pyrheliometer or a thermoelectric pyranometer). Thermal-type radiation sensors are employed by most of the specialized companies (for example Eplab, Kipp & Zonen and Eko).

2.3.1 Pyrheliometer

A pyrheliometer is used to measure direct solar radiation from the sun and its marginal periphery (JMA training workshop, 2013). To measure direct solar radiation correctly, its receiving surface must be arranged to be normal to the solar direction. For this reason, the instrument is usually mounted on a sun-tracking device called an equatorial mount.

Standard and secondary standard solar radiation instruments are pyrheliometer. The water flow pyrheliometer, designed by Abbot in 1905, was an early standard instrument which used cylindrical blackbody cavity to absorb radiation that is admitted through a collimating tube. Water flows around and over the absorbing cavity, and measurements of its temperature and flow rate provide the means for determining the absorbed energy. Various modification on the designs has been done in the course of time. Secondary standard pyrheliometer, that were calibrated against the standard instrument was devised.

The most common secondary standard pyrheliometer are described briefly below

- The Abbot silver disc pyrheliometer

  The Abbot silver disc pyrheliometer was built by Abbot in 1902 and modified in 1909 and 1927, uses a silver disc 38 mm in diameter and 7 mm thick as the radiation receiver.

- The Ångström compensation pyrheliometer

The Ångström compensation pyrheliometer build by K. Ångström in 1893 compensation pyrheliometer are two of the important secondary standard pyrheliometer and modified in several times since then. In this instrument two identical blackened manganin strips are arranged so that either one can be exposed to radiation at the base of collimating tubes by moving a reversible shutter. Each strip can be electrically heated, and each is fitted with a thermocouple. With one strip shaded and one strip exposed to radiation, a current is passed through the shaded strip to heat it to the same temperature as the exposed strip. When there is no difference in temperature, the electrical energy to the shaded strip must equal the solar radiation absorbed by the exposed strip.

One of the strip is exposed to the radiation, the other is screened to strip in order to keep the attached junction of the thermos-element in the middle of the strip at the same temperature as the junction at the middle of the illuminated strip. The two strip are then interchanged so that the strip previously covered is illuminated, and vice-versa. The intensity of the radiation is computed from the mean value obtained from measurement of the current.

The Abbot and Ångström instruments are used as secondary standards for calibration of other instruments, and there is a pyrheliometric scale associated with each of them. The first scale, based on measurements with the Ångström instrument, was established in 1905 (the Ångström scale of 1905, or AS05). The second, based on the Abbot silver disc pyrheliometer (which was in turn calibrated with a standard water flow pyrheliometer) was established in 1913 (the Smithsonian scale of 1913, or SS13). The schematic diagram of the silver-disk pyrheliometer is shown in Figure 2.3.

Operational or field instruments are calibrated against secondary standards and are the source of most of the data on which solar process engineering designs must be based. Brief descriptions of two of these, the Eppley normal-incidence pyrheliometer (NIP) and the Kipp & Zonen actinometer are included here. The Eppley NIP is the instrument in most common use in the United States for measuring beam solar radiation, and the Kipp & Zonen instrument is in wide use in Europe.

The detector is at the end of the collimating tube, which contains several diaphragms and is blackened on the inside. The detector is a multi-junction thermopile coated with Parson's optical black. Temperature compensation to minimize sensitivity to variations in ambient temperature is provided. The aperture angle of the instrument is 5.7^{o}, so the detector receives radiation from the sun and from an area of the circumsolar sky two orders of magnitude larger than that of the sun.

The Kipp & Zonen actinometer is based on the Linke-Feussner design and uses a 40-junction constantan-manganin thermopile with hot junctions heated by radiation and cold junctions in good thermal contact with the case. In this instrument the assembly of copper diaphragms and case has very large thermal capacity, orders of magnitude more than the hot junctions. On exposure to solar radiation the hot junctions rise quickly to temperatures above the cold junction; the difference in the temperatures provides a measure of the radiation. Other pyrheliometers were designed by Moll-Gorczynski, Yanishevskiy, and Michelson. The pyrheliometer has a drawback defining the beam radiation as the detector are not able to distinguish between the forward scattering radiation coming for the circumsolar sky and the beam radiation. The WMO recommends that calibration of pyrheliometer only be undertaken on days in which atmospheric clarity meets or exceeds a minimum value.

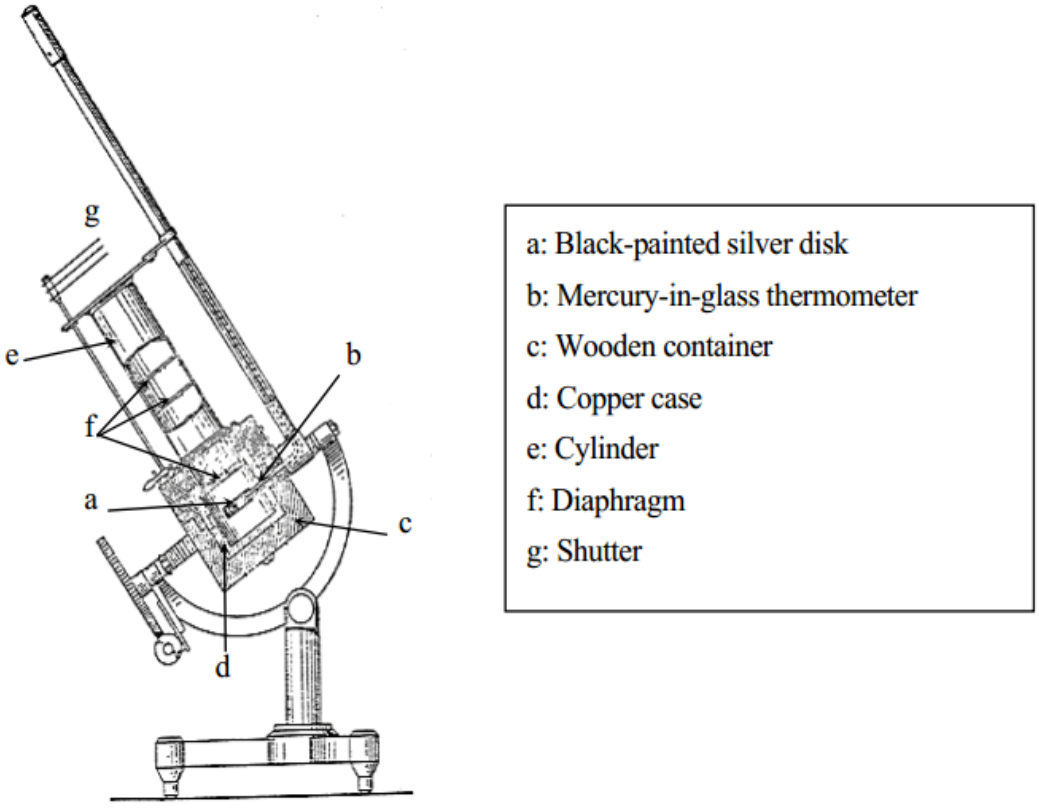

Figure 2.3: Schematic diagram of silver-disk pyrheliometer

(Source: JMA training workshop manual, RIC, WMO, 2013)

2.3.2 Pyranometer

Instruments for measuring total (direct beam and diffuse) radiation are referred to as pyranometers, and it is from these instruments that most of the available data on solar radiation are obtained.

The World Meteorological Organization (WMO) describes the pyranometer as an instrument ‘‘for measuring solar radiation from a solid angle of 2π into a plane surface and (with) a spectral range of 0.3 to 3.0mm’’ (WMO 1997). The detectors for these instruments must have a response independent of wavelength of radiation over the solar energy spectrum. In addition, they should have a response independent of the angle of incidence of the solar radiation. The detectors of most pyranometers are covered with one or two hemispherical glass covers to protect them from wind and other minor effects; the covers must be very uniform in thickness so as not to cause uneven distribution of radiation on the detectors. There are several kinds of pyranometer such as Eppley 180^{o} (No longer manufactured), Epplet precision spectral pyranometer (PSP), Moll-Gorczynski, Trickett-Norries (Groiss) pyranometers has been widely used in different parts of the world.

2.3.2.1 Principle component of pyranometer

The principle component of the pyranometer are illustrated in Figure 2.4.

Dome

The domes of a pyranometer can be considered transparent to solar radiation and opaque to most of the infrared radiation (Kipps and Zonen, 2006). The outer dome exchanges infrared radiation with the atmosphere, the outer space and the inner dome. The outer dome is considered to be nearly opaque in the IR wavelength. The inner dome also exchanges heat with the outer dome and the absorber. The dome material of the radiometer defines the spectral measurement range of the instrument. In general, about 97 – 98% of the solar radiation spectrum will be transmitted through the domes and will be absorbed by the detector. The solar irradiance can come from any direction within the hemisphere above the radiometer and therefore the domes are designed to minimize errors in measurement at all incident angles.

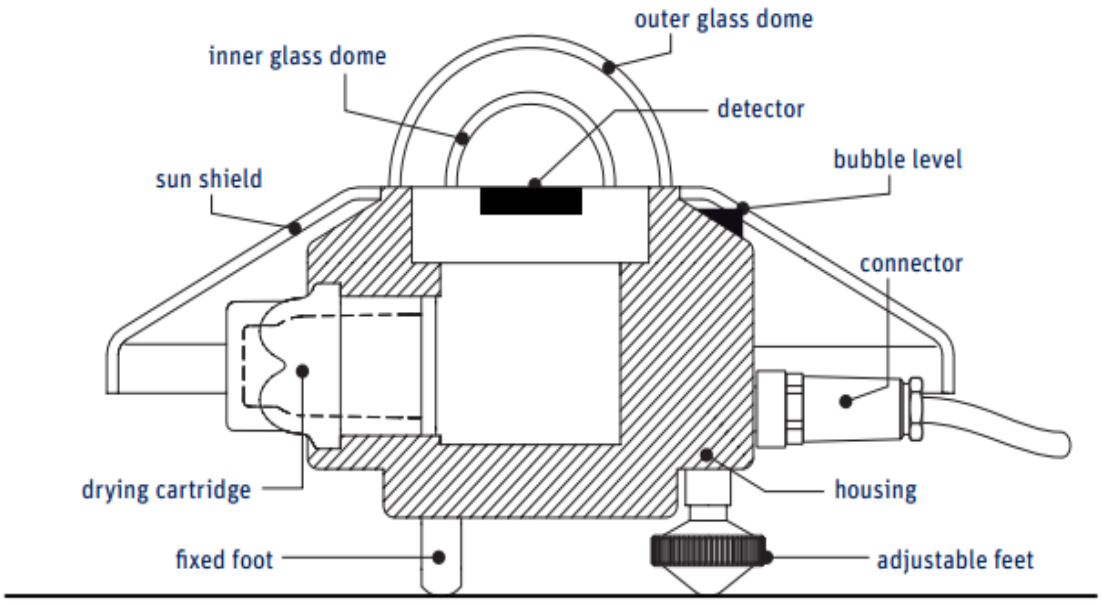

Figure 2.4: Schematic diagram of the component of the pyranometer

(Source: Kipps and Zonen, Instruction manual, 2015)

Detector

The thermopile sensing element is made up of a large number of thermocouple junction pairs connected electrically in series. The absorption of thermal radiation by one of the thermocouple junctions, called the active (or 'hot') junction, increases its temperature. The differential temperature between the active junction and a reference ('cold') junction kept at a fixed temperature produces an electromotive force directly proportional to the differential temperature created.

Housing

The radiometer housing comprises of anodized Aluminium parts which are light weight and give a high mechanical and thermal stability to the instrument. Due to its fine mechanical construction all pyranometers are virtually sealed and comply to the international standard IP 67. Each pyranometer model can be levelled by using the bubble level and two levelling

feet. The bubble level is situated next to the dome of the instrument and due to the special shape of the sun shield it is visible from above. The sun shield acts to protects all the external parts from radiation and to reduce solar heating of the housing.

Drying cartridge

In case moisture enters the radiometer body the silica-gel desiccant regulates the humidity level inside the pyranometer. Initially the desiccant will have an orange color. After some time, it becomes saturated with moisture and the color will change to become clear (transparent).

2.3.2.2 Physical properties of pyranometer:

a. Zero offset

Zero offset occurs when the sensor does not absorb radiation with wavelengths in the spectral range of the instrument and there is still a signal. Two types of zero offset can occur: type A zero offset, which is related to the thermal energy flux exchanged among the absorbing sensor, the glass dome and the sky and type B zero offset, which depends on the body temperature of the pyranometer (Padovan and Col, 2010).

A dome acts as both protection and a filter to the sensor. It also isolates the thermopile from convection. However, a dome alters the radiation balance between the sensor and the target, and introduces the dome effect. The thermal offset originates from a difference of temperature across the internal components of the instrument. The outer dome is usually colder than the body of the instrument and therefore colder than the inner dome, which in turn is colder than the absorber. The domes are transparent to a large fraction of the solar spectrum (0.3-2.5 μ m) whereas the body, although painted white, absorbs part of the solar radiation. The temperature gradient can therefore be greater during daytime than at night

Ji and Tsay (2000), developed an analytical model of the energy balance of the pyranometer to relate the instrument temperatures to the instrument offset. In this analysis the heat flux arriving at the detector is defined by Equation 2.24.

$$S = \left(\frac{1-\rho_d}{\varepsilon_s} + \rho_d \right) k\alpha\Delta V + \varepsilon_d (\sigma T_s^4 - \sigma T_d^4) + \tau(\sigma T_s^4 - L_{irr}) \qquad (2.24)$$

Here,

S	is the shortwave irradiance
α_s	is the thermopile constant
σ	is the Stenfan-Boltzman constant
ΔV	is the output voltage of the thermopile
L_{irr}	is the longwave irradiance
ε_s , ε_d	are the sensor and dome longwave emittances, respectively
τ	is the longwave transmittance
T_s , T_d	are the sensor and dome temperature, respectively.

The incident solar radiation corresponds to the voltage output of the thermopile and the thermal offset. The thermal dome effect of a pyranometer, can cause an underestimation of the downward irradiance exceeding 10 Wm^{-2} (Bush et al., 2000). Philipona (2002), reported that the pyranometer calibration in conjunction with thermal offsets and pyranometer thermal control demonstrate an underestimation of clear sky solar global, as well as diffuse irradiance by 8-20 Wm^{-2}, caused by pyranometer differential cooling. Field measurements with ‘‘conditioned’’ and ‘‘unconditioned’’ pyranometers demonstrate that the so-called night offset is present and considerably larger during daytime measurements, and this not only for diffuse but also for global pyranometer measurements.

Gulbrandsen (1978), in his study suggested an experiment to derive the offset signal from the measurements when the pyranometer is working during daytime which takes advantage of the fast response of the thermopile of the instrument. In his experiment he used a cap to shade the dome and the detector from all solar radiation in order to simulate the night time conditions (absence of solar irradiance) during daytime. However, the IR exchange between the dome and the detector, which is the cause of the thermal offset, remains unchanged. The output of the thermopile is then driven solely by the exchange of IR. Due to the fast response of the thermopile, the output of the instrument will rapidly follow the IR exchange. The IR exchange can be considered constant and equal to the IR exchange prior to capping during at least 30 second, after that the dome starts to reach the radiative

equilibrium with the body of the instrument. According to Dutton et al. (2001), the typical offset errors are on the order of 5–20 Wm^{-2} (95% limits), with extreme cases of 30 Wm^{-2} observed less than 0.1% of the time. These errors can be corrected to within 4 Wm^{-2} (in the daytime mean) when using verified correction functions determined from the relationship between night-time offsets and net IR thermal forcing. He further suggests three possible ways to address the thermal offset issue by redesigning the instrument to minimize the temperature gradient and the emissivity differences between the dome and the body of the PSP, determine the temperatures of the dome and body compute the error term and to develop a quantitative surrogate for the error term using available data.

b. Directional response

The directional error is an individual feature and depends on imperfections of the glass dome, angular reflection properties of the black paint and tolerance in the pyranometer construction. The sensor surface of the typical thermopile pyranometer is not lambertian and hence do not have perfect cosine response. Ideally, the pyranometer has a directional response "cosine response" which is influenced by the quality, dimension and the construction of the dome of the instrument (Martínez et al. 2009). The maximum deviation from the ideal cosine repose of the pyranometer is given up to 80^o angle of incidence with respect to 1000 Wm^{-2} irradiance at normal incidence (0^o) (Kipp and Zonen, CM21, Instruction manual).

The directional response for diffuse instruments in clear conditions is typically equivalent to the cosine response at zenith angles between 45^o and 60^o. Provided one has diffuse instruments with small deviation cosine response errors (say less than 63%) between 0^o and 70^o zenith angle and monotonic trends in this zenith angle range, the resulting variation in the diffuse response is small (less than 1%).

The magnitude for these directional errors can be minimized in conditions of scattered cloud conditions (with associated anisotropic sky radiance distributions) by choosing a detector with minimal variations in cosine response.

Michalsky et al. (1995), performed an automated cosine response test bench, to investigate and compare the cosine response of several commercial instruments. The study reported that the detector had directional error between the optical and the mechanical axe ranging between 0.1^o to 0.6^o, which may affect the measurement of the global solar radiation when the direct bean radiation is dominant.

Michalsky et al. (1999), in their study indicated that the non-ideal angular response of most pyranometer limits their accuracy to about 3%, or 20 -30 Wm^{-2}, for instantaneous clear sky measurements.

This tends to confirm that the major cause of the relative poor performance of the unshaded pyranometers as a group is due to the error introduced by the direct solar beam, especially at these larger zenith angles experienced during winter. It should be noted that different instruments have different cosine responses. In addition, if it can be shown that a given pyranometer has very small to negligible cosine error, the pyranometer can produce results nearly as accurate as the component sum. The radiation to a flat horizontal lambertian receiver such as pyranometer is proportional to zenith angle which peaks at 45^o and falls to zero at 0^o and 90^o and for the Eppley instrument whose cosine response relative to the perfect receiver decreases monotonically at higher angles of incidence, the calibration at 45^o is sensitive to the largest contribution of sky radiation and is too high relative to radiation received at lower angles of incidence and too low relative to radiation received at higher angles of incidence, thereby achieving some balance through offsetting errors. Thus, a pyranometer with an imperfect angular response will still have some error, but can be minimized.

c. Response time and ambient temperature

Pyranometer sensitivity changes with time and with exposure to radiation. The quality of the thermopile pyranometer is based on its time response and ambient temperature compensation The response time of a pyranometer sensor (usually seconds) is the time required to reach 95% of its final output signal. It is determined by the physical properties of the thermopile and the radiometer construction. The time response (1/e) of the basic thermal detection scheme for the PRT-based pyranometer without electronic enhancement is approximately 10s, and electronic compensation is used to enhance the time response to approximately 1s (Beaubien et al., 1998). CMP/CMA series radiometers have a fast response, which makes them suitable for measuring solar radiation under variable weather conditions.

The output of a thermopile is nonlinear and is influenced by ambient air temperature changes. Thermopile response is sensitive to temperature; usually the maximum deviation of the pyranometer sensitivity for a change in the ambient temperature within an interval of 50 K (Padovan and Col, 2010). These influences are usually corrected by means of

thermistor compensation circuitry. A fundamental requirement of any pyranometer is that its response be a function of the prevailing solar irradiance and not to changes in ambient air temperature.

2.3.3 Shaded pyranometer

The diffuse solar radiation can be measured by shielding a pyranometer from the direct beam solar by mounting of with a shade-ring or shadow-ring. Drummond (1956), explained the use of the shade-ring for the screening of the direct solar beam incorporating the shadow-ring correction to compensate for the sky energy. Theoretically, the angle subtended by a shadow ring at the receiver surface should be kept as small as possible, in order to reduce, to a minimum, the zone of sky which is unavoidably cut off by the ring.

Ohmura et al. (1998), explained the need of horizontal shadow band protect the pyranometer dome from being illuminated by the direct solar irradiance at low solar elevation and the angle sustained should be less than 5°, that is, covering base angles from 85° to 90°. He further suggested that the shaded pyranometer is less prone to directional error because its signal is the result of an integrated directional response. Here the signal is the product of the scattered radiation and $\sin(2\mu)$, where is the zenith angle and the integrated response is equivalent to directional responses between 40^o and 55^o. Generally, 10^o of the sun is shaded from the pyranometer throughout the year (Forgan, 1980). A critical shortcoming of the sunshade technique is its inability to determine zero offset, thus for the estimation of the global irradiance zero offset must be accounted correctly (Halthore and Schwartz, 2000). The use of shaded-ring or shadow bad is useful to avoid errors due to non-ideal angular responses of pyranometers lowering the uncertainty (Michalsky et al., 1999), but does not resolve pyranometer diffuse sky radiation problems that can lead to sub-Rayleigh irradiance values (Cess et al., 2000).

2.4 Sky condition and cloud type

Clouds are one of the most important moderators of the earth radiation budget and one of the least understood. According to WMO, the cloud is defined as s hydrometeor consisting of minute particles of liquid water or ice, or of both, suspended in the free air and usually not touching the ground which may also include non-aqueous liquid or solid particles

such as those present in fumes, smoke or dust. The appearance of the cloud is determined by the nature, sizes, number and distribution in space of its constituent particles. The appearance of the cloud is best described in terms of the dimensions, shape, structure, texture, luminance and color of the cloud. These factors determine the characteristics and form of the cloud. The effect that clouds have on the reflection and absorption of solar and terrestrial radiation is strongly influenced by their shape, size, and composition.

Clouds do not decrease the irradiance by a fixed amount instead they attenuate the sunlight by a certain percentage for that cloud type (Reno et al., 2012). Clouds are a major meteorological phenomena related to the hydrological cycle and affect the energy balance on both local and global scales through interaction with solar and terrestrial radiation.

Clouds may form at any altitude and under a wide variety of conditions such as rising of parcel of air into the atmosphere, mixing of two masses of air at different at different temperature, orographic influences, frontal system, cyclonic activity and convection (Weisberg, 1981). Cloud classification divides cloud into several types, or genuses. Meteorologist roughly classify high, middle and low clouds as well as those with vertical development.

Several studies have been done on cloud classification using satellite images as well as ground measurement as the cloud cover modulates the amount of solar radiation reaching the ground (Inoue, 1987; Calbo and Pages, 2001; Pfister et al., 2003; Calbo and Sabburg, 2008; Buch et al., 1995; Martínez -Chico et al., 2011; Inoue and Kimura, 2004, Long et al., 2006 and many more). Lutz et al. (2003) compared a spilt window (Inoue, 1987) and multi-spectral cloud classification for the MODIS observation with high efficiency but had some limitation for the thin clouds. Automated method for the real time classification of the all-sky imager were conducted by Heinle et al. (2010), based on the 12 features of cloud listed by WMO. Martínez -Chico et al, (2011), classified the cloud according to the altitude by using ground-based measurement of the solar radiation and the images of the total sky imagers (TSI). Wu et al. (2015), proposed a method to automatically recognize four different sky condition based on the extreme learning machine. Davies and Mckay (1982), proposed 'Mac Model' used the cloud layer optics (total cloud information) for the estimation of solar irradiance. Various type of classification such as block-based classification (Cheng and Yu, 2015), pixel based (Souza-Echer et al 2006), K-nearest and neural network (Singh and Glennen 2005), texture, class and shape features with K-nearest neighbor (Xia et al. 2015), feature extraction technique (Kliangsuawan and Heednacram, 2015), based on structure features of infrared images (Liu et al., 2011) and many more. The measurement of solar

radiation should be useful to derive sky and cloud characteristics as the solar radiation at a given site is affected by the meteorological variable which is further affected by the cloud cover (Calbó and Pages, 2001). O'Malley and Duchon (1996), used an analysis of the time series of irradiance from a pyranometer for the assessment of cloud type. Duchon and O'Malley (1999), used both the mean and the standard deviation of global irradiance in 21-min windows to categorize seven cloud types. Long and Ackerman (2000), used measurements of the down-welling global and diffuse shortwave radiation to identify periods of clear skies.

Table 2.1: Classification of the clouds based on altitude (WMO, 1975)

Class of cloud	Name	Height of base	Temperature at base	Main constituent	Precipitation	Appearance
High clouds	Cirrus (Ci)	5 -14 km	20°C to -60° C	Ice	No	White philaments, fibrous
	Cirrocumulus (Cc)	5 -14 km	20°C to -60° C	Ice	No	White patches or layers
	Cirrostratus	5 -14 km	20°C to -60° C	Ice	No	Translucent cloud veil
Medium clouds	Altocumulus (Ac)	2 -7 Km	10°C to -30°C	Water with some ice	Occasional	White grey layers
	Altostratus (As)	2 -7 Km	10°C to -30°C	Water with some ice	Occasional	Grey sheets with ice in row
Low clouds	Nimbostratus (Ns)	1 -3 km	10°C to - 15°C	Water and ice	Good rain	Dark grey layer
	Stratocumulus (Sc)	0.5 - 2 km	15°C to - 5°C	Water	Little rain	Grey patchy sheets
	Stratus (St)	0.5 km	20°C to - 5°C	Water	Drizzle	Grey uniform layer
Clouds with vertical growth	Towering cumulus or large cumulus	0.5 - 2 km	15°C to - 5°C	Water	Small showers	Detached clouds grow vertically
	Cumulonimbus (Cb) or Thunderstorm	0.5 - 2 km	15°C to - 5°C	Water	Heavy rain	Huge towering clouds

2.5 Chapter summary

This chapter discusses about the fundamental of solar radiation which are of utmost important for the study of the local climate. Here the basic components of the solar radiation such as direct beam solar radiation, diffuse solar radiation and global solar radiation and its measurement using various types of radiometers had been discussed.

The amount of solar radiation reaching the earth's surface is affected by various parameters such as aerosols, water vapor, various kinds of gases present in the atmosphere. Among various components clouds are one of the most important moderators of the earth radiation budget. Thus understanding the effect of the clouds on the amount of solar radiation plays a critical role for understanding the temporal and spatial change in the local climate.

CHAPTER 3

3. Ground based measurement of the solar radiation using pyranometer network

This chapter mainly focuses on the ground-based measurement of the distribution of solar radiation in the Matsuyama plain using pyranometer network. The objective of this chapter is to explore a method to investigate the distribution of the solar radiation and cloud characteristics by analyzing the temporal and spatial variation of the clear sky rate, which is defined as the ratio of blocked solar radiation to the total radiation, tested using pyranometer network and referencing the cloud image taken by a fisheye camera. This is new approach to examine the cloud type and may provide complemental information for the study of the local climate of the study area.

3.1 Site description

Matsuyama plain is located in the north-western part of the Shikoku island, which is the smallest province among the four provinces of Japan, located south of Honshu and east of island of Kyushu, Japan. It is mainly composed of alluvial fan formed by flooding of Shigenobu River and its territories. The plain covers about 20 km east-west and about 17 km north-south, with a total area of about 100 km^2. The northern part of the plain is urbanized whereas the rice paddy fields, farms are located in the surrounding countryside. Figure 3.1 shows the land use category of the Matsuyama plain created on the basis of land use classification of digital national land information (Geospatial Information Authority, GIA, Japan). The study area is being rapidly urbanized and the effect of urbanization has been observed in various researches based on the area. The difference in the land use in between the central city and the suburb along the Shigenobu River is clearly visible which makes is an appropriate area to study the impact of urbanization in the local climate.

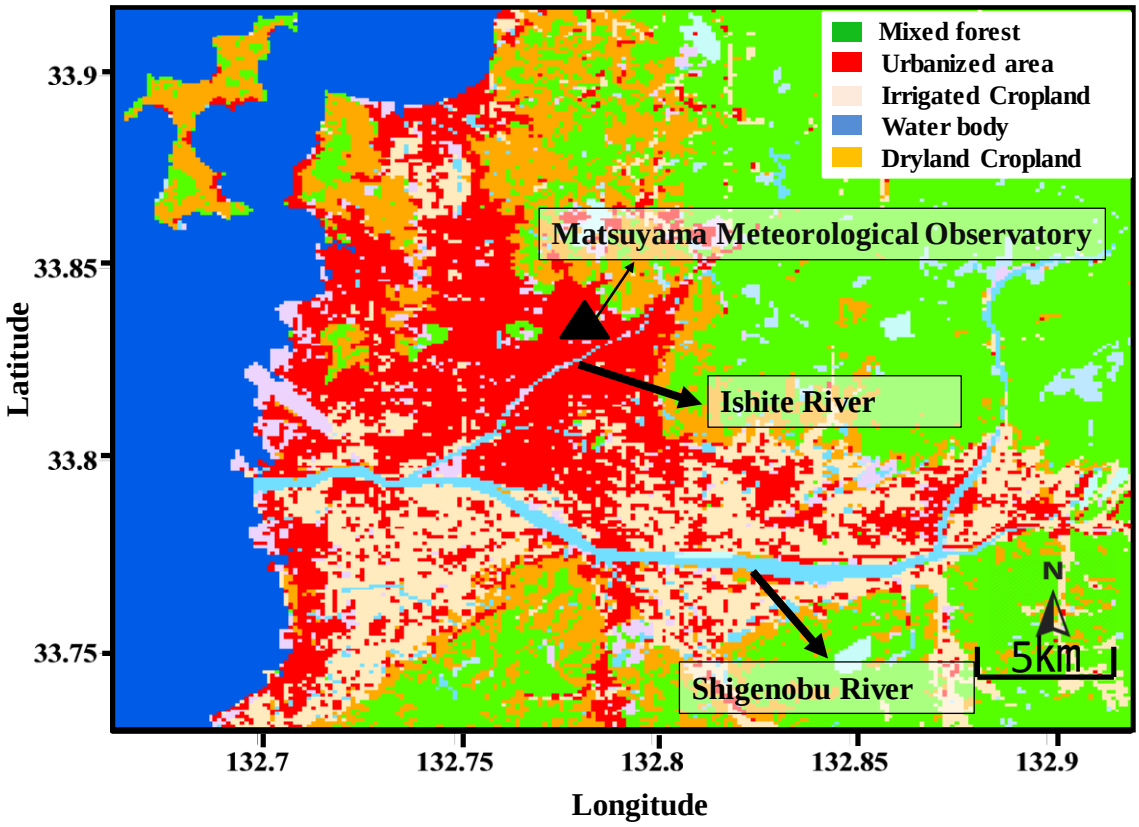

Figure 3.1: Land-use category of the Matsuyama Plain

3.2 Measurement of the solar radiation

The global solar radiation is mainly measured using a pyranometer. A pyranometer measures the hemispheric broadband solar radiation available to drive the daytime surface energy budget which integrate the effects of the cloud. The time series of irradiance captures the character of the cloudiness weighted toward the portion of the sky where the sun is located and provides the basis for estimating cloud type (Duchon and O'Malley, 1999).

Thus, to understand the distribution of the amount of solar radiation in the study area, continuous measurement of the global solar radiation is conducted with the help of pyranometer. The pyranometer used in the study is CMP-3EU (Kipp and Zonen) provided by Prede Cooperation Limited, Japan and was installed at various observation points in the Matsuyama plain (Figure 3.2). The specification of the pyranometer is provided in the Table 3.1.

Figure 3.2: The pyranometer (CMP-3EU, Kipp and Zonen) installed at Ehime University

A separate observation apparatus consisting of a data logger connected to the pyranometer was used to continuously record the amount of solar radiation The pyranometer does not require any power and supplies a low voltage of 0 to 20 mV in relation to the amount if incoming radiation. The data are recorded as voltage and the amount of solar radiation is calculated by dividing the observed data in voltage by the sensitivity coefficient of each pyranometer.

The instruments were placed on different sites of the study area where the continuous supply of power might not be possible for its operation. So a solar panel was mounted on the top of the apparatus to supply the power for the data logger. Data logger, battery and charge controller were kept inside a box to prevent damage from rainwater as indicated in Figure 3.3. The solar panel used and the housing of the apparatus was made by DreamLink Cooperation, Limited and the fast type data logger manufactured by M.C.S Cooperation Limited. The continuous measurement of the radiation was conducted from July 2014 till date.

Table 3.1: Specification of the pyranometer used for the radiation measurement (CMP-3EU, Kipp and Zonen)

ISO 9060:1990	Second Class
Spectral range	300 to 2800 nm (50% points)
Sensitivity	5 to 20 μV/W/m^2
Response time	18 sec (95%)
Zero offset A	< 15W/m^2 (Thermal radiation 200 W/m^2)
Zero offset B	< 5W/m^2 (Temperature change 5K/hr)
Directional response (up t0 80^o with 1000 W/m^2 beam)	< 20 W/m^2
Temperature dependence of sensitivity (-10^{o}C to +40^{o}C)	< 5%
Operational temperature range	(-40^{o}C to +80^{o}C)
Maximum solar irradiance	2000 W/m^2
Field of view	180^o
Internal resistance	20 to 200 Ω

a)

b)

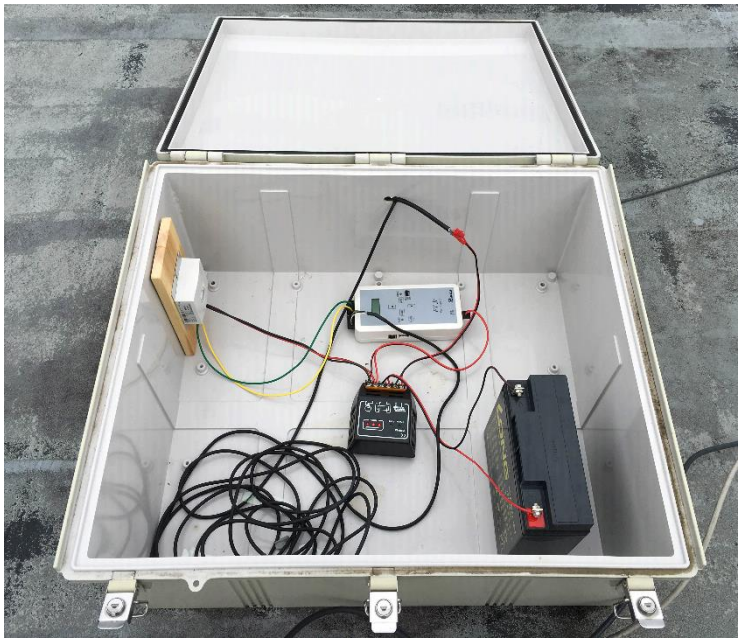

Figure 3.3: a) Apparatus mounted with solar panel, b) data logger and battery for radiation measurement

3.3 The ground network of pyranometer in Matsuyama

During July 2011, the pyranometer were installed at two locations focusing mainly in the urban area (Daiichi) and rural area (Suiden) of the Matsuyama plain. For the instrumentation, the branch office of the Daiichi, Higashiishi (132.812962^{o}E, 33.778939^{o}N) was selected. The surrounding area mainly consists of commercial buildings, residential apartments and paved roads (Figure 3.4a). In rural area the instrument was installed in the backyard of the water pumping facility, Masaki-cho (132.771509^{o}E, 33.79559^{o}N). The surrounding area comprised of paddy field (Figure 3.4 b). Upward and downward shortwave

a)

b)

Figure 3.4: Solar radiation measurement a) urban area and b) rural area

and longwave radiation intensities were measured using CNR-4 (Kipp and Zonen) for the urban site and MR-40 (EKO) for the rural site, respectively.

The representation of the distribution of the amount of radiation and cloud coverage of the entire Matsuyama plain was not sufficient from the ground-based observation from just using two observations points. Thus, to cover the entire study area, the ground-based measurement site needs to be increased to get the overall idea of the distribution of the solar radiation and its effect on the cloud formation. Hence, later from July 2014, in order to understand the temporal and spatial distribution of the amount of solar radiation in the study area, a pyranometer network was established by installing the instrument at 7 observation points within the Matsuyama plain. The observation site was selected so as to include the whole observation area i.e. from coastal area to inland area, urban area to rural area. The site and the condition of the instrumentation of the pyranometer is shown in Figure 3.5 whereas, the detail of the location of the pyranometer network in the Matsuyama plain is given in the Table 3.2, respectively. The instrument at all observation points are installed on the rooftop

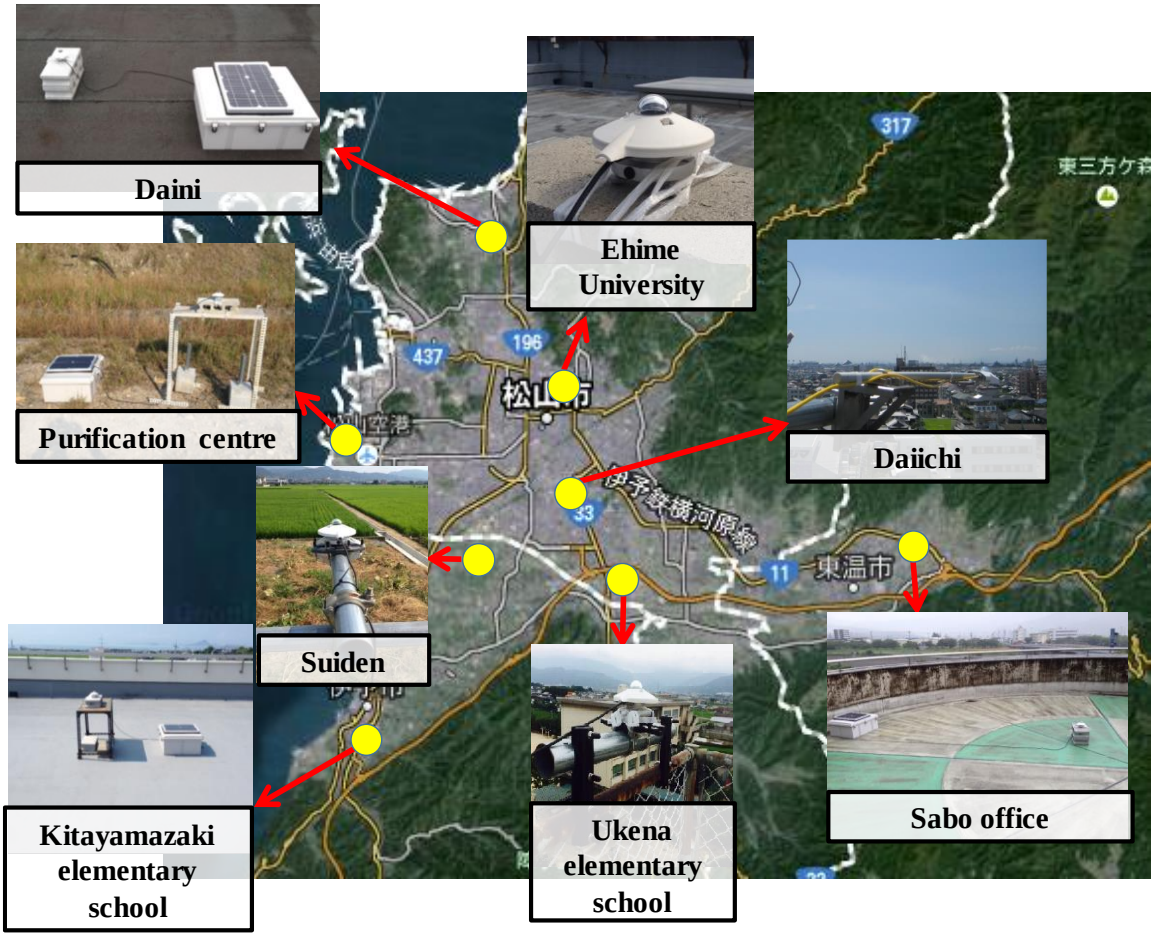

Figure 3.5: The site and condition of the pyranometer installed in the Matsuyama plain

of a building or an open field as indicated in Figure 3.5, so during this study the sky view factor for all observation was considered as 1, as the obstruction of the solar radiation due to presence of any infrastructure or trees is negligible. The sky view of all the observation site is represented in Figure 3.6.

3.3.1 Calibration of the pyranometer

Due to the sensitivity of the device, the precise measurement of solar radiation requires frequent calibration and maintenance (Ohmura et al., 1998). The irradiance value (Global solar radiation) can be simply computed by dividing the output signal of the pyranometer by its sensitivity as given in the Equation 3.1.

Table 3.2: Observation site and location of the pyranometer in the Matsuyama plain

Location	Coordinates	Remarks
Ehime University	132.771509°E, 33.850238°N	Urban area
Purification centre	132.692013°E, 33.826732°N	Coastal and industrial area
Kitayamazaki elementary school	132.694759°E, 33.741957°N	Rural area
Suiden	132.738013°E, 33.795585°N	Rural area
Ukena elementary school	132.7974°E, 33.79317°N	Rural area
Sabo office (Shikoku regional development Bureau, MLIT)	132.888278°E, 33.804344°N	Inland area
Daini (Ministry of Land, Infrastructure, Transport and Tourism office, Branch 2, Horie)	132.749°E 33.8895°N	Coastal area
Daiichi (Ministry of Land, Infrastructure, Transport and Tourism office, Branch 1, Higashiishi)	132.812962°E, 33.778939°N	Urban area

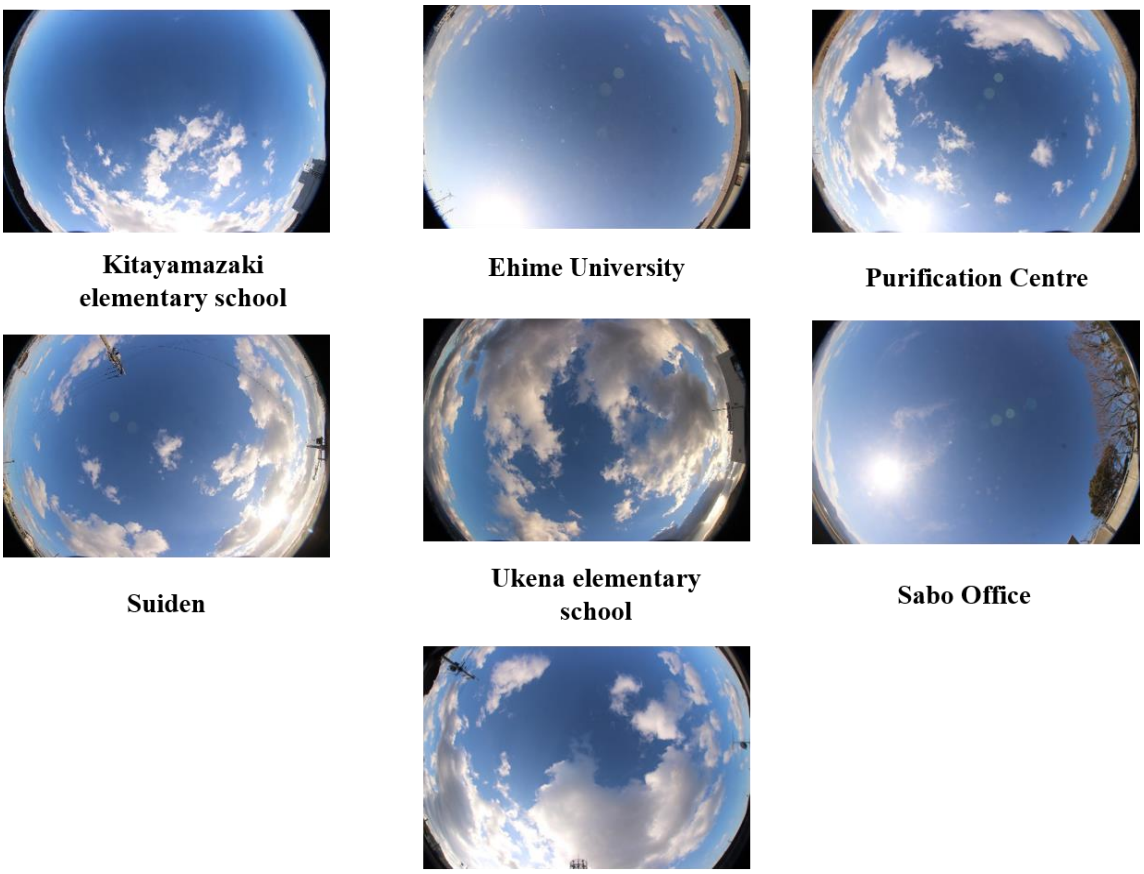

Figure 3.6: Sky view of the solar radiation observation sites in the Matsuyama plain

$$Global\ solar\ raditaion = \frac{Output\ voltage\,(\mu V)}{Sensitivity\ of\ \ pyranometer\,(\mu V/W/m^2)} \qquad (3.1)$$

The sensitivity of the pyranometer is the ratio of voltage output to the irradiance level (outside the instrument in the plane of the sensing element). The sensitivity of pyranometer is unique and is determined by the manufacturers' laboratory by comparison against the standard pyranometer. The sensitivity of the pyranometer changes with time and with exposure to radiation thus periodic calibration of the instrument is advised.

The pyranometer used in the study is calibrated once a year. For the calibration all the pyranometer are collected at the Ehime University and placed side by side to each other so that all the instrument views the same sky dome. The calibration was conducted for one week continuously from 6:00 AM to 18:00 PM. The outputs value of all the pyranometer over the calibration time period is averaged and the calibration factor is computed on the

basis of the average value. Here, the output value of pyranometer installed at Kitayamazaki elementary school was taken as a reference for the determination of the calibration value of other pyranometer. The output value of all observation every minute was subtracted from the value of Kitayamazaki and the final average value of one week is considered as the calibration factor of the respective observation site.

The sensitivity coefficient of the pyranometer along with the calculated correction factor for 2014 and 2015 for all the observation site is listed in Table 3.3. The amount of global solar radiation was then calculated using the following Equation 3.2.

$$Global\ solar\ raditaion = \frac{Output\ voltage\,(\mu V)}{\underset{(\mu V/W/m^2)}{Sensitivity\ of\ \ pyranometer}} + correction\ \ factor \qquad (3.2)$$

Table 3.3: Sensitivity coefficient and the correction factor of pyranometer based on observation site

Observation site	Sensitivity coefficient	Correction factor (2014)	Correction factor (2015)
Kitayamazaki elementary school	6.84	0	0
Ehime University	10.03	3.564827	
Purification Centre	6.77	-0.369849	-1.75302
Suiden	6.81	8.80843	-3.50305
Ukena elementary school	6.9	0.516691	0.075713
Sabo office (Shikoku regional development Bureau, MLIT)	6.77	-2.2633	-0.5387
Daini (Ministry of Land, Infrastructure, Transport and Tourism office, Branch 2, Horie)	16.3	-3.90428	1.793891

3.3.2 Sampling frequency

The observation of the distribution of the solar radiation is basically conducted in two phases. The initial section includes the observation of the solar radiation at two observation sites (Daiichi (Higashiishi) and Suiden) of the study area from July 2011 to September 2011. The sampling frequency of the radiation data was 10 minutes. Here, in total 29 days; 12 days in July, 12 days in August and 5 days in September was taken into account for the analysis of the difference in the amount of radiation between the urban and the rural area.

Secondly, the observation of the amount of solar radiation was conducted in a much larger scale using the pyranometer network so as to cover the entire Matsuyama plain. The observation was carried out continuously from August 2014 till date. The radiation data at an interval of 1 second is measured by the pyranometer whereas the average data per minute is recorded by the data logger and was further used in the study. Here, the radiation dataset from August 2015 to December 2015 was used for the analysis. In total 50 days; 7 days in August, 7 days in September, 16 days in October, 9 days in November and 11 days in December was taken into consideration.

The objective of the study to analyze the variation in the amount of solar radiation using the clear sky rate as an index to investigate the characteristic and state of the cloud, thus to avoid the fully cloudy condition or cloudless condition (sunny day), we selected the days with fair weather condition, that is, days with a sunshine percentage ranging between 40% - 80%. Such days were identified using the sunshine hours and weather condition data available from the Matsuyama Local Meteorological Observatory under Japan Meteorological Agency (JMA).

3.4 Clear sky rate

Maximum radiation on the earth is received under cloudless and clear skies (Iqbal, 1983). Clear sky models estimate the terrestrial solar radiation under a cloudless sky as a function of the solar elevation angle, site altitude, aerosol concentration, water vapor, and various atmospheric conditions (Badescu, 1997). Numerous studies have been conducted for the estimation of the solar radiation and clouds parameter based on the clear sky irradiance.

Calbó et al. (2001); Duchon and O'Malley (1999); Tovar et al. (2001), and many more have use the clear-sky irradiance model or clearness index for the estimation of the temporal variation of the global solar radiation. Gueymard (2012), Reno et al. (2012), have tested several clear sky models and reported the variation among the models with the difficulty in the measurement of the direct solar radiation due to its dependency on the aerosol condition. They further illustrated that the choice of models will depend on the accuracy desired in an individual analysis and thus user caution is necessary.

As the amount of solar radiation varies with both time and latitude; thus we consider the clear sky rate to estimate the percentage of solar radiation blocked due to the presence of cloud. For the simple determination of the temporal and spatial variation of the solar radiation we hereby use the clear sky rate as an indicator to determine the obstruction of the solar radiation due to the presence of the cloud. Here, each study month was divided into groups of 10 days (For example: September is divided into 3 groups, i.e. September 1 – September 10, September 11- September 20 and September 21 – September 30, respectively) and the data with the highest amount of solar radiation every minute was taken into consideration to create a virtual time series data of a virtually sunny day. Then time series data of the virtually sunny day was compared with the real time series data of the target day to calculate the clear sky rate.

The clear sky rate is defined as the ratio of solar radiation of target day to the radiation of a virtually sunny day as shown in Equation 3.3.

$$Clear\ sky\ rate = \frac{Radiation\ of\ a\ target\ day}{Radiation\ of\ a\ virtually\ sunny\ day} \qquad (3.3)$$

Figure 3.7 shows the relationship between the radiation of the target day, the radiation of a virtually sunny day and the clear sky rate of September 15, 2011. The clear sky rate varies between one and zero. A clear sky rate of one indicates a sunny weather whereas values closer to zero indicate cloudy condition causing the blocking of the solar radiation.

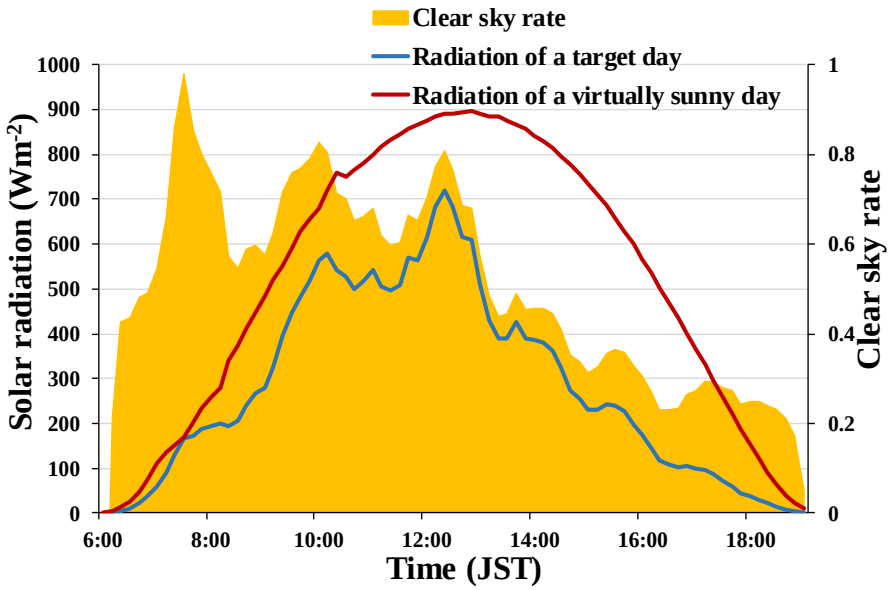

Figure 3.7: Relationship between the virtually sunny day, solar radiation of a target day and the clear sky (September 15, 2011)

3.5 Temporal variation of the clear sky rate

3.5.1 Diurnal variation of the clear sky rate

To understand the distribution of the solar radiation in the study area we consider the diurnal variation of the solar radiation. As it is already mentioned the distribution of the solar radiation starts to increase after the sunrise until it reaches a peak around the afternoon and then gradually starts decreasing until the sunset. To observe the variation in the distribution of the solar radiation due to the presence of the cloud we selected a day with partially cloudy condition. Figure 3.8 shows an example of the diurnal variation of solar radiation in urban and rural area of August 3, 2011. Here, the decrease in the amount of solar radiation is considered due to blockage of radiation by the cloud. Comparing the diurnal variation of the solar radiation, the amount of radiation in the rural area was observed to be higher than the urban area.

To further clarify the difference in the solar radiation distribution between the urban and rural area, we studied the effect of clear sky rate from 6:00 to 18:00, the time period where the blockage of solar radiation due to cloud can be observed. Figure 3.9 shows one-hour average of the clear sky rate from 6:00 to 18:00 representing an average value of 29 days (July to September, 2011) in the urban and rural area of the Matsuyama plain, respectively. Here, the clear sky rate was found to be smaller in the morning and then tends to increase with time eventually reaching a peak around mid-day and start decreasing from

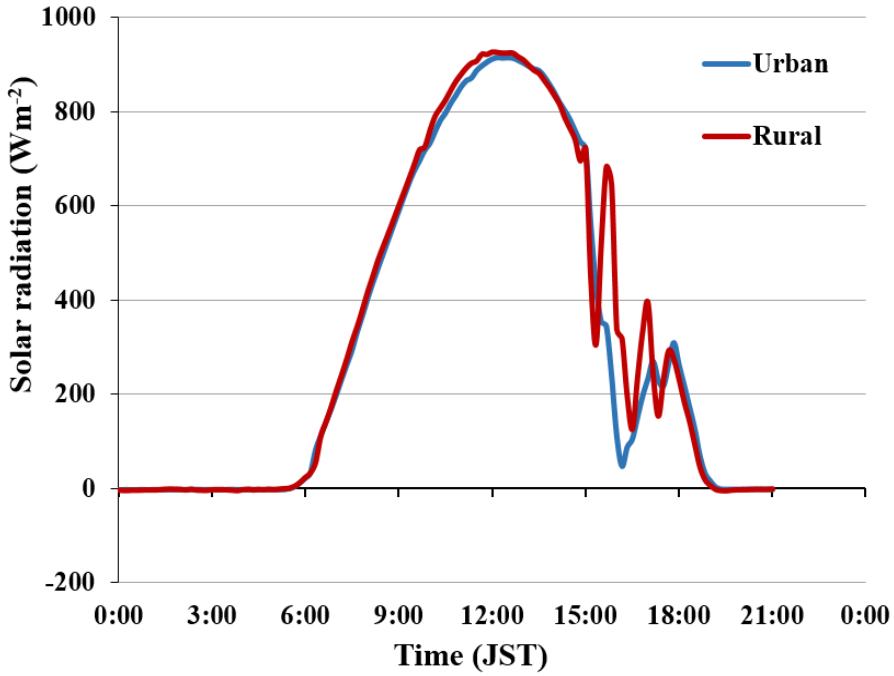

Figure 3.8: Diurnal variation of the solar radiation (August 3, 2011)

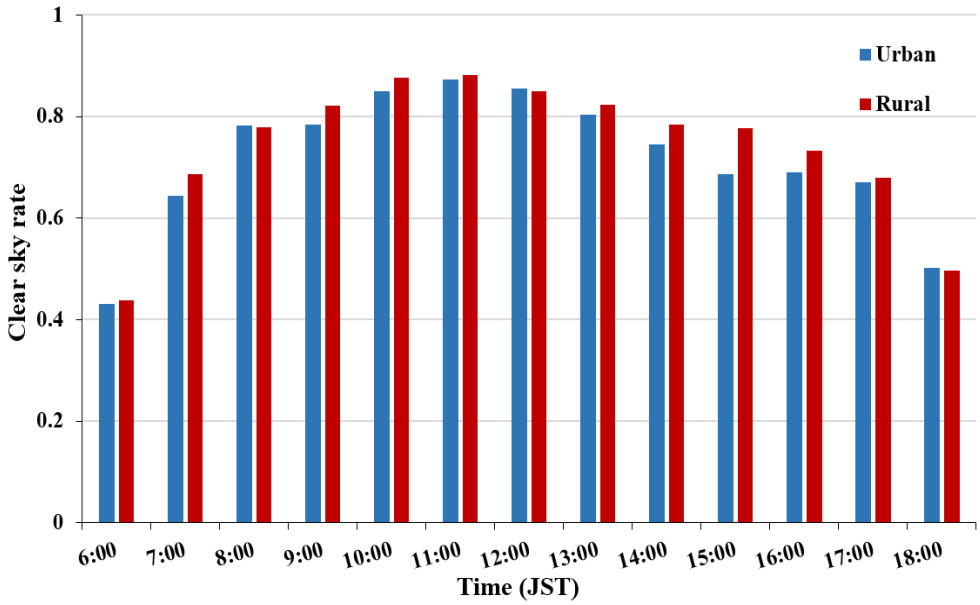

Figure 3.9: Hourly average of the clear sky rate from 6:00 to 18:00

the noon in both urban area and rural area. It suggests that the formation of cloud is likely to occur during the early morning and from afternoon. This is in agreement with the results of Asai et al. (1998), in which he has used the geostationary meteorological satellite observations to study the diurnal variation of the clouds. Rabin et al. (1990), highlighted that the convective cloud formation during the summertime are more during the daytime over the land surface. Similar results were obtained by Rastogi et al. (2016), in his study based in the coastal California, where the cloud coverage was found to be high during the afternoon due to the influence of the sea breeze and rainfall to occur during morning. The dominancy of cloud distribution during the morning and the evening in summer season in the island of Hawaii was studied by Barnes et al. (2016). Comparing the results, the clear sky rate in urban area was found to be smaller than that in the rural area especially in the afternoon which is believed to be due to the presence of clouds.

Figure 3.10 shows the comparison of the clear sky rate temporally averaged from 13:00 to 17:00 of the urban and rural area, respectively. In urban area the clear sky rate is observed to be smaller as compared to the rural area for most of the analysis days. This indicates that the cloudy condition appears more in the urban area as compared to the rural area. Figure 3.11 shows the difference in clear sky rate between the urban area and the rural area from the values represented in Figure 3.10. The difference is obtained by subtracting the clear sky rate of the urban area by the clear sky rate of the rural area. The larger number of analysis days with positive difference value indicates the formation of clouds in urban area to be more than in the rural area. Here, the difference in clear sky rate ranging from 0 to 0.15 is dominant while such day with difference up to 0.45 was also observed. Thus, the differences in the clear sky rate between the rural and urban area were observed, which in turns suggests that the development of clouds are more in urban areas than the rural area within the Matsuyama plain.

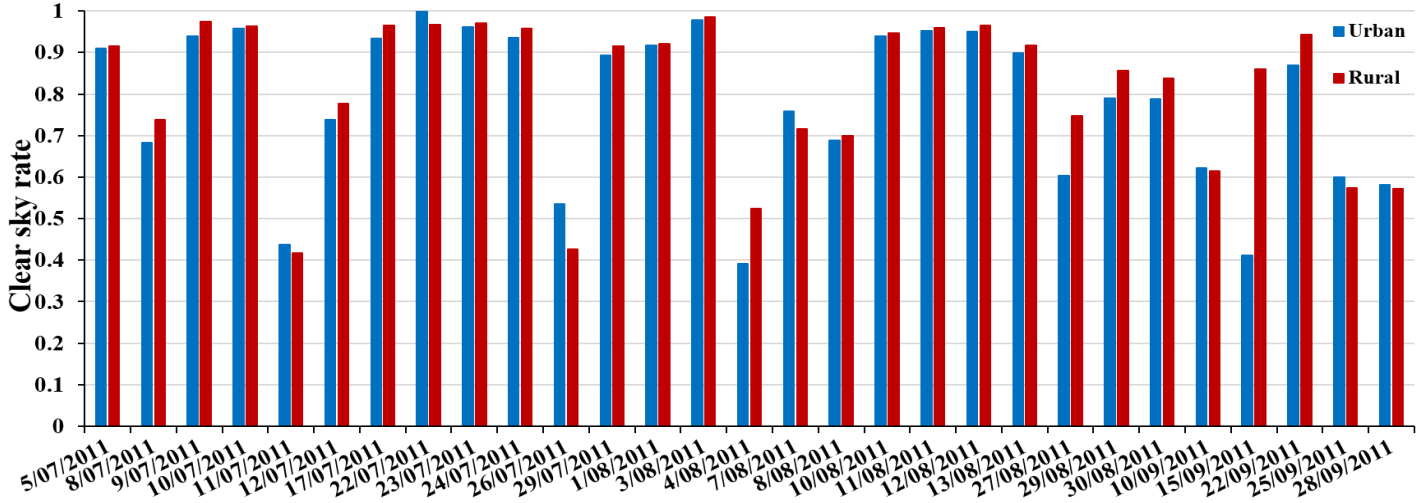

Figure 3.10: Clear sky rate temporally averaged from 13:00 to 17:00

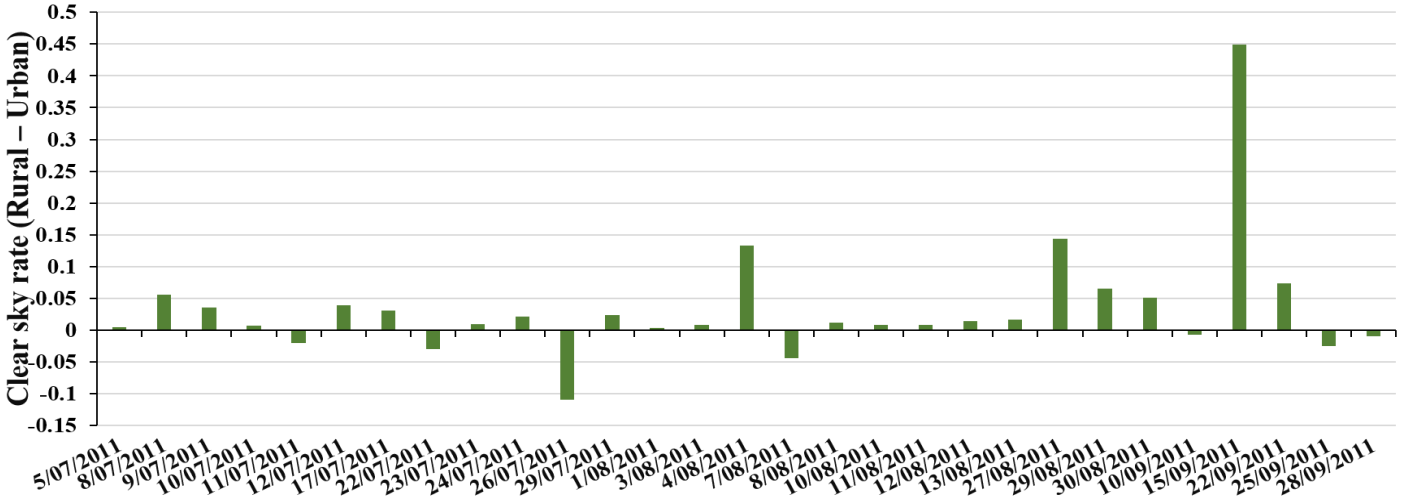

Figure 3.11: Difference of the clear sky rate temporally averaged from 13:00 to 17:00 (Rural clear sky rate– Urban clear sky rate)

3.5.2 Monthly variation

The amount of the solar radiation in the earth surface varies throughout the year so considering the monthly variation of the radiation is of utmost importance for the study of radiation as well as the local climate. Hence, considering this factor monthly variation of the clear sky rate was taken into consideration. Here, the datasets of August 2015 to December 2015 was taken into account for the analysis. The monthly average of the clear sky rate of the 7 observation points (refer Figure 3.5) is represented in Figure 3.12. The variation in the clear sky rate within each month from August to December can be observed throughout the study period. Here, the clear sky rate is found to be smallest during morning and from afternoon with highest value around mid-day. Further, the clear sky rate in December was found to be smaller especially around the afternoon as compared to other month. This suggest that the cloudy condition tends to appear more during the winter season. This detailed monthly variation of the solar radiation is further explained in section 3.6.

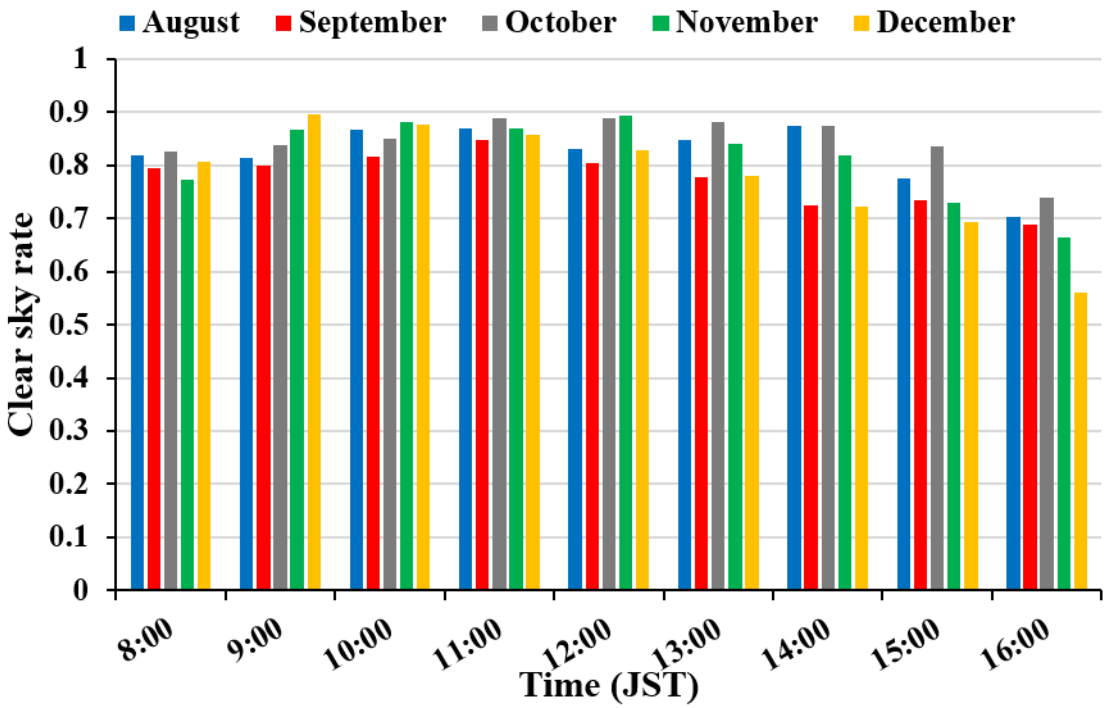

Figure 3.12: One-hour monthly average of the clear sky rate of the 7 observation point

3.6 Spatial variation of the clear sky rate

3.6.1 One-hour time standard variation

The difference in the distribution of the solar radiation between the urban and rural area in the Matsuyama plain suggests the variation of the state and clouds types within the area. Thus to further investigate the state of the clouds, we evaluated the temporal standard deviation of the clear sky rate by using the pyranometer network observation datasets.

Figure 3.13 shows the monthly 1-hour average data of the time standard deviation of the Matsuyama plain for 50 observation day from August 2015 – December 2015. Here, the clear sky rate closer to zero indicates cloudy condition whereas, the clear sky rate closer to one indicates sunny weather condition. It can be observed that the standard deviation varies from August to December within the range of 0 to 0.5 along with the clear sky rate for the study area.

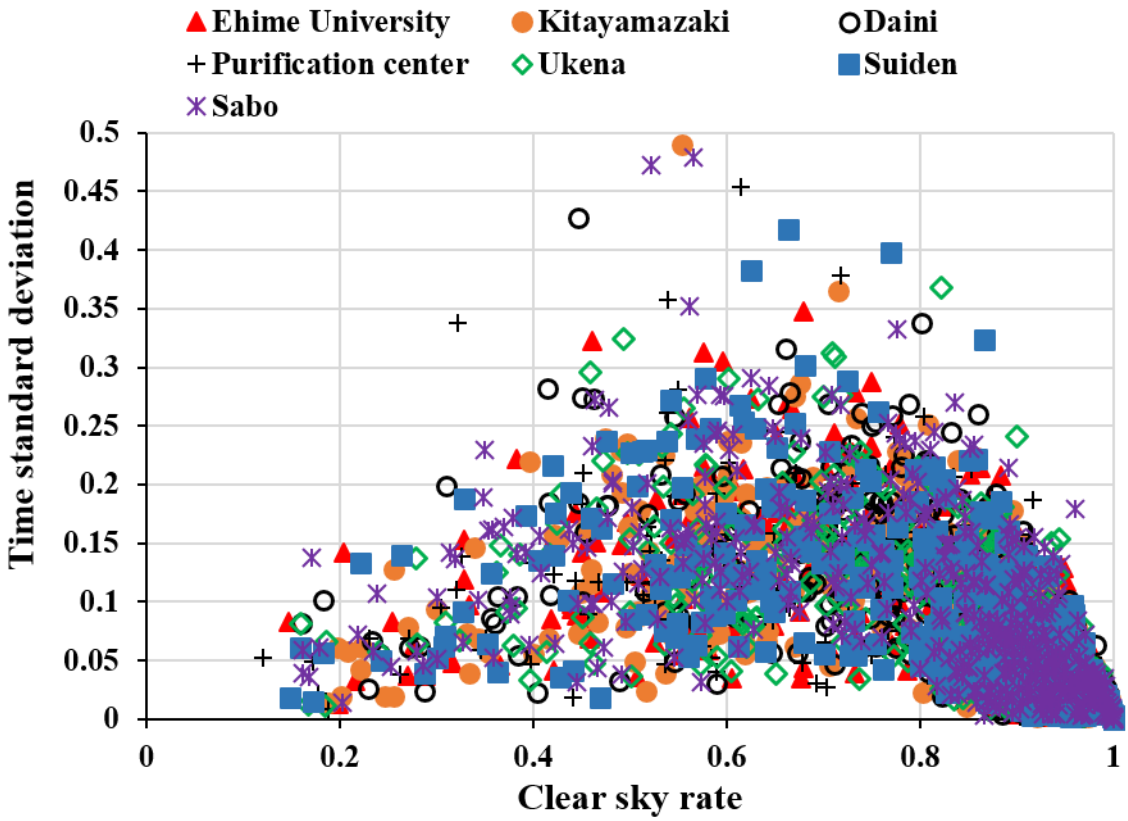

Figure 3.13 Monthly one-hour average time standard deviation and the clear sky rate for the Matsuyama plain

The average diurnal variation of the clear sky rate for the 5 month (i.e. August to December) in Figure 3.14 shows the maximum clear sky rate around mid-day whereas the decrease in clear sky rate can be observed in the morning and through evening. The solar radiation in the mid-day is higher as compared to morning or from late afternoon as during mid-day, the sun is positioned high in the sky and less solar radiation is scattered or absorbed (Balakrishnaiah et al., 2016). This indicates that the amount of radiation around mid-day is maximum with less coverage of cloud, whereas the cloud cover might be high during morning and around evening.

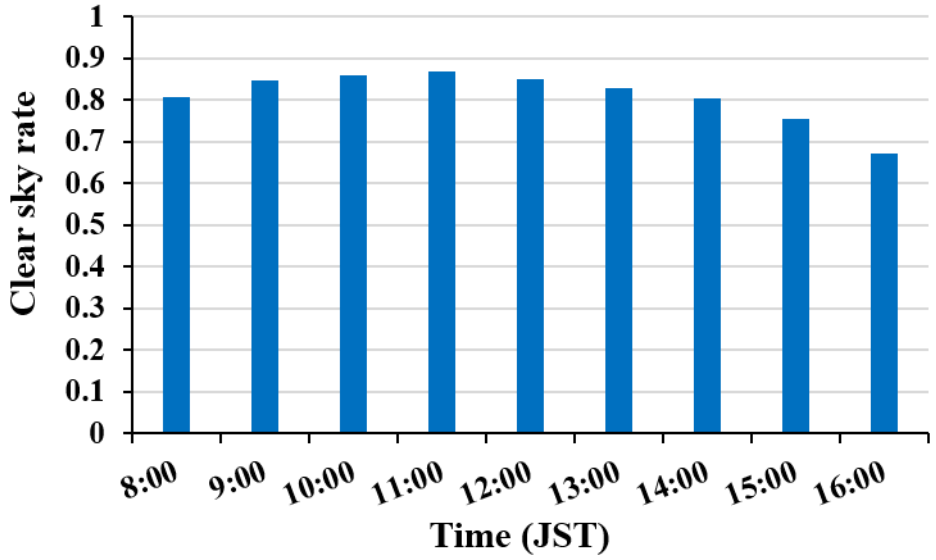

Figure 3.14: Average diurnal variation of the clear sky rate for the 5 month (August to December, 2015)

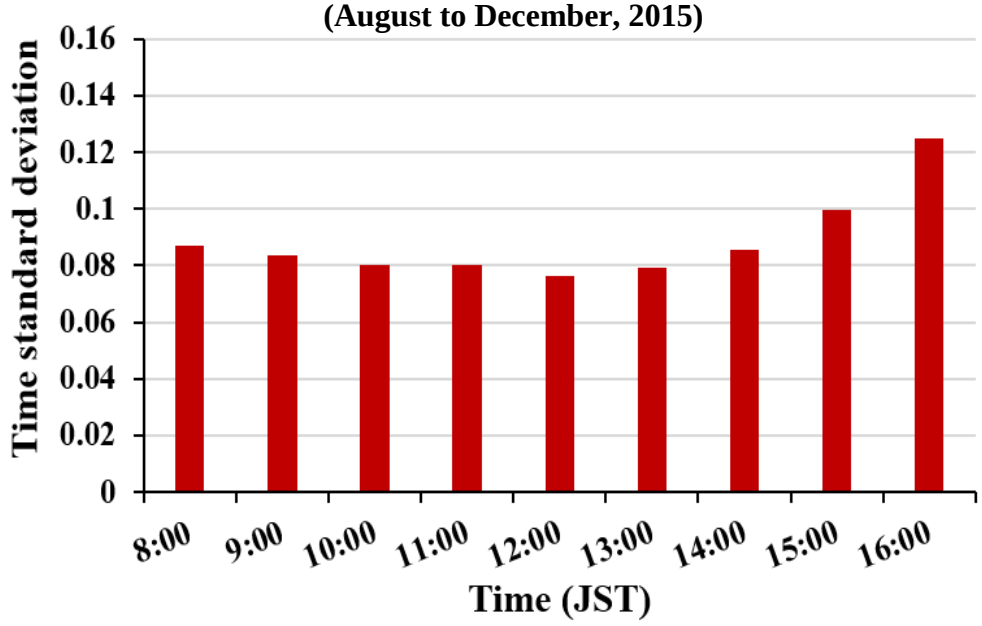

Figure 3.15: Average diurnal variation of the time standard variation for the 5 month (August to December, 2015)

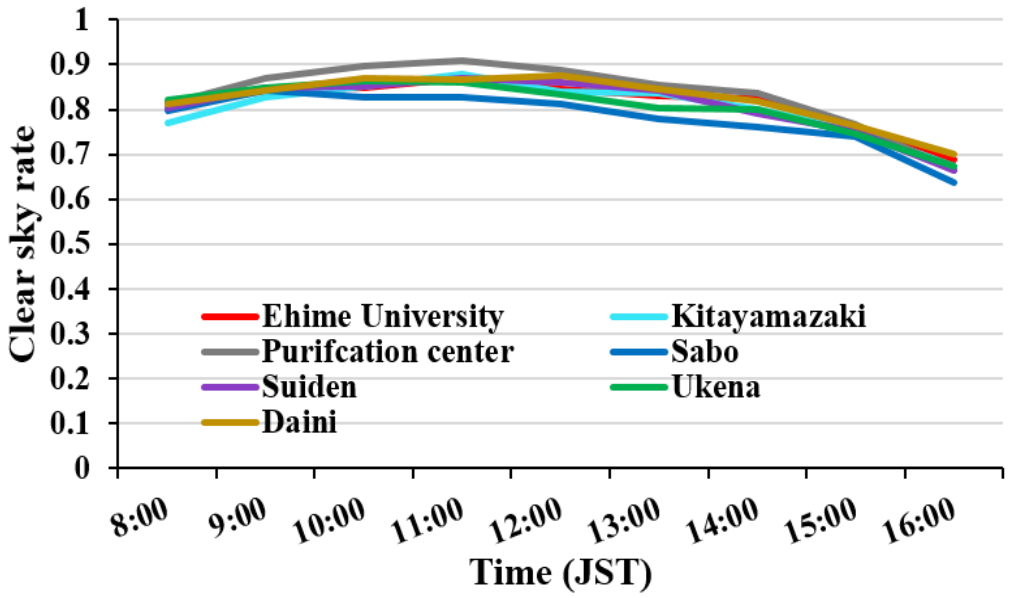

Figure 3.16: Diurnal variation of the one hour monthly averaged clear sky rate for the 7 observation site

Similarly, the average diurnal variation of the standard deviation for the 5 months of the study period is presented in Figure 3.15. Here, the standard deviation is observed to be minimum during the mid-day whereas the increase in the standard deviation can be observed during the morning and around evening. This in turn suggests that the standard deviation tends be larger in the presence of clouds or vice-versa.

Figure 3.16 shows the diurnal variation of the one hour monthly averaged clear sky rate for the 7 observation site. Here, we see that the clear sky rate generally varies within the range of 0.6 to 0.9. As explained earlier, the clear sky rate was observed to be maximum during the mid-day with decrease in the clear sky rate in the morning and afternoon for all the observation site. But the difference in the clear sky rate between all the observation site was not remarkable. Thus the study of the monthly variation of the clear sky rate in detail is recommended.

3.6.2 Monthly spatial variation

During the solar radiation measurement period, the month of August and September is considered as summer season, October and November as Autumn and December as winter season, respectively. Here, Figure 3.17 shows the diurnal variation of the average value of clear sky rate for each month from August to December. Here we can observe that the clear sky rate generally, varies for 0.6 to 1 in all months except in December (Figure 3.17 e.) where the clear sky rate below 0.6 is observed. This suggests that the cloudy condition tends to appear more in winter season as compared to other season.

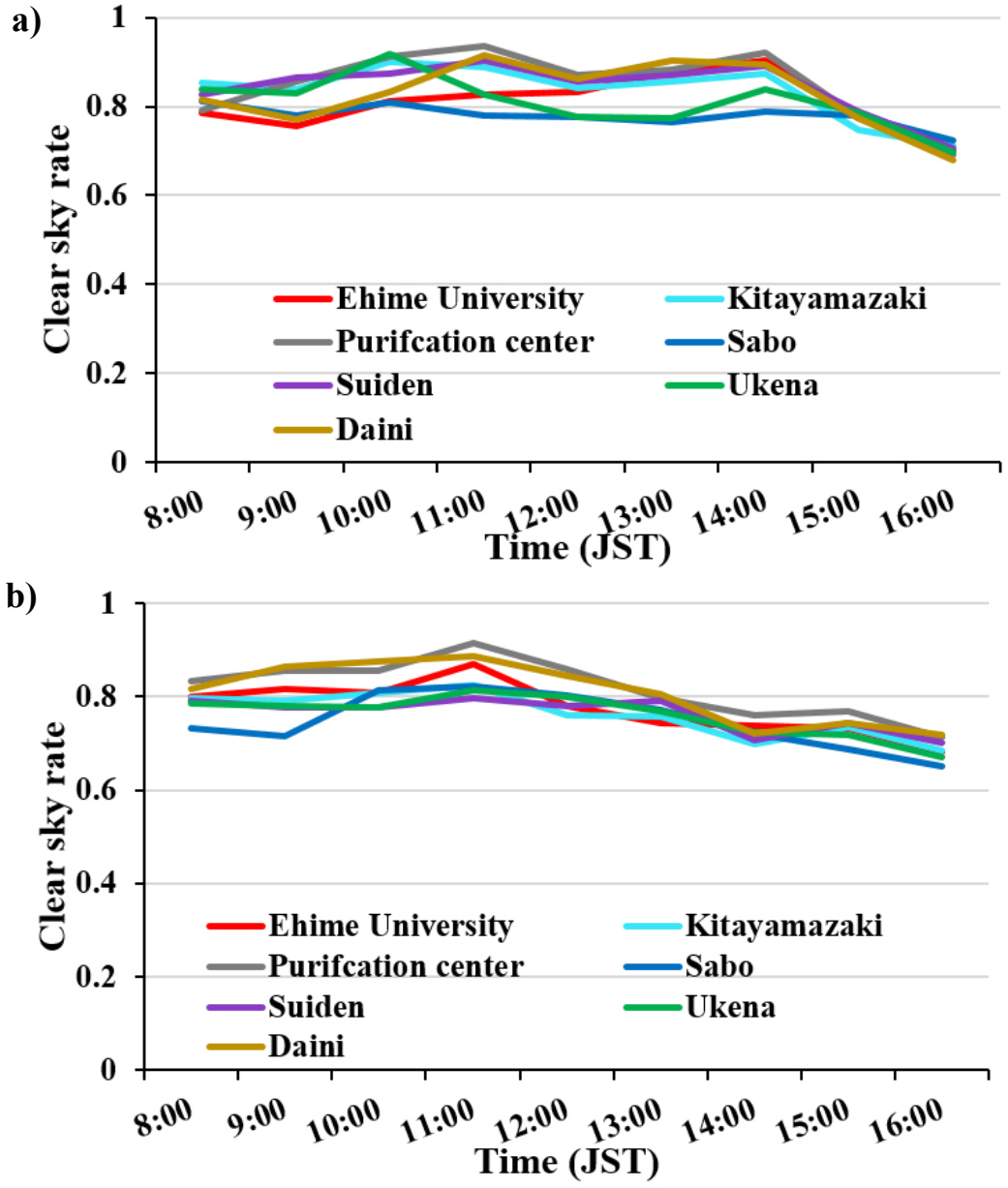

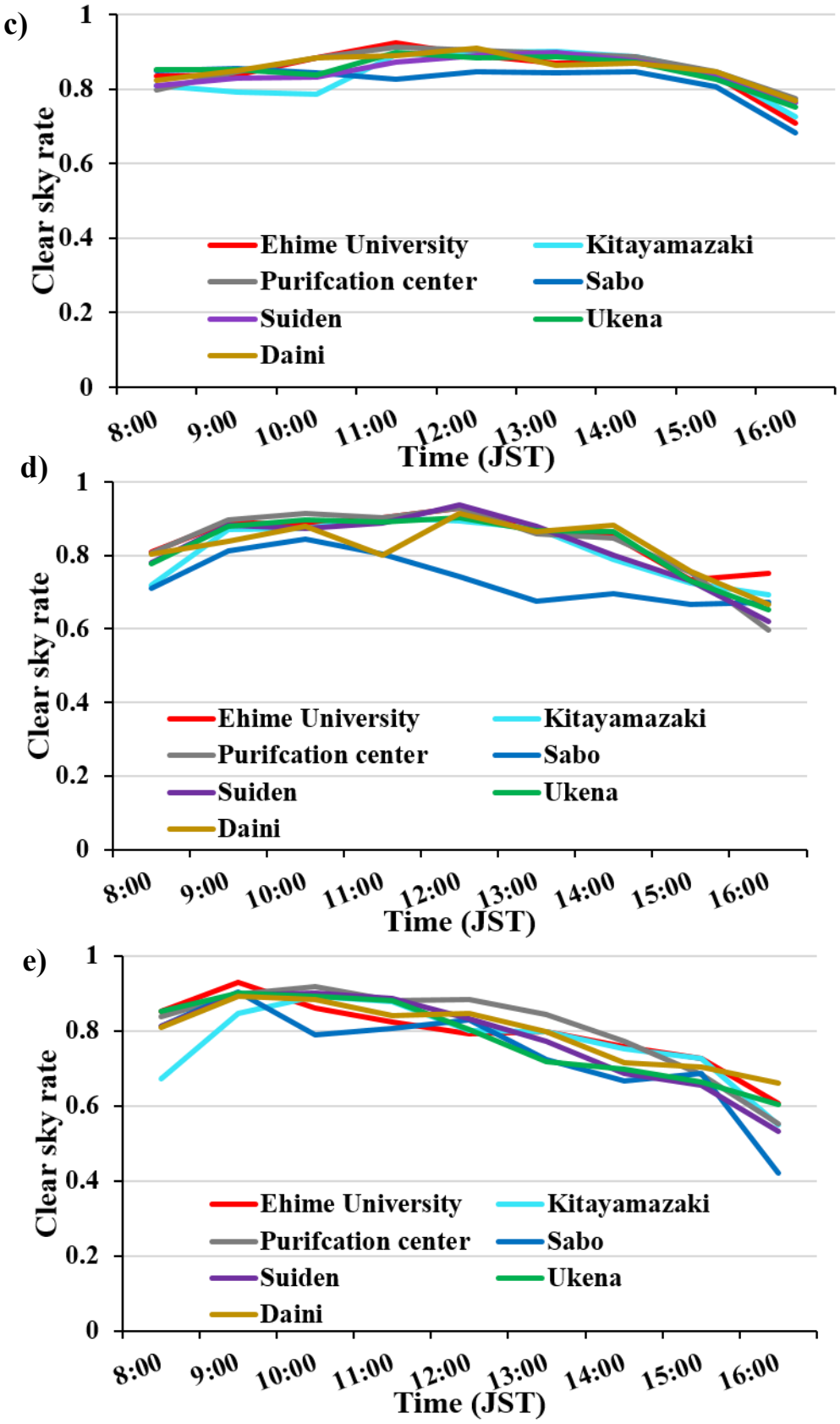

Figure 3.17: Diurnal variation of the average value of clear sky rate for each month, a) August, b) September, c) October, d) November and e) December, respectively

Also, in all the study period, the clear sky rate of the Sabo office was found to be the smaller among all the observation point with a minimum value observed in December. Additionally, the difference in the clear sky rate in the Sabo office is seen to be higher during the afternoon time. This indicates that the cloud tends to develop around the Sabo area especially during the afternoon period as compared to the other observation site.

Further the monthly one-hour averaged of the time standard deviation was taken into consideration to study the state of the cloud in the observation area. Here, we observe that for all the observation site, the clear sky rate generally varies from 0 to 1 with a higher percentage of the observation data closer to one within the time standard deviation between 0 to 0.5 (Refer Figure 3.13). The time standard deviation is large particularly between the clear sky rates of 0.4 to 0.6. To elaborate the result, we divided the observed clear sky rate into 3 sub-groups;

1. Clear sky rate ranging from 0 to 0.4
2. Clear sky rate between 0.4 to 0.6 and
3. Clear sky rate between 0.6 to 1

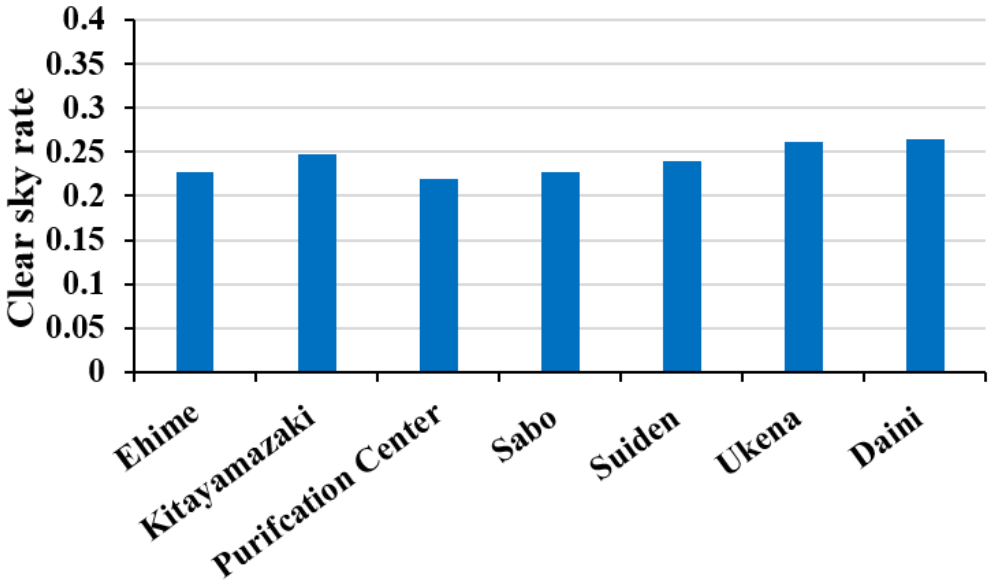

Figure 3.18: Monthly average of clear sky rate ranging from 0 to 0.4

Here, Figure 3.18 shows the clear sky rates for all observation sites ranging between 0 to 0.4, which generally represents the cloudier weather condition. Here, the smaller clear sky rate was observed in the Purification center and the Sabo office. Similarly, comparing the urban and the rural area, the clear sky rate in the Ehime University (urban area) is seen to be smaller as compared to Suiden (rural area). This indicates that the cloudy condition appears to be more in the urbanized area of the Matsuyama plain as compared to the rural area.

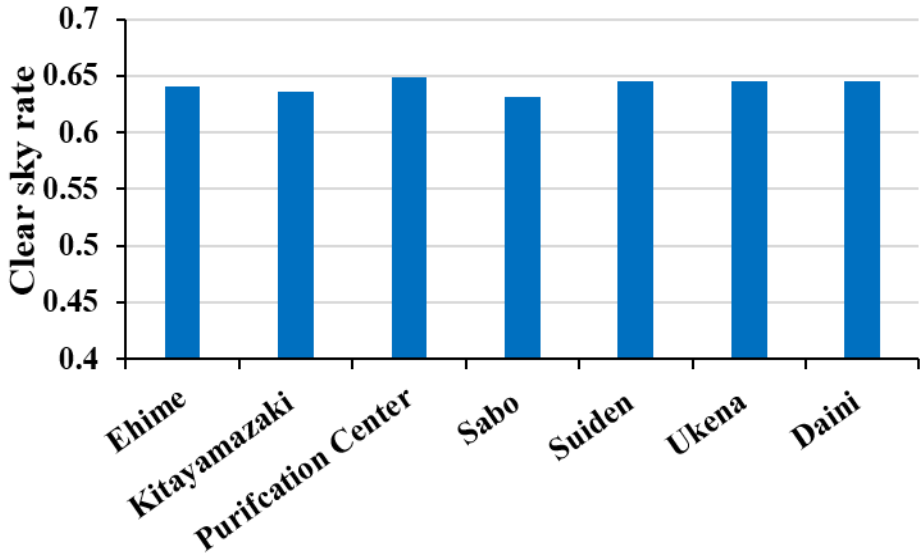

Figure 3.19: Monthly average of clear sky rate ranging from 0.4 to 0.6

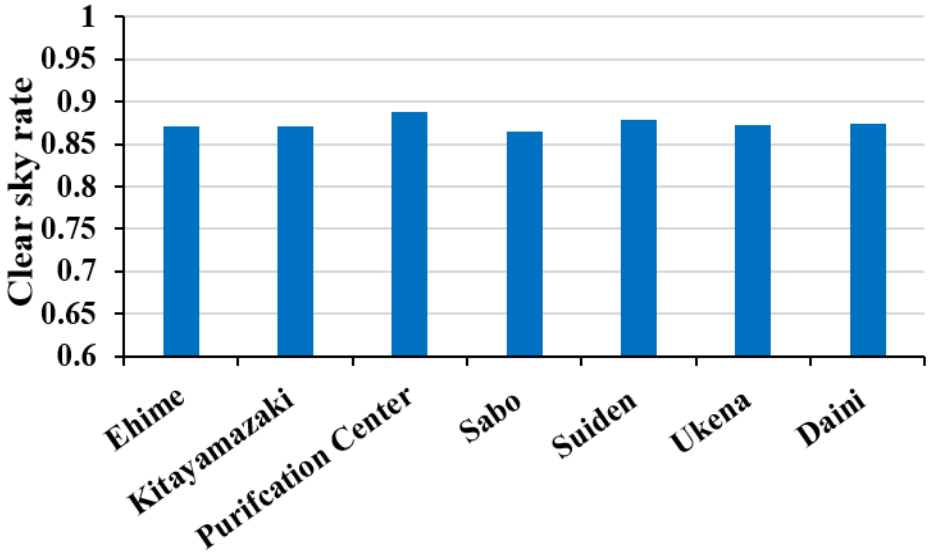

Figure 3.20: Monthly average of clear sky rate ranging from 0.6 to 1

Figure 3.19 represents the clear sky rates between 0.4 to 0.6 where the highest time standard deviation was observed for all the observation site. Here, the highest and the smallest clear sky rate was observed at the Purification center and the Sabo office, respectively whereas for all the other observation points, the clear sky rate was almost similar. Similarly, Figure 3.20 shows the clear sky rate ranging between 0.6 to 1, which mostly represents a fine weather condition. Here, the maximum clear sky rate was observed to be almost 0.9 at the Purification center whereas smaller clear sky rate was found at the Sabo office.

The monthly average of the time standard deviation for all the observation sites are given in Figure 3.21. Here, the smallest standard deviation is observed during October for all the observation point. The monthly average of the time standard deviation as shown in the Figure 3.22 indicates the highest and the smallest standard deviation is observed at the Sabo office and the purification center, respectively.

Thus, from the above results we can conclude that the clear sky rate in the Sabo office was found to be smaller compared to other observation sites, which indicates the presence of cloud around Sabo office to be larger. This further suggests that the inland area of the Matsuyama tends to have cloudier condition. The effect of the wind in the formation of the cloud is explained in the next section.

Also, the cloudy condition in the urbanized area (Ehime University) was observed to be slight larger than compared to the rural area (Suiden and Ukena) of the Matsuyama Plain. This is according to the result of Moriwaki et al. (2013), as discussed in the Chapter 1.

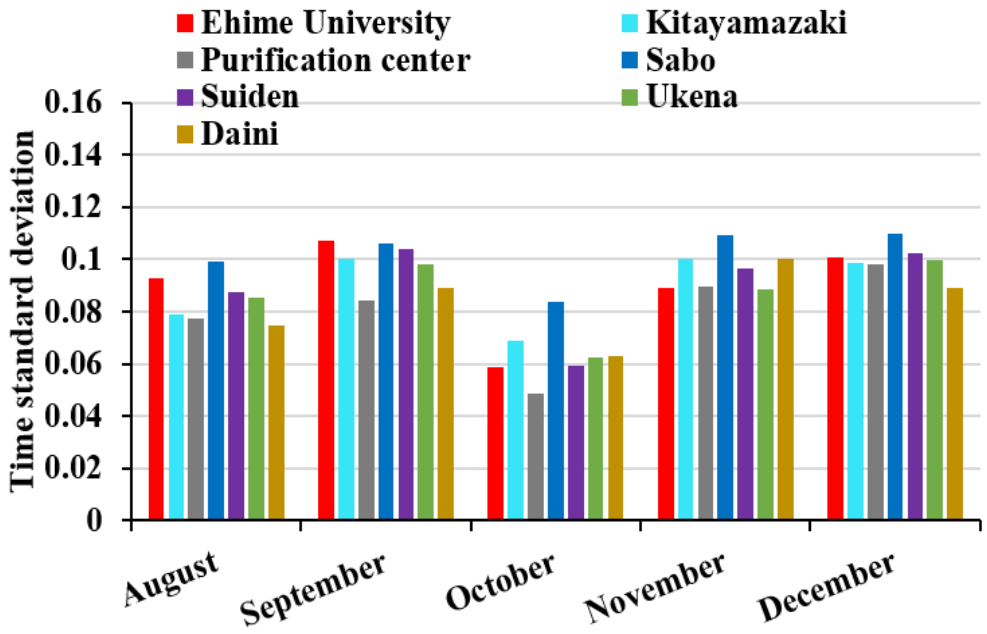

Figure 3.21: Monthly average of the time standard deviation

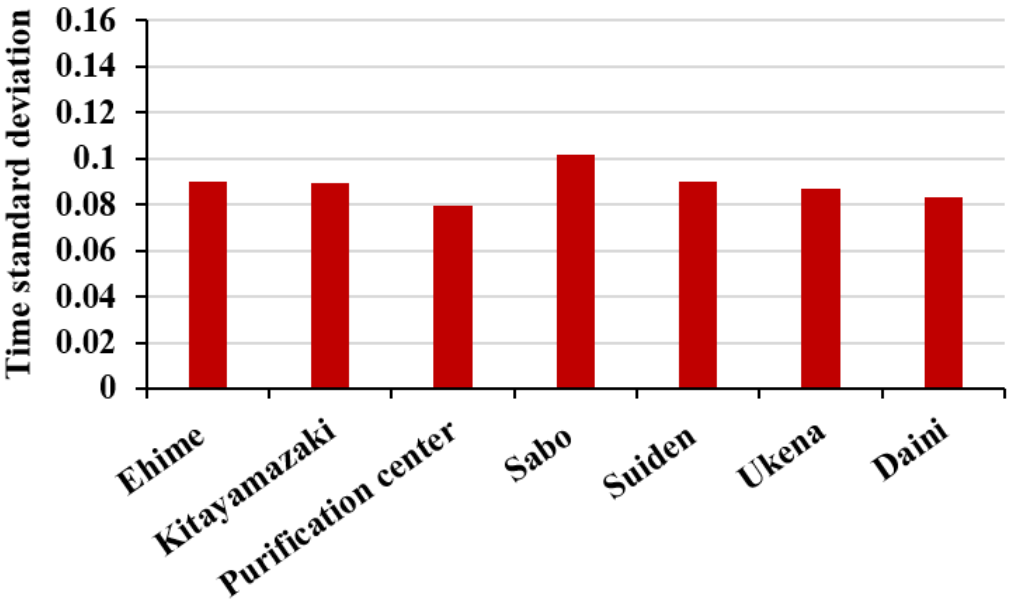

Figure 3.22: Spatial variation of the monthly averaged time standard deviation

3.7 Whole sky photography

Historically, cloud measurements from the surface were accomplished by human observations, annotating the amount of clouds covering the sky and distinguishing the types of clouds according to their appearance, but this data collection was expensive and subjective (Martínez-Chico et al., 2011). This lead to detecting and quantification to the cloud using automated devices. Many studied have focused on the detection and classification of the clouds using satellite information (Bosch et al., 2010, Perez et al., 2002, Inoue and Kimura, 2004). but satellite retrievals have known weaknesses in quantifying small and/or low-altitude cloud features due to their limited spatial resolution and unknown surface influences on the measured radiances. Then there are issues with differences in viewing geometry between satellite- and ground-based sensors associated with cloud features (Goodman and Henderson-Sellers, 1988). One sky characteristic difficult to determine from a downward pointing satellite sensor is solar obstruction (Long et al., 2006). Moreover, the access to satellite information is not universal so for the remote locations where the accessibility of

Figure 3.23: Whole-sky camera installed at the Ehime University

the satellite images is difficult, the best alternative to study the sky condition along with the detection and classification of the cloud is the ground-based imaging or ground-based whole sky photography.

Whole sky images provide important information on the classification of the clouds based on the photographs taken from the ground at regular interval (Reno and Stein, 2013). Sabburg and Long (2004), asserted that the use of whole sky imaging system has the ability to understand and accurately quantify the effect of the cloud on the irradiance. They also suggested the use of high quality images can improve the result. The use of ground-based whole sky images for the study of clouds and its impact on the distribution on the solar radiation has been used by many researchers (Pfister et al., 2003, Buch et al., 1998, Calbó and Sabburg, 2008 and others).

For this purpose, the whole-sky camera (Canon Inc., ES Kiss X5) was installed at the rooftop of the Engineering building 2 of Ehime University as shown in Figure 3.23. The camera was mounted with a fisheye lens (Canon EF 8-15mm f/4L USM) which delivers 180^{o} diagonal angle of view of all images with imaging format ranging from the full frame to APS-C. With its Ultrasonic Motor (USM) and floating focus system offers auto focus which is fast and exact.

The fisheye lens follows the equidistant projection where the image position away from center is the same for every degree of subject angle away from the center. Mathematically, the perspective projection is expressed as follows:

$$R = f\theta \qquad (3.4)$$

Where,

R is the radial distance or the distance between the center of the image and the image point

f is the focal length

θ is the angle between the optical axis and the incoming light beam in radian

Using the above mathematical expression developed for the projection type, knowing the focal length of the lens and the radius of the image, the θ can be calculated.

Table 3.4: Specification and location of the Whole-sky camera

Name	Whole sky camera
Type	Canon Inc. camera mounted with fisheye lens (Field view 180^{o})
Focal Length of camera	8mm – 15mm
Installed location	Engineering Building 2, Ehime University (132.771509 ^{o}E, 33.850238 ^{o}N)
Photo interval	10 minutes
Installation date	July 2014

Further using these values and the vertical height of the cloud, the horizontal distance of the image can be estimated. This method is used for the estimation of the visible distance of the cloud distance in the study area.

The specification and the location of the whole sky camera is provided in Table 3.4. The camera has been setup to take photograph of whole sky at an interval of 10 minutes from July 2014 till date. The whole sky photographs were further used to study the development, movement and types of clouds during the analysis period.

3.8 Data validation

The analysis results discussed in the above sections show the dominance of cloud in the inland and the urbanized area of the Matsuyama plain. But the characteristics of the clouds and its type is important for the study of climate. Thus, the obtained results were verified using the whole sky photographs and numerical model.

3.8.1 Model validation

The study of the distribution of the solar radiation using the observation dataset of July to September 2011 indicates the tendency for the cloud formation is more in urban area than in rural area. This was further validated by the numerical simulation and numerical experiment of the cloud cover using a mesoscale model WRF.

The Weather Research and Forecasting (WRF) Model is a sophisticated numerical weather prediction system that solves the compressible non-hydrostatic Euler equations cast in flux form on a mass-based terrain-following vertical coordinate system. The model serves a wide range of meteorological applications across scales from tens of meters to thousands of kilometers. The effort to develop WRF began in the latter part of the 1990's and was a collaborative partnership principally among the National Centre for Atmospheric Research (NCAR), the National Oceanic and Atmospheric Administration (represented by the National Centers for Environmental Prediction (NCEP) and the Forecast Systems Laboratory (FSL)), the Air Force Weather Agency (AFWA), the Naval Research Laboratory, the University of Oklahoma, and the Federal Aviation Administration (FAA) (Skamarock et al., 2008). NCEP (National Centers for Environmental Prediction) FNL (Final) Operational Global Analysis data on 1.0 × 1.0 degree grids for every six hours were used for the study. The model uses a terrain-following sigma coordinate in the vertical, with 28 levels. The analysis data include parameters such as surface pressure, sea level pressure, geopotential height, temperature, sea surface temperature, soil values, ice cover, relative humidity, u- and v- winds, vertical motion, vorticity and ozone. A global land use/land cover (LULC) database classified according to the United States Geological Survey (USGS) LULC system is provided with WRF. For radiative transfer associated with clouds, the current schemes in WRF normally use preset tables to represent shortwave and longwave processes associated with clouds. For shortwave radiation, the current choices in WRF include the Dudhia scheme with a simple downward integration of solar flux, accounting for clear-air scattering, water vapor absorption, and cloud albedo and absorption. In past several studies, radiative fluxes and cloud cover from satellite data have been widely used and proved to useful for the cloud simulation by weather forecast model (Gautier et al., 1980; Yang et al., 1999). These study were mostly based on coarse time and spatial resolution.

The WRF model was set up by using four nested domains of 30, 7.5, 1.87 and 0.469 km horizontal grid spacing and 28 vertical level for domain 1, 2, 3 and 4, respectively as indicated in Table 3.5. The simulation was run from August 3, 2011 to August 4, 2011 with the 24 hours spin up time. Figure 3.24 shows the comparison of the diurnal variation of the amount of solar radiation of observed and simulated result in both urban and rural area, respectively. Here the amount of radiation starts decreasing from the afternoon in both urban and rural area, which in turns suggests the decrease in the solar radiation in the urban area to be more as compared to the rural area. The decrease in the solar radiation should be due to the presence of the cloud. Despite the overestimation of the amount of radiation by the simulation the diurnal trend of the solar radiation is similar to the observation result. The overestimation of the shortwave radiation partly explains the underestimation of the of clouds and absence of effects of aerosols. The difficulty in the simulation of the cloud and its underestimation of the cloud coverage for short time duration has been reported by Guichard et al. (2003).

Table 3.5: Model setup and resolution setting of the study

	Horizontal grid number (grid points)	Horizontal domain size (km)	Horizontal grid spacing (km)	Vertical grid number (grid points)
Domain1	**75×70**	**2250×2100**	**30**	**28**
Domain2	**85×81**	**637.1×607.5**	**7.5**	**28**
Domain3	**69×81**	**129.7×152.3**	**1.875**	**28**
Domain4	**73×73**	**34.2×34.2**	**0.469**	**28**

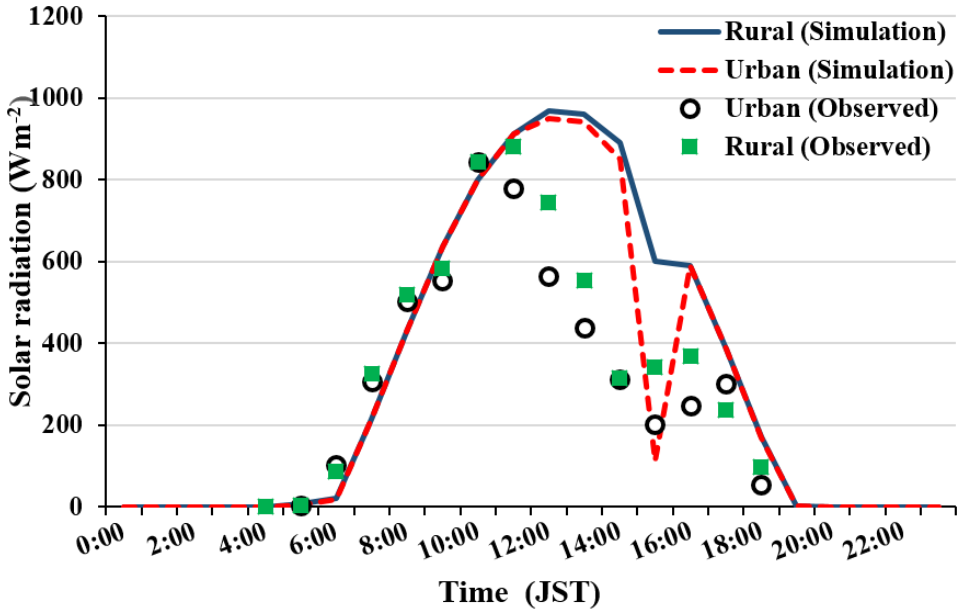

Figure 3.24: Comparison of the diurnal variation of the solar radiation from the numerical simulation and observation (August 4, 2011)

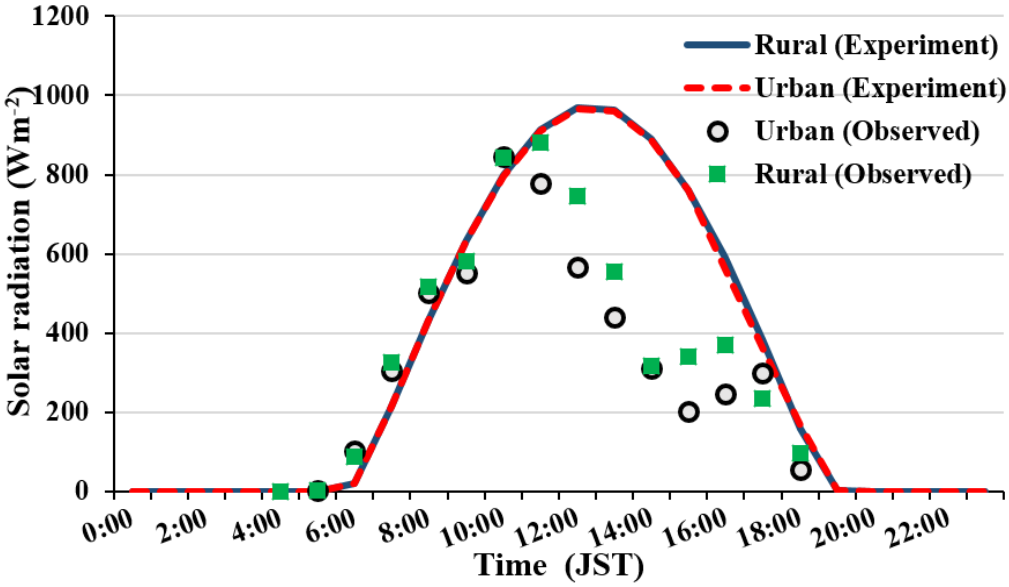

Figure 3.25: Comparison of the diurnal variation of the solar radiation from the numerical experiment and observation (August 4, 2011)

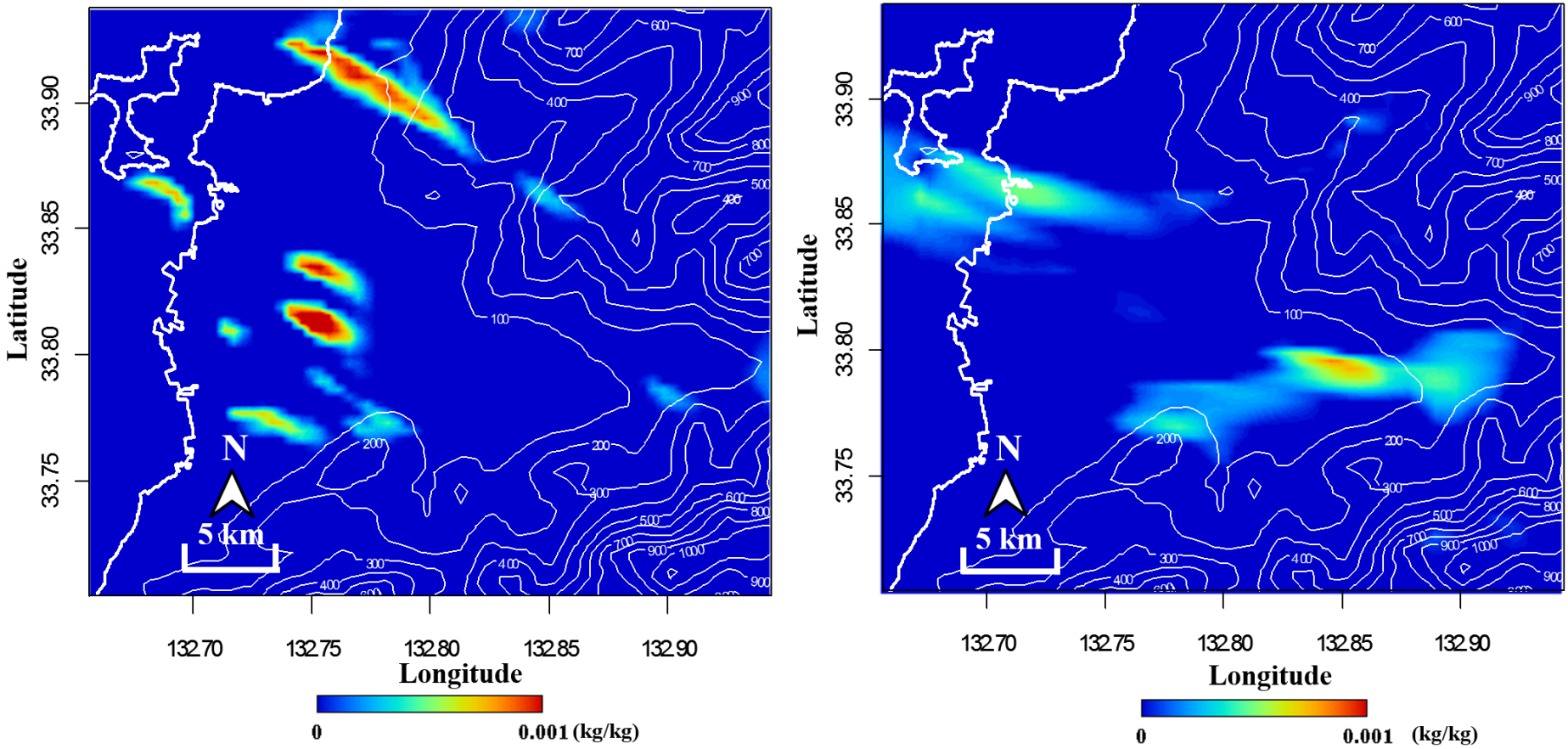

Figure 3.26: Distribution of average cloud water mixing ratio (kg/kg) in the vertical column on August 4, 2011 at 15:00 from a) the numerical simulation and b) Numerical experiment

For further investigation of the impact of land use on the cloud formation we conducted a numerical experiment of August 4, 2011 using the land use category of approximately 40 years ago. In the experiment we used the land use data of 1976 provided by the Ministry of Land, Infrastructure, Transport and Tourism (MLIT), Japan. In the experiment we found that the amount of radiation on both urban and rural area is same as shown in Figure 3.25 which clearly suggests absence of cloud at the time period. Cloud fraction varies greatly with the cloud water mixing ratio (Xu and Randall, 1996) and stratiform cloud increases almost linearly with the cloud mixing water ratio (Ghan and Easter, 1992). The cloud water mixing ratio as shown in Figure 3.26 also indicates that the cluster of cloud with high cloud water tends to appear in the northern part, namely, urban area of the Matsuyama plain.

Thus comparing the results of the numerical simulation and the numerical experiment we can conclude that the development of the cloud in the Matsuyama plain is effected by the difference in the land use pattern.

The model validation i.e. numerical simulation and the numerical experiment, used in this study mainly focused on the distribution of the solar radiation based on the different land-use category. The results suggested the underestimation of the clouds over the study area which might be due to the microphysics schemes selected during the simulation or other influencing factors. Thus, detail study of the cloud cover at different altitude level becomes necessary to understand the properties of the cloud. Bukovsky and Karoly (2009), indicated the WRF simulation might have error when considering the nested domain for the modelling. The scarcity of the observation data with the fine temporal and spatial resolution makes it difficult to properly validate the high resolution model simulated cloud data (Otkin and Greenwald, 2008). Hence for the comprehensive study of the distribution of the solar radiation and cloud cover over the Matsuyama plain, use of cloud microphysics scheme along with various parametrization schemes over a long-period of time is recommended for the future study.

3.8.2 Whole-sky photography

The ground-based whole sky photographs was used to study the cloud characteristics and type based on the analysis result. For this, the solar radiation observation dataset from August to December 2015 was taken into consideration. As the whole-sky camera was installed only at one observation point (i.e. Ehime University), the monthly one-hour average time standard deviation from 8:00 to 16:00 and clear sky rate of Ehime University was used for the validation. The relation between the monthly average time standard deviation and clear sky rate at Ehime University is presented in Figure 3.27. Here, the clear sky rate for Ehime University mostly varied between 0.2 to 1 within the time standard deviation of 0 to 0.35. In order to study the relation between the clear sky rate and time standard deviation and its correlation with the state of the cloud, the clear sky rate was divided into 5 sub-groups:

1. Clear sky rate from 0 to 0.2
2. Clear sky rate from 0.2 to 0.4
3. Clear sky rate from 0.4 to 0.6
4. Clear sky rate from 0.6 to 0.8 and
5. Clear sky rate from 0.8 to 1

Again, within these 5 sub-groups, the maximum and minimum time standard deviation was taken into consideration

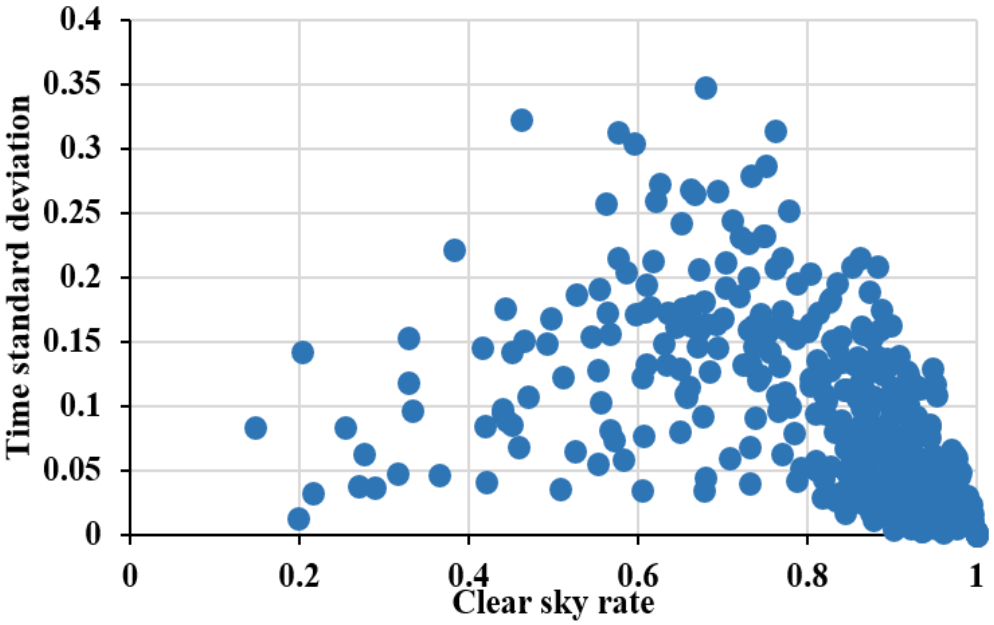

Figure 3.27: One-hour time standard deviation and clear sky rate for Ehime University

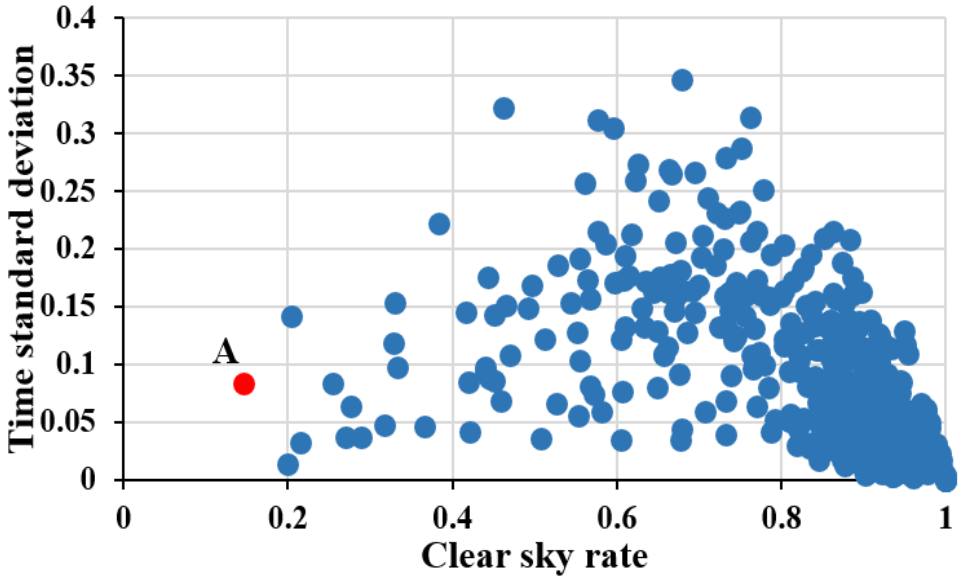

Figure 3.28: Observation of the clear sky rates between 0 to 0.2

Figure 3.28 focuses on the clear sky rates between 0 to 0.2. As the observation data between the clear sky rate was found to be minimum, we considered only one-point dataset (Red point, A) to study the state of the cloud. The one-hour time standard deviation from

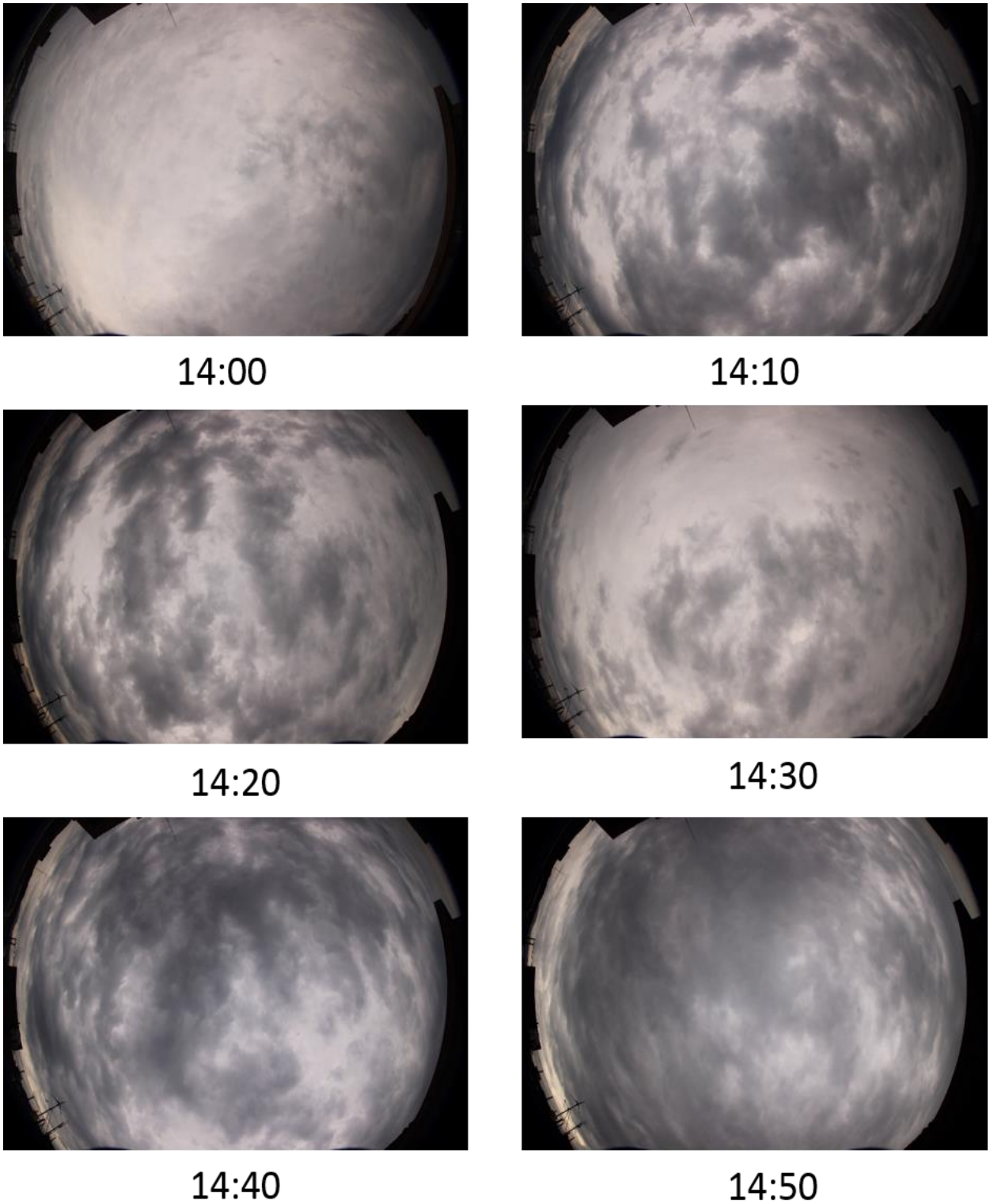

Figure 3.29: Whole-sky photographs of December 2, 2015 at an interval of 10 minutes

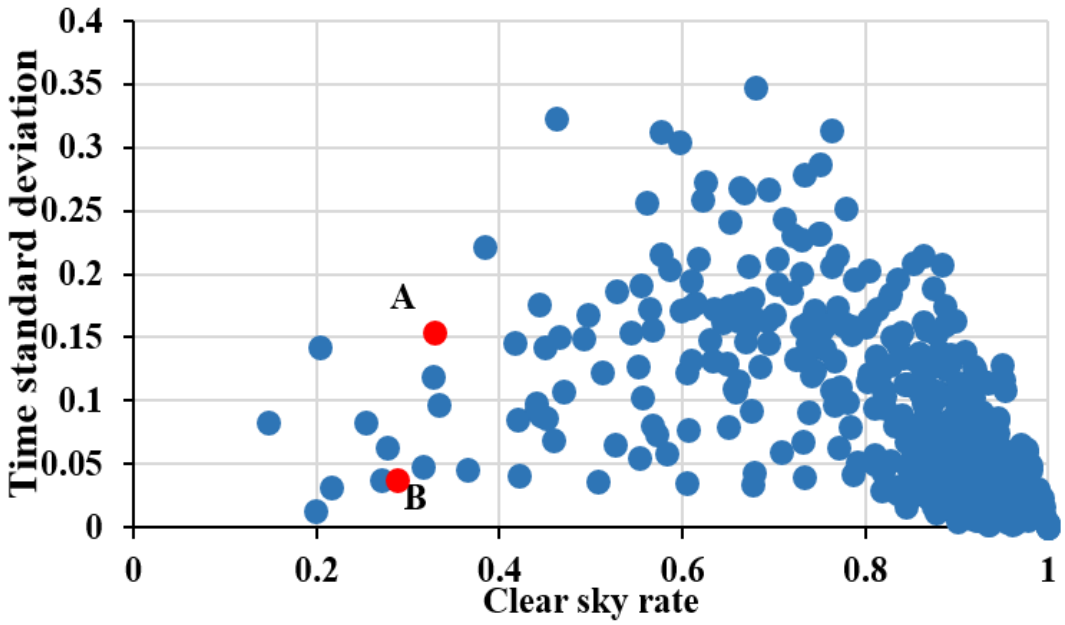

Figure 3.30: Observation of the clear sky rates between 0.2 to 0.4

14:00 to 14:59 on December 2, 2015 was found to lie between the clear sky rates of 0 to 0.2. The lower value of the clear sky rate suggests the presence of the cloud which is verified by the whole-sky photographs of the time period. The whole-sky photographs from 14:00 to 14:50 at an interval of 10 minutes is presented in Figure 3.29. Here, the presence of low level clouds such as nimbostratus or cumulonimbus cloud are seen to cover the entire sky over the study area. This in turn suggest that the cloud might be accompanied by rain in near time. Thus, the smaller clear sky rate and time standard deviation indicates a cloudy condition throughout the time period which can bring precipitation.

Next, we consider the clear sky rates between 0.2 to 0.4 as shown in Figure 3.30. Here, the red point A and red point B indicates the maximum and minimum time standard deviation, respectively. The maximum time standard deviation is observed from 15:00 to 15:59 on December 26, 2015. During this time period, the presence of low level to medium clouds such as stratocumulus or altostratus can be observed to cover the sky with occasionally clear sky condition at times as indicated by the whole- sky photographs of an hour presented in Figure 3.31. This type of clouds can sometimes bring rain along the time period. Similarly, the minimum time standard deviation was observed from 11:00 to 11:59 on December 13, 2015 indicated by point B (Figure 3.30). The images of the sky during the time period is presented in Figure 3.32. As indicated in the Figure 3.32, the entire sky was seen to be covered with low cloud such stratus or stratocumulus for an hour.

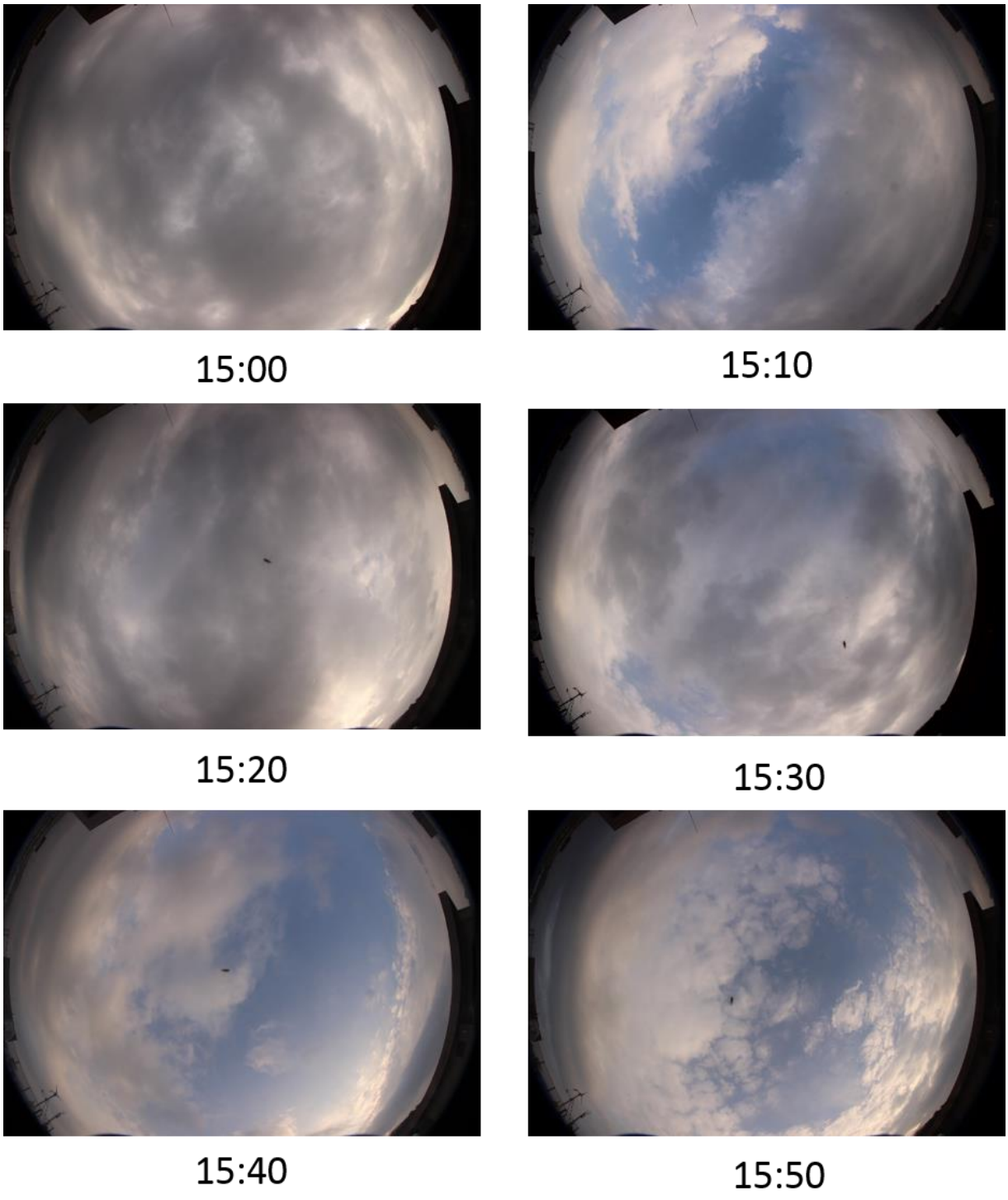

Figure 3.31: Whole-sky photographs of December 26, 2015 at an interval of 10 minutes

Here, within the same clear sky rate the types of the cloud were observed to differ along with the time standard deviation. Also, the cloud coverage during the minimum time standard deviation is seen to be more as compared to the maximum time standard deviation during the observation time. The clear sky rate less than 0.4 might result in precipitation during the course of time

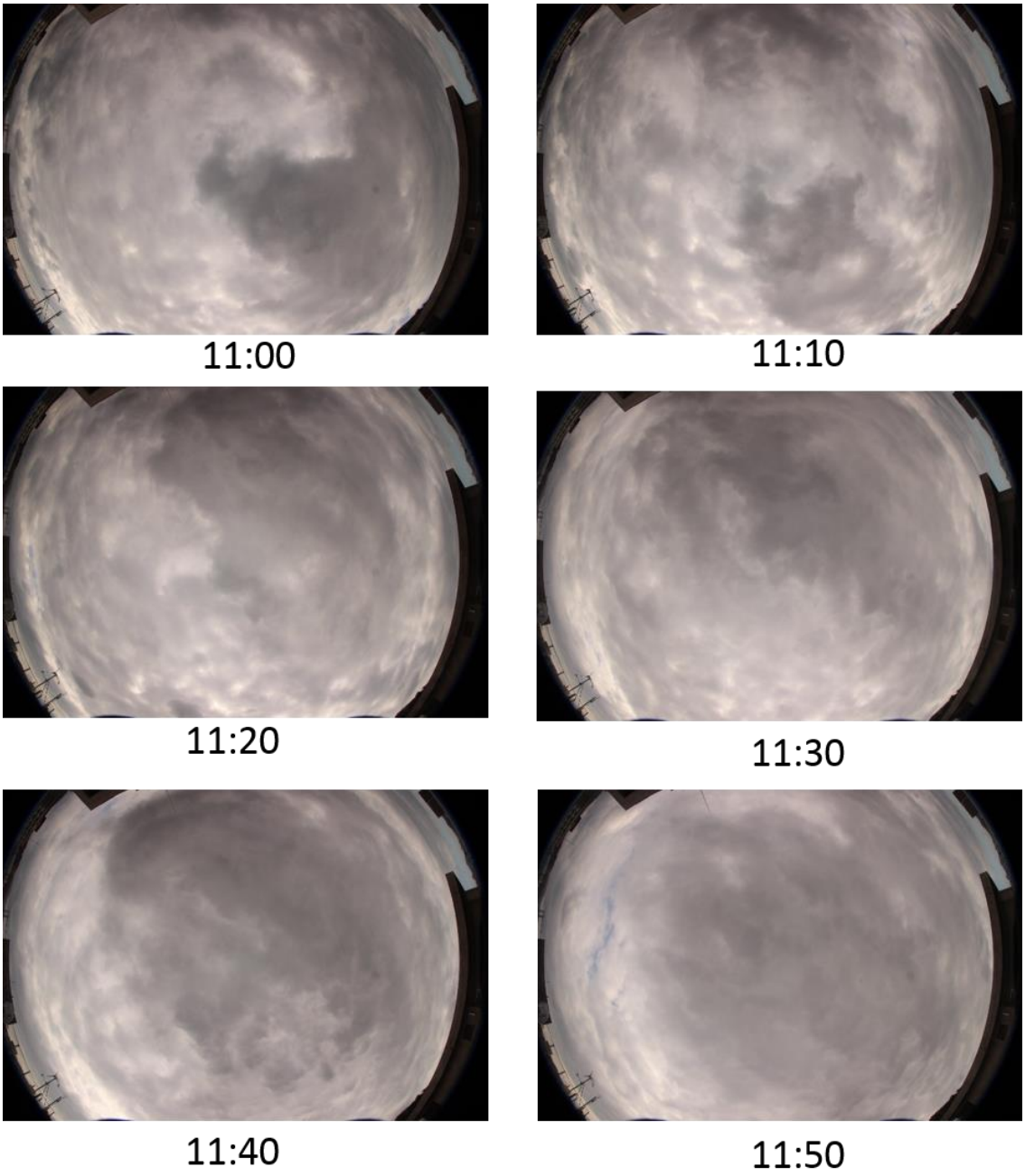

Figure 3.32: Whole-sky photographs of December 13, 2015 at an interval of 10 minutes

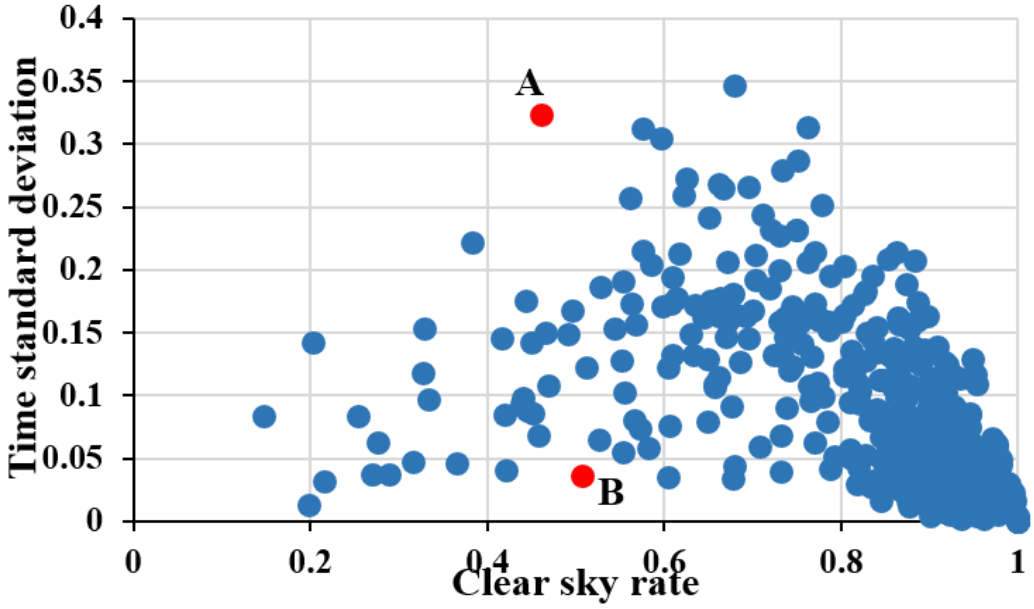

Figure 3.33: Observation of the clear sky rates between 0.4 to 0.6

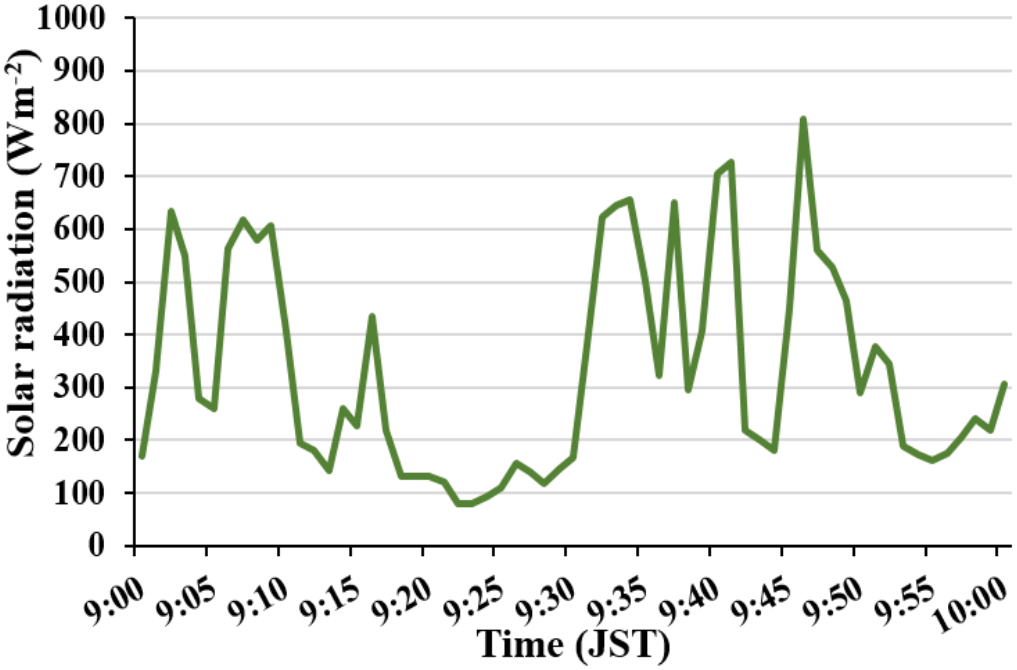

Figure 3.34: Amount of solar radiation from 9:00 to 10:00, September 13, 2015

The clear sky rates between 0.4 to 0.6 is shown in Figure 3.33. Similar to the above cases, the maximum and the minimum time standard deviation was considered to study the state of the cloud. Here, maximum time standard deviation (red point A) was observed from 9:00 to 9:59 on September 13, 2015.

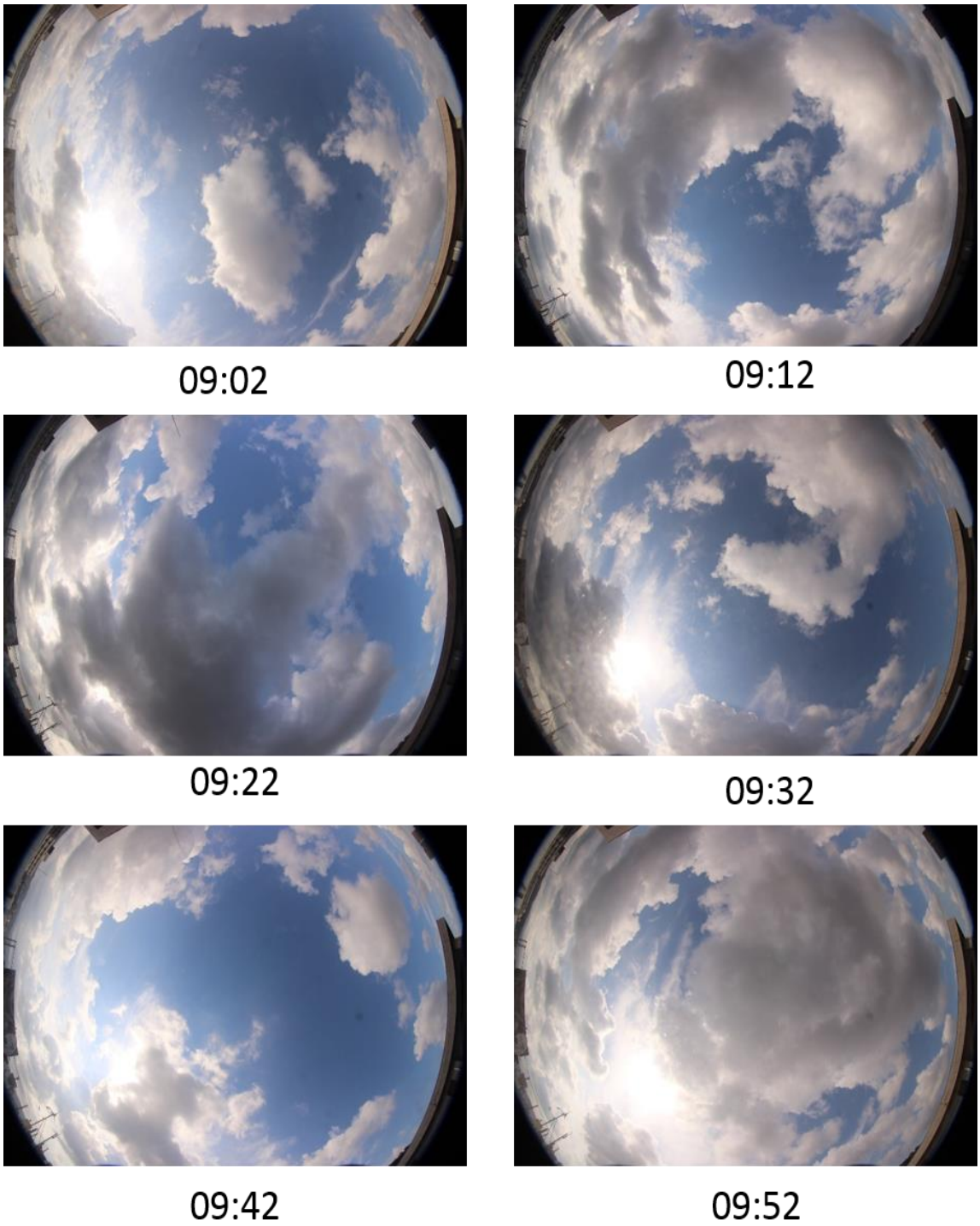

Figure 3.35: Whole-sky photographs of September 13, 2015 at an interval of 10 minutes

This distribution of the solar radiation from 9:00 to 9:59 of the target day is indicated in Figure 3.34, which shows the variation in the amount of solar radiation during the type period. This suggests that the variation of the radiation might be due to the variation in the cloud distribution. This is evident through the presence of cumulus clouds observed during the time period as indicated in Figure 3.35. Here, we observe that the cloud cover area is shifted as the time passes which suggests the movement of the cloud during the observation time. The decrease in the amount of solar radiation can be clearly noticed during the presence of cloud.

Within the same range of the clear sky rates, the minimum time standard deviation is observed from 14:00 to 14:59 on September 22, 2015 (red point B in Figure 3.33). The distribution of the amount of solar radiation from 14:00 to 14:59 as presented in Figure 3.36 doesn't show much variation in the distribution of the solar radiation which in turn suggests the presence of cloud throughout the time. This is further verified by the whole-sky photographs of an hour illustrated in Figure 3.37. This shows the presence of medium to high raised cloud such as altostratus or cirrostratus cloud.

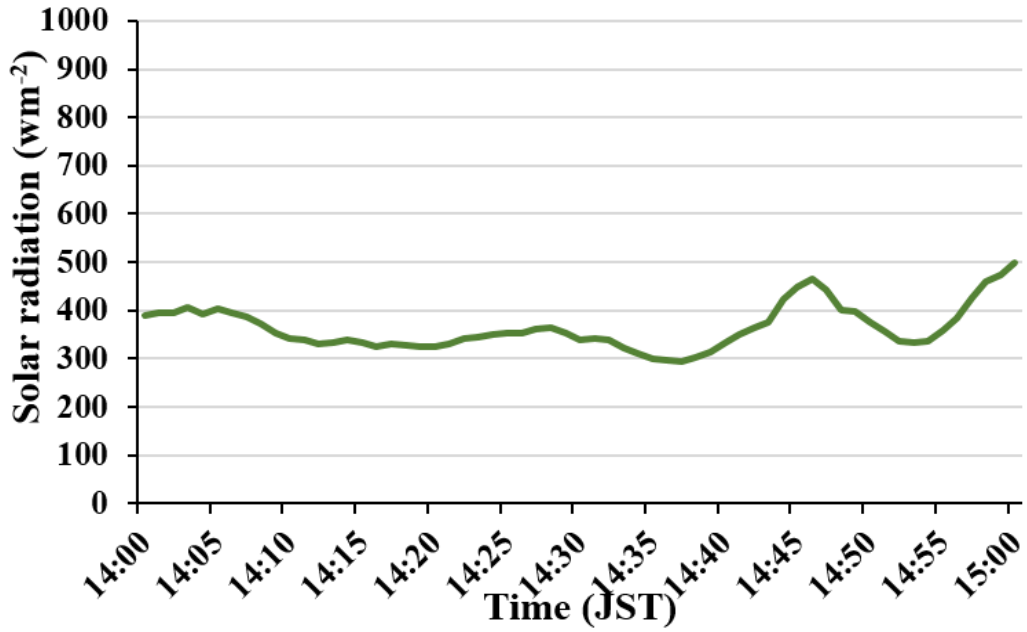

Figure 3.36: Amount of solar radiation from 14:00 to 15:00, September 22, 2015

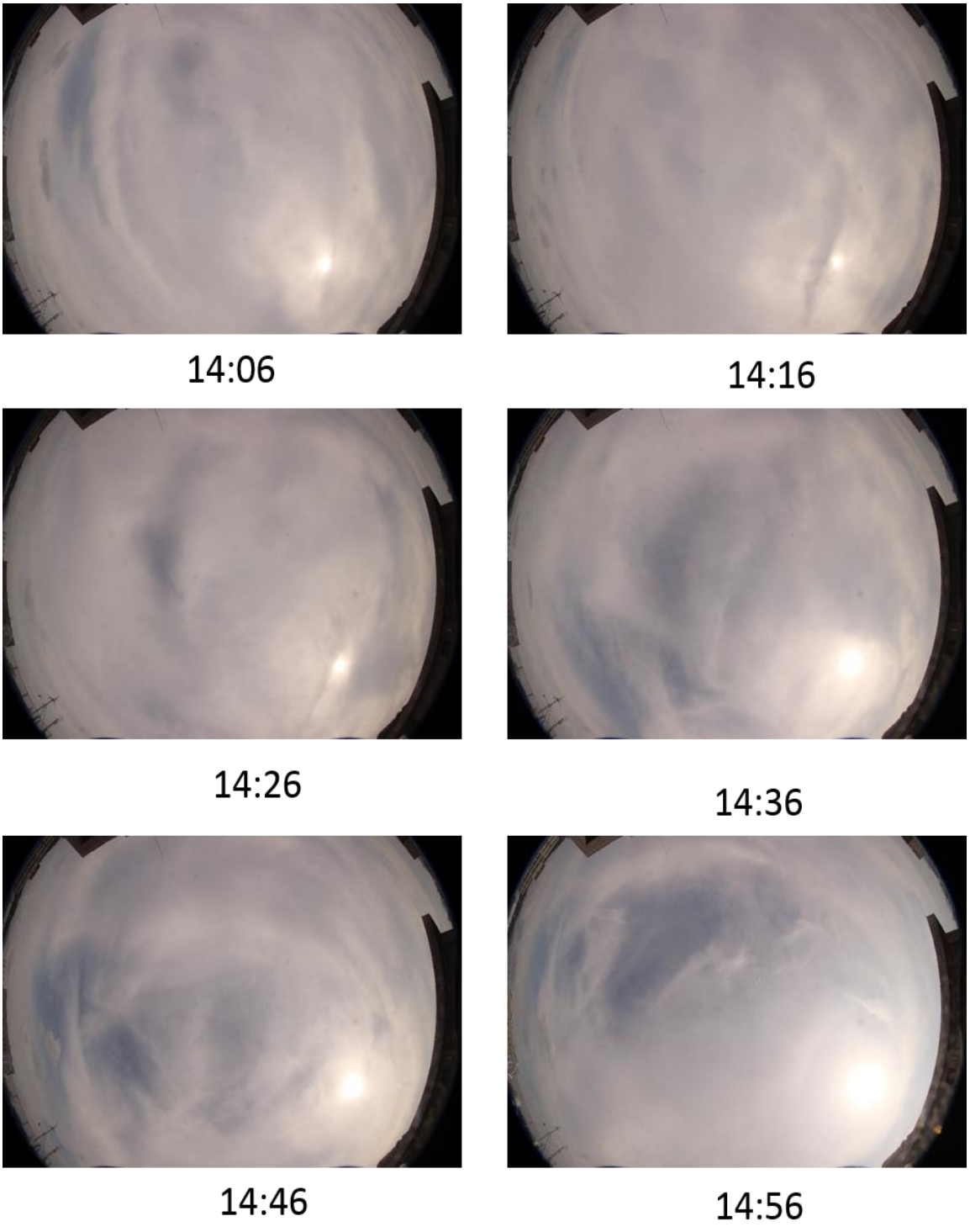

Figure 3.37: Whole-sky photographs of September 22, 2015 at an interval of 10 minutes

Thus, the difference in the sky condition and cloud type was clearly observed with the maximum and minimum time standard deviation within the same range of the clear sky rate of 0.4 to 0.6.

Again, we consider the clear sky rates varying between 0.6 to 0.8, where the maximum and minimum time standard deviation is observed as represented in Figure 3.38. Here, the range of the time standard deviation varied from about 0.03 to 0.35. The maximum time standard deviation was observed from 8:00 to 8:59 on December 13, 2015 (red point A). During the time period the clear sky was seen for most of the time with only few strands of clouds over the sky as indicated by the whole-sky photographs presented in Figure 3.39. Around 8:00 AM cumulus cloud was observed around eastern sides of the observation site but along the course of time only high raised clouds such as cirrus were seen to be dominant. Similarly, the minimum time standard deviation was observed from 15:00 to 15:59 on November 11, 2015 (red point B) in Figure 3.38. As indicated by the whole-sky photograph in Figure 3.40, the presence of high-raised cloud such as cirrostratus or cirrus were found to cover the sky through the entire time period. The remarkable difference in the cloud cover were observed between the observation data of the maximum and the minimum time standard deviation in the clear sky rates ranging from 0.6 to 0.8.

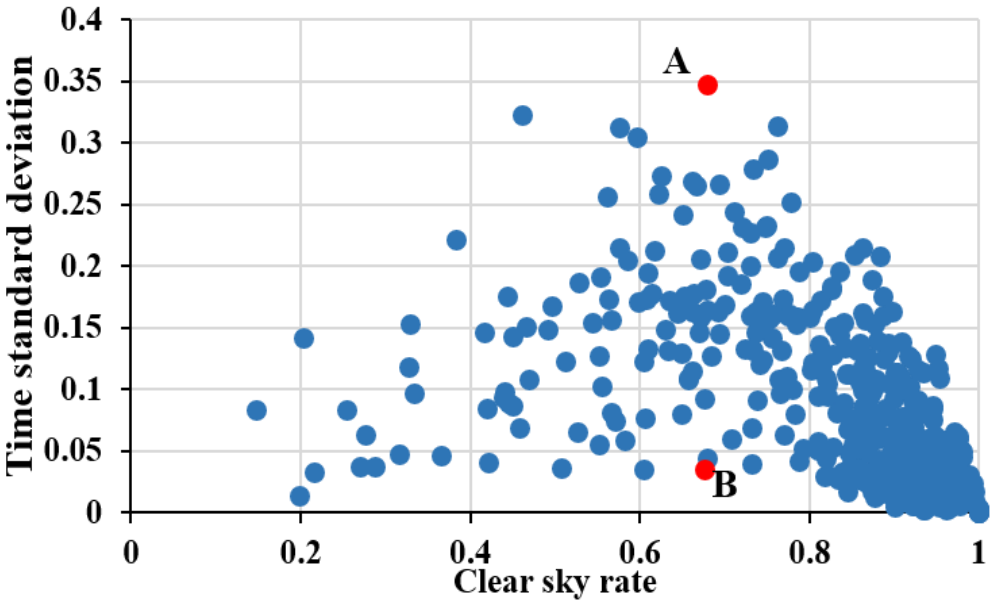

Figure 3.38: Observation of the clear sky rates between 0.6 to 0.8

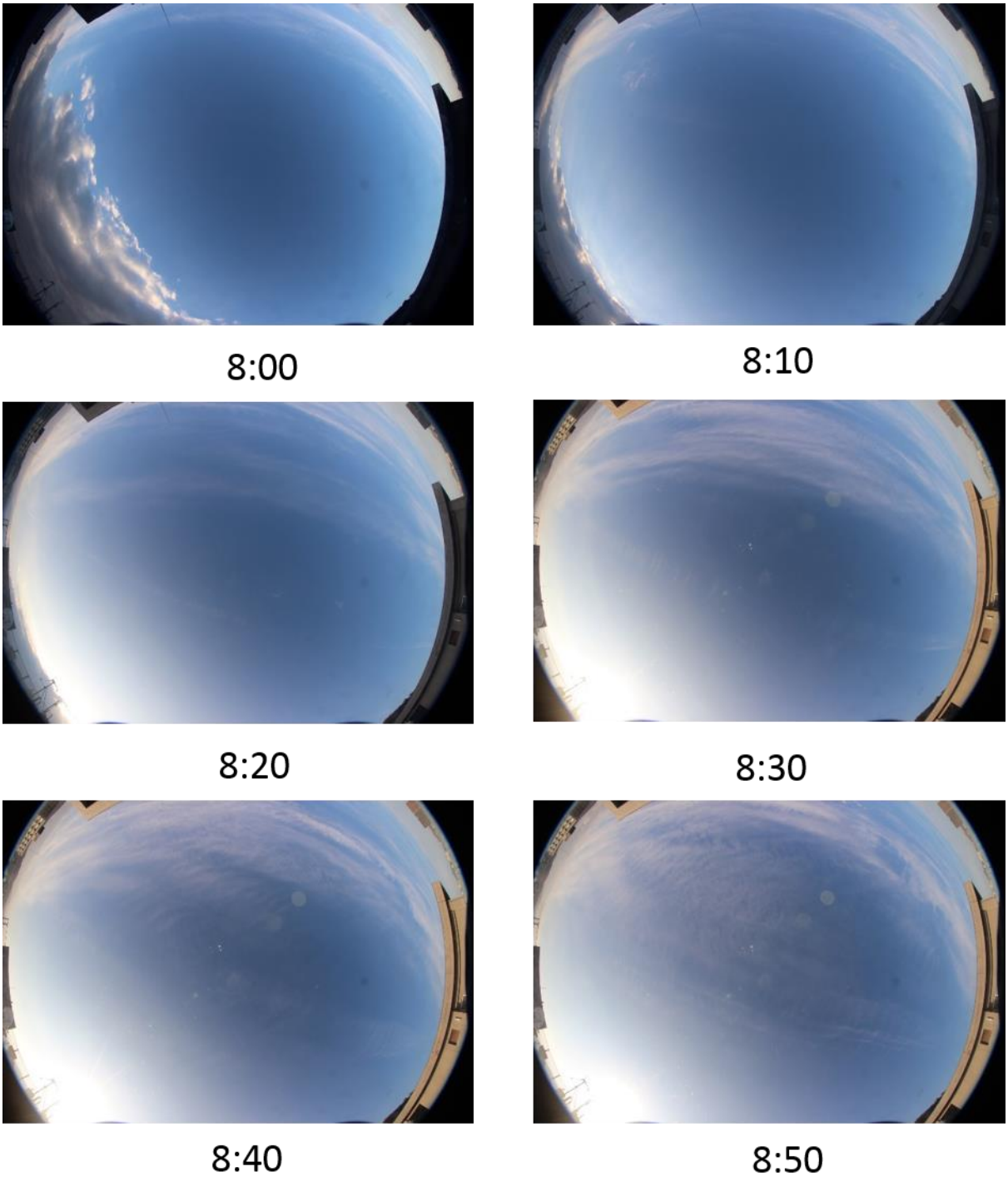

Figure 3.39: Whole-sky photographs of December 13, 2015 at an interval of 10 minutes

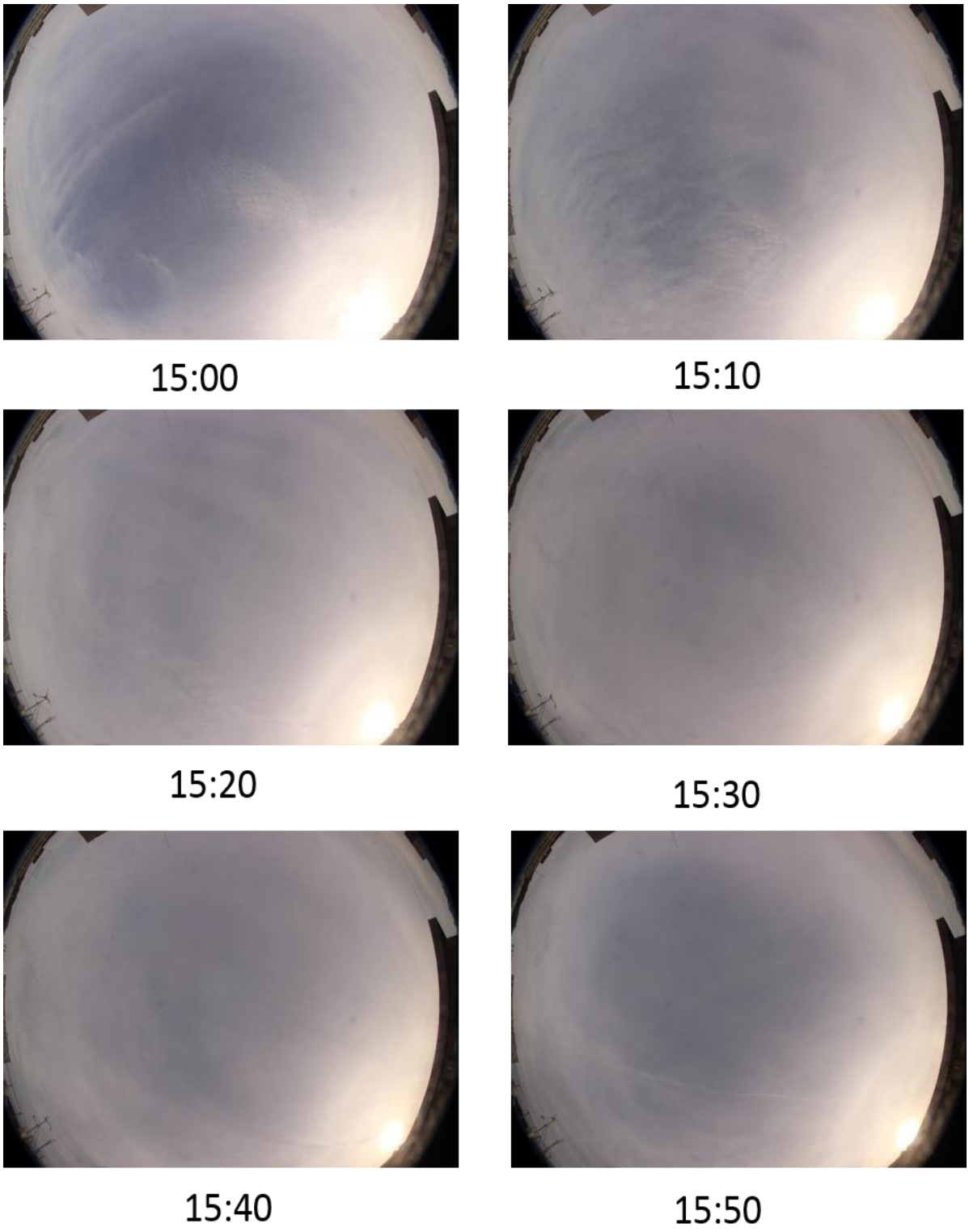

Figure 3.40: Whole-sky photographs of November 11, 2015 at an interval of 10 minutes

Finally, we consider the clear sky rates ranging between 0.8 to 1 as indicated in the Figure 3.41. The larger percentage of the observation data was observed within this range of the clear sky rate within the time standard deviation varying from 0 to 0.25. Here, the maximum time standard deviation was observed on December 18, 2005 from 15:00 to 15:59 (red point A). The whole-sky photograph presented in Figure 3.42 shows a clear sky weather condition with few patches of cumulus or altocumulus clouds occasionally present in the sky. Here, the larger percentage of the observation data were found with time standard deviation equals to zero. Thus, among all the observed value, we chose the value with clear sky rate of approximately 0.9 and time standard deviation equals to zero. Here, the minimum time standard deviation was observed on October 29, 2015 from 12:00 to 12:59 (red point B in Figure 3.41). As per the explanation of the clear rate in section 3.6, the observation value closer to 1 indicates the clear weather condition. This is also evident by the whole-sky photographs of the time period as shown in Figure 3.43.

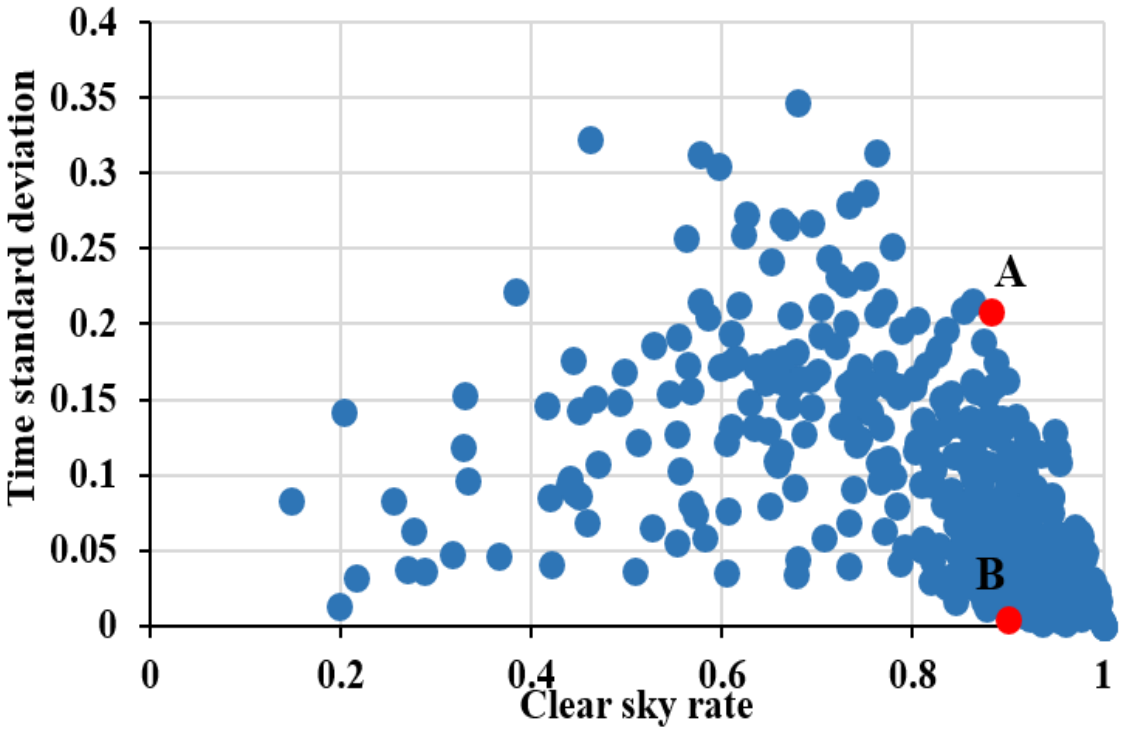

Figure 3.41: Observation of the clear sky rates between 0.8 to 1

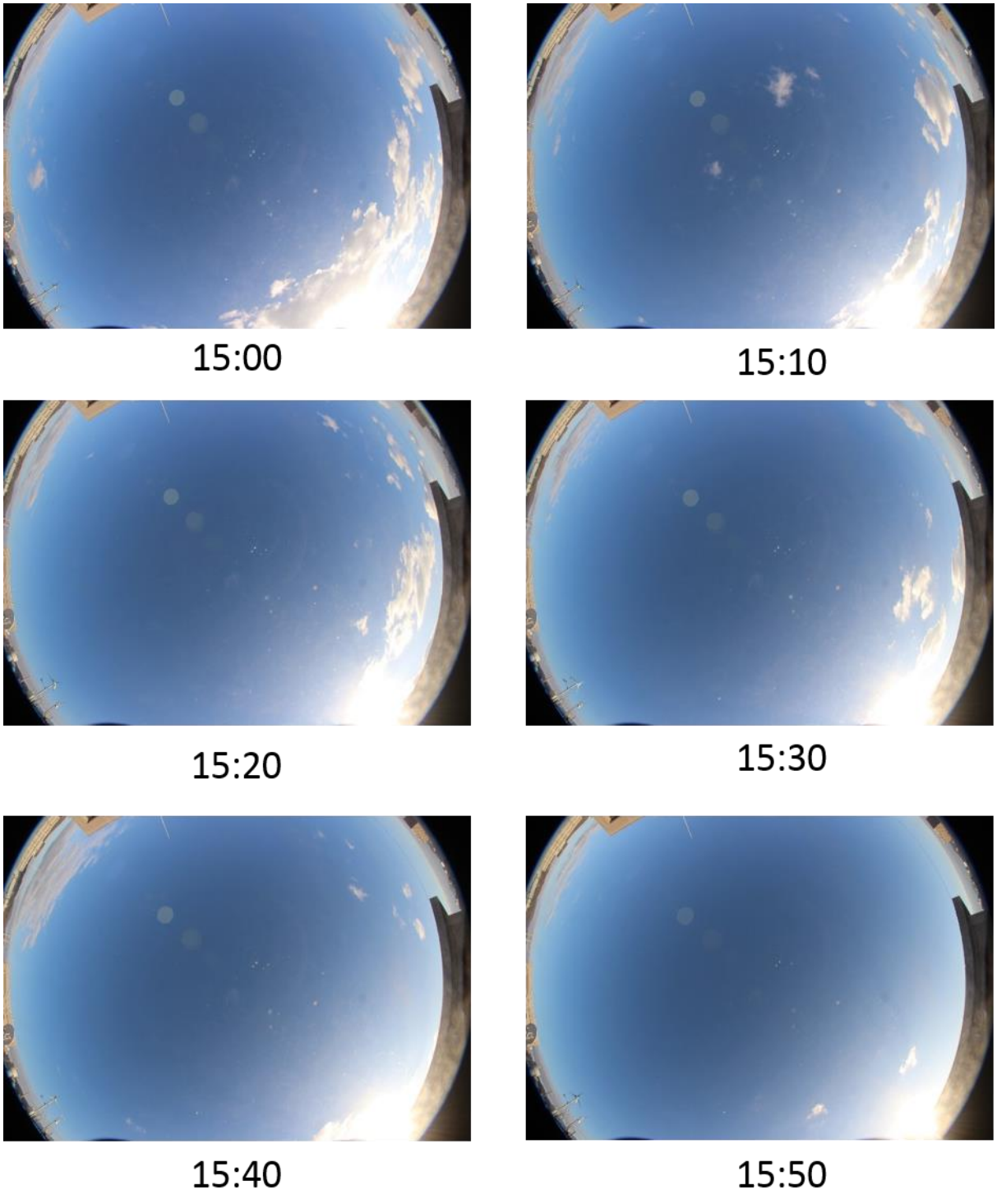

Figure 3.42: Whole-sky photographs of December 18, 2015 at an interval of 10 minutes

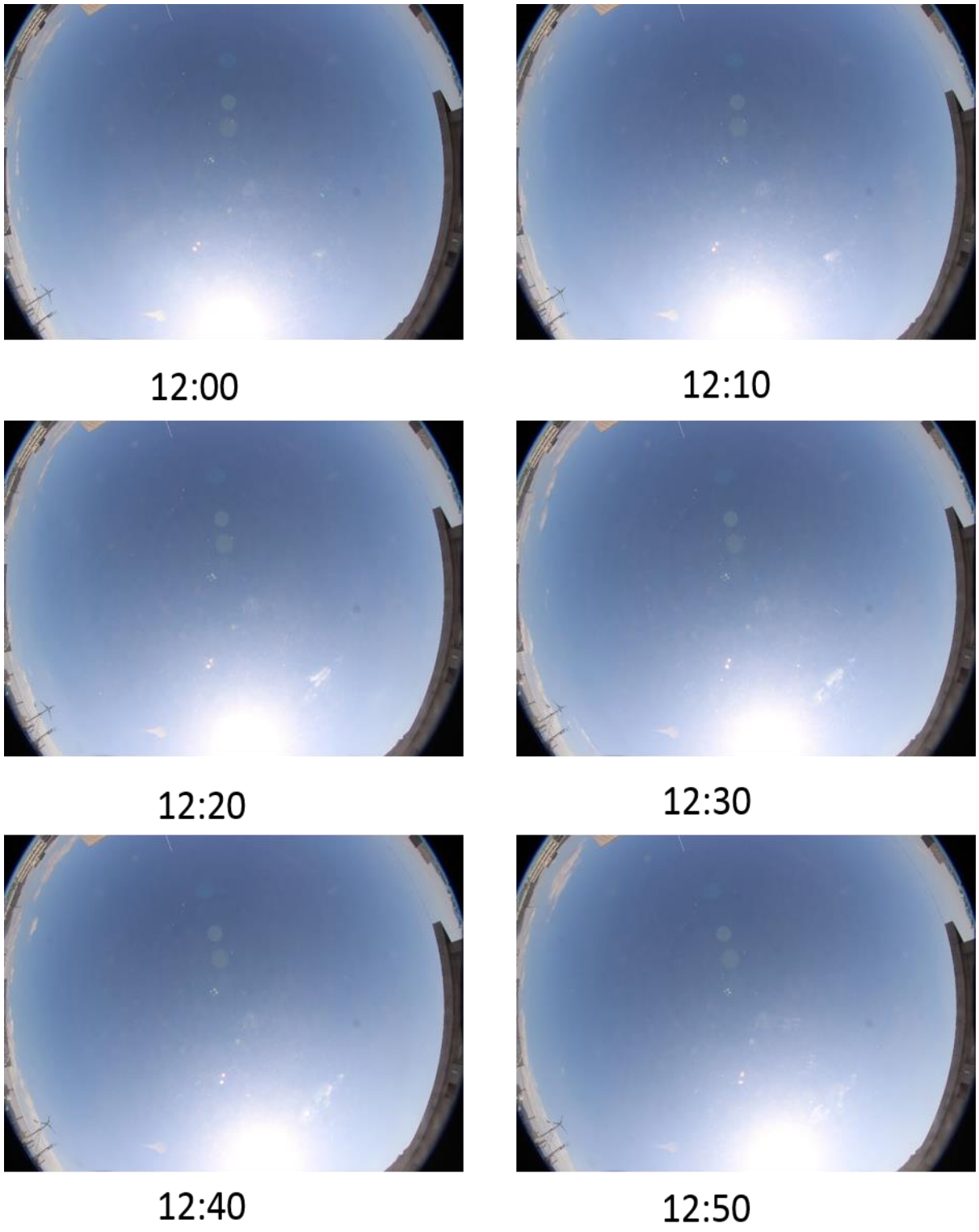

Figure 3.43: Whole-sky photographs of October 29, 2015 at an interval of 10 minutes

Thus from all the above explanation of different ranges of the clear sky rate and the maximum and the minimum time standard deviation within those sub-groups shows the variation of the clouds state and types. The observation value with maximum time standard deviation for all the sub-groups of the clear sky rate generally indicated the presence of low to medium cumulus clouds varying from cumulonimbus to altocumulus. We observed that the maximum time standard deviation at different range of clear sky rate generally shows the variation of the amount of solar radiation during the observation time period. Similarly, for all the ranges of the clear rate except from 0.8-1, at minimum time standard deviation, the entire sky over the observation points was found to be covered mostly with stratus clouds varying from low level cloud such as stratus or stratocumulus to high raised clouds such as cirrostratus or cirrus. Similar results were also explained by Duchon and O'Malley (1999), in their study for the estimation of the cloud type using the pyranometer observation in Oklahoma, Alaska and the south west Pacific.

3.9 Effect of wind factor

In Matsuyama plain, the local wind circulation has very important role in variation in the weather pattern. The plain is usually dominated by the sea breeze (westerly wind) is dominant in the daytime usually from 9:00 to 17:00 followed by the land breeze through evening. The three phenomena of sea breeze i.e. northwesterly, southwesterly and convergence of sea breeze are observed along the plain. Kusaka et al. (2000) demonstrated that the urban effect enhances horizontal convergence around the urban area and the modification of the wind system over 85 years due to the alternation of the land-use in the Kanto area of Japan. Orville (1968), demonstrated the vertical wind shear to simulate the cloud formation which might be of slow growth and dissipating type or rapid development of the cloud Rastogi et al. (2016), based on their study in the coastal California have observed that the convergence of the surface wind as it approaches the island causes the lifting of the air to the condensation level, resulting in the cloud formation. Tokinaga et al. (2009), found the increase in sensible heat due to the influence of northwesterly wind which in turn upward motion of the moisture causing the cloud to grow higher. Kitada et al. (1997), documented the mechanism of the formation of the inland high temperature in the coastal area of Japan which is in turn influenced by the urbanization and the sea breeze front.

As explained earlier during the daytime, the humid air (sea breeze) is transferred to the inland area especially through the southern part of the Matsuyama plain i.e. irrigated cropland and along the Shigenobu River (Fujimoto et al., 2010). The difference of water vapor content in the Matsuyama plain is high during nighttime (dominance period of land breeze from 18:00 PM to 8:00 AM, whereas the difference in small during the daytime (dominance period of sea breeze from 9:00 AM to 17:00 AM). The difference tends to be smaller in the afternoon, which suggests that the local sea breeze contributes to an increase in the water vapor content over inland regions through the moist air advection from the coastal regions causing more clouds formation in the inland area of the Matsuyama plain as compared to the coastal area during late afternoon. Occasionally, localized heavy rainfall in the Matsuyama plain is found due to the convergence water vapor generated by the sea breeze during the daytime.

On December 13, 2015 a maximum time standard deviation was observed for the clear sky rates between 0.6 to 0.8 from 8:00 to 8:59 as indicated in Figure 3.39. Similarly, on the same day, the minimum time standard from 11:00 to 11:59 was observed as indicated in Figure 3.32. Figure 3.44 shows the diurnal wind profile of the day which indicates the starting of the sea breeze approximately from 11:00. So, the difference in the cloudy condition might be due to the transfer of the due to the influence of the sea breeze.

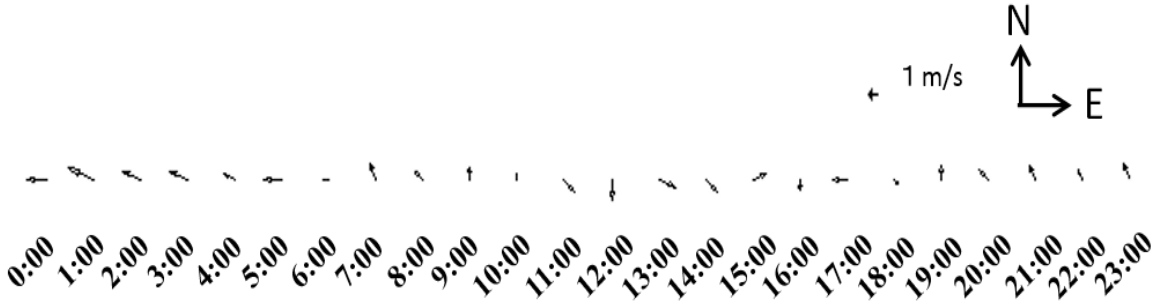

Figure 3.44: Diurnal wind profile of December 13, 2015

3.10 Chapter summary

The ground-based pyranometer network monitoring was used for the study of the temporal and spatial distribution of the solar radiation in the Matsuyama plain. Here, clear sky rate was used as the index to identify the reduction of the radiation due to the presence of the clouds. The statistical analysis (standard deviation) of the time series of the one hour pyranometer observation suggested the presence of the cloud be more in the inland and the urbanized area of the Matsuyama plain. Further, the cloud characteristics and the type was studied based on the maximum and the minimum time standard deviation for clear sky rate for 0 to 0.2, 0.2 to 0.4, 0.4 to 0.6, 0.6 to 0.8 and 0.8 to 1, respectively. The whole-sky photographs were used for the validation of the observation result. Generally, the minimum time standard deviation, the cloud coverage was observed to be more as compared to the maximum time standard deviation for the different clear sky rate. The presence of medium to high raised cloud was observed with small time standard deviation whereas with high time standard variation of clouds from low level to high raised cloud were observed with the dominance of cumulus cloud. Therefore, the temporal and spatial variation of the distribution of the solar radiation along with the variation in the cloud types was observed during the observation period within the study area.

CHAPTER 4

4. Estimation of the power generation using solar panels

The chapter includes the study to explore the potential of ground-based measurement of the solar radiation using photovoltaic system within the Matsuyama plain. The method for the estimation of the global solar radiation using the solar panel, including the separation of the different components of the solar radiation, estimation of the solar radiation on the slope and finally, the estimation of the global solar radiation from the solar radiation on the slope using the conversion factor and the output ratio of the panel is discussed in detail. The study further focuses on the photovoltaic network established in the Matsuyama plain for monitoring the distribution of the solar radiation and the cloud coverage within the area to facilitate the study for the understanding of the local climate.

4.1 Site Introduction

Matsuyama plain is a small city located on the north-eastern part of Shikoku island is one of the smallest and least populated cities of Japan. The annual daily mean temperature of Matsuyama for 2013-2015 is approximately 16.6^{o}C with annual sunshine duration of more 2000 hours making it appropriate for the production of solar energy. Matsuyama city has challenged to pioneer the effort for the realization of the significant reduction of greenhouse gases such CO_2 and use of renewable energy. Under the "Matsuyama Sunshine Project," citizens, companies and the city administration cooperate with the aim of preventing global warming and creating industries. As a part of this project, efforts are being made to promote the introduction of photo voltaic power generation in public facilities, houses and offices, etc., sell environmental values generated by above mentioned facilities as " the Green Energy Certificates" to companies, and support environmental business models such as new energy and energy-saving. Matsuyama city was selected as the “Environmental Model city” in March 15, 2013. The city has been providing subsidy to individuals for the installation of the solar panel in households, private companies etc. solar panels have been installed in almost 66 public facilities including offices, elementary school by the end of 2013 which

included average power generation of 5.6% with the target of production of 151,000 kW energy by 2020.

Hence, with the increasing number of the solar panel, Matsuyama plain was selected as the study site for the dense monitoring of the radiation using the photovoltaic network in order to monitor the effect of urbanization. The description of the study site is explained in detail in Chapter 3.

4.2 Instrumentation

As indicted in the Chapter 2**,** the solar panels mounted on the roof are usually of various types and installed at a fixed angle in much larger scale. The use of solar panels has been increasing from houses, commercial building and schools, and thus, the main objective of this study is to propose a method to estimate the global solar radiation using the Photovoltaic (hereafter PV) system. The temporal variation pattern of the solar radiation and PV power of the solar panel is in high agreement with each other (Figure 4.1) which indicates that the estimation of the global solar radiation using a PV system might be possible. For the estimation of the global solar radiation, panels installed horizontally and at a tilt angle of 20^{o} due south was taken into consideration.

To fulfill the objective of the study initially solar panel installed at Ehime University was taken into account. In this study the solar panels (single crystal hybrid

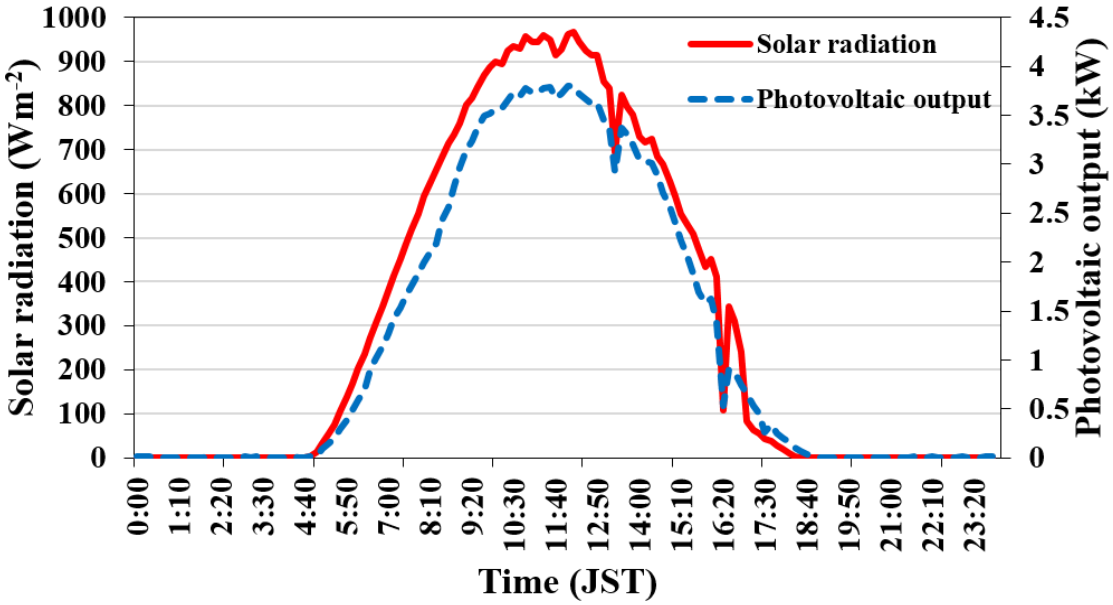

Figure 4.1: Temporal variation of the solar radiation and PV power of the solar panel (June 4, 2013)

module VBHN233SJ01A manufactured by Panasonic cooperation) were installed on the rooftop of Engineering building 2, Ehime University, Matsuyama (132.771509^{o} E, 33.850238^{o} N). The solar panels were installed horizontally and at a tilt angle of 20^{o} due south.

a. Horizontally installed solar panel

In this study, the rooftop of a 10 story Engineering building roof, Ehime University was selected for the installation of solar panels. In total 20 sheets of solar panels (rated output

a)

b)

Figure 4.2: a) Horizontally installed panels and b) pyranometer installed along with the panels for the solar radiation measurement

of 233W) were installed horizontally as shown in Figure 4.2 a. An alternating power inverter was used to convert the PV power of the panels. Here, along with the panels, a pyranometer (Eko Seiki Co. Ltd., MS-602 as shown in Figure 4.2b) was installed for the measurement of the solar radiation.

b. Solar panels installed at an angle

To receive the maximum exposure of the sun over the course of a year, solar panels should be tilted at an angle approximately equal to a site's latitude. The installation of panels in general building has additional limitations such as the building shape, direction of the house and surrounding structures. Therefore, it is necessary to consider all these factors before the panel installation. In this study, we installed the panel at a tilt angle of 20^{o} due south as solar panels with similar settings has been installed in many elementary schools and junior high schools in the study area.

The installation site was the rooftop of a 6 story building at Ehime University, which is approximately 50m away south from a 10 story building as described in the previous section. Solar panels with the same specification, as explained in section 4.2 a) was used for the measurement, but here the panels were tilted at an angle of 20^{o} due south (Figure 4.3).

Figure 4.3: Solar panel installed at a tilt angle of 20^{o} due south

The power generated by the solar cell is usually represented by a correlation curve of the voltage and the current which is known as I-V (current-voltage) characteristic curve. At a given intensity, a solar panel's output current and operating voltage are determined by the characteristic of the load. The power that one module can produce is seldom enough to meet requirements of a home or a business, so the modules are linked together to form an array. Most PV arrays use an inverter to convert the DC power produced by the modules into alternating current that can power lights, motors, and other loads. The modules in a PV array are usually first connected in series to obtain the desired voltage; the individual strings

Figure 4.4: Electronic load, Array, 3721A

Figure 4.5: Pyranometer (Kipp & Zonen, CMP-3) installed along with the titled solar panel

Figure 4.6: Combination of a pyranometer (Kipp & Zonen, CMP-3), sunlight shielding device and solar tracking device to measure the direct beam and diffuse solar radiation

are then connected in parallel to allow the system to produce more current. Solar panels are typically measured under STC (standard test conditions) or PTC (PVUSA test conditions), in watts.

In this study an electronic load (Array, 3721A) was used to collect the maximum output from the PV system. The Array 3721A used in the study is shown in Figure 4.4. Here, the electronic load is set to a constant voltage mode (CV mode), to obtain the maximum output the voltage has been automatically control at a voltage of 25 ~ 40V, and the output is obtained by using a programing language for the computation and then the continuous observation was carried out for the study period.

At a distance of 5m from the panel, a pyranometer (Kipp & Zonen, CMP-3) was installed to measure the global solar radiation as explained in Chapter 3 (Figure 4.4). As explained in Chapter 2, some part of the solar radiation is diffused by the fine particles such as aerosol in the atmosphere. The global solar radiation is the sum of the direct beam solar radiation and the diffuse solar radiation. Thus, in this study the direct beam solar radiation was measured using a pyrheliometer (Prede, PCH-2) whereas diffuse solar radiation was measured using combination of pyranometer (Kipp & Zonen, CMP-3), sunlight shielding

device and solar tracking device (Prede, PHSX-2GPSEU) as shown in the Figure 4.6. An additional pyranometer (Kipp & Zonen, CMP-3) was also installed along with the tilted solar panels for the measurement of the radiation on the slope.

4.2.1 Data Used

As explained earlier, a photovoltaic system and a pyranometer installed at the Ehime University was used for the estimation of the global solar radiation and the validation of the proposed estimation method. Regarding this the amount of radiation was observed continuously and simultaneously from June 2014 till date. Here, the measured one-minute dataset of the PV power of the solar panel was taken into consideration for the estimation of the global solar radiation in a titled solar panel. Since the PV power of the solar panel depends on the size and type and material used in the solar panel, the maximum output of the panel is determined using output ratio which is defined as the ratio of the PV power of the solar panel to its rated output.

Here, data from June to August was considered as summer data and December as winter data. Among these months, several days depending on the weather condition such as sunny, partially cloudy and cloudy days were selected using the meteorological information from the Matsuyama meteorological observatory which is operated under the Japan Meteorological Agency (JMA).

4.3 Estimation of global solar radiation

Solar panel is rated by its direct current power under standard test conditions (JISC8918 air mass (AM)1.5 spectrum has a power density of $1000 Wm^{-2}$ at module temperature of 25℃). That is a 12% efficient solar cell having $1m^2$ of surface area during the maximum sunlight (at solar noon at equator) will produce 120W of power. Thus, the power ratio which is defined as the ratio of the PV power to the rated output of the solar panel may be used as the first estimation of solar radiation. The maximum operating efficiency of the module is found at AM approximately equal to 1.5 (Parratta et al., 1998, Randall and Jacot, 2003). When mounted outdoors, PV modules typically operates at higher temperature than those under the standard condition. According to Bucher (1997), the power output of a PV module decreases by approximately 0.4% per degree for the crystalline silicon modules

whereas lower relative temperature coefficient is observed for the amorphous silicon module. The comparison of the different photovoltaic modules is studied by many researchers such as Shah et al. (1999), Chianese et al. (2000), Randall and Jacot (2003), Green et al. (2015) and many more.

However, in practice, the conversion loss in the power conditioner, the electric resistance loss during wiring, aging of the panel and dust accumulation causes reduction in the PV output and even if the estimated solar radiation from a panel is 1000 Wm^{-2} the true output value might be less than the rated output. Bucher (1997), found the efficiency of the PV module is subject to loss under the outdoor operation where the weather condition changes with respect to time. Similarly, according to Merten and Andreu (1998), the irradiance in the summer results in slightly higher in summer compared to winter season due to variation in the temperature. Camani et al. (1998), in his study based on the comparison of the 11 module, have found the loss of power in the panel with respect to the exposure duration

Therefore, in order to incorporate the effects of environmental factors, power ratio is corrected using a conversion factor for the estimation of the global solar radiation as explained later in the Chapter. The PV power of solar panels installed at an inclination is considered to be proportional to the amount of solar radiation on the slope. Therefore, to estimate the global solar radiation, it is necessary to convert the solar radiation on a slope to the global solar radiation on a horizontal plane. Thus, for this conversion the separation of the solar radiation into the direct beam solar radiation and the diffuse solar radiation becomes necessary.

Cheng et al. (2006), developed an empirical approach for estimating the solar radiation on a tilt planes with an inclination of 0^o to 90^o using the monthly ratio of the tilted plane irradiation to the horizontal irradiation with no ground reflection for the building energy application. For the accurate calculation of the amount of solar radiation falling on a solar panel tilted at an angle from the horizontal surface, a series of calculation must be done. The calculation of the extra-terrestrial radiation, global solar radiation and different components of the solar radiation is discussed in Chapter 2.

4.3.1 Conversion factor

The global solar radiation I (Wm^{-2}) is estimated using the output ratio P and the conversion factor c (Wm^{-2}) as expressed in Equation 4.1.

$$I = cP \qquad (4.1)$$

In case of the solar panels installed at an inclination the amount of solar radiation $I_{\beta\gamma}$ (kWm^{-2}) and the output ratio $P_{\beta\gamma}$, the amount of solar radaition can be determined using the output ratio and a coversion factor c as shown in Equation 4.2.

$$I_{\beta\gamma} = cP_{\beta\gamma} \qquad (4.2)$$

The equation can be further modified as Equation 4.3.

$$c = I_{\beta\gamma} / P_{\beta\gamma} \qquad (4.3)$$

In this study, the conversion factor "c" is determined using the output ratio $P_{\beta\gamma}$ and the amount of solar radaition on a slope $I_{\beta\gamma}$. The amount of solar radiation on a slope is measured using a pyranometer installed at same inclination as the panels.

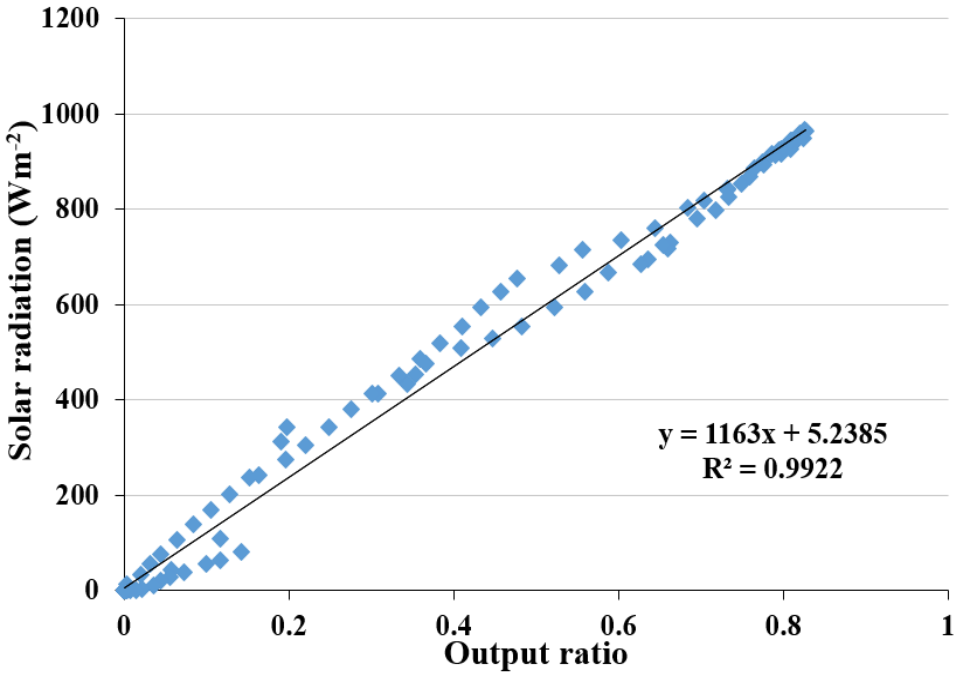

Figure 4.7: Correlation between the measured solar radiation and output ratio of the panel (June 4, 2014)

For the estimation of the conversion factor, the output ratio of the solar panel of the coefficient identification day is taken and a correlation diagram using the amount of solar radiation and the output ratio is constructed. Using the linear regression, the value of the conversion factor is estimated as shown in the Figure. For the calcuation of c, a sunny weather condition was selected depending on the season. The estimation method of c for June 4, 2014 is representated in Figure 4.7. Here, the value of the conversion factor is used as 1163 Wm^{-2} for the estimation of the solar radiation. Here each year was separeted into four seasons; March to May as Spring, June to August as Summer, September- November as Autumn and December – Febraury as Winter, respectively for the determination of the conversion factor.

4.3.2 Horizontally installed panel

The global solar radiation I (Wm^{-2}) is estimated using the output ratio P and the conversion factor c (Wm^{-2}) as expressed in Equation (4.1). The conversion factor was determined in advance by using P and the measured solar radiation of a sunny day in summer. In this study, c was determined using the dataset where P is greater than 0.1. The calculated c was used for the estimation of the total solar radiation for the other analysis days. In this study the c was basically calculated for two cases:

1. Case-A: constant conversion factor with respect to the time and
2. Case-B: conversion factor varying with respect to time (i.e. Temporal variation of the conversion factor)

Figure 4.8 shows the diurnal variation of the solar radiation on June 4, 2014 (sunny day), output ratio and temporal variation of the conversion factor, respectively. The similar variation pattern of the measured global solar radiation and the output ratio indicates that the global solar radiation estimation using a PV system might be possible. Here, the higher output ratio was observed when the conversion factor was smaller or vice-versa. We can observe that the conversion factor is generally larger than 1000 Wm^{-2} and peaks around the time of sunrise and sunset. In other words, the power generation efficiency is higher during the midday whereas the efficiency decreases during sunrise and sunset.

Under the standard test condition without any loss, the conversion factor must be equal to 1000 Wm^{-2} (Equation 4.1), but here the minimum value observed during the midday of a sunny day in summer season is about 1200 Wm^{-2} (Figure 4.8 c). That is, even in a sunny day, the maximum PV power is not in accordance with the rated output. This might be due to the conversion loss in power conditioner, the electrical resistance loss during the wiring, loss due to dust accumulation on the panel surface. Thus, for the solar panels to be used as a solar radiation sensor, accurate calculation of the conversion factor is necessary for the estimation of the global solar radiation.

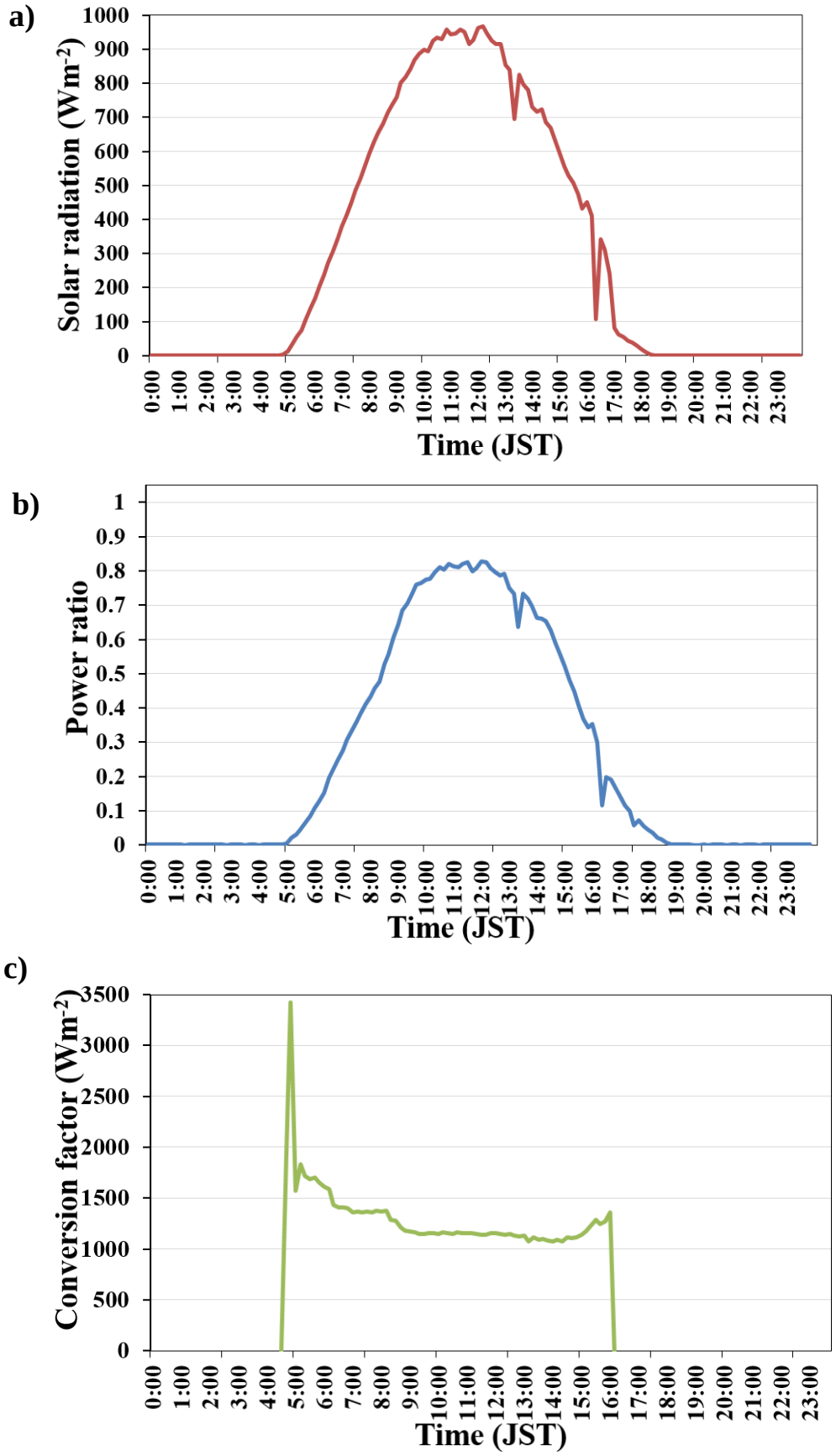

Figure 4.8: Diurnal courses of (a) global solar radiation (June 4, 2014), (b) output ratio and (c) conversion factor

4.3.3 Solar panel installed at an angle

4.3.3.1 Separation model of solar radiation components

The total amount of solar radiation falling on a horizontal surface is generally defined as the global solar radiation. Global solar radiation is comprised of the direct beam solar radiation arriving directly at the earth's surface and the diffuse solar radiation on the horizontal surface.

Global solar radiation is generally expressed as the sum of direct beam and the diffuse solar radiation as expressed in Equation 4.4.

$$I = I_b + I_d \qquad (4.4)$$

where,

I is the global solar radiation

I_b is the direct beam solar radiation and

I_d is the diffuse solar radiation

Various models such as Erbs et al. model (1982), Lam and Li model (1996), and others based on the empirical formula describe the diffuse fraction as the ratio of the diffuse solar radiation to the global solar radiation (I_d / I).

In this study, we adopted the relation proposed by Erbs et al. (1982), for the estimation of the diffuse solar radiation as represented in Equation 4.5

$$\begin{cases} \dfrac{I_d}{I} = 1.0 - 0.99\dfrac{I}{I_o} \; for \; \dfrac{I}{I_o} \le 0.22 \\ \dfrac{I_d}{I} = 0.9511 - 0.1604\dfrac{I}{I_o} + 4.388\left(\dfrac{I}{I_o}\right)^2 - 16.638\left(\dfrac{I}{I_o}\right)^3 + 12.336\left(\dfrac{I}{I_o}\right)^4 \\ \quad for \; 0.22 < \dfrac{I}{I_o} \le 0.80 \\ \dfrac{I_d}{I} = 0.165 \; for \; 0.80 < \dfrac{I}{I_o} \end{cases} \qquad (4.5)$$

where,

I_o is the extra-terrestrial radiation on a plane perpendicular to the Sun's rays in Wm^{-2} (obtained from the astronomical calculation, Chapter 2)

I / I_o is the clearness index

Figure 4.9 shows the relationship between the diffuse fraction and the clearness index of the measured solar radiation and the result of the Erb et al. model on September 3, 2014. The measured diffuse fraction is in slight agreement with the result of the Erbs et al. model. The Erbs et al. model exhibits a tendency to overestimate or underestimate the direct beam solar radiation value depending on the type of day, location and season (Vijayakumar et al., 2005, Jacovides et al., 2006). According to Gansler et al. (1995), the models developed for the estimation of the diffuse fraction for hourly data can result to error when applied short time data. This study basically focuses on the estimation of the global solar radiation, and thus the determination of the diffuse fraction is out of scope for this study.

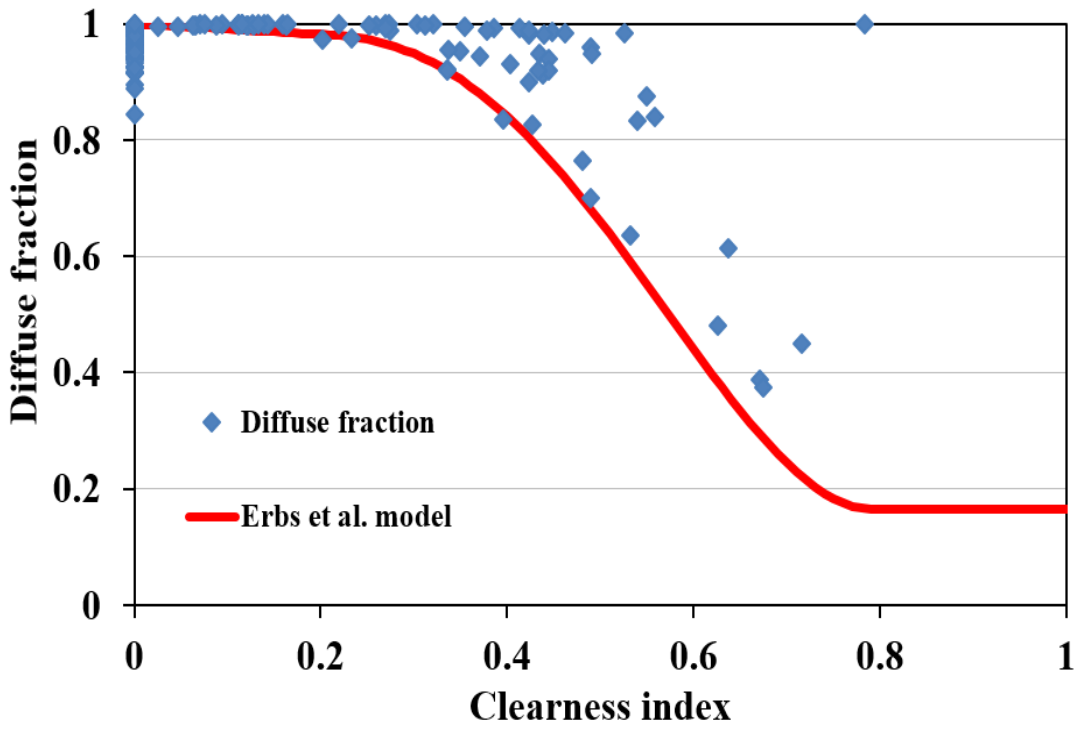

Figure 4.9: Relationship between the diffuse fraction and the clearness index (September 3, 2014)

4.3.3.2 Solar radiation on a slope

Solar radiation on a slope with the inclination angle β and the azimuth angle γ (0 when facing south), is expressed as the sum of the direct beam solar radiation, diffuse solar radiation and the reflected solar radiation (Equation 4.6).

$$I_{\beta\gamma} = I_{b\beta\gamma} + I_{d\beta\gamma} + I_{r\beta\gamma} \qquad (4.6)$$

The direct beam solar radiation on a slope is expressed by Equation 4.7.

$$I_{b\beta\gamma} = I_b \times \frac{\sin h \cos\beta + \cos h \sin\beta \cos(\gamma - \phi)}{\sin\phi \sin\delta + \cos\phi \cos\delta \cos\omega} \qquad (4.7)$$

where,

h is the solar elevation angle

δ is the declination angle of the sun

ϕ is the local latitude and

ω is the hour angle.

Similarly, the reflected solar radiation $I_{r\beta\gamma}$ is expressed by Equation 4.8.

$$I_{r\beta\gamma} = I\alpha(1 - \cos\beta)/2 \qquad (4.8)$$

where, α is the albedo (assumed to be 0.2).

In this study, all the faces of the panels are assumed to be Lambertian, and thus the reflected solar radiation is isotropic. The diffuse solar radiation $I_{d\beta\gamma}$ on a slope is estimated by using Equation 4.9.

$$I_{d\beta\gamma} = I_d(1 + \cos\beta)/2 \qquad (4.9)$$

Thus, the solar radiation on a slope can be determined from the global solar radiation I, direct beam solar radiation I_b and the diffuse solar radiation I_d.

4.3.3.3 Global solar radiation on slope

The visible area from a tilted solar panel is a hemisphere that consists of part of the sky and the earth's surface respectively. In this study, the global solar radiation is estimated on a slope as explained below.

1. For the estimation of solar radiation on a slope we take Equation 4.2 into consideration. Here, the conversion factor c is determined empirically using the horizontal panels. For simplicity c is considered to be constant irrespective of time.
2. Assuming Equation 4.5 is applicable for the calculation of the diffuse solar radiation on slope $\frac{I_{d\beta\gamma}}{I_{\beta\gamma}}$ was calculated.
3. Equation 4.9 is modified to $I_d = \frac{2I_{d\beta\gamma}}{1+\cos\beta}$ by substituting the observed result in step 2.
4. Modifying the Equation 4.6, we obtain Equation 4.10.

$$I_{b\beta\gamma} + I_{r\beta\gamma} = I_{\beta\gamma} - I_{d\beta\gamma} \qquad (4.10)$$

In the above equation, the left hand side is the sum of Equation 4.7 and Equation 4.8.

$$I_{b\beta\gamma} + I_{r\beta\gamma} = I_b \times \frac{\sin h\cos\beta + \cos h\sin\beta\cos(\gamma-\phi)}{\sin\phi\sin\delta + \cos\phi\cos\delta\cos\omega} + (I_b + I_d)\alpha(1-\cos\theta)/2 \qquad (4.11)$$

Solving for I_b we get,

$$I_b = \frac{I_{b\beta\gamma} + I_{r\beta\gamma} - I_d\alpha(1-\cos\theta)/2}{\frac{\sin h\cos\beta + \cos h\sin\beta\cos(\gamma-\phi)}{\sin\phi\sin\delta + \cos\phi\cos\delta\cos\omega} + \alpha(1-\cos\theta)/2} \qquad (4.12)$$

Here, $I_{b\beta\gamma} + I_{r\beta\gamma}$ in Equation 4.12 is equal to $I_{\beta\gamma} - I_{d\beta\gamma}$ in Equation 4.10. So, $I_{\beta\gamma}$ and $I_{d\beta\gamma}$ calculated from step 1 and 2 and I_d from step 3 is substituted into Equation 4.12 to compute the direct beam solar radiation.

Finally, the diffuse solar radiation I_d calculated from step 3 and the direct beam solar radiation I_b from Equation 4.12 is substituted into Equation 4.2 to estimate the global solar radiation on a slope.

It must be noted that simple assumptions, such as the uniformity of the diffuse solar radiation (Equation 4.2), the reflected solar radiation from the ground surface are isotropic (Equation 4.9), and applying Erbs et al. model (1982), for the estimation of the diffuse solar radiation on a slope. These assumptions facilitate to estimate the global solar radiation from the solar radiation on a slope.

4.3.4 Photovoltaic network

To study the temporal and spatial distribution of solar radiation and sky condition, the photovoltaic network established by the installation of solar panels at 25 elementary and junior high school in the study area was taken into consideration. The observation sites within the study area is represented in Figure 4.10. Similarly, the observation site name (schools name) and the coordinates of the site are presented in Table 4.1. The numbering of

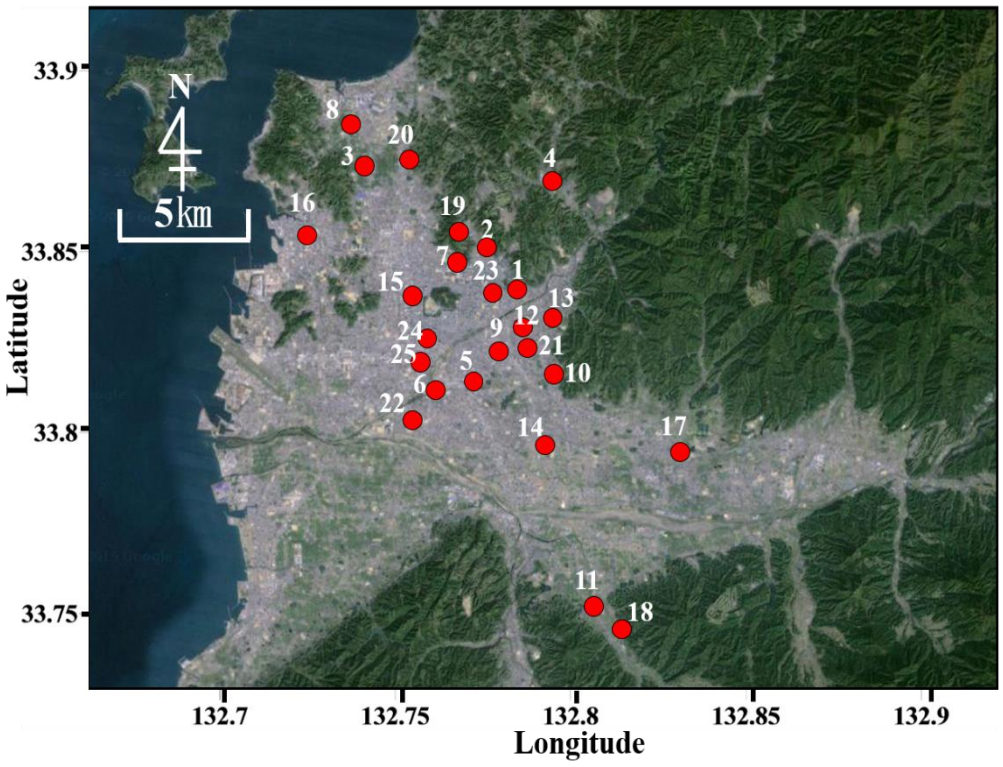

Figure 4.10: The solar panel installation site in the Matsuyama plain (25 installation site)

the observation sites in Figure 4.10 is matched with the serial number of the school name listed in the Table 4.1.

Table 4.1: Solar panel installation site along a with the coordinates

S. no	Observation site	Coordinates
1	Dougo elementary school	132.791662°E, 33.845403°N
2	Higashi junior high school	132.774008°E, 33.850182°N
3	Hisaeda elementary school	132.740315°E,33.871360°N
4	Idai elementary school	132.798435°E, 33.877338°N
5	Ishii elementary school	132.777061°E, 33.811326°N
6	Ishiikita elementary school	132.767817°E, 33.818911°N
7	Katsuyama junior high school	132.764543°E, 33.851686°N
8	Kita junior high school	132.734888°E, 33.883442°N
9	Kitakume elementary school	132.798414°E, 33.820500°N
10	Kume elementary school	132.806738°E, 33.810614°N
11	Kutani junior high school	132.818895°E, 33.758426°N
12	Kuwabara elementary school	132.793488°E, 33.835224°N
13	Kuwabara junior high school	132.805835°E, 33.836703°N
14	Minamidaini junior high school	132.793335°E, 33.795123°N
15	Misake elementary school	132.752910°E, 33.847576°N
16	Miyamae elementary school	132.720818°E, 33.859440°N
17	Ono junior high school	132.836523°E, 33.807106°N
18	Sakamoto elementary school	132.825615°E, 33.749666°N
19	Shimizu elementary school	132.766742°E, 33.851999°N
20	Shiomi elementary school	132.755231°E, 33.874595°N
21	Takunan junior high school	132.783630°E, 33.829195°N
22	Tsubaki junior high school	132.754094°E, 33.808125°N
23	Yasaka elementary school	132.782033°E, 33.840146°N
24	Yugun elementary school	132.782033°E, 33.840146°N
25	Yuushin Junior high school	132.753742°E, 33.824921°N

The panel installed in all schools were manufactured by Kyocera cooperation, Japan with the manufacturing date varying between 2009 - 2012. The observation data of the power generation of the solar panel installed in the Matsuyama plain was provided by professor Shinji Tsuzuki of Department of Electrical and Electronic Engineering, Ehime University, Japan.

The panels in all the observation sites are mostly installed at an angle of 20^{o}. As the azimuth angle of each school are different, depending on the location the installation angle of the panel ranged from south-southeast to south-southwest. Power obtained by the solar power is a direct current (DC), however, the electric equipment utilized for the measurement is generally intended for alternating current (AC). Therefore, to utilize the electric power obtained by solar panel, it is necessary to convert the DC power to AC power. Thus power conditioner is installed along with the solar panel to convert the DC power to the AC power. The power conditioner used at all the observation sites is manufactured by GS Yuasa corporation, Japan.

The observation of the solar radiation using the photovoltaic system in the Matsuyama plain started from 2014 and since then the number of panel installation has been increasing. The solar radiation dataset was recorded every minute and the observation time (i.e. every hour, minutes and seconds of the observation) was considered for the analysis.

4.4 Comparison of the estimated and the measured global solar radiation

4.4.1 Solar radiation in a horizontal surface

In order to check the performance of the proposed estimation method, days with various weather conditions (i.e. sunny day, partially cloudy day and cloudy day) in the August were taken into consideration. Here, Figure 4.11 shows the comparison of the measured and estimated global solar radiation using the conversion factor calculated from the dataset of June 4, 2014 (as indicated in Figure 4.7) where, Figure 4.11a represents sunny weather condition, Figure 4.11 b. represents partially cloudy weather condition and Figure 4.11 c. represents the cloudy or rainy weather condition, respectively. The diurnal variation

of the measured and estimated global solar radiation was observed to be similar for all the observation day irrespective of the weather condition.

During the partially cloudy day (Figure 4.11 b) and the cloudy day (Figure 4.11 c), the reduction in the solar radiation due to the presence of the clouds for both measured and estimated datasets were in accordance with each other. The correlation coefficient as the goodness of fit index along with the Root Mean Square Error (RMSE), Mean Error (ME), Normalized Standard Error of the Estimation (NSEE) was used to measure the degree of association between the measured and the estimated solar radiation. The results of the goodness of fit indices of the measured and estimated global solar radiation as shown in Table 4.2 shows a high correlation coefficient of 1.00 (rounded to two decimal places). The global solar radiation for December was estimated using the conversion factor of summer season as represented in Figure 4.12. Here, slight decrease in the correlation coefficient was observed in winter season (values inside the bracket in Table 4.2). Since the trajectory of the sun during winter is smaller, there is a possibility that the shadow of the handrail wall might reflect on the panels. Thus, a different conversion factor using the sunny day in winter season might improve the observation results.

Similar to the summer season, a sunny day of December 5, 2014 was selected to calculate c for winter season. The calculated c was then used to estimate the global solar radiation on sunny, partially cloudy and cloudy days, respectively. Since, a partially cloudy weather condition was not observed in December, a cloudy day with a sunny condition around 13:00 was selected as a partially cloudy day.

Further, the global solar radiation for December was estimated using the conversion factor of winter season (December 5, 2014) as represented in Figure 4.13. Here, the measured global solar radiation and the estimated global solar radiation with similar variation patterns were observed. Also, similar trend of the reduction in the solar radiation due to the presence of the clouds for both measured and the estimated global solar radiation was observed as indicated by the partially cloudy day (Figure 4.13 b) and cloudy day (Figure 4.13 c) datasets.

The correlation coefficient as the goodness of fit index along with the Root Mean Square Error (RMSE), Mean Error (ME), Normalized Standard Error of the Estimation (NSEE) of the measured and the estimated solar radiation are shown in Table 4.2 which shows a high correlation coefficient equal or greater than 0.99 (rounded to two decimal places) is observed which is higher as compared to the dataset using the conversion factor of summer season. Thus, for the accurate estimation of the global solar radiation, the conversion factor for each season must be calculated. The overall observed result of both summer and

winter season suggests that the proposed estimation method can be used for monitoring the temporal variation of the solar radiation.

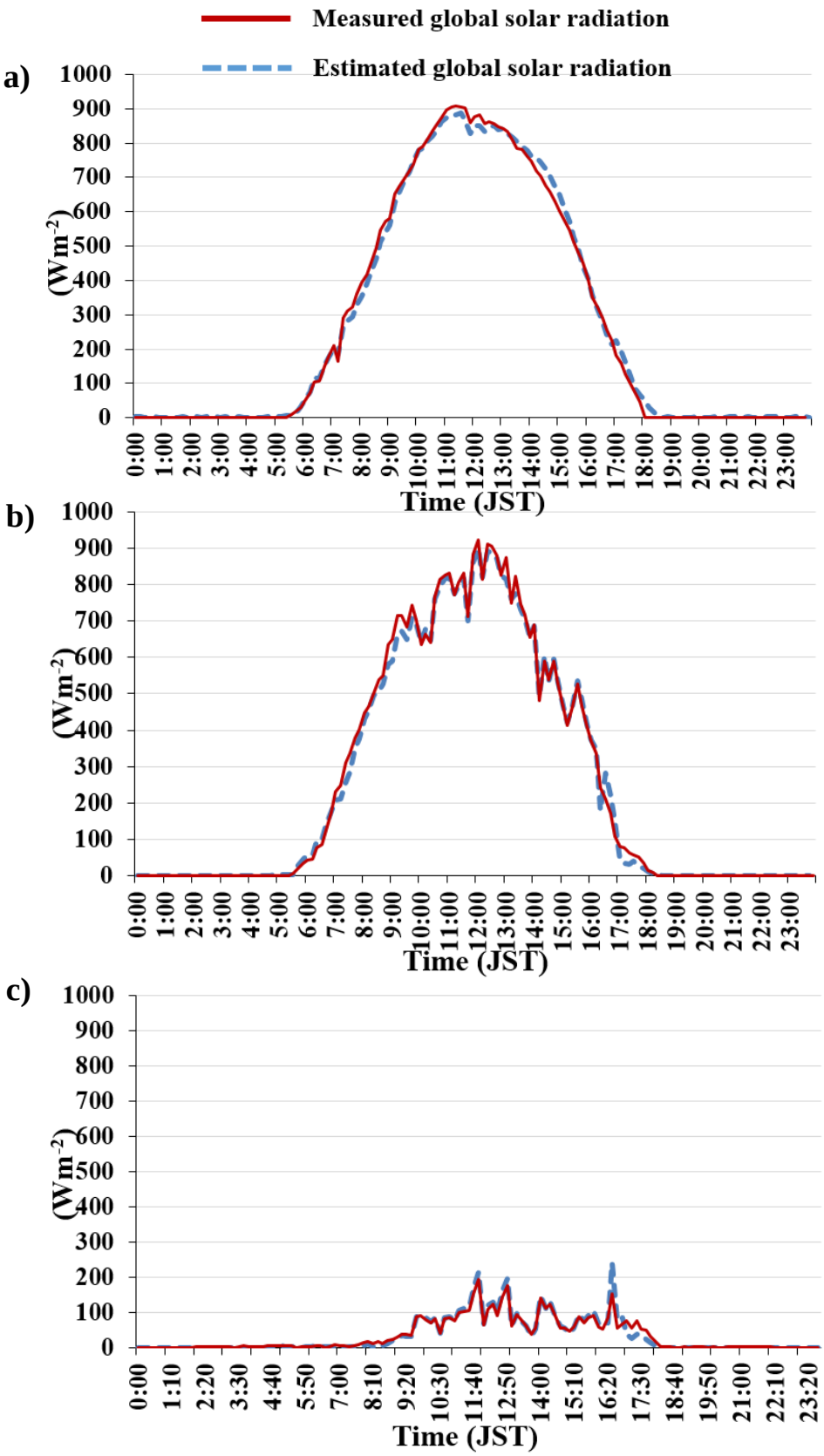

Figure 4.11: The measured and estimated and global solar radiation for(a) sunny day (August 12, 2014), (b) partially cloudy day (August 9, 2014) and (c) cloudy day (August 25, 2014)

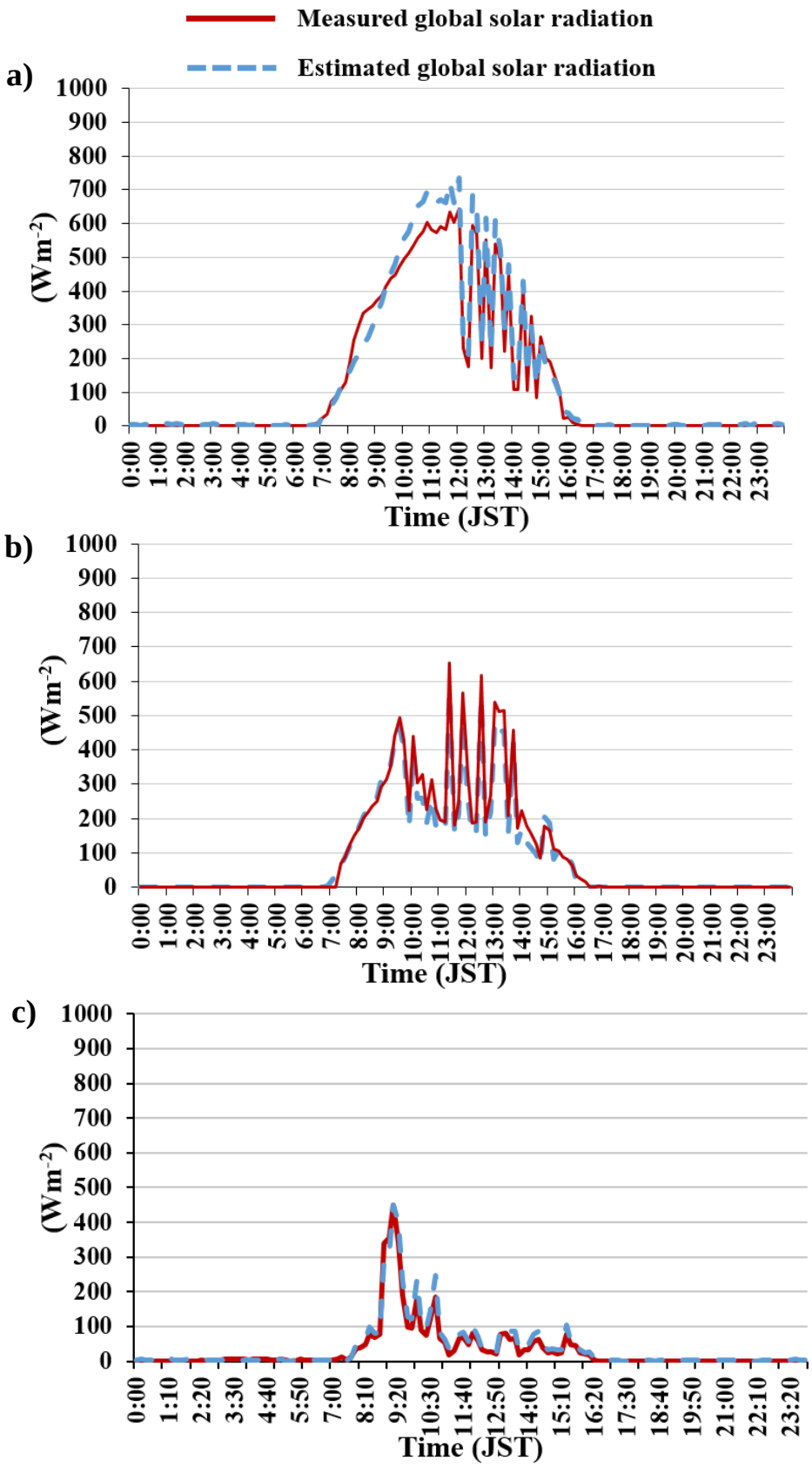

Figure 4.12: The measured and estimated global solar radiation for (a) sunny day (December 2, 2014), (b) partially cloudy day (December 4, 2014) and (c) cloudy day (December 10, 2014) using conversion factor of summer

Table 4.2: Goodness-fit index of the measured and estimated global solar radiation using the horizontal panel (Temporal variation of the conversion factor)

Date	Weather	Correlation coefficient	RMSE[*2] ($W\ m^{-2}$)	ME[*3] ($W\ m^{-2}$)	NSEE[*4]	Remarks
Summer						
June 4	Sunny	1.00	0	0	0.00	Coefficient identified day
Aug 12	Sunny	1.00	30	-19	0.05	
Aug 9	Partially cloudy	1.00	26	-9	0.05	
Aug 25	cloudy	1.00	10	-8	0.14	
Winter						
Dec 5	Sunny	1.00	0	0	0.00	Coefficient identified day
Dec 2	Sunny	1.00 (0.99)[*5]	28 (48)	3 (-26)	0.08 (0.14)	
Dec 4	Partially cloudy	0.99 (0.99)	27 (32)	12 (-16)	0.11 (0.13)	
Dec 10	Cloudy	0.99 (0.98)	18 (24)	11 (-3)	0.16 (0.20)	

[*1] *Calculated using the data from sunrise to sunset. Correlation coefficient, NSEE is rounded to decimal three. RMSE, ME was rounded one decimal place.*

[*2] *RMSE: Root Mean Square Error*

[*3] *ME: Mean Error*

[*4] *NSEE: Normalized Standard Error of the Estimation*

[*5] *Winter numbers in bracket indicate the values obtained using the conversion factor of summer.*

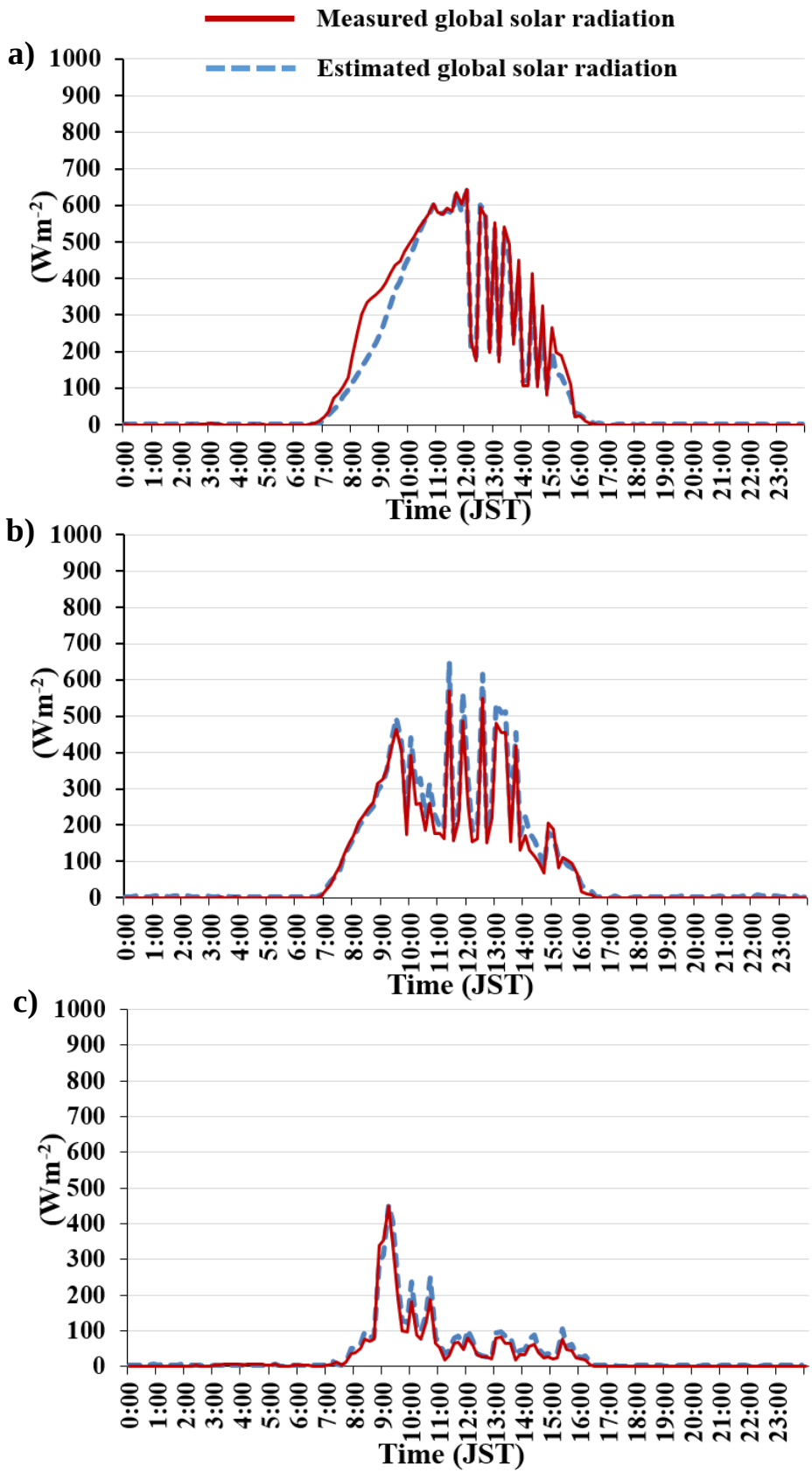

Figure 4.13: The measured and estimated global solar radiation for (a) sunny day (December 2, 2014), (b) partially cloudy day (December 4, 2014) and (c) cloudy day (December 10, 2014)

Table 4.3: Goodness-fit index of the measured and the estimated global solar radiation using the horizontal panel (Using constant conversion factor irrespective of time)

Annotations are same as Table 4.2

Date	Weather	Correlation coefficient	RMSE*2 (W m^{-2})	ME*3 (W m^{-2})	NSEE*4	Remarks
Summer						
June 4	Sunny	1.00	43	-10	0.07	Coefficient identified day
Aug 12	Sunny	1.00	35	-22	0.06	
Aug 9	Partially cloudy	1.00	36	-14	0.07	
Aug 25	Cloudy	1.00	7	1	0.09	
Winter						
Dec 5	Sunny	0.99	47	-22	0.13	Coefficient identified day
Dec 2	Sunny	0.99	48	-17	0.14	
Dec 4	Partially cloudy	0.99	33	-9	0.13	
Dec 10	Cloudy	0.98	23	-1	0.20	

For the estimation of the global solar radiation, we also considered a case with a constant conversion factor irrespective of time. We found that the estimation of the global solar radiation using a constant conversion factor is also possible with a high correlation coefficient of 0.98 to 1.00 as indicated in Table 4.3. In general, the conversion factor is time dependent (changes significantly in the morning and the evening) but taking the variation of the conversion factor into account is not critical for the estimation of the global solar radiation because the magnitude of solar radiation is small in the morning and the evening. The RMSE and ME (also in Table 4.2 and Table 4.3) indicates the underestimation of the

proposed estimation method. However, this study was carried out to explore the potential of using the PV system to study the variation of the solar hence, only the variation pattern of the solar radiation along and the correlation coefficient is taken into consideration which fulfills the objective of this research.

4.4.2 Solar panels installed at an angle

A sunny day (cloudy at times) of September 3, 2014 was selected to estimate the global solar radiation in a solar panel with a tilt angle of 20^o due south. Using the above expression, the global solar radiation was estimated for the concerned day. Here, Figure 4.14 shows the direct beam solar radiation, diffuse solar radiation and measured global solar radiation which clearly indicates the presence of clouds in the morning and the afternoon.

Figure 4.15 shows the measured solar radiation on a slope, the estimated solar radiation on a slope and the measured global solar radiation, respectively. The variation pattern of the amount of solar radiation in all three cases are in agreement with each other especially during the morning and the afternoon when there is presence of the clouds. Here, the blue solid line in Figure 4.15 represents the estimated solar radiation on a slope which is closer to the measured solar radiation on the slope (red dashed line) rather than the measured global solar radiation (Green solid line). This indicates that the estimated global radiation has been little overestimated as compared the measured global solar radiation which might be due to some errors during the conversion method of the solar radiation on a slope. Thus, for the estimation of the global solar radiation, a reliable method to convert the solar radiation on a slope to the global solar radiation is necessary.

Similarly, Figure 4.16 shows the relationship between the measured global solar radiation and the estimated global solar radiation using a tilted solar panel. The similar variation patterns show that the amount of solar radiation can be reproducible from the PV system using the method to estimate the global solar radiation described in the study. This is further supported by the goodness-fit index with high correlation of 0.99 as shown in Table 4.4. Thus, the validity of the method for the estimation of global solar radiation using solar panels at a tilt angle of 20^o was confirmed with high correlation

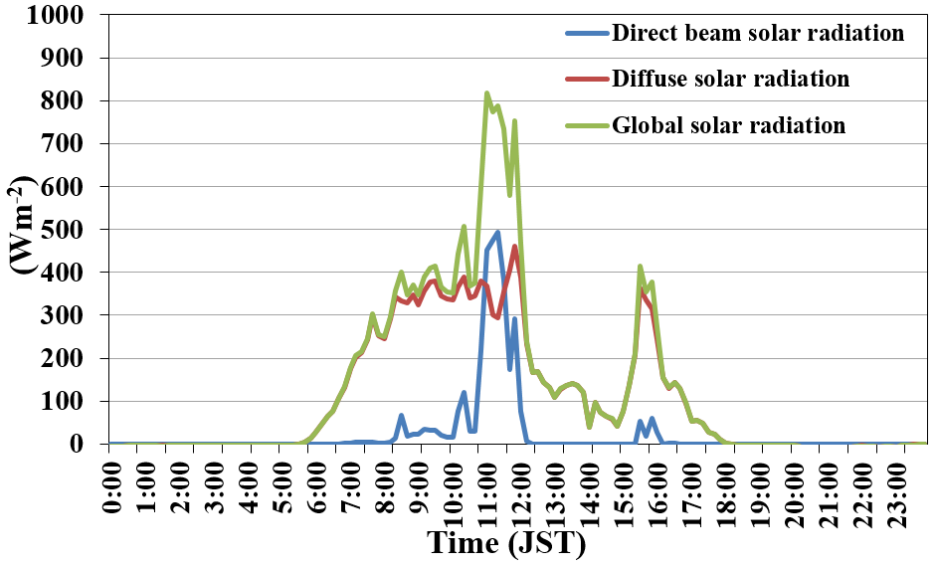

Figure 4.14: Direct beam solar radiation, diffuse solar radiation and global solar radiation (September 3, 2014)

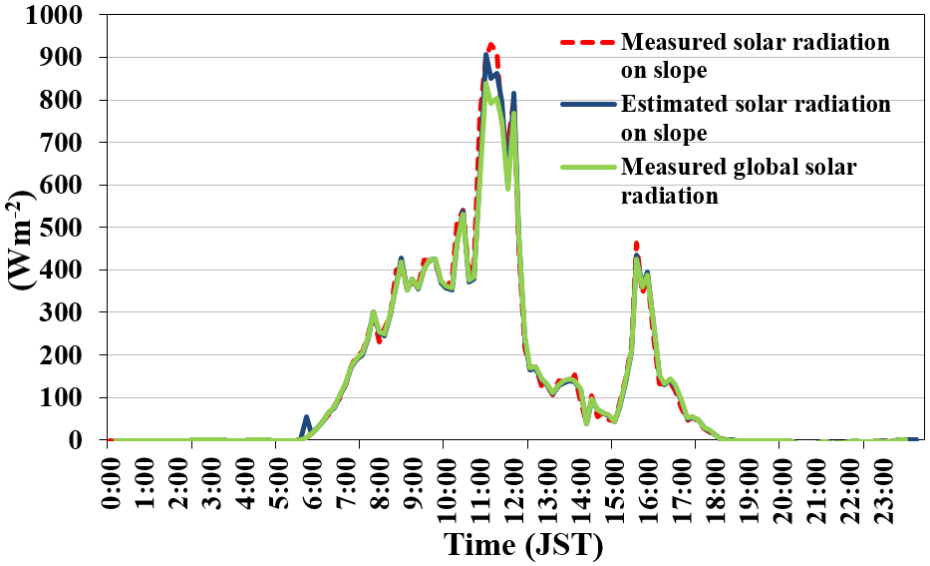

Figure 4.15: Measured solar radiation on slope, estimated solar radiation on slope and measured global solar radiation (September 3, 2014)

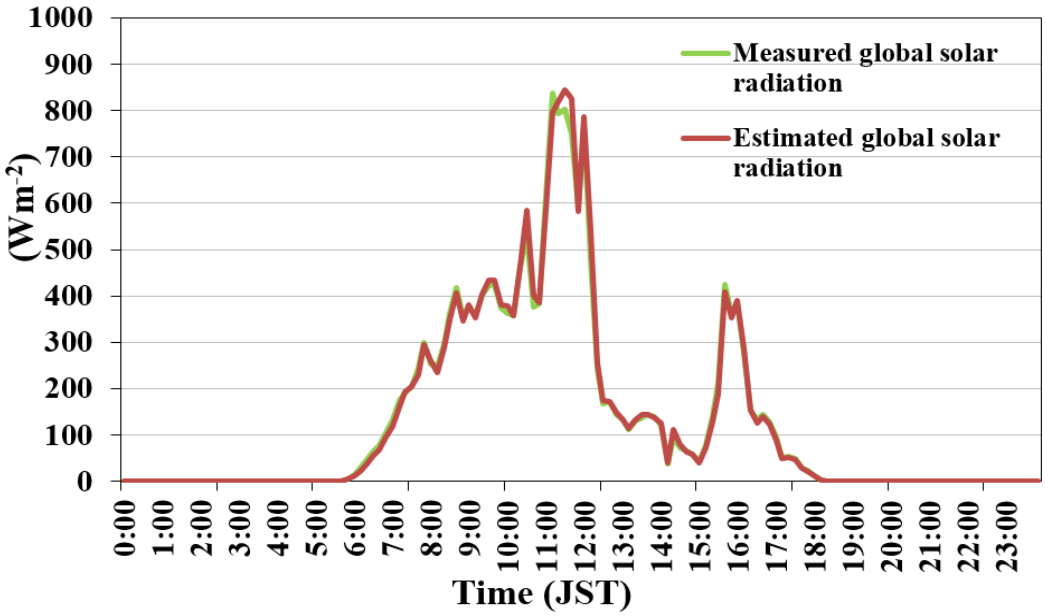

Figure 4.16: Measured global solar radiation and estimated global solar radiation using a tilted panel (September 3, 2014)

Table 4.4: Goodness-fit index of the estimated and the measured global solar radiation amount for a tilted panel

Annotation same in Table 4.2.

Date	Correlation coefficient	RMSE*2 (W m^{-2})	ME*3 (W m^{-2})	NSEE*4	Remarks
Sept 3	0.99	17	1	0.05	

4.4.3 Estimation of the global solar radiation using the photovoltaic network

One of the major objective of this research is to study the temporal and spatial variation of the solar radiation and the distribution of cloud in the Matsuyama plain for the better understanding of the local climate. Matsuyama being smaller area, the satellite data might have some weaknesses when it comes to smaller spatial resolution. Similarly, using the pyranometer ground- based study throughout the area might not be financially feasible. Thus, the use of the solar panel which has already been installed in many buildings, houses, school can be the best alternative for the temporal and spatial variation of the solar radiation.

The validity of the method for the estimation of global solar radiation using solar panels in a horizontal panel and at a tilt angle of 20^{o} was confirmed with high correlation as explained in section 4.4.1 and 4.4.2. Further to elaborate the study, the estimation of the global solar radiation in the Matsuyama plain, the photovoltaic network as explained in section 4.3.4 was taken into consideration.

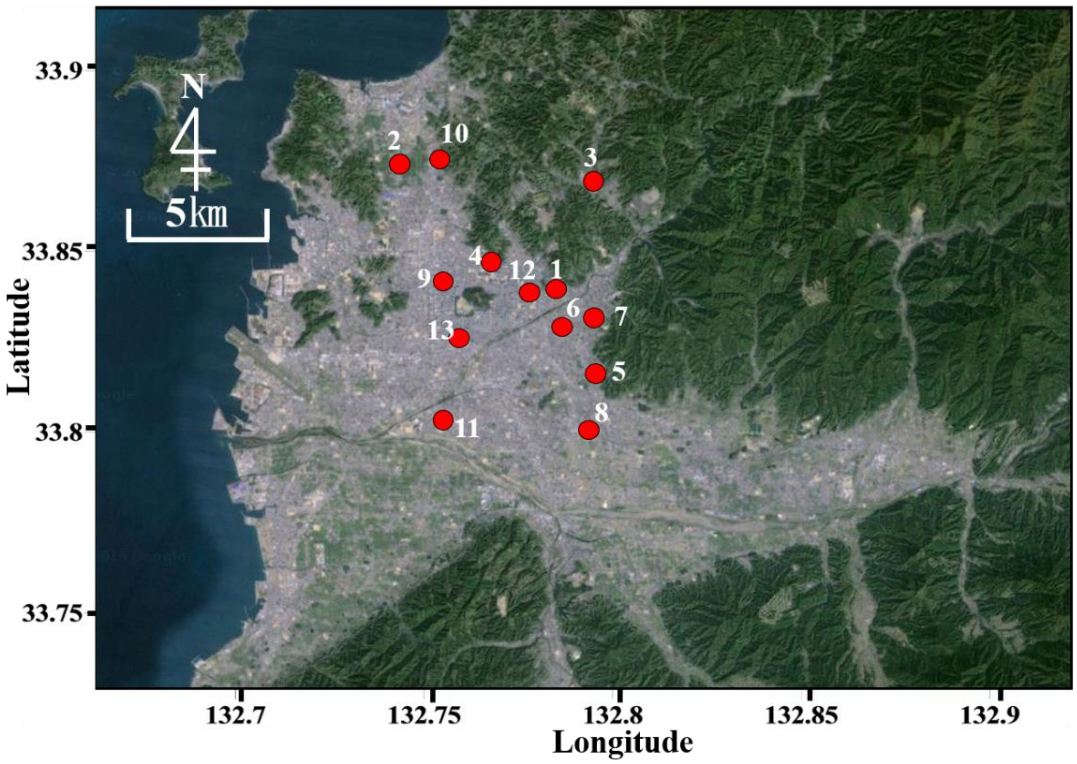

Figure 4.17: The solar panel installation site used in the study (13 installation site)

Table 4.5: Solar panel installation site considered for the study and the rated output of the panel at each site

S. no	Observation site	Rated output (kW)
1	Dougo elementary school	15
2	Hisaeda elementary school	7.5
3	Idai elementary school	15
4	Katsuyama junior high school	20
5	Kume elementary school	20
6	Kuwabara elementary school	20
7	Kuwabara junior high school	10
8	Minamidaini junior high school	30
9	Misake elementary school	10
10	Shiomi elementary school	20
11	Tsubaki junior high school	20
12	Yasaka elementary school	15
13	Yugun elementary school	10

The installation of the panel has been done in different time period and due to technical problems during the observation period, the observation data for all the site were not available throughout the year. Thus to include the most of the observation site among the 25 schools listed in the Table 4.1, only 13 observation sites were considered in this study. The location and the name of the schools along with the rated output of the panel is given in Figure 4.17 and Table 4.5, respectively.

As in previous section, the estimation of the global solar radiation was conducted for August (summer) and December (winter), here autumn season mainly October is taken is account. For the estimation of the conversion factor, October 6, 2015 (sunny weather condition) was considered. For the simplicity of the study, constant conversion factor irrespective of the time is considered. The conversion factor for all the observation site were calculated using the correlation between the observed solar radiation on a slope and the output ratio of the panel of the respective sites. Here, as an example the correlation between the observed solar radiation on a slope and the output ratio of the target day at Dougo

elementary school is shown in Figure 4.18. The estimated conversion factor and the correlation coefficient of all the observation site are summarized in Table 4.6. As the data of October 6, 2015 at Ehime university was missing, we used the conversion factor calculated in summer season (August 3, 2015).

From the Table 4.6, we can observe that the conversion factor of almost all observation points are of similar range with a difference of ±0.14, whereas in case of Hisaeda elementary school the conversion factor is the highest. Figure 4.19 shows the correlation diagram of the Hisaeda elementary school of the conversion factor determination day (October 6, 2015). Here the maximum amount of measured solar radiation is 1000 Wm^{-2} and the maximum output ratio is about 0.6 whereas in case of Dougo elementary school the maximum output ratio is about 0.9. This in turn suggest that the power generation of the panel is only about 60% of the rated output. As the power loss is large there is the possibility that the panel at Hisaeda elementary school might not have been be working properly.

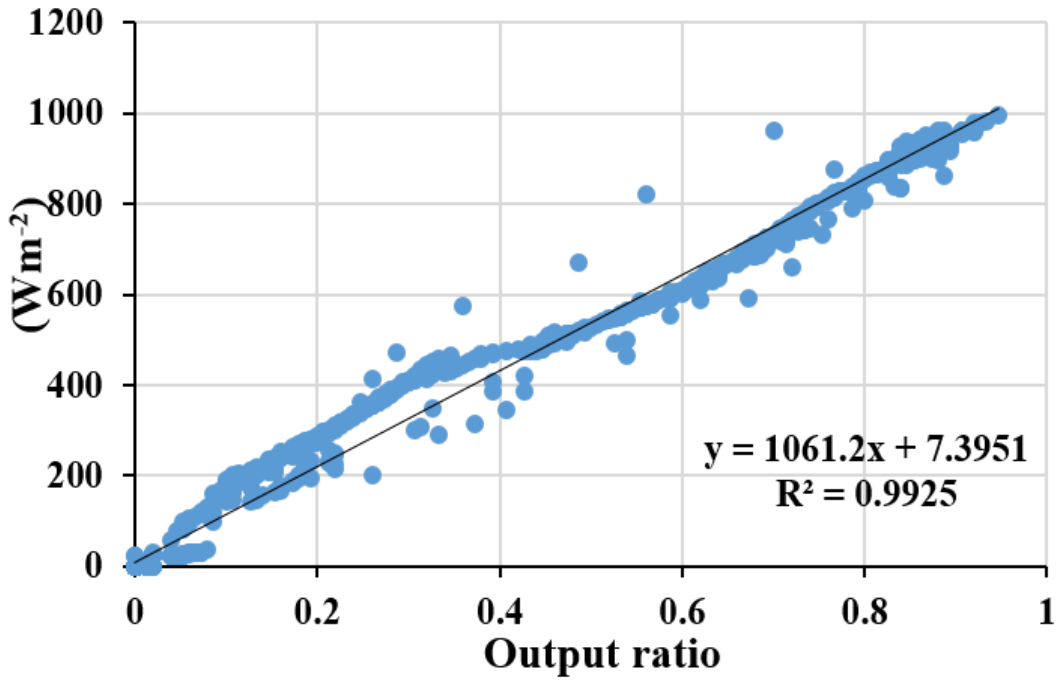

Figure 4.18: Correlation between the measured solar radiation and output ratio of the panel (Dougo elementary school, October 06, 2015)

Table 4.6: Site specific conversion factor and the correlation coefficient of the panel observation

S. no	Observation site	Conversion factor (Wm^{-2})	Correlation coefficient
1	Dougo elementary school	1061.2	0.9925
2	Hisaeda elementary school	1647.6	0.9953
3	Idai elementary school	1074.2	0.9968
4	Katsuyama junior high school	1058.5	0.9983
5	Kume elementary school	1108.5	0.9966
6	Kuwabara elementary school	1068.5	0.9940
7	Kuwabara junior high school	1072	0.9946
8	Minamidaini junior high school	1084	0.999
9	Misake elementary school	1143.9	0.9956
10	Shiomi elementary school	1062.3	0.9988
11	Tsubaki junior high school	1085	0.9987
12	Yasaka elementary school	1104.8	0.9962
13	Yugun elementary school	1036.1	0.9933
14	Ehime University	1205	0.9935

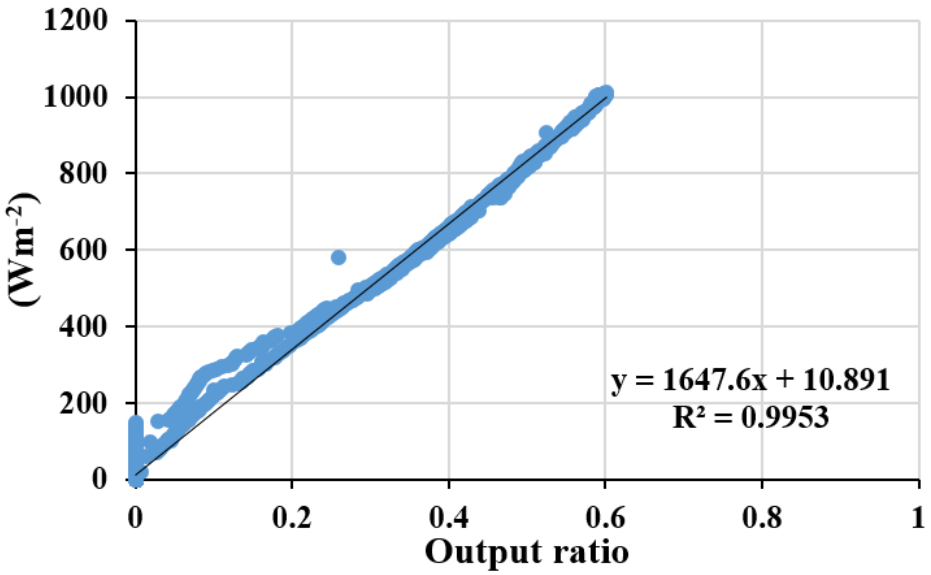

Figure 4.19: Correlation between the measured solar radiation and output ratio of the panel (Hisaeda elementary school, October 6, 2015)

Using the calculated conversion factor and the methodology described in section 4.3.3.2, the estimation of the global solar radiation for all the observation sites were conducted. To monitor the distribution of the solar radiation and the cloud coverage for the photovoltaic network sites a slightly overcast day of October 9, 2015 was taken into consideration. The high correlation between the estimated global solar radiation and the measured solar radiation on the slope was observed. The correlation coefficient for all the observation site of the target day is listed in Table 4.7. Here, the high correlation coefficient, greater than 0.99, between the estimated and measured solar radiation for all observation site suggests that the photovoltaic network can be used to study the distribution of the solar radiation in the Matsuyama plain.

Table 4.7: The correlation coefficient of the estimated global solar radiation and the measured solar radiation on the slope (October 9, 2015)

S. no	Observation site	Correlation coefficient
1	Dougo elementary school	0.9975
2	Hisaeda elementary school	0.9967
3	Idai elementary school	0.9973
4	Katsuyama junior high school	0.9986
5	Kume elementary school	0.9970
6	Kuwabara elementary school	0.9963
7	Kuwabara junior high school	0.9971
8	Minamidaini junior high school	0.998
9	Misake elementary school	0.9952
10	Shiomi elementary school	0.9981
11	Tsubaki junior high school	0.998
12	Yasaka elementary school	0.9973
13	Yugun elementary school	0.9983
14	Ehime University	0.9982

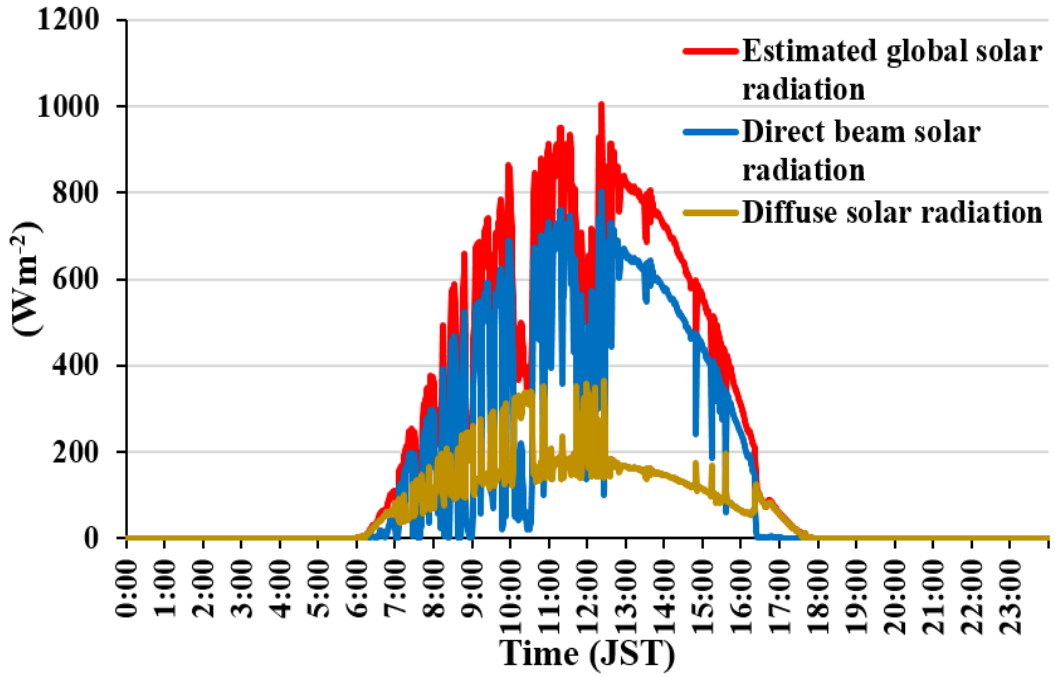

Figure 4.20: Estimated global solar radiation, direct beam solar radiation and diffuse solar radiation at Ehime University (October 9, 2015)

Similarly, Figure 4.20 shows the estimated global solar radiation, direct beam solar radiation and diffuse solar radiation at Ehime University. Here, the reduction is radiation due to the presence of cloud before noon is clearly visible, and the weather condition starts to become clear from around 13:00. The possibility of the extraction of the local clouds and the weather condition represented in Figure 4.20 is checked by using the whole sky photographs taken at the Ehime University (The detail of the whole-sky photograph and its instrumentation is explained in Chapter 3).

Here, considering the height of the cloud to be 1000m, and the elevation of the observation point to lie between 10^o to 90^o (i.e. Zenith angle 0^o to 80^o), the range of the area cover by the whole-sky photographs is identified. Further we focus on the time period of 1 hour from 12:00 to 13:00 to study the distribution of the cloud. The diurnal variation of the estimated global solar radiation at Dougo Elementary (South-east south from Ehime University) and Katsuyama junior high school (West from the Ehime University) is represented in Figure 4.21 and Figure 4.22, respectively.

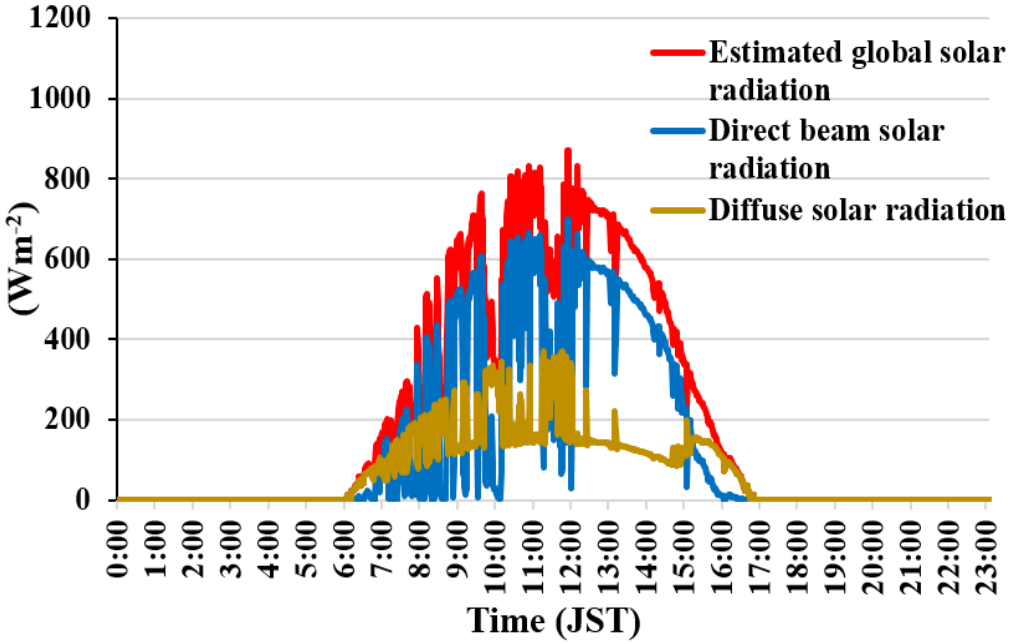

Figure 4.21: Estimated global solar radiation, direct beam solar radiation and diffuse solar radiation at Dougo elementary school (October 9, 2015)

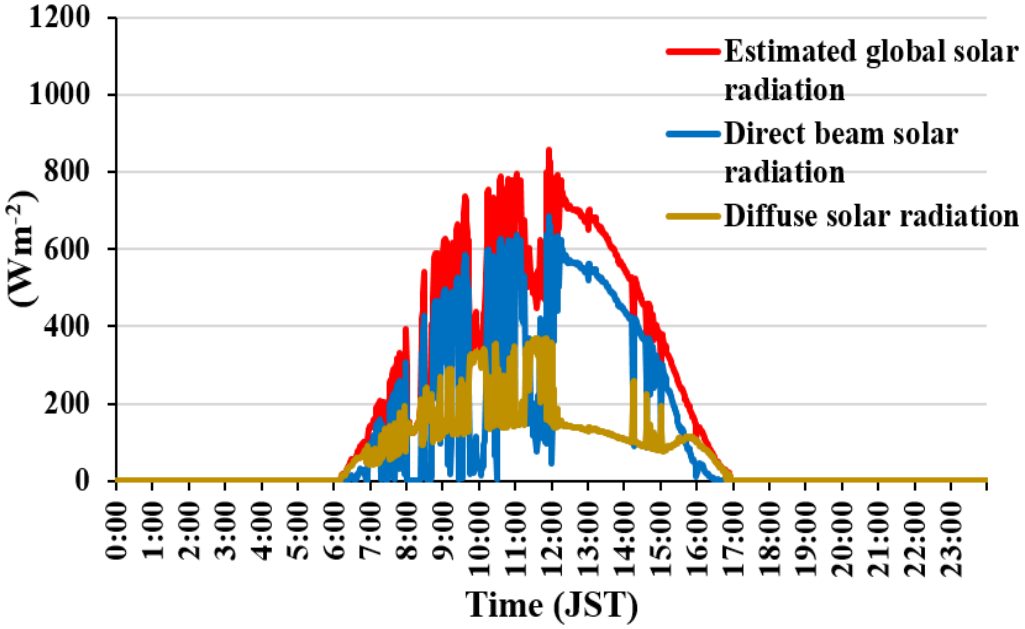

Figure 4.22: Estimated global solar radiation, direct beam solar radiation and diffuse solar radiation at Katsuyama elementary school (October 9, 2015)

The whole-sky photographs presented in Figure 4.23 (b) represents the sky condition from 12:00 to 13:00 at an interval of every 20 minutes. It must be noted that the photo taken by the whole-sky camera is inverted so the photograph was rearranged to match the real direction of the study area. Here, the presence of the cloud towards the eastern side from the Ehime University as compared to the western side at 12:20 can be observed clearly. This is in accordance to the Figure 4.21 and Figure 4.22 which shows presence of cloud in the Dougo elementary school as compared to that in the Katsuyama junior high school during the time period.

Looking at the photo at 12:40 much clear weather in the western part is observed whereas clouds were still prevalent in the eastern side. The distribution of the radiation at the Katsuyama junior high school also suggests the amount of radiation to be high during the time period. Here, some clouds tend to appear in the south western side. Due to the missing data of the observation site in the south western part of the study area, the validity of the sky condition could not be conducted. Similarly, at 13:00 much clear weather condition is observed which is in accordance to the all the above Figures (Figure 4.20, Figure 4.21 and Figure 4.22, respectively) which show higher amount of solar radiation during the time period.

The validity of the whole-sky photographs is further studied using the spatial distribution of the amount of solar radiation during the same time period (i.e. 12:00 to 13:00 of October 9, 2015). Figure 4.23 (a) represents the spatial distribution of the amount of solar radiation, where the black color represents minimum amount of solar radiation whereas the white color indicates the highest amount of the solar radiation, respectively. The distribution of the solar radiation clearly suggests the solar radiation to be blocked due to the presence of the cloud at 12:00 almost in all part of the area. Along the time period from 12:00 to 13:00 the increase in the amount of solar radiation has been observed throughout the study area. Looking at the spatial distribution of solar radiation at 12:20, the low amount of radiation is observed along the eastern side of the plain as compared to the western side which is in accordance to the whole-sky photographs of the same time period. Again looking at 12:40 the radiation is seen to smaller along the section of the eastern and southern part of the area which is believed to be due to the presence of cloud at the time.

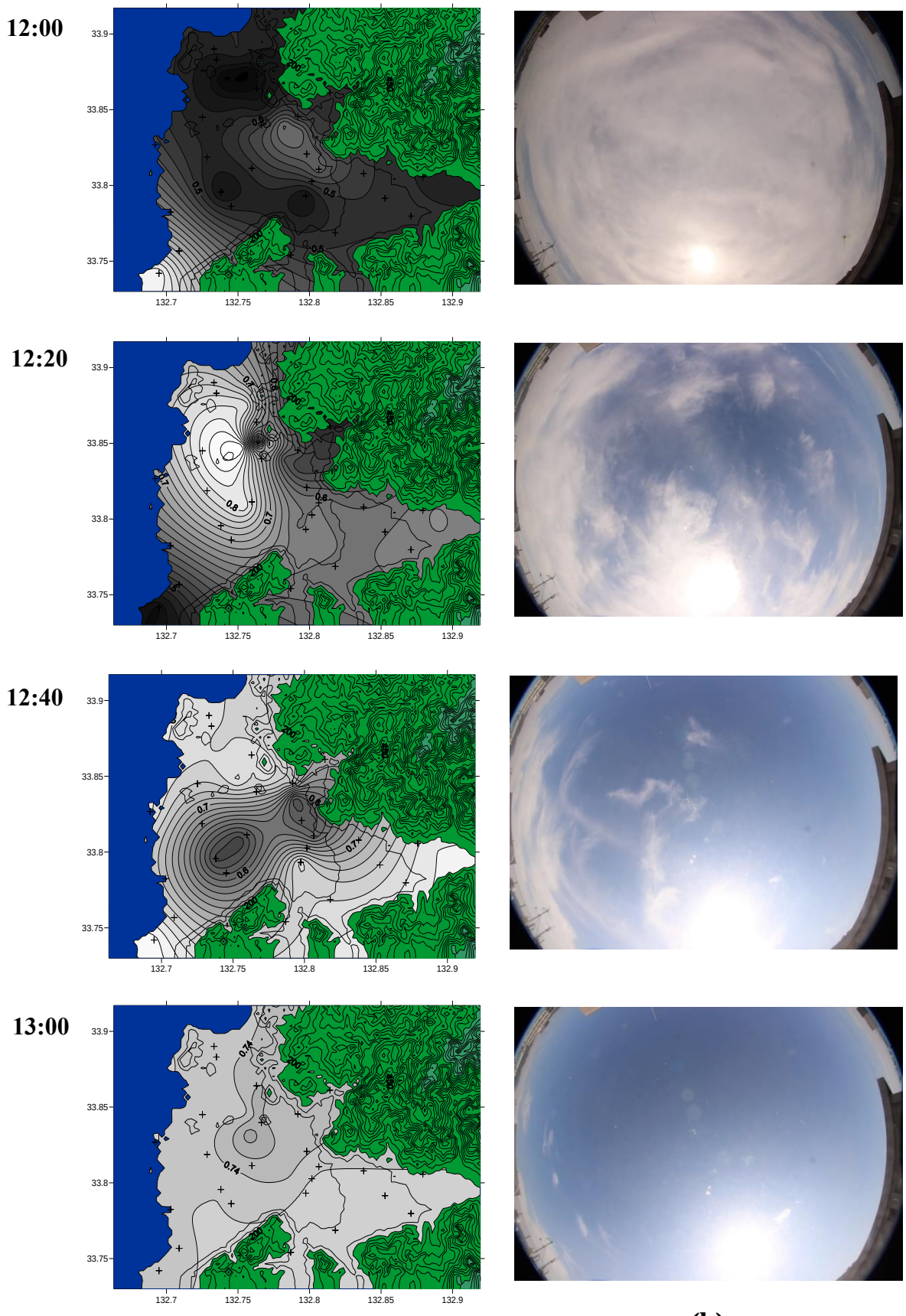

Figure 4.23: (a) Spatial distribution of the solar radiation and (b) whole-sky photograph from 12:00 to 13:00 (October 9, 2015)

Similarly, at 13:00 the distribution of the amount of radiation along the Matsuyama plain is almost constant, which indicates the prevalence of fair weather (sunny condition) during the time period. Here along the observation time period, the spatial distribution of the solar radiation and the distribution of the cloud studied from the whole-sky photographs were in agreement with each other. The potential of using the estimated global solar radiation to monitor the distribution of the solar radiation and the cloud coverage was studied with the help of the whole-sky photography.

Hence, the proposed method for the estimation of the global solar radiation using the photovoltaic system was studied with high efficiency. This reflects that the study of the distribution of the solar radiation and the characteristic of the cloud is possible using the dense monitoring of the photovoltaic network which in turn suggest that the study of the local climate and rainfall pattern is possible using the existing photovoltaic network all over the world.

4.5 Temporal standard variation of the clear sky rate

After the estimation of the global solar radiation using the photovoltaic system with high efficiency, it is important to study the temporal and spatial variation of the cloud which of the utmost importance for the understanding the local climate and prediction of disasters events such as localized torrential rainfall. Thus, the study was carried out to explore the potential for using the statistical analysis (standard deviation) of time series of one hour averaged estimated solar radiation using the photovoltaic system installed at a tilt angle of 20^{o} at Ehime University to study the state of the cloud. Ehime University was selected as the observation site due to the presence of observation data throughout the study period.

The methodology of the calculation of the clear sky rate was same as used for the pyranometer network as explained in Chapter 3. The observation was conducted from August to November 2015.

Figure 4.24 shows the monthly 1-hour average data of the time standard deviation of the Matsuyama plain for 39 observation day from August 2015 to November 2015. The variation of the clear sky rates between 0.2 to 1 is observed within the varying range of the time standard deviation between 0 to 0.3. The diurnal variation of the clear sky rate for all the observation showed the decrease in the amount of radiation in the morning and late afternoon which was in agreement to the observation using the pyranometer network.

To further elaborate the result, the one-hour average of the monthly value is presented in the Figure 4.25. The smallest and highest clear sky rate was observed in September and October, respectively which suggests the presence of cloudy condition to be more in September as compared to other months of summer or autumn. Further, the monthly average of the one-hour time standard deviation shows the maximum observation value in September whereas the minimum value was observed in the month of October as presented in Figure 4.26. This indicates that there is the variation in the sky condition during each observation month (refer Chapter 3).

The diurnal and the monthly variation in the clear sky rate and the one-hour time standard deviation calculated using the estimated global solar radiation observed from the photovoltaic system is in accordance to the measured global solar radiation using the pyranometer network. Hence, the monitoring of the solar radiation distribution and cloud

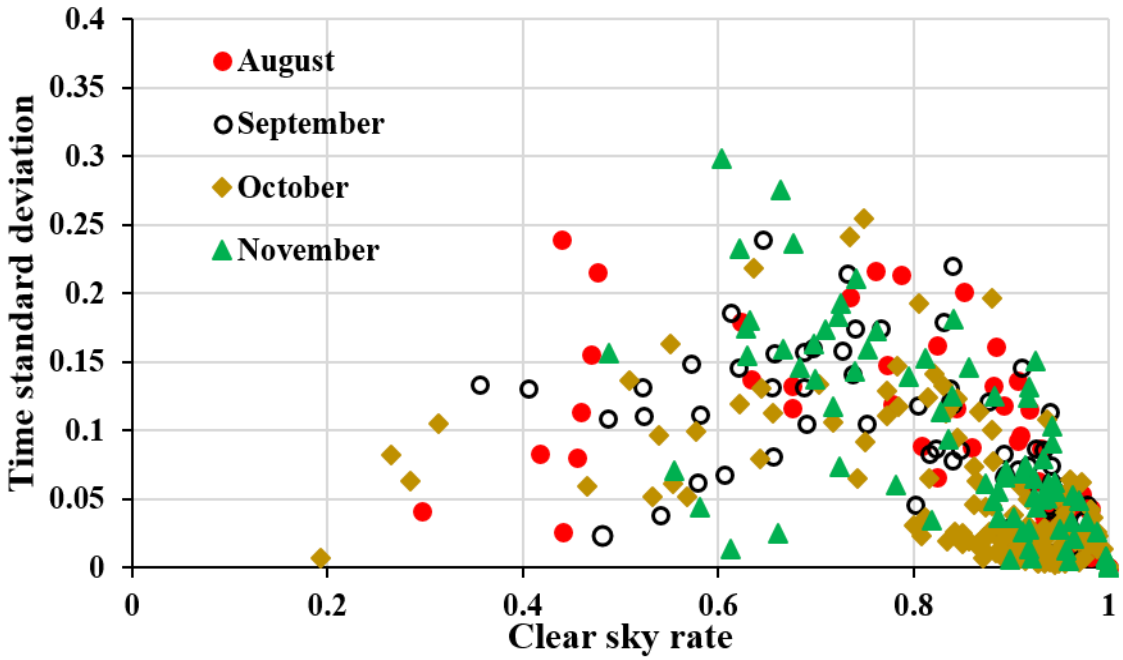

Figure 4.24: One-hour averaged time standard deviation of the clear sky rate (Ehime University)

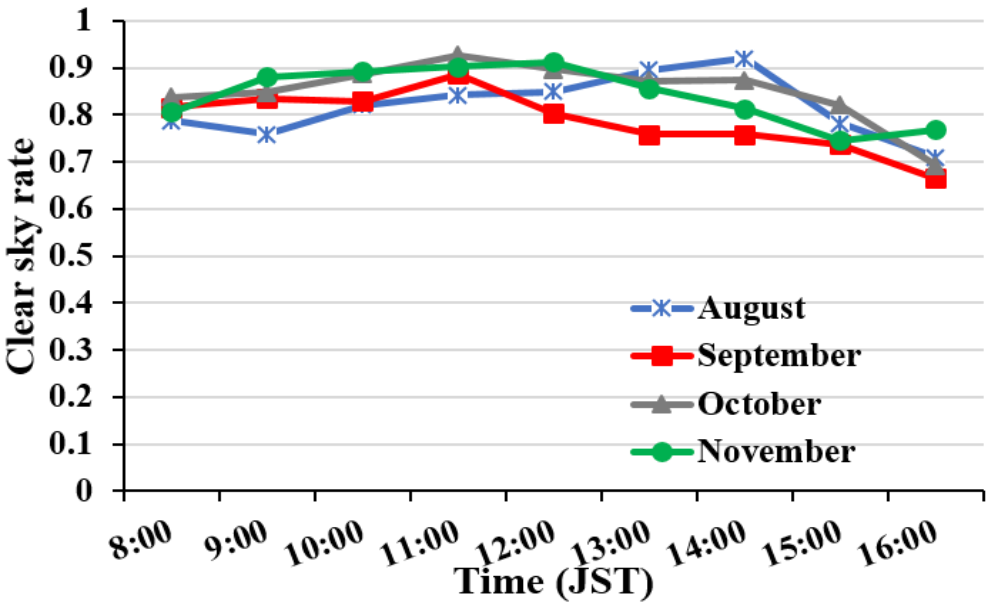

Figure 4.25: Diurnal variation of one-hour monthly average of the clear sky rate (Ehime University)

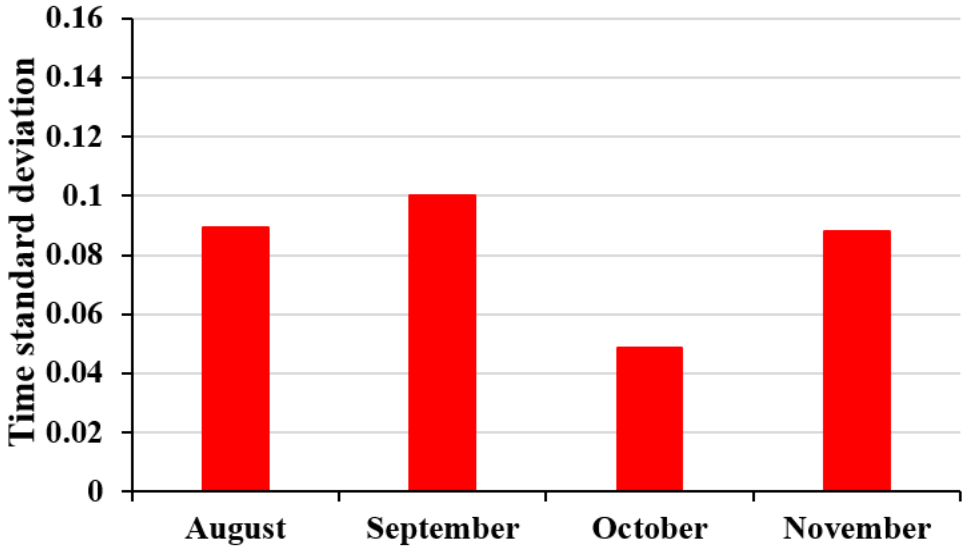

Figure 4.26: Monthly average of the time standard deviation at Ehime University

condition is applicable using the photovoltaic network. The detailed temporal and the spatial variation of the solar radiation using the one-hour time standard deviaion of the clear sky rate using the photovoltaic network and relation to sky condition using the whole-sky images is discussed further in Chapter 5.

4.6 Chapter summary

The estimation of global solar radiation using photovoltaic system was proposed and examined on the basis of in-situ measurements. Solar panels were installed horizontally and at a tilt angle of 20^{o} due south. The estimated global radiation and the measured solar radiation were observed to be in high correlation. For a tilted panel, the simple conversion of solar radiation on a slope to global solar radiation resulted in poor estimation. Thus, the conversion method using the separation of solar radiation as direct beam and diffuse radiation improved the estimation with a high correlation. As solar panels have already been installed in many houses, commercial buildings, schools, the estimation method proposed in this study is promising for the monitoring of the spatial and temporal variation of the solar radiation, which is beneficial for the local climate studies such as torrential rainfall, urban heat island phenomena. The temporal variation of the photovoltaic observation was used to study the sky condition, which efficiently reproduced the distribution of the solar radiation in all sky condition which was validated by the whole-sky images and the spatial distribution of the radiation during the time period. To further elaborate the use of the photovoltaic network for the monitoring of the local climate of the study area, the one-hour time standard deviation of the clear sky rate was taken into consideration. The proposed method was further validated using dataset of the pyranometer observation. In general, the meteorological observations are used to estimate the energy from a PV system (Yoshida et al. 2013), but in this study, the global solar radiation estimated using a PV system is promising to understand the temporal variation of the solar radiation which, is a unique approach in itself for the study of local climate.

CHAPTER 5

5. Comparison of the solar radiation dataset

This chapter mainly focuses on the temporal and spatial variation of the solar radiation observation using the photovoltaic network in the Matsuyama plain. Here, the one-hour time standard deviation of the clear sky rates was considered for the analysis. Similarly, the observation results calculated from the estimated global solar radiation from the PV system and measured global solar radiation from pyranometer was compared to validate the potential of the PV system to be used for the study of local climate.

5.1 Distribution of the estimated global solar radiation

In the Chapter 4, we discussed the possibility of the estimation of the global solar using the photovoltaic system. The similar variation pattern of the diurnal variation of the solar radiation during all the weather condition suggests that the estimated radiation can be

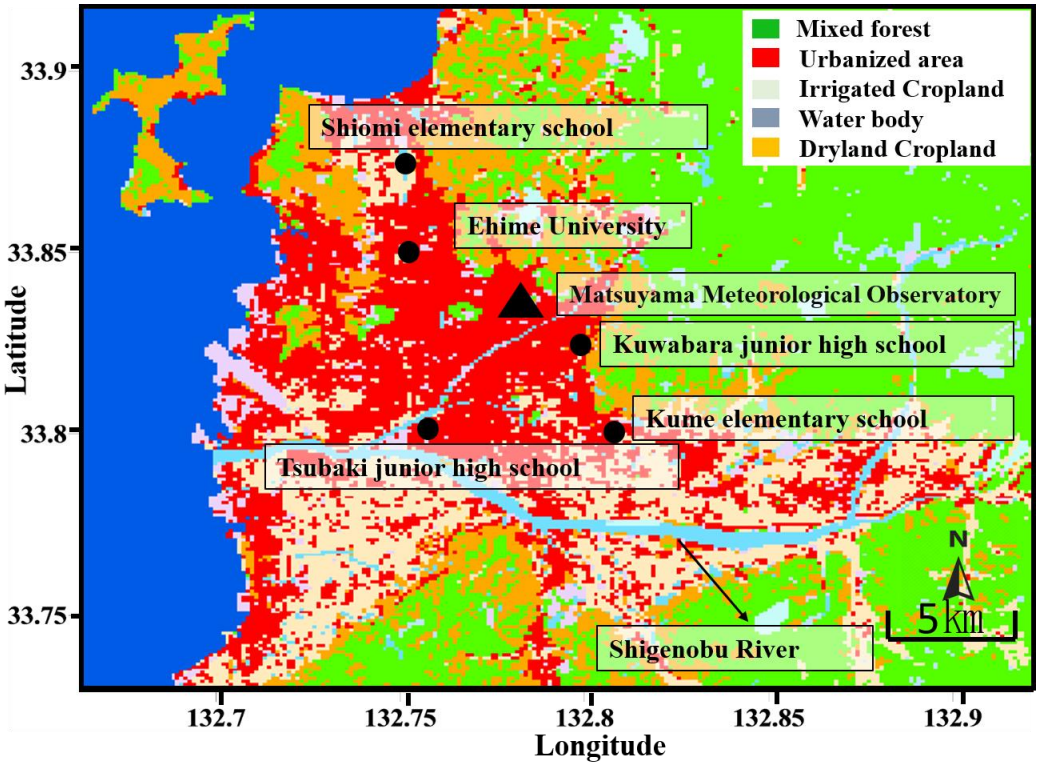

Figure 5.1: The land-use category of the observation site in the Matsuyama plain

used for the study of the local climate of the Matsuyama plain. To further elaborate the study, we consider the statistical analysis (one-hour time standard deviation) and clear sky rate for the temporal and spatial variation of the solar radiation from the estimated global solar radiation.

In order to fulfil the objective, we selected 5 observation site including Ehime University and the schools in the study area (solar panels installation sites described in Chapter 4). The land use category of the observation site is represented in Figure 5.1.

As, explained in earlier chapter, due to the limitation in the number of observation days and operational sites a month of October 2015 was only considered for the analysis of the temporal and spatial variation of the solar radiation in the 5 PV system installed sites. The one-hour averaged time standard deviation and the clear sky rate of the observation site is presented in Figure 5.2. The variation of the time standard deviation within the range of 0 to 0.4 for the clear sky rate between 0 to 1 is observed with maximum percentage of the observation value within the clear sky rate ranging between 0.8 to 1 was observed. The largest time standard deviation is seen at the Shiomi elementary school whereas the more

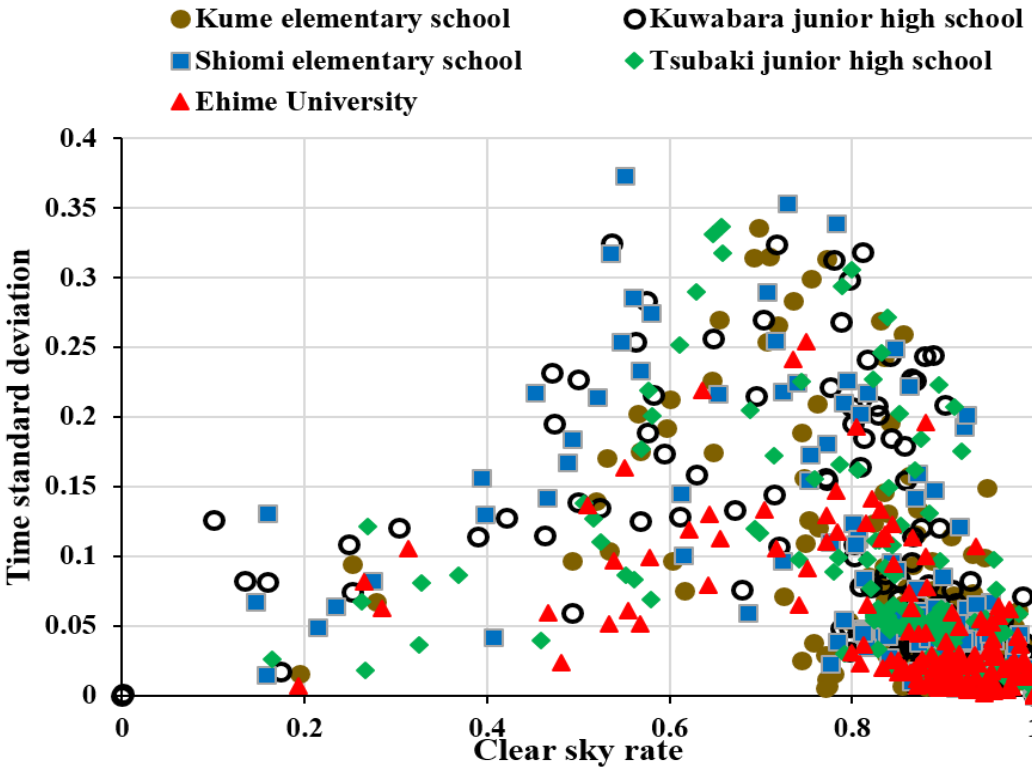

Figure 5.2: Monthly one-hour average time standard deviation and the clear sky rate for the solar panel sites

observation data of Kuwabara junior high school was found to lie within the minimum range of the clear sky rate i.e. 0 to 0.2.

The average temporal variation of the clear sky rate from 8:00 to 16:00 is shown in the Figure 5.3. The clear sky rate was found to observed to be smaller during the morning and the evening in the similar manner as explained in the Chapter 3. Further the diurnal variation of the hour monthly averaged clear sky rate for the 5 observation site. The clear

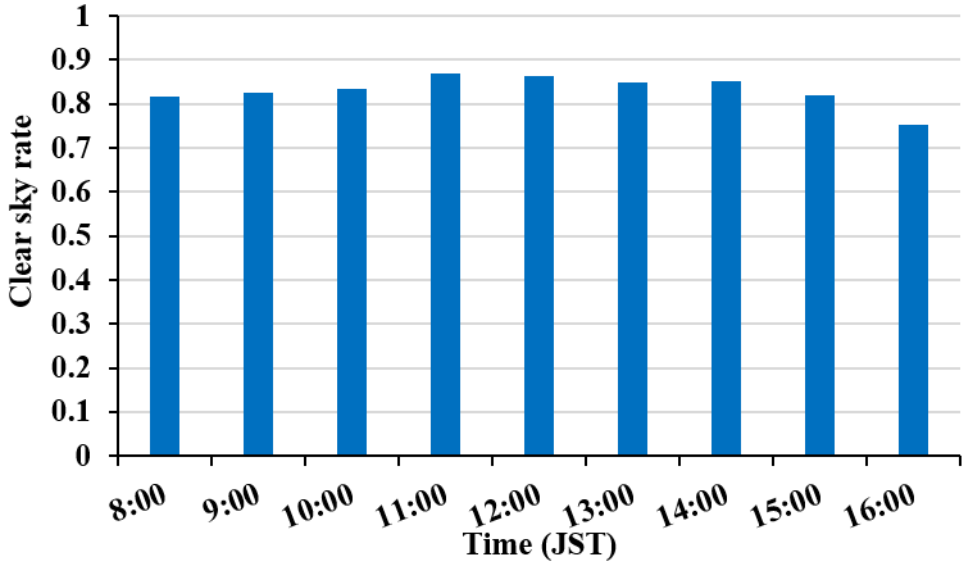

Figure 5.3: Average diurnal variation of the clear sky rate for the 5 month (August to December, 2015)

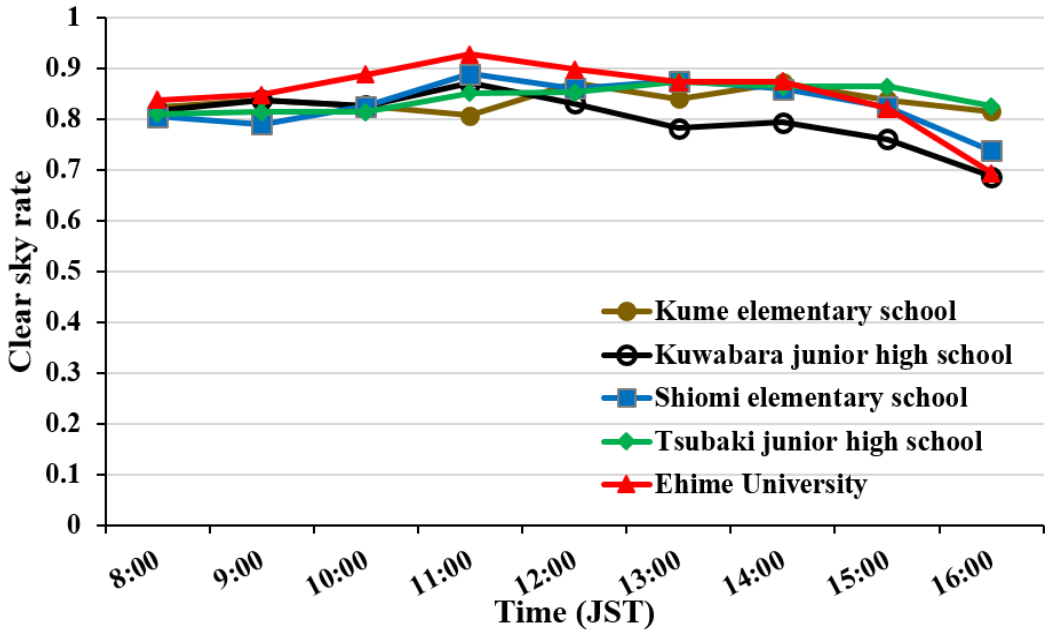

Figure 5.4: Diurnal variation of the one hour monthly averaged clear sky rate for the 5 observation site

sky rate generally varied from 0.6 to 1. Here, the clear sky rate at the Kuwabara junior high school was found to be smallest among all the other observation sites. The decrease in the clear sky rate was observed to be noticeable from the afternoon through late afternoon. As described in the previous chapters, the Matsuyama plain is dominated by the sea breeze during the daytime and the humid air is transferred to the inland area especially through the southern part of the Matsuyama plain i.e. irrigated cropland and along the Shigenobu River. Kuwabara junior high school lies on the hilly area, north of the Shigenobu river as depicted in Figure 5.1 and the formation of the cloud in the area might be due to the moist air carried by the wind along the area. The orographic effect on the formation of the cloud and precipitation has been explained by Brutsaert (2005), where he highlighted that the precipitation is more on the windward slope depending on the direction of wind. Hence, the clear sky rate calculated from the estimated global solar radiation can be used for the determination of the solar radiation distribution along the study area and the characteristic of the cloud.

5.2 Comparison of the measured and estimated global solar radiation

The validation of the estimated global solar radiation for the temporal and spatial distribution of the solar radiation within the Matsuyama plain was studied with high

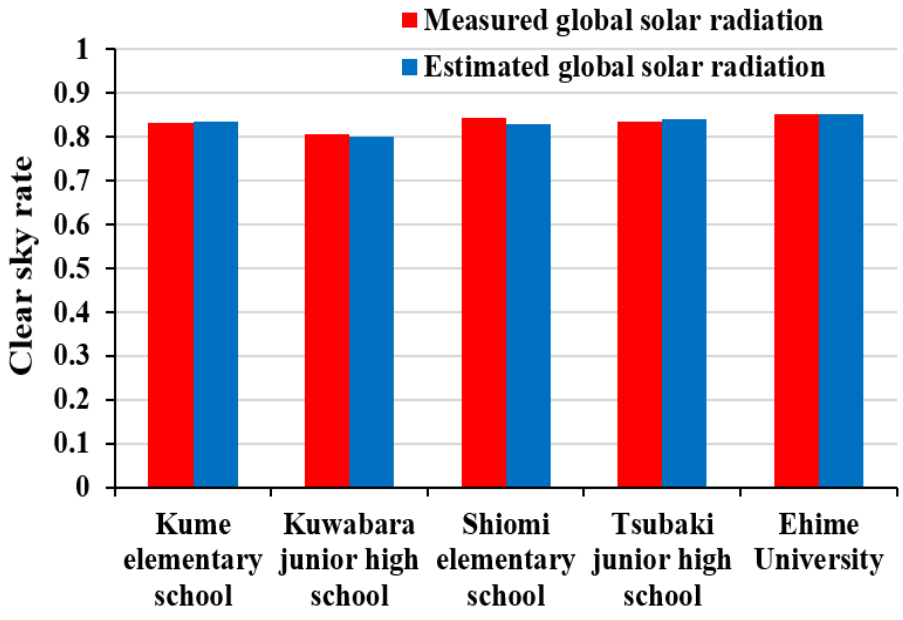

Figure 5.5: Spatial distribution of the clear sky rate for the 5 observation site

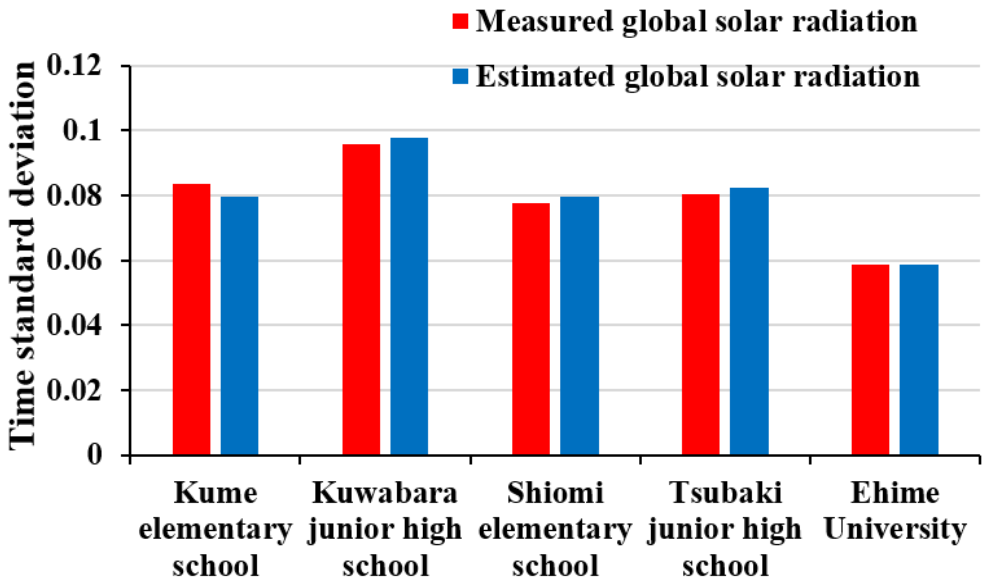

Figure 5.6: Spatial distribution of the one-hour averaged time standard deviation for the 5 observation site

correlation. But the comparison between the measured global solar radiation and the estimated global solar radiation becomes necessary for the use of the photovoltaic system where the pyranometer observation or other source of observation data are limited. Thus, for this purpose we compared the clear sky rate and the time standard deviation of the measured and estimated global solar radiation.

Here, Figure 5.5 represents the comparison of the clear sky rates of the measured global solar radiation in the observation sites using pyranometer and the estimated global solar radiation using the solar panels. The clear sky rate for both the measured and estimated global solar radiation is in high agreement with each other. The clear sky rate at the Kuwabara junior high school was found to be smaller for both measured and estimated radiation. Similarly, the clear sky rate of other observation sites was almost similar (i.e. all observation sites lies within the urbanized area). As the land-use category of all the observation points are almost similar, thus the difference in the clear sky rate might not be significant. This results are further evident from the average time standard deviation of the observation site as indicated in Figure 5.6 where the time standard deviation of the Kuwabara junior high school is significantly larger compared to the other observation site.

To understand the monthly variation of the clear sky rate from the measured and estimated global solar radiation we considered the observation data from August to November

at Ehime University. The comparison of the one-hour average of the clear sky rate of the pyranometer observation and the estimated global solar radiation from the solar panel is represented in Figure 5.7. Here, the vertical axis represents the clear sky rate calculated from the estimated global solar radiation whereas the horizontal axis represents the clear sky rate calculated from the pyranometer observation during the study period. As described earlier the maximum percentage of the clear sky rate was observed closer to one for both measured and estimated clear sky rate, with almost no observation value closer to zero. The clear sky

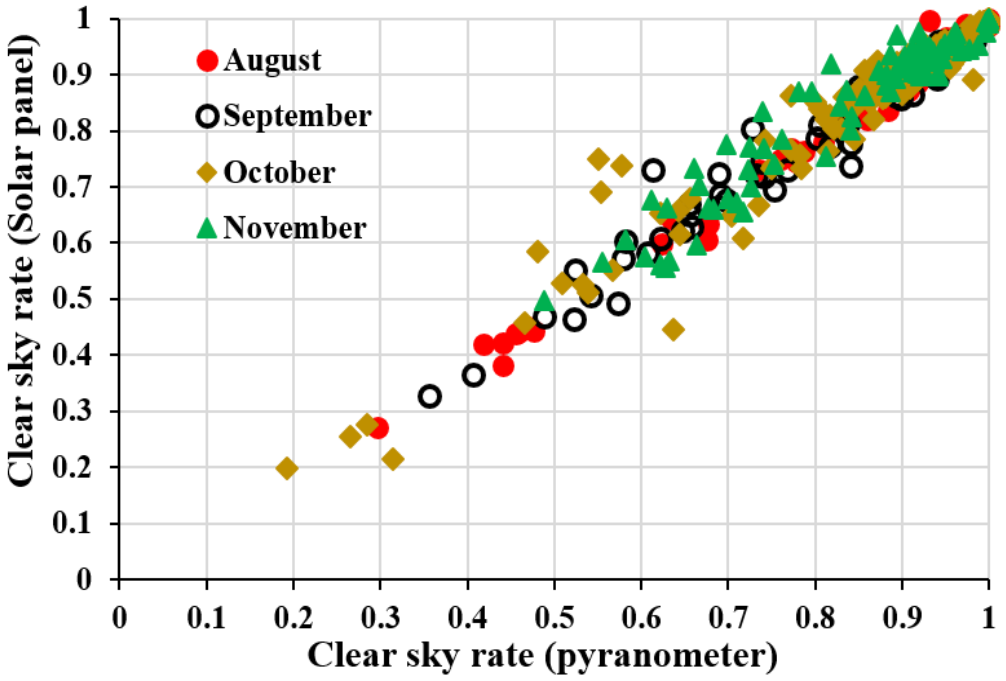

Figure 5.7: Comparison of the clear sky rate of solar panel and pyranometer observation at Ehime University

Table 5.1: Correlation coefficient of the clear sky rate of the solar panel and the pyranometer observation at Ehime University

Observation month	Correlation coefficient
August	0.99
September	0.98
October	0.97
November	0.97

rate of measured and estimated global solar in the Figure 5.7 were found to be in high correlation.

This is further evident through the correlation coefficient of the observation data listed in Table 5.1 where correlation of more than 97% is observation for all the observation months from August to November. Thus, using the estimated global solar radiation, the distribution of the solar radiation and the reduction of the radiation due to the presence of the cloud can be reproduced with high efficiency.

5.3 Cloud classification using the estimated global solar radiation

The efficiency of the estimation method of the PV system to reproduce the global solar radiation was discussed in the previous section. But for the study of the local climate the characteristic and the types of the clouds is important. The cloud characteristic and types using the one-hour time standard deviation and the clear sky rate of the pyranometer observation dataset was discussed in Chapter 3. Thus, when comparing the measured and the estimated global solar radiation, the reproducibility of the cloud characteristic and type also must be taken into consideration.

In order to fulfil this objective, we consider the four months estimated global solar radiation at the Ehime University from August to November 2015 due to installation of the

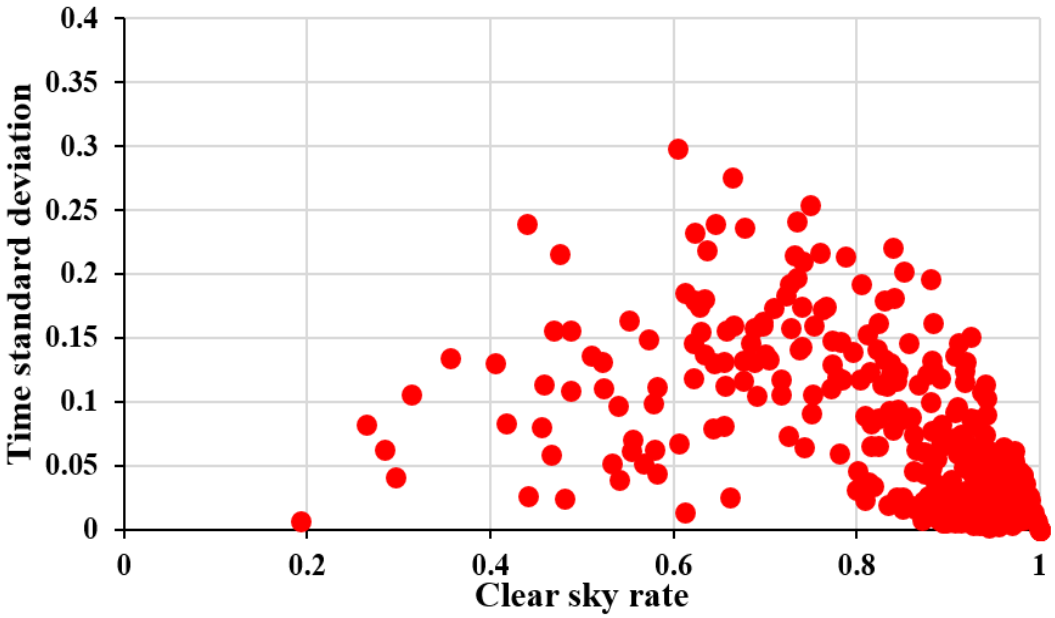

Figure 5.8: Monthly one-hour average time standard deviation and the clear sky rate for the solar panel at Ehime University

whole-sky camera at the specific site. Here Figure 5.8 represents the monthly one-hour average time standard deviation and the clear sky rate for the months of August to November from 8:00 to 16:00. The clear sky generally varied from 0.2 to 1 within the time standard deviation ranging from 0 to 0.3.

The whole-sky photographs taken at an interval of 10 minutes during the observation months were taken into consideration to study the type of the clouds based on the different ranges of the clear sky rate and the time standard deviation, respectively. The detail of the whole-sky photography and the instrumentation is discussed in Chapter 3 of the thesis.

Here, we consider maximum and the minimum time standard deviation within the different ranges of the clear sky rate from 0 to 0.2, 0.2 to 0.4, 0.4 to 0.6, 0.6 to 0.8 and 0.8 to 1, respectively. The same methodology for the study of the cloud types as discussed in Chapter 3 was taken into account. Within each range of the clear sky rates a maximum and the minimum value of the time standard deviation was selected as indicated by the black point in the Figure 5.9, respectively.

First, we consider the clear sky rate between 0 to 0.2 with the only observation value within the range. The minimum time standard deviation was observed from 15:00 to 15:59 on October 8, 2015. The observation data is indicated by a black point (A) in Figure 5.9. According to the definition of the clear sky rate, the smaller clear sky rate indicates the

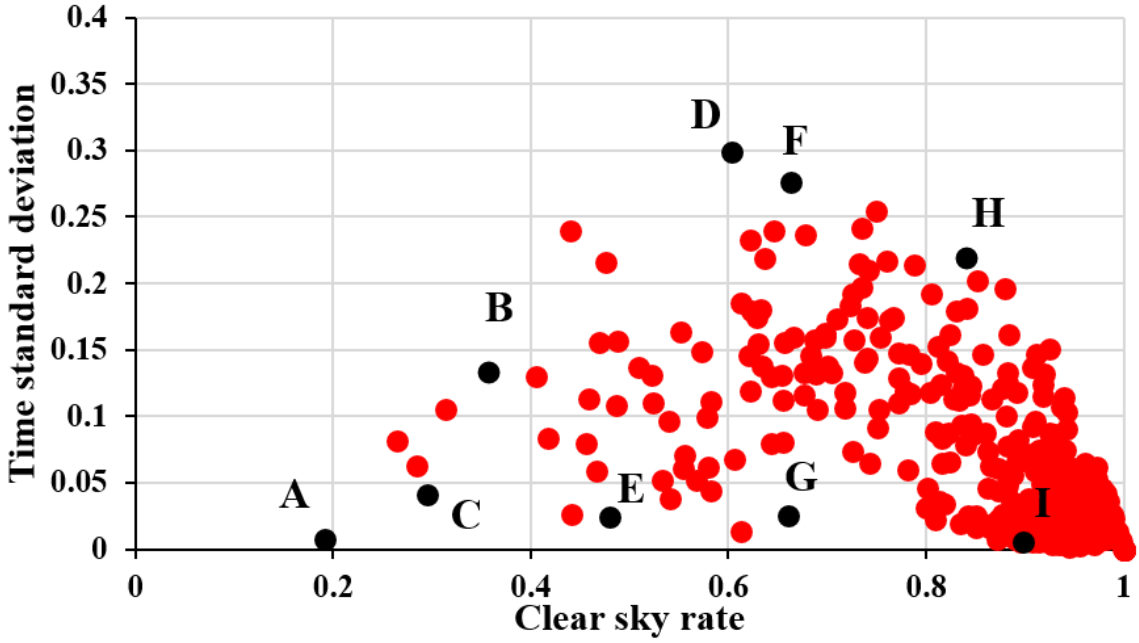

Figure 5.9: Observation of the maximum and minimum time standard deviation along the clear sky rate

cloudy condition so the observation value within the range between 0 to 0.2 suggested the cloudy condition. This is further evident from the whole-sky images from 15:00 to 15:50 at an interval of 10 minutes as shown in Figure 5.10. Here, the presence of low level clouds such as nimbostratus or cumulonimbus cloud are seen to cover the entire sky over the study area.

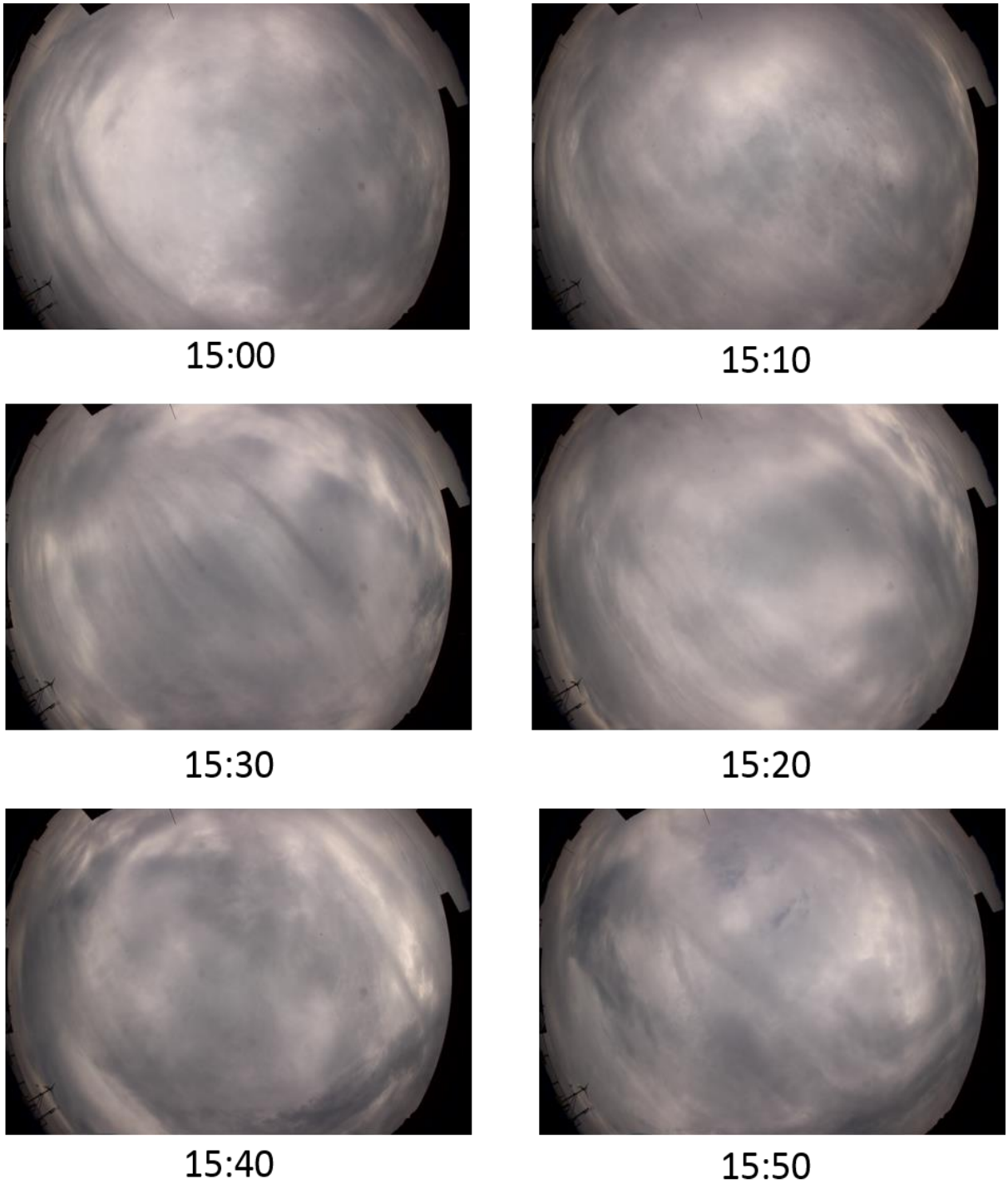

Figure 5.10: Whole-sky photographs of October 8, 2015 from 15:00 to 15:50 at an interval of 10 minutes

For the clear sky rate ranging between 0.2 to 0.4, the clear sky rate was observed from 8:00 to 8:59 on September 13, 2015 (black point B in Figure 5.9). During this time period, the presence of low level to medium clouds such as stratocumulus or altostratus can be observed to cover the sky with much clear weather condition around 8:50 as indicted in Figure 5.11.

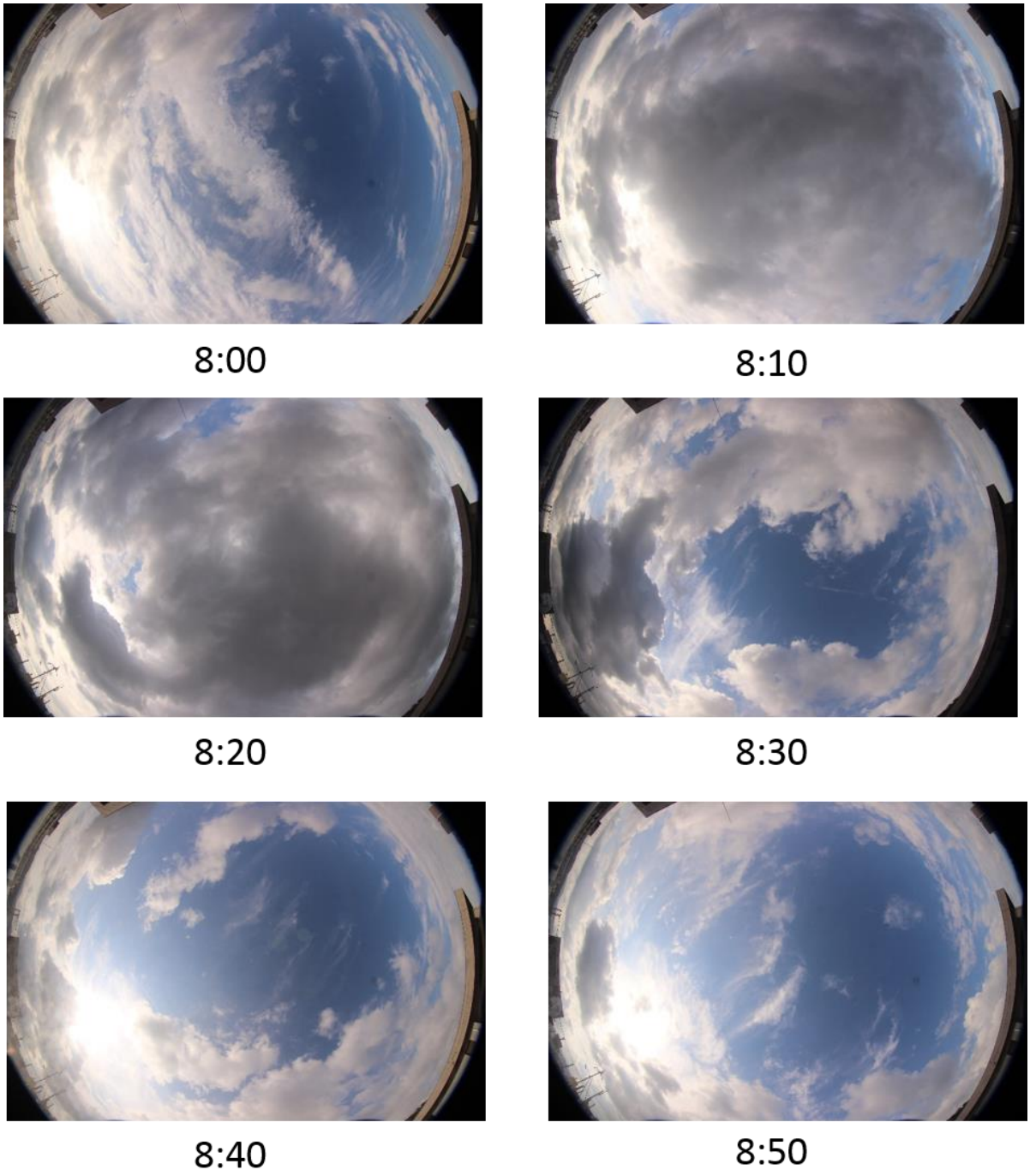

Figure 5.11: Whole-sky photographs of September 13, 2015 from 8:00 to 8:59 at an interval of 10 minutes

Similarly, the minimum time standard was observed from 14:00 to 14:59 on October 8, 2015 ((black point C in Figure 5.9). The images of the sky during the time period is presented in Figure 5.12 which clearly shows the presence of the low level clouds such stratus or stratocumulus during the entire observation period.

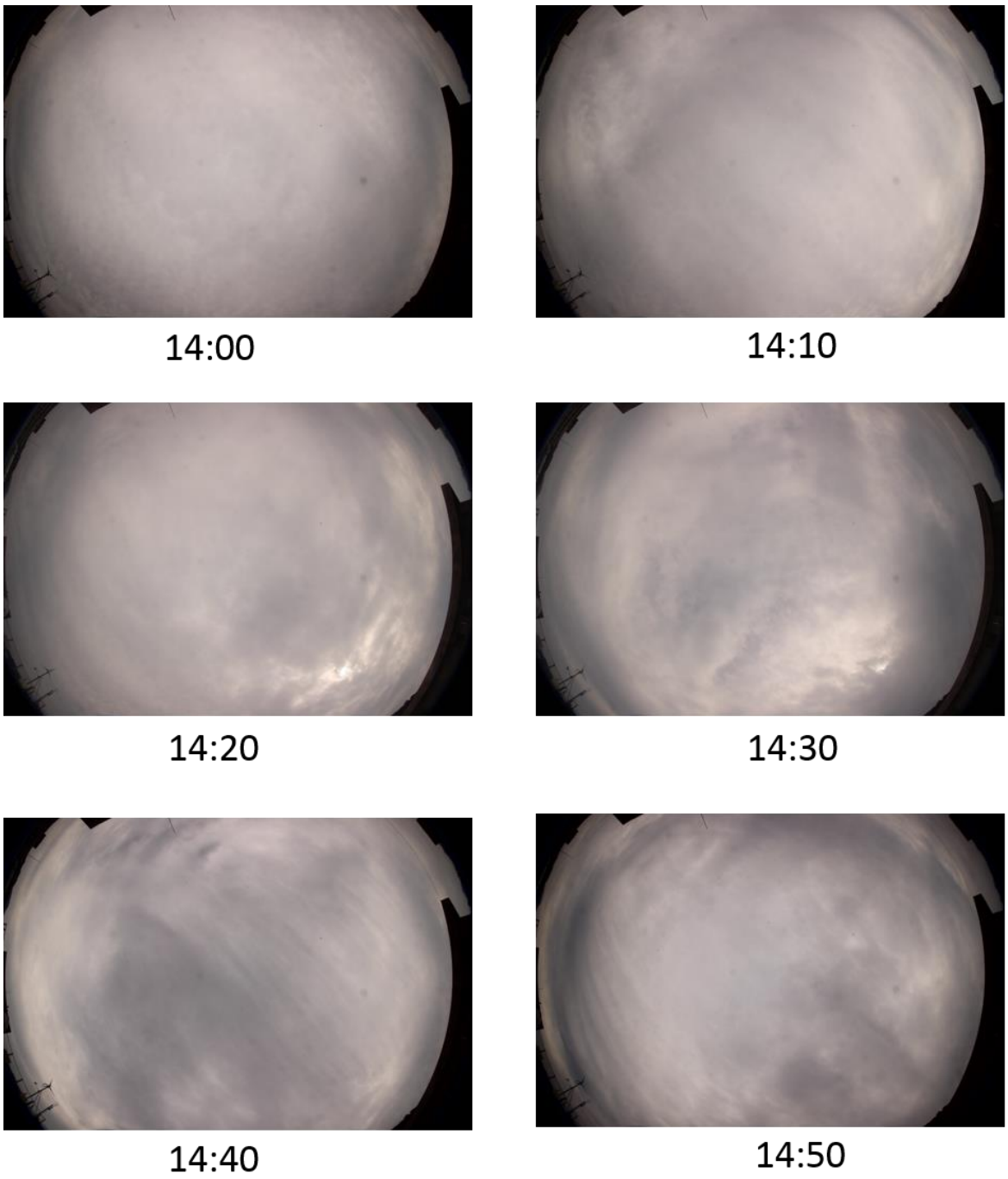

Figure 5.12: Whole-sky photographs of October 8, 2015 from 14:00 to 14:50 at an interval of 10 minutes

Again, we consider the clear sky rate varying between 0.4 to 0.6. The maximum time standard deviation was observed from 10:00 to 10:59 on November 15, 2015 as indicated black point D in Figure 5.9. During the time period the cloudy as well as sunny weather condition can be observed as indicated in Figure 5.13. The dominance of the cumulus clouds during the time period can be seen throughout the observation period.

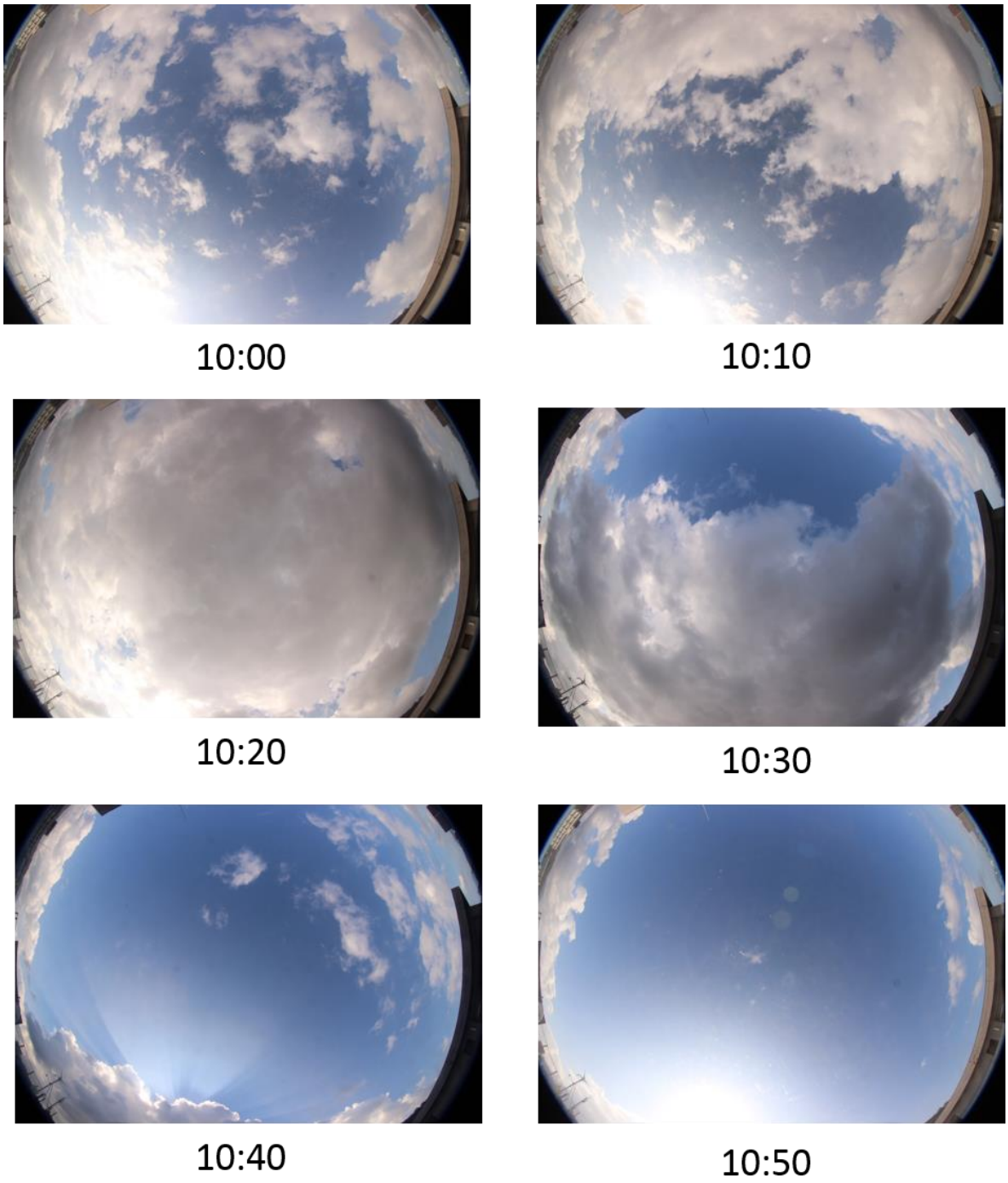

Figure 5.13: Whole-sky photographs of November 15, 2015 from 10:00 to 10:50 at an interval of 10 minutes

Similarly, the minimum time standard deviation was observed from 14:00 to 14:59 on September 22, 2015 (Black point E in Figure 5.9). As indicated by the whole-sky photograph of the target day from 14:06 to 14:56 represented in Figure 5.14, the presence of high-raised cloud such as cirrostratus or cirrus were found to cover the sky through the entire time period.

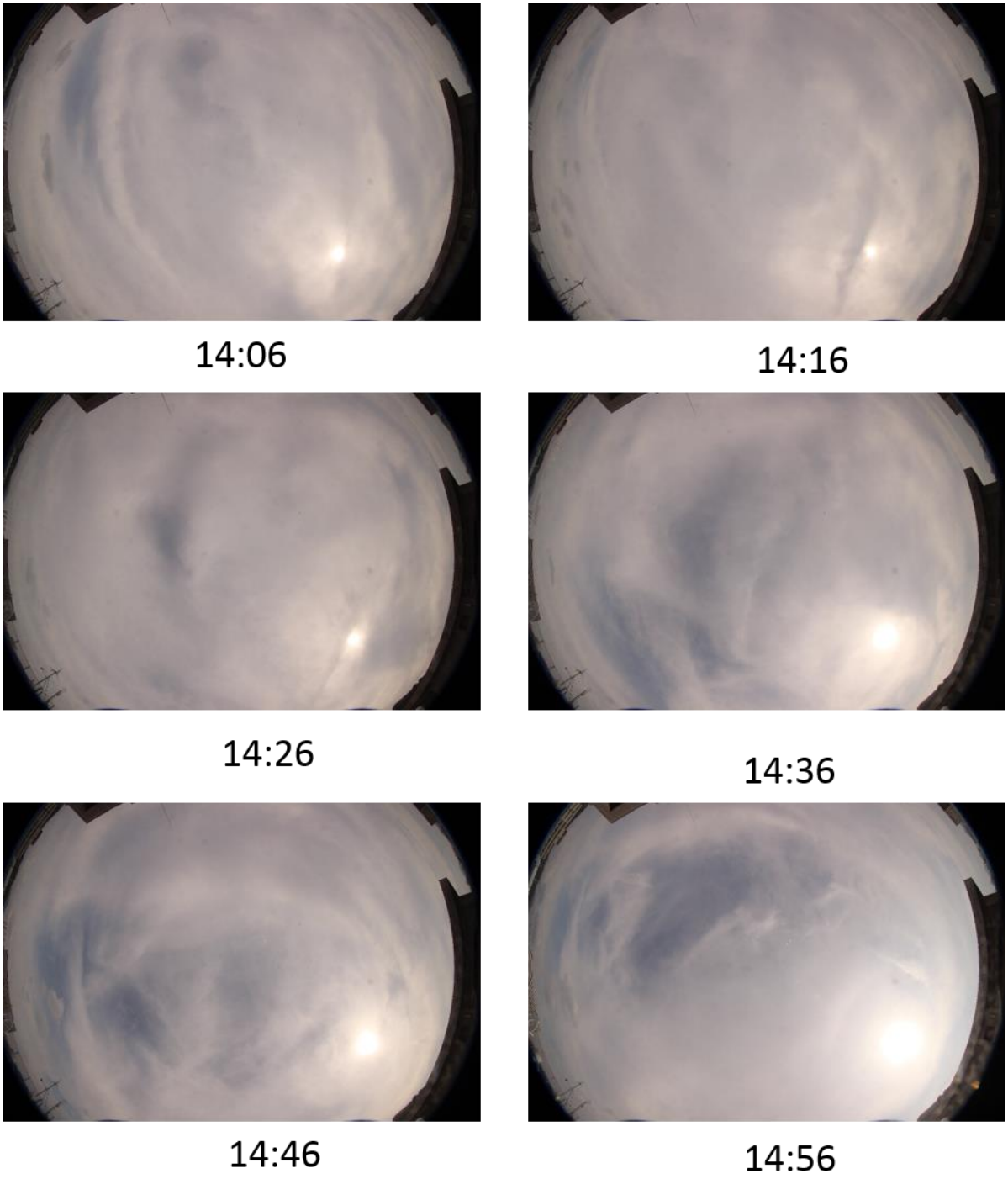

Figure 5.14: Whole-sky photographs of September 22, 2015 from 14:06 to 14:56 at an interval of 10 minutes

The maximum and the minimum time standard deviation for the clear sky rates ranging between 0.6 to 0.8 is taken in consideration. The maximum time standard deviation was observed from 9:00 to 9:59 on October 13, 2015 as indicated by the black point F in Figure 5.9. During the observation time, the presence of patches of cumulus clouds were observed as indicated in Figure 5.15.

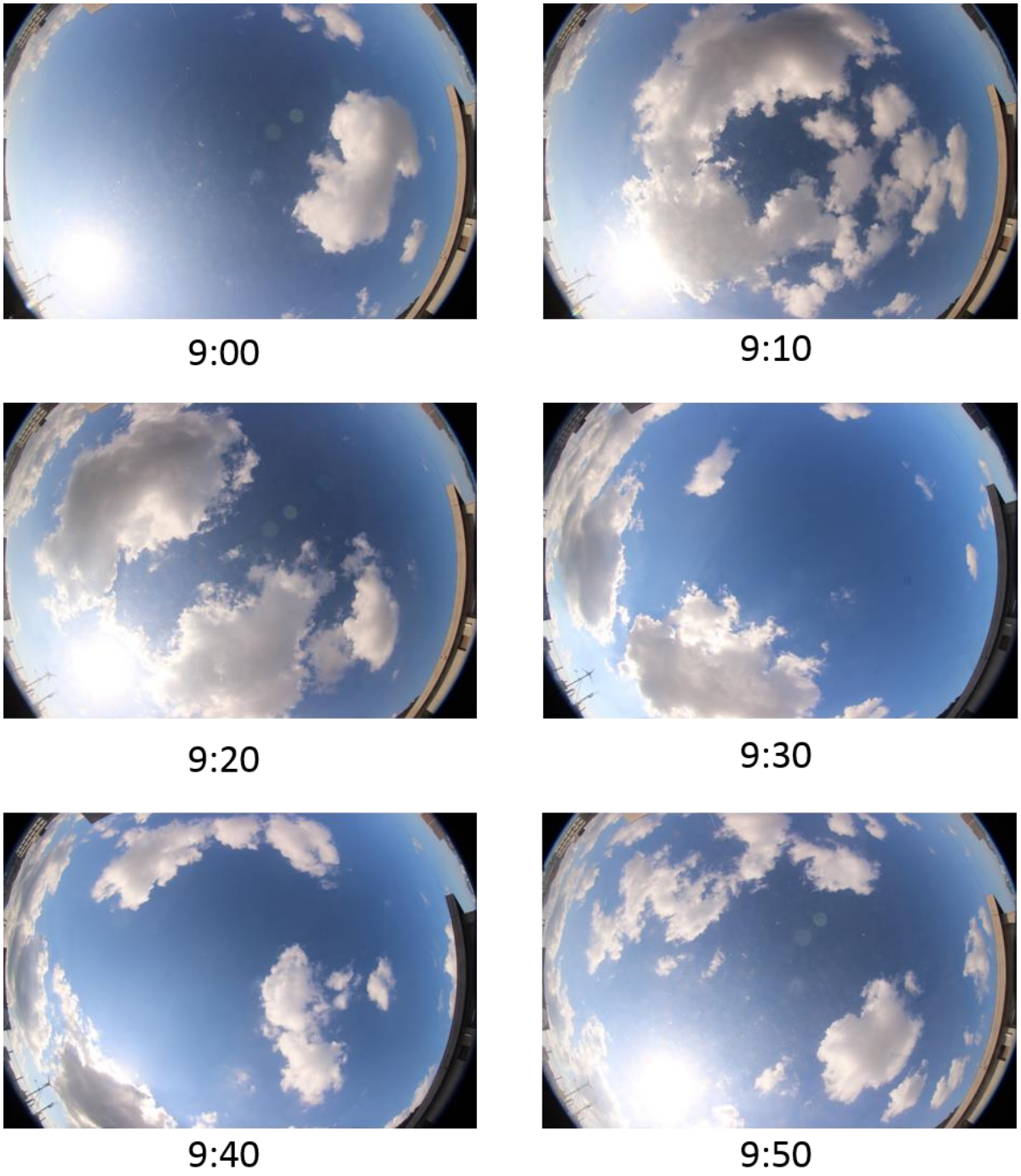

Figure 5.15: Whole-sky photographs of October 13, 2015 from 9:00 to 9:50 at an interval of 10 minutes

The minimum time standard deviation was observed from 15:00 to 15:59 on November 11, 2015 represented by the black point G in Figure 5.9. As indicated by the whole-sky photograph in Figure 5.16, the presence of high-raised cloud such as cirrostratus or cirrus were found to cover the sky throughout the observation time period.

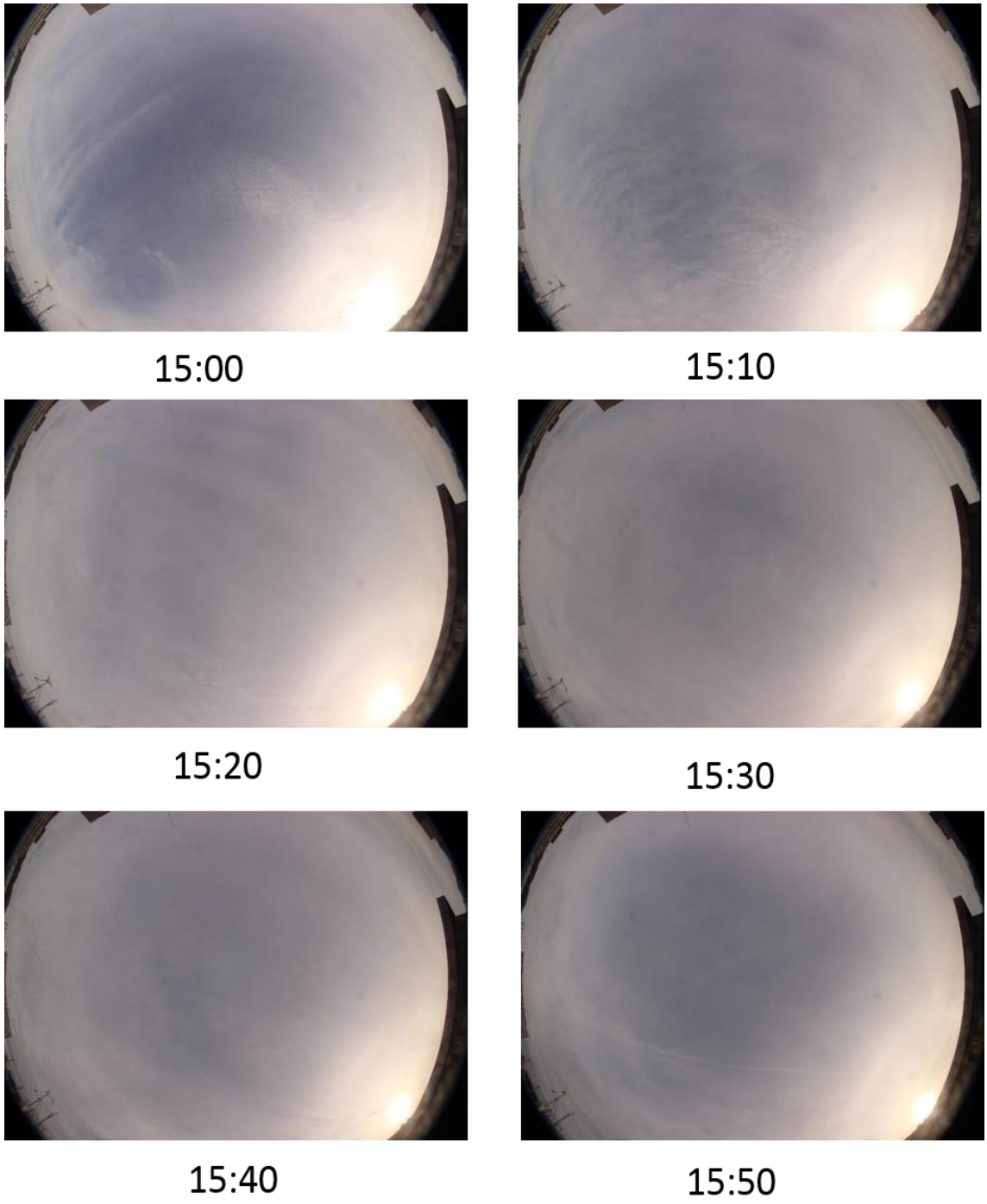

Figure 5.16: Whole-sky photographs of November 11, 2015 from 15:00 to 15:50 at an interval of 10 minutes

Finally, the clear sky rates ranging between 0.8 to1 and the maximum and the minimum time standard deviation within the range was taken into consideration. The maximum time standard deviation was observed from 11:00 to 11:59 on September 20, 2015 as indicated by the black point H in Figure 5.9. During the time period the presence fine clouds such as high raised cloud i.e. cirrus was observed as indicated by Figure 5.17.

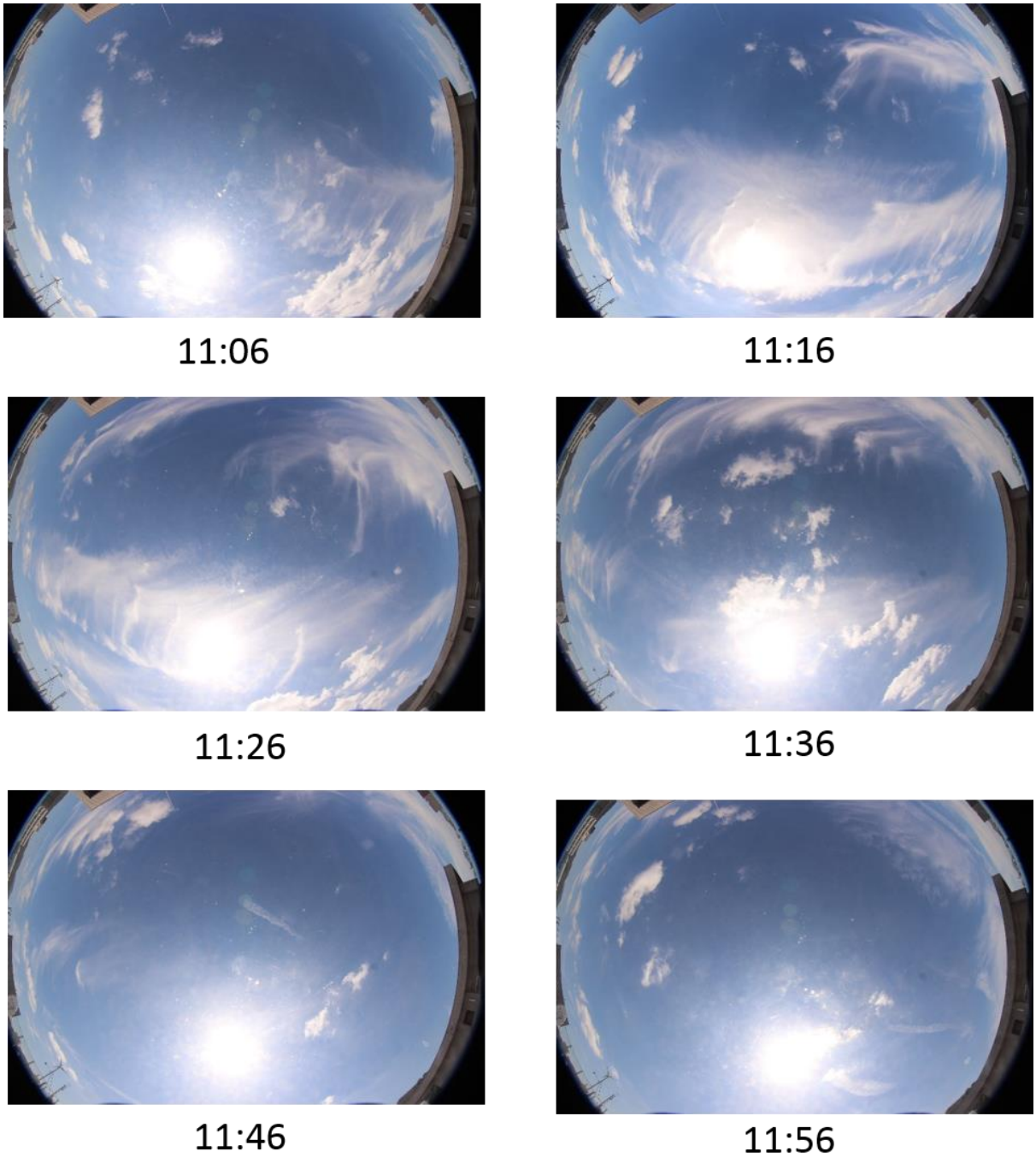

Figure 5.17: Whole-sky photographs of September 20, 2015 from 11:06 to 11:56 at an interval of 10 minutes

Similarly, the minimum time standard deviation was observed from 12:00 to 12:59 on October 29, 2015 represented by the black point I in Figure 5.9. During the time period cloudless condition was observed throughout the time period as indicated in Figure 5.18. Thus, the clear closer to 0 shows cloudy weather condition and closer to 1 shows no presence of the clouds, respectively

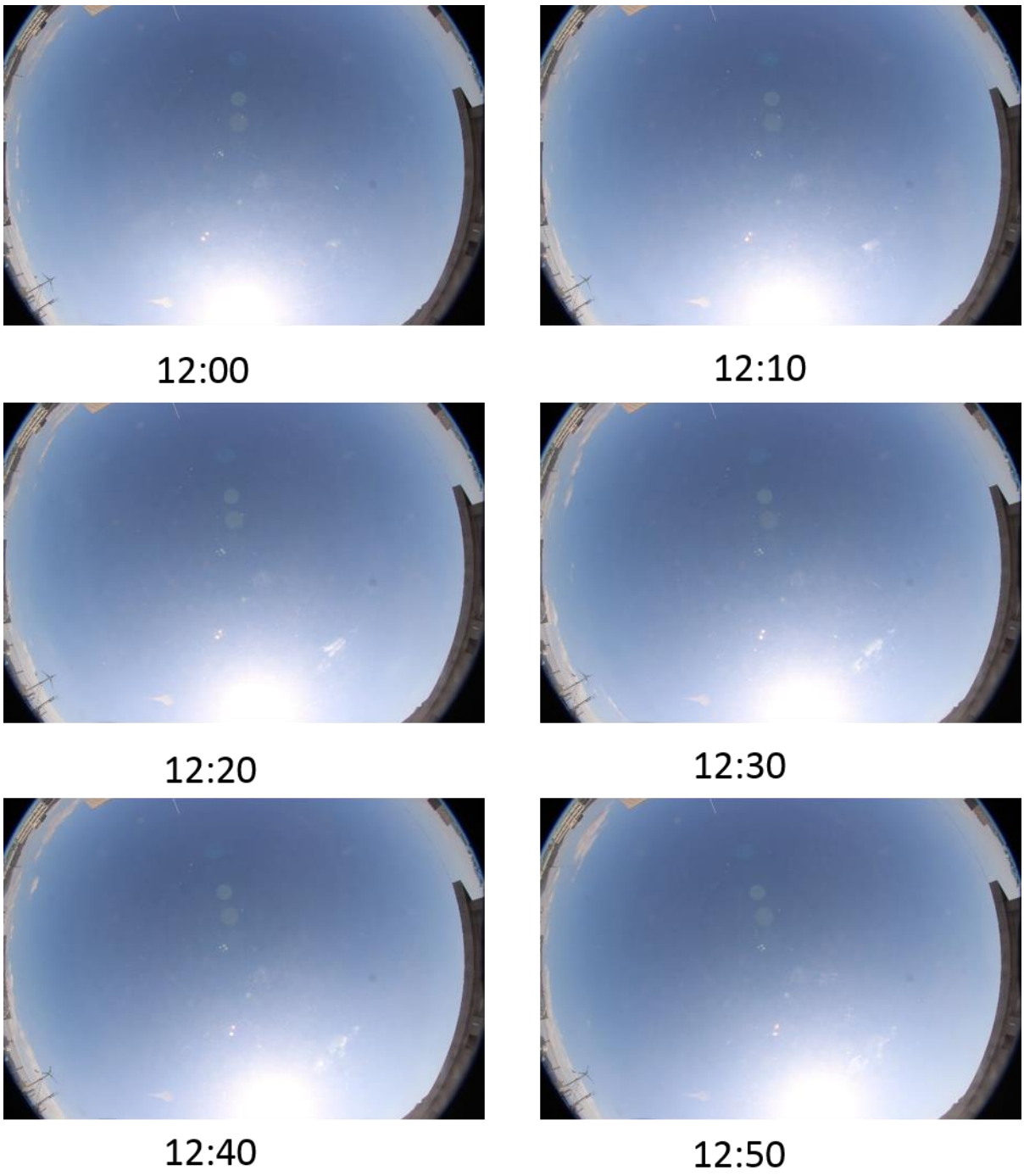

Figure 5.18: Whole-sky photographs of October 29, 2015 from 12:00 to 12:50 at an interval of 10 minutes

From all the above observation we found that the sky condition and the cloud type and state varied with the difference in the time standard deviation even within the same range of the clear sky rate. Generally, the minimum time standard deviation indicates the presence of the cloud coverage to be more which included medium to high raised clouds whereas the maximum time standard deviation indicated to be presence of low to medium cloud such as cumulus over the time period.

According to Figure 5.2, we observed the highest time standard deviation was observed at the Shiomi elementary school within the clear sky rates between 0.4 to 0.8 which indicates the presence of cumulus to altocumulus clouds to be more in the area during the observation period. Similarly, looking at the clear sky rate between 0 to 0.4, more observation data at Kuwabara junior high school were observed, which indicate the cloudy condition to be more in that area with dominance of high raised clouds such as cirrus or cirrostratus.

The observed result of the cloud condition from the clear sky rate and the time standard deviation calculated using the estimated global solar radiation is in agreement to the sky condition studied using the pyranometer observation as described in Chapter 3. Thus, the temporal and the spatial distribution and the type of the cloud and can be studied from the estimated global solar radiation using the photovoltaic system. Hence, the dense monitoring of the photovoltaic system is applicable for the study of the local climate.

5.4 Chapter summary

The chapter discussed about the spatial variation of the global solar radiation using the photovoltaic network in the Matsuyama plain. The observation results from the estimated global solar radiation from the PV system and measured global solar radiation from the pyranometer observation was compared. The measured and the estimated global solar radiation was in high agreement with each other for all the observation sites. The presence of cloud was observed to be more in the mountainous side of the study area as compared to other observation sites. Similarly, the monthly variation of the measured and estimated global solar radiation was also in high correlation. Thus, the applicability of the estimated global solar radiation to study the distribution of the solar radiation was studied.

The study further shows that the recognition of cloud types from the estimated global solar radiation using the solar panel is possible. Here, using the estimated global solar

radiation observation was used for the study the cloud characteristics and cloud type. For this purpose, the one-hour time standard deviation and the clear sky rate at the Ehime University was taken into consideration. The types of the cloud and the sky condition was further verified using the whole-sky images taken at an interval of 10 minutes during the observation period. The difference in the cloud type were observed within the different ranges of the clear sky rate and the time standard deviation. The presence of the thick cloud such as cumulus or altocumulus along with the movement of the cloud were observed whereas with the minimum time standard deviation the dominance of the high raised cloud such as cirrus or cirrostratus were observed to cover the entire sky during the observation period. Thus the photovoltaic network can be used to monitor the distribution of the solar radiation and cloud characteristics within the study area.

CHAPTER 6

6. Synthesis

6.1 Improvement in the solar radiation measurement

One of the most important aspect of the local climate is the study of the solar radiation distribution and the cloud characteristics. Based on this objective, the ground-based measurement of the solar radiation in the Matsuyama plain has been conducted from 2010. The study was based on the measurement in the two observation site mainly concentrating on the urban and rural area of the plain. The main objective of the study was to see the impact of the differences in land-use on the clouds formation due to the obvious contrast in land use between the urban and rural area along the Shigenobu River in the Matsuyama plain. During the entire study, clear sky rate was taken as an index to identify the reduction of the solar radiation due to the presence of the cloud. The clear sky rate was found to be smaller in the morning and late afternoon with a maximum value around mid-day. For the analysis, days with the fair weather days with sunshine percentage ranging from 40% to 80% was selected on the basis of the meteorological data available from the Matsuyama meteorological observatory under the Japan Meteorological Agency (JMA). The observation result showed the cloud formation to be more in the urban area as compared to the rural area as described in the Chapter 4. The observation results were validated with the numerical simulation and numerical experiment using the WRF model. The result was supported by the previous studies conducted related to the urban climates in the Matsuyama plain. As, the observation of the solar radiation in just two sites were not sufficient

6.1.1 Pyranometer network

Further to study the temporal and the spatial variation of the solar radiation and the cloud variation along the Matsuyama plain, a pyranometer network was established with the installation of 7 pyranometer at different sites along the area so as to cover various land-use categories (Chapter 3). The observation of the solar radiation was continuously monitored from 2014 till date at an interval of 1 minute. The diurnal and monthly variation of the clear

sky rate was studied from August to December, 2015. The one-hour time standard deviation of the clears sky rate for all the observation sites were taken into account for the analysis. The 5 monthly average of the clear sky rate indicated the clear sky rate to be smallest during December, which in turn suggested the clear sky rate to be highest during the mid-day for all the observation period. Similarly, the average diurnal variation of the one-hour time standard deviation for 5 month shows minimum value during the mid-day. During the observation period, the clear sky rates between 0 to 1 within the time standard deviation of 0 to 0.5.

After the study of the temporal variation of the solar radiation, we focused on the spatial variation of the solar radiation distribution within the study area. The time standard deviation of the clear sky rate for all the observation sites were calculated for 5 months of the study period. The diurnal variation of the clear sky rate also suggested the amount of solar radiation to be maximum during the mid-day for all the observation sites. During the analysis the clear sky rate at the inland area (Sabo office) of the Matsuyama plain was found to be lowest among all the observation points. The monthly spatial variation of the clear sky rate was considered to study the variation in the solar radiation distribution. The clear sky rate for winter (i.e. December) was found to be lowest compared to summer and autumn season. In all the observation month, the clear sky rate at the inland area was found to be smallest but the difference was not remarkable. Thus, for detailed study, the clear sky rate was divided into 3 sub-groups; clear sky rate ranging from 0 to 0.4, 0.4 to 0.6 and 0.6 to 1, respectively. The overall results were in agreement to the previous results which clearly showed the clear sky rate to be smallest in the inland area and highest at the coastal area (i.e. Purification center and Daini) as compared to all the observation sites. Similarly, comparing the urban and the rural area, the cloud presence in the clear sky rate in the urbanized area (i.e. Ehime University) was found to be slightly smaller as compared to the rural area (i.e. Suiden or Ukena elementary school). The observed result further suggests that the cloudier condition tends to appear more in the inland and the urbanized area whereas fine weather condition is observed in the rural and the coastal area of the Matsuyama plain, respectively.

Thus, the distribution of the solar radiation and the sky condition of the Matsuyama was studied using the pyranometer network. Though the pyranometer network was established to monitor the local climate of the study area was useful and reliable, but the observation data might not be sufficient for the overall monitoring of the study area. Further, establishing pyranometer network in all the area of interest might not be financially and practically feasible. In today's world the use of solar panels has been increasing rapidly from

houses, commercial building and schools as a source of alternative energy. Thus, the use of the already installed solar panel might be an alternative source for the study of distribution of the radiation and sky condition. Hence, the potential of using a photovoltaic system as a solar radiometer was studied.

6.1.2 Photovoltaic network

The annual sunshine hour and the annual mean temperature of the Matsuyama plain makes its an appropriate site for the production of solar energy. Matsuyama selected as the "Environmental Model city" in March 15, 2013 has shifted its interest towards the renewable source of energy such as solar power. During the course of time, installation of the solar panel all over the area has been increasing. Thus, if the solar panel can be used as a radiometer, the study of the local climate in the area can be conducted more efficiently and on much larger spatial scale.

The agreement between the temporal variation pattern of the solar radiation and the photovoltaic power of the solar panel indicates that the estimation of the global solar radiation using a PV system might be possible. For the estimation of the global solar radiation, panels installed horizontally and at a tilt angle of 20^{o} due south was taken into consideration.

Initially the solar installed at the Ehime University was considered for the estimation of the global solar radiation. Due to the conversion loss in the power conditioner, the electric resistance loss during wiring, aging of the panel and dust accumulation causes reduction in the PV power resulting in the PV output to be less than the rated output. Therefore, in order to incorporate the effects of environmental factors, the power ratio is corrected using a conversion factor for the estimation of the global solar radiation. The global solar radiation is estimated using the power ratio and the conversion factor (determined using the power ration and the measured solar radiation on a sunny day). The calculated c was used for the estimation of the total solar radiation for other analysis days. It should be noted that, the c was calculated for two cases, Case-A: constant conversion factor and Case-B: temporal variation of the conversion factor.

The PV power of solar panels installed at an inclination is considered to be proportional to the amount of solar radiation on the slope. Therefore, to estimate the global solar radiation, it is necessary to convert the solar radiation on a slope to the global solar

radiation on a horizontal plane. Thus, for this conversion the separation of the solar radiation into the direct beam solar radiation and the diffuse solar radiation becomes necessary. In the separation model simple assumptions were taken into consideration such as the reflected solar radiation from the ground surface are isotropic, the uniformity of the diffuse solar radiation and using the Erbs et al. model, 1982 for the estimation of the diffuse solar radiation on a slope. These assumptions facilitate the estimation of the global solar radiation from the solar radiation on a slope (Chapter 2). The global solar radiation can be estimated using a conversion factor of a sunny day, regardless of the weather condition, but using the same conversion factor might result in an error in different season. Thus, a conversion factor for each season is recommended for the accurate estimation. To estimate the global solar radiation using a tilted solar panel, it is necessary to convert the solar radiation on a slope to the global solar radiation on a horizontal plane. Thus, for this conversion the separation of the solar radiation into a direct beam solar radiation and diffuse solar radiation becomes necessary. The validity of the method proposed for the estimation of global solar radiation using solar panels at a tilt angle of 20^{o} due south was confirmed with high correlation (Chapter 4). This study mainly focuses on the potential of a PV system to explore the temporal variation pattern of the solar radiation and for this purpose only the variation patterns of the solar radiation were taken into consideration which fulfils the objective of the study and further confirms the good performance of the proposed estimation method.

Further the study focused on the temporal and spatial variation of the solar radiation using the photovoltaic network in the Matsuyama plain i.e. solar panel installed at 25 elementary and junior high school in the study area. The conversion factor was calculated for all the observation sites with high correlation. The calculated conversion factor was used for the estimation of the global solar radiation for all the observation site. Here, the high correlation coefficient, greater than 0.99, between the estimated and measured solar radiation was observed for all observation site. This suggests that the photovoltaic network can be used to study the distribution of the solar radiation in the Matsuyama plain. The similar variation pattern of the diurnal variation of the solar radiation during all the weather condition suggests that the estimated radiation can be used for the study of the local climate of the Matsuyama plain.

To further elaborate the study, we consider the statistical analysis (one-hour time standard deviation) and clear sky rate for the temporal and spatial variation of the solar radiation using the estimated global solar radiation. Among the photovoltaic site, 5 sites were

taken into consideration for the analysis. The variation of the time standard deviation within the range of 0 to 0.4 for the clear sky rate between 0 to 1 is observed with maximum percentage of the observation value within the clear sky rate ranging between 0.8 to 1. Here, the clear sky rate at the Mountainous side (Kuwabara junior high school) was found to be smallest among all the other observation site. The decrease in the clear sky rate was observed to be noticeable from the afternoon through evening. Similarly, the largest time standard deviation was observed at the coastal area (Shiomi elementary school) of the Matsuyama plain. As, the photovoltaic network was concentrated on the urbanized area, thus the variation according to the land-use category was not remarkable. Thus, for the detailed monitoring of the distribution of the solar radiation to the study is to incorporates all the observation sites of the photovoltaic network so as to cover the entire plain.

6.2 Accuracy of the solar radiation dataset

The potential of using the PV system and the photovoltaic network to explore the temporal and spatial variation pattern of the solar radiation was studied with high correlation. Also, the similar variation pattern of the diurnal variation of the solar radiation during all the weather condition suggests that the estimated radiation can be used for the study of the local climate of the Matsuyama plain. In order to use the PV system as a solar radiometer, the accuracy of the estimated global radiation need to be confirmed. Thus, for this purpose we compared the clear sky rate and the time standard deviation of the measured (pyranometer observation) and estimated global solar radiation (PV system) as explained in Chapter 5. The clear sky rate and the time standard deviation for both the measured and estimated global solar radiation is in high agreement with each other for all observation site. The clear sky rate calculated from both the measured and the estimated global solar radiation suggests the presence of the cloud cover to be more around the mountainous area of the study area irrespective of all the observation site being located in the urbanized area of the Matsuyama plain. As, Matsuyama plain is influenced by the sea breeze during the daytime, and the moist air is carried along the major river (Shigenobu River) especially along the south-western part which might result in the cloudy condition along the mountainous side and the inland areas of the area during the afternoon or along the evening time. Similarly, considering the monthly variation of the clear sky rate of the measured and estimated global solar radiation at the Ehime University, a high correlation of more than 97% was observed for all the

observation month. Here, the estimated global solar radiation from the PV system is in accordance with the measured global solar radiation from the pyranometer. Thus, using the estimated global solar radiation, the distribution of the solar radiation and the reduction of the radiation due to the presence of the cloud can be reproduced with high efficiency.

6.3 Improvement in the cloud classification to model solar variability

The study was further verified using the whole sky images taken by a camera mounted with a fish-eye lens (Canon EF 8-15mm f/4L USM, field view of 180^{o}) installed at the rooftop of Engineering building of the Ehime University (Chapter 3). To study the sky condition and cloud type, the relation between the one-hour time standard deviation and clear sky rate was taken into account for both the measured global solar radiation (pyranometer observation) and the estimated global solar radiation (photovoltaic system). The clear sky rate varied from 0 to 1 indicating the cloudy and clear sky condition, respectively. The clear sky rate was classified into subgroup; 0 to 0.2, 0.2 to 0.4, 0.4 to 0.6, 0.6 to 0.8 and 0.8 to 1, respectively. Among each subgroups of the clear sky rate, the maximum and the minimum time standard deviation was considered to study the sky condition. Observing the whole-sky photographs, the cloudy condition with dominance of the low clouds such as nimbostratus or cumulonimbus cloud was observed over the time period. For the clear sky rate ranging from 0.2 to 0.4, the maximum time standard deviation indicated the presence of low to medium clouds whereas the minimum time standard deviation showed the dominance of low clouds such as stratus or stratocumulus over the observation period. The clear sky rate ranging between 0.4 to 0.6 with maximum time standard deviation suggests the presence of cumulus clouds within the entire time period, along with variation in the radiation due to the movement of the cloud over the sky. Similarly, with the minimum time standard deviation, the fine clouds such as cirrus were observed to cover the entire sky. The variation in the sky condition was remarkable with the difference in the time standard deviation within the same range of the clear sky rate. Again, the clear sky rates between 0.6 to 0.8 was considered and the maximum and the minimum time standard deviation was taken into account. The maximum time standard deviation indicated a much finer weather condition compared to other ranges of the clear sky rate with the presence of the few stands of thin cloud such as cirrus and cumulus clouds. Whereas, with the minimum time standard deviation the cloud coverage over the area was remarkably large and the entire sky was seen to be covered high

raised cloud such as cirrus. Finally, the clear sky rates between 0.8 to 1 indicated a clear weather condition with few patches of the cumulus or altocumulus cloud observed with the maximum time standard deviation and a cloudless condition with the minimum time standard deviation, respectively.

Thus, the cloud type and sky condition are seen to vary with the different range of the time standard deviation even within the same range of the clear sky rate. The cloud type and the sky condition for both the measured and the estimated global solar radiation were found to be in agreement to each other (Chapter 3 and Chapter 5). The dominance of the cumulus cloud was observed with the maximum time standard deviation and low level to high raised clouds such as stratus to cirrus with the minimum time standard deviation, respectively. The cloud coverage was found to be more for the observation data with minimum time standard deviation as compared to the observation data with maximum time standard deviation. Usually, the observation data below the clear sky rate of 0.4 indicates much cloudier condition with dominance of dark water bearing clouds such as cumulonimbus or nimbostratus with the chances of precipitation in later hours. Hence, the cloud type and its characteristics can be reproduced with the one-hour time standard deviation of the clear sky rate for both the pyranometer and photovoltaic observation.

The validation of the observation data using the whole-sky images was based on one observation site only (i.e. Ehime University). Thus, for the detailed study on the classification of the cloud and the spatial variation of the cloud distribution, incorporating the whole-sky images of other sites might give much reliable results. The study of the state of the cloud gives the images of the cloud condition during the observation period which can be used for the study of the cloud effect in different part of the study area to understand the local climate. Further, this opens and interesting filed for exploring the cloud classification based on different criteria such as cloud pixel, cloud color and many more.

6.4 Key outcome of the thesis

The main aim of the thesis is to study the local climate of the Matsuyama plain using the ground-based measurement of the solar radiation. The ground-based measurement generally includes two section; the first section includes the measurement of the solar radiation using the pyranometer observation and the second section includes the estimation of the global solar radiation using the photovoltaic network.

Taking clear sky rate as an index to measure the reduction of the solar radiation due to the presence of the cloud. The one-hour time standard deviation of the clear sky rate for the 7 sites of the pyranometer network was initially considered to monitor the temporal and spatial variation of the solar radiation and the cloud coverage over the Matsuyama plain (Chapter 3). The pyranometer network included the different land-use categories such as coastal region, Inland region, urbanized area and rural area, respectively. The diurnal variation of the clear sky rate showed the presence of the cloud to be more in the morning and the late afternoon with maximum value around mid-day. Similarly, the monthly average of the clear sky indicated the presence of the cloud to be more in winter as compared to other observation month especially through afternoon. Following the manner, the spatial variation of the solar radiation in the study area was considered. The clear sky rate at the inland area of the Matsuyama plain was found to be smallest compared to all other observation site. Further comparing the clear sky rate of the urban and rural area, the clear sky rate at the urban area was found to be smaller than the rural area. Thus, the temporal and spatial distribution of the solar radiation for the entire study period shows the tendency of cloud formation to be more in the urbanized and the inland area of the study area.

As, the pyranometer network sites were limited for the monitoring of the solar radiation distribution of the entire study area. The establishment of the pyranometer might not be feasible in all the area where the other sources of meteorological data are not available. Thus, considering this fact, the potential of using the photovoltaic system as a radiometer was studied. The correlation between the temporal variation pattern of the solar radiation and PV power of the solar panel suggests the estimation of the global solar radiation is possible. Considering, the increasing number of the solar panels in the study area, the method for the estimation of the global solar was introduced (Chapter 4). The estimation of global solar radiation using PV system was proposed and examined on the basis of the in-situ measurements. The solar panels installed horizontally and at a tilt angle of 20^{o} due south was taken into consideration. To estimate the global solar radiation using a tilted solar panel, it is necessary to convert the solar radiation on a slope to the global solar radiation on a horizontal plane. Thus, for this conversion the separation of the solar radiation into a direct beam solar radiation and diffuse solar radiation was conducted (Chapter 2 and Chapter 4). The validity of the method proposed for the estimation of global solar radiation using solar panels at a tilt angle of 20^{o} was confirmed with high correlation irrespective of the season.

Further, the spatial variation of the estimated global solar radiation was studied using the photovoltaic network in established within the study area. The photovoltaic

network basically consists of the solar panel installed at various elementary and junior high school of the Matsuyama plain. The estimation of the global solar radiation at all the observation site was confirmed with high correlation and were in turn supported by the whole-sky images which confirms the distribution of the cloud and the reduction in the amount of solar radiation during the observation period. To elaborate the sky condition and the solar radiation distribution in the area, the temporal and the spatial variation of the one-hour time derivative of the clear sky rate was taken into account. The diurnal and the monthly variation of the clear sky rate was to be smallest near the mountainous side of the urbanized area of the plain. The decrease in the clear sky rate was observed from the afternoon when the plain is dominated by the sea breeze. Thus, the wind direction and speed plays an important role in the distribution of the cloud in the Matsuyama plain. The one-hour average of the time standard deviation and the clear sky calculated from the measured global solar radiation from the pyranometer network and the estimated global solar radiation from the photovoltaic network was in high agreement with each other for all the observation points. Also, the monthly variation of the clear sky rate from the measured and the estimated global solar radiation showed high correlation for all the observation month. Thus, the all the above result confirms the accuracy and the good performance of the proposed estimation method for the monitoring of the solar radiation.

One of the objective of the study is to monitor the reduction of the solar radiation due to the presence of the cloud. Thus the cloud distribution and the sky condition over the study area was monitored using the whole-sky camera installed at the Ehime University. To understand the characteristic and the type of the cloud the clear sky rates were divided into subgroups and within each group the maximum and the minimum value of the time standard deviation was taken into account. The clear sky rate below 0.4 with smaller time standard deviation showed the cloud coverage to be more as compared to other groups whereas the clear sky rate value closer to 1 with minimum time standard deviation showed a clear weather condition. The maximum time standard deviation within the clear sky rates between 0.4 to 0.6 shows the dominance of the cumulus clouds and the observation value with minimum time standard deviation showed the entire sky to be covered with the cloud during the observation period with the dominance of high raised clouds such as cirrostratus to cirrus. Thus, the difference in the cloud coverage and type was evident from the whole-sky photographs during the one-hour observation period. Both measured and the estimated global solar radiation indicted the similar cloud type and sky condition for the different ranges of the clear sky rates. Thus, the temporal and the spatial variation of the solar radiation

was used to study the cloud characteristics and the type in the Matsuyama plain using the pyranometer and the photovoltaic system.

Hence, we conclude that the photovoltaic system can be used as a radiometer to monitor the temporal and the spatial distribution of the solar radiation and the cloud type and sky condition in the Matsuyama plain. This study is applicable for all the megacities and urbanizing areas with increasing number of PV system for monitoring the effects of urbanization. The estimation of the global solar radiation can be beneficial for understanding the local climate studies such as torrential rainfall and urban heat island phenomena.

6.5 Future scope

The main objective of the study is to monitor the distribution of the solar radiation and the cloud coverage over the study area for understanding the local climate. The target of the study is the prediction of the localized torrential rainfall for the prevention and mitigation of the rainfall disaster.

Recently, events of torrential rainfall have been observed in the Matsuyama plain such as on July 9, 2015 and August 8, 2015 indicating the increasing trend of the localized

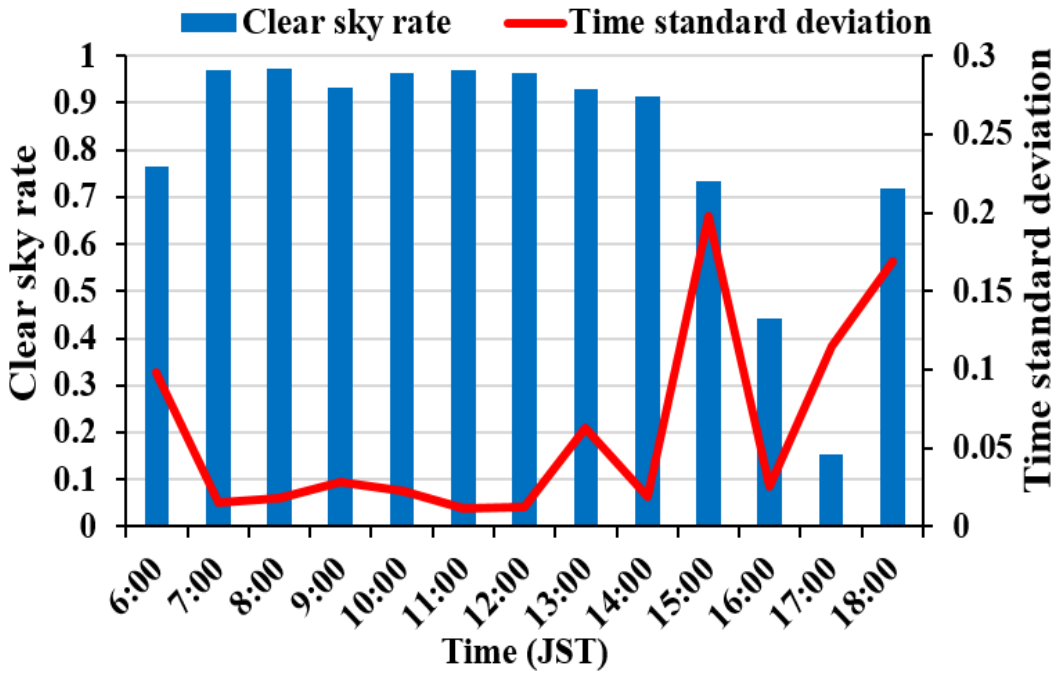

Figure 6.1: Diurnal variation of the one-hour time standard deviation and the clear sky rate for August 8, 2015 using the photovoltaic system

rainfall in the area. Considering the rainfall events of August 8, 2015 which recorded a rainfall of 15.5 mm within 10 minute at Kamibayashi (Inland area of the Matsuyama plain) around 17:10, which slowly shifted towards the central area where 8.5mm per 10 minute was recorded at the Matsuyama meteorological observatory around 17:30. Figure 6.1 shows the diurnal variation of the clear sky rate and the time standard deviation for the target day. The remarkable decrease in the clear sky rate approximately an hour before the rainfall events was observed. Thus, to further elaborate the observation, the correlation of the precipitation and the clear sky rate was further taken into consideration. Here, the time period of the rainfall and the reduction of the clear sky rate was in high agreement with each other as indicated in Figure 6.2. Thus, the clear sky can efficiently reproduce the reduction in the amount of solar radiation during the rainfall event.

The air pressure on the target day was taken into consideration to see the relation between the air pressure and the rainfall event. The continuous monitoring of the air pressure at different sites in the Matsuyama plain has been conducted since August 2015. During a sunny weather condition the air pressure starts decreasing around 8:00 in the morning through late afternoon from where it starts to increase again. During the torrential rainfall the sudden increase in the air pressure was observed especially at the Sabo office (inland area) at the time where the decrease in the clear sky rate was observed as indicated in Figure 6.3.

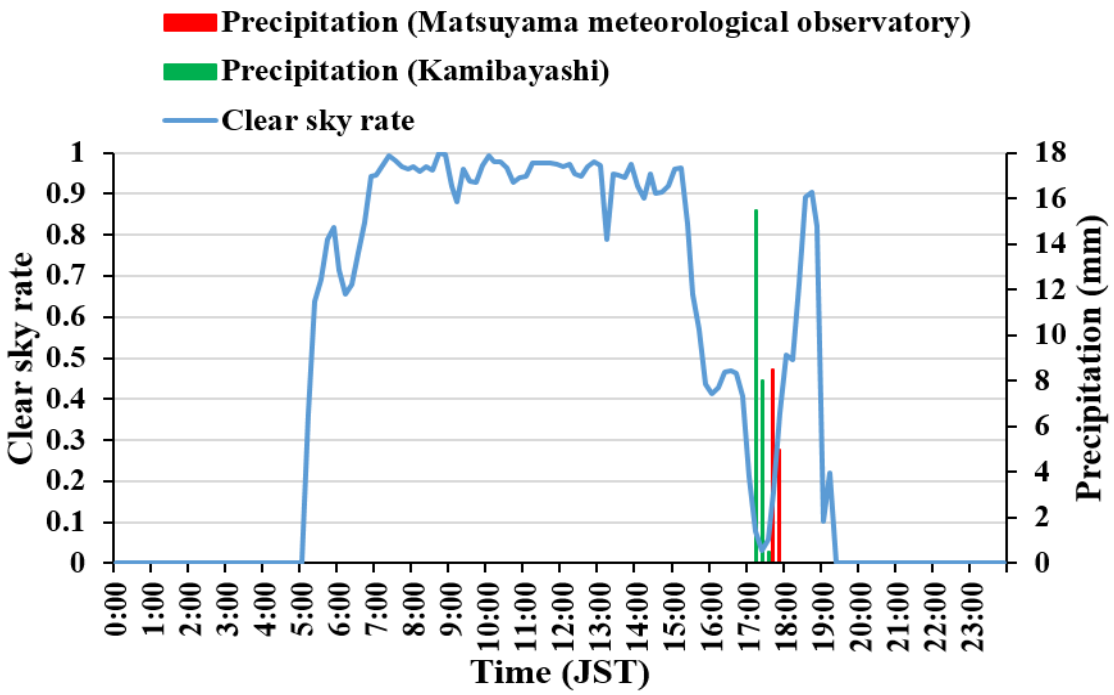

Figure 6.2: Relation between the clear sky rate and the precipitation event on August 8, 2015

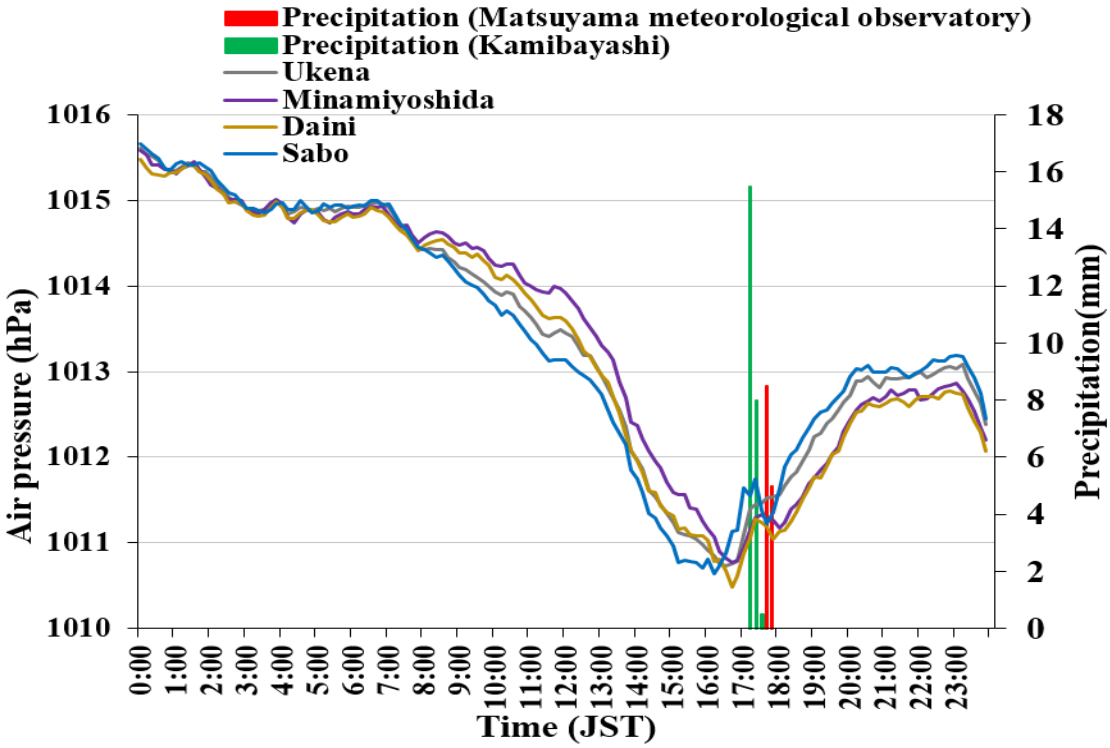

Figure 6.3: Relation between the air pressure and the precipitation event on August 8, 2015

As Matsuyama is dominant by the sea breeze during the daytime thus, the wind direction and speed has an important role in determining the weather condition of the area. During the rainfall event, the change in the wind direction from sea breeze to land breeze is observed with much stronger wind velocity. The rainfall event started from the inland area moving to the central area and finally towards the coastal area. The shifting of the rainfall from the inland area to the central part of the plain is believed to be elicited by the wind.

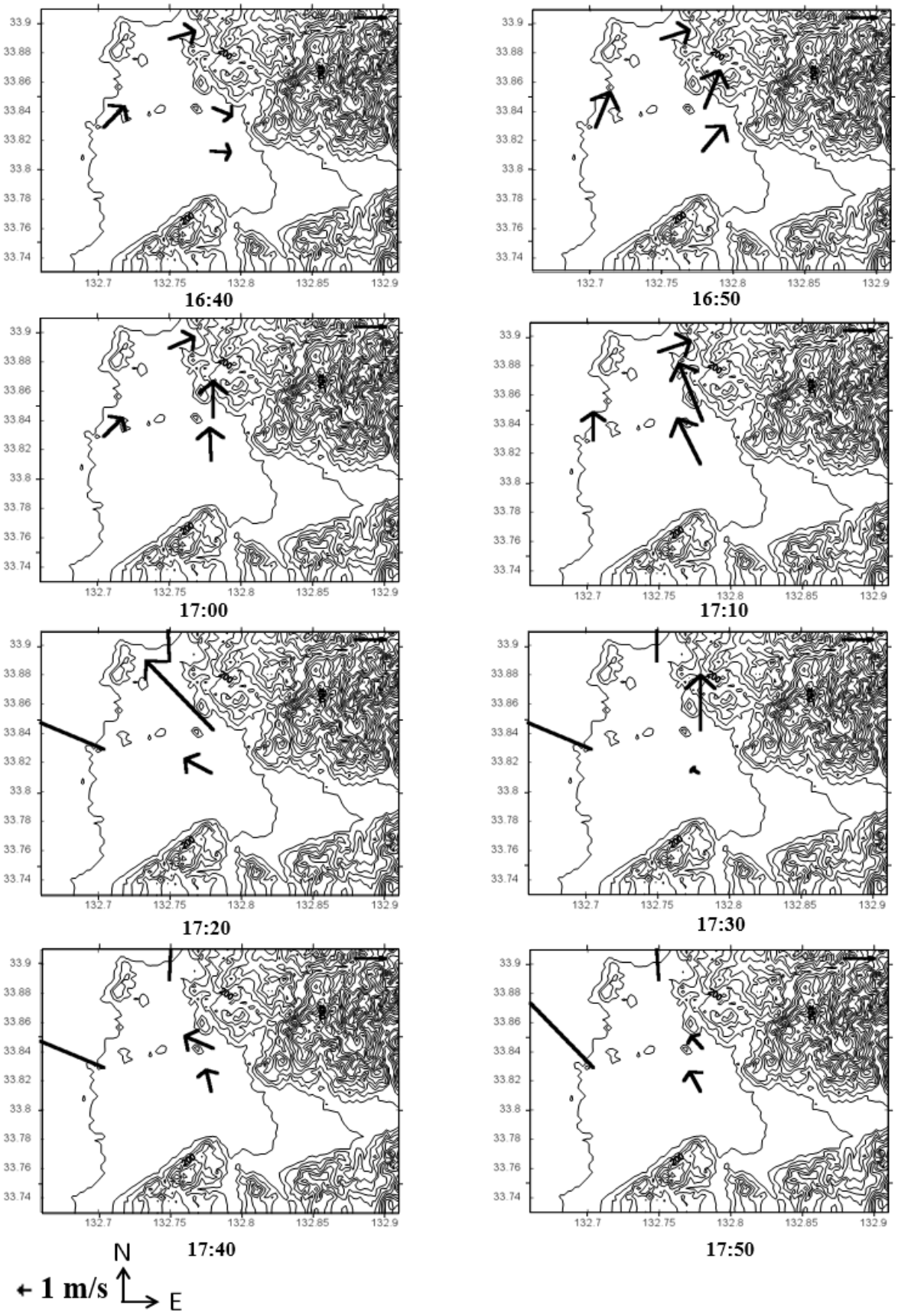

Figure 6.4: Wind profile of August 8, 2015 from 16:40 to 17:50 at an interval of 10 minutes

Here, the phenomenon of the localized rainfall event was observed which was followed by the prompt decrease in the clear sky rate approximately an hour before the event which in turn resulted in the increase in the air pressure. Thus, the dense monitoring of the various meteorological parameter such as solar radiation, air pressure, wind velocity and direction can be used for the prediction of the localized rainfall in the Matsuyama plain as was indicated in the background of the study (Chapter 1).

Hence, for the accurate monitoring of the local climate and the predication of the localized rainfall, dense photovoltaic monitoring of the solar radiation in order to cover the entire study area based on the land-use categories is recommended. Similarly, the clouds characteristics and types must be studied in detail based on various parameters such as cloud color, altitude, image pixel size and so on. The increase in the observation site of the whole-sky images can be used to monitor the difference in the cloud type and coverage over the area.

Relation between the different meteorological parameters must be studied for the overall monitoring the local climate. Further, more events of torrential rainfall need to be taken into considered to study the generation mechanism and the characteristics of such rainfall events. Finally, the numerical simulation for the distribution of the cloud coverage and the rainfall events is recommended the study of the rainfall pattern and the effect of wind for the early prediction and weather forecasting.

REFERENCES

Ackerman, S. A., Strabala, K. I., Menzel, W. P., Frey, R. A., Moeller, C. C., and Gumley, L. E. (1998). Discriminating clear sky from clouds with MODIS. Journal of Geophysical Research, Vol. 103, No. D24, pp. 32-141.

Angström, A., and Rodhe, B. (1966). Pyrheliometric measurement with special regards to the circumsolar sky radiation, Tellus XVIII, 1, pp. 25-33.

Asai, T., Ke S., and Kodama, Y. (1998). Diurnal Variability of Cloudiness over East Asia and the Western Pacific Ocean as Revealed by GMS during the Warm Season. Journal of the Meteorological Society of Japan, Vol 76, No. 5, pp. 675-684.

Balakrishnaiah, G., Reddy, L., and Reddy, R. R. (2016). Evaluation of Clearness and Diffuse Index at a Semi-Arid Station (Anantapur) using Estimated Global and Diffuse Solar Radiation. International Journal of Advanced Earth Science and Engineering, Vol. 51, No. 1 pp. 347-363.

Badescu, V. (1997). Verification of some very simple clear and cloudy sky models to evaluate global solar irradiance. Solar Energy, Vol 61, No. 4, pp. 251-264.

Barnes, M. L., & Miura, T. (2016). An assessment of diurnal, and seasonal cloud cover changes over the Hawaiian island using terra and Aqua MODIS. Journal of Climate, Vol. 29, pp. 77-90.

Beaubien, D. J., Bisberg, A., and Beaubien, A.F. (1998). Investigations in pyranometer design. Journal of Atmospheric and Oceanic Technology, Vol. 15, pp. 677-686.

Behr, H. D. (1997). Solar radiation on tilted south oriented surfaces: validation of transfer-models. Solar Energy, Vol. 61, No. 6, pp. 399-413.

Besharat, F., Dehgnan, A. A., and Faghih, A. R. (2013). Empirical models for estimating global solar radiation: A review and case study. Renewable and Sustainable Energy Reviews, Vol. 21, pp. 798-821,

Bindi, M., and Miglietta, F. (1991). Estimating daily global radiation from air temperature and rainfall measurements. Climate Research, Vol. 1, pp. 117-124.

Bird, R. D., and Riordan, C. (1986). Simple solar spectral model for direct and diffuse irradiance on horizontal and titled planes at the Earth's surface for cloudless atmosphere. Journal of Climate and Applied Meteorology, Vol. 25, pp. 87-97.

Bland, W. L. (1996). Uncertainty of daily isolation estimates from a mesoscale pyranometer network. Journal of Atmospheric and Oceanic Technology, Vol. 13, pp. 255-261.

Bornstein, R., and Lin, Q. (2000). Urban heat islands and summertime convective thunderstorms in Atlanta: three case studies. Atmospheric Environment, Vol 34., No. 3, pp. 507-516.

Bosch, J. L., Batlles, F. J., Zarzalejo, L. F., and López, G. (2010). Solar resources estimation combining digital terrain models and satellite images techniques. Renewable Energy, Vol. 35, pp. 2853-2861.

Brustsaert, W. (2005). Hydrology: An Introduction, Cambridge University press, pp. 618.

Buch, K. A., Sun, C. H., and Thorne, L. R. (1998). Cloud classification using whole-sky imager data. Proceeding of Fifth Atmospheric Radiation Measurement (ARM) Science Team Meeting, San Diego, CA, U.S. Dept. of Energy, pp. 35-39.

Bucher, K. (1997). Site dependence of the energy collection of PV modules. Solar Energy Materials and Solar cells, Vol 47, pp. 85-94.

Bukovsy, M. S., and Karoly, D. J. (2009). Precipitation simulation using WRF as a nested regional climate model. Journal of Applied Meteorology and Climatology, Vol 48, pp. 2152-2159.

Burain, S. J., and Shepherd, J. M. (2005): Effects of urbanization on the diurnal rainfall pattern in Houston. Hydrological Processes, Vol 19, pp. 1089-1103.

Bush, B. C., Valero, F. P., Simpson, A. S., and Bignone, L. (2000). Characterization of thermal effects in pyranometers: A data correction algorithm for improved measurement of surface insolation. Journal of Atmospheric and Oceanic Technology, Vol. 17, No. 2, pp. 165-175.

Calbó, J., González, J. A., and Pagès, D. (2001). A method for sky-condition classification from ground-based solar radiation measurements. Journal of Applied Meteorology, Vol.40, pp. 2193-2199.

Calbó, J., and Sabburg, J. (2008). Features extraction from whole-sky ground-based images for cloud-type recognition. Journal of Atmospheric and Oceanic Technology, Vol. 25, pp. 3-14.

Camani, M., Cereghetti, N., Chianese, D., and Rezzonico, S. (1998). Comparison and behaviour of PV modules. Proceedings of the 15th European Photovoltaic Solar Energy Conference, Vienna, pp. 2344-2349.

Cess, R. D., Zhang, M. H, Minnis, P., Corsetti, L., Dutton, E. G., Forgan, B. W., Garber, D. P., Gates, W. L., Hack, J. J., Harrison, E. F., Jing, X., Kiehl, J. T., Long, C. N.,

Morcrette, J. J., Potter, G. L., Ramanathan, V., Subasilar, B., Whitlock, C. H., Young, D. F., and Zhou, Y. (1995). Absorption of solar radiation by clouds: Observation versus models. Science, Vol 267, pp. 496-499.

Cess, R. D., Qian, T., and Sun, M. (2000). Consistency tests applied to the measurement of total, direct and diffuse shortwave radiation at the surface. Journal of Geophysical Research, Vol 105, No. D20, pp. 24,881-24,887.

Changnon, Jr S. A., Huff, F. A., and Semonin, R. G. (1971). METROMEX: An investigation of inadvertent weather modification. Bulletin of the American Meteorological Society, Vol. 52 No. 10, pp. 958-968.

Changnon, S. A., Shealy, R. T., and Scott, R. W. (1991). Precipitation changes in fall, winter, and spring caused by St. Louis. Journal of Applied Meteorology, Vol. 30, pp. 126-134.

Cheng, C. L., Chan, C. Y., and Chen, C. L. (2006). An empirical approach to estimating monthly radiation on south-facing titled planes for building application. Energy, Vol. 31, pp. 2940-2957.

Cheng, H. Y., and Yu, C. C. (2015). Multi-model solar irradiance prediction based on automatic cloud classification. Energy, pp. 579-587.

Chianese, D., Cereghetti, N., Rezzonico, S., and Travaglini, G. (2000). 18 types of PV modules under the lens. 16th European Photovoltaic Solar Energy Conference and Exibition (EPVSEC).

Coulson, K. L. (1975). Solar and Terrestrial Radiation, Academic Press Inc. (LONDON), pp. 319.

Davies, J. A, Schertzer, W., and Nunez, M. (1975). Estimating global solar radiation. Boundary layer Meteorology, Vol 9, Issue 1, pp. 33-52.

Davies, J. A., and McKay, D. C. (1982). Estimating solar irradiance and components. Solar Energy, Vol. 29, No. 1, pp. 55-64.

Davies, J. A., and Mckay, D. C. (1989). Evaluation of selected models for estimating solar radiation on horizontal surfaces. Solar Energy, Vol 43, No. 3, pp. 153-168.

Davies, F., Middleton, D. R., and Pearson, G. N. (2004). Observations of boundary layer depth over an urban/rural transition. AMS Fifth Conference on Urban Environment, Vancouver.

Dee, D. P., Uppala, S. M., Simmons, A. J., Berrisford, P., Poli, P., Kobayashi, S., Andrae, U., Balmaseda, M. A., Balsamo, G., Bauer, P. and Bechtold, P., Beljaars, A. C. M., Berg, L., Bidlot, J., Bormann, N., Delsol, C., Dragani, R., Fuentes, M., Geer, A. J.,

Haimberger, L., Healy, S. B., Hersbach, H., Holm, E. V., Isaksen, L., Kallberg, P., Kohler, M., Matricardi, M., McNally, A. P., Monge-Sanz, B. M., Morcrette, J. J., Park, B. K., Peubey, C., Rosnay, P., Tavolato, C., Thepaut, J. N., and Vitart, F. (2011). The ERA-Interim reanalysis: Configuration and performance of the data assimilation system. Quarterly Journal of the Royal Meteorological Society, Vol 137, No. 656, pp.553-597.

Diak, G. R., Bland, W. L., and Mecikalski, J. (1996). A note on first estimates of surface insolation from GOES-8 visible satellite data. Agricultural and Forest Meteorology, Vol. 82, pp. 219-226.

Drummond, A. J. (1956). On the measurement of sky radiation, Archiv für Meteorologie, Geophysik und Bioklimatologie, Serie B, Meteorologie und Geophysikpp, Vol. 7, Issue 3, pp. 413-436.

Duchon, C. E., and O'Malley, M. S. (1999). Estimating cloud type from pyranometer observations. Journal of Applied Meteorology, Vol 38, pp. 132-141.

Duffie, J. A., and Beckman, W. A. (1980). Solar Engineering of Thermal Processes, John Wiley & Sons, Inc., USA.

Dutton, E. L., Michalsky, J. J., Stoffel, T., Forgan, B. W., Hickey, J., Nelson, D. W., Alberta, T. L., and Reda, I. (2001). Measurement of broadband diffuse solar irradiance using current commercial instrument with a correction for thermal offset errors. Journal of Atmospheric and Oceanic Technology, Vol. 18, pp. 297-314.

Erbs, D. G., Klein, S. A., and Duffie, J. A. (1982). Estimation of the diffuse radiation fraction for hourly, daily and monthly average global radiation. Solar Energy, Vol.28, No.4, pp. 293-302.

Forgan, B. W. (1980). The influence of sky radiance distribution on the measurement of diffuse irradiance with shadowbands. Arch. Met. Geoph. Biokl., Ser. B, Vol. 28, pp. 373-384.

Forgan, B. W. (2011). Solar radiation measurement. WMO RAV Meteorology Workshop, Melbourne, Bureau of Meteorology, Australian Government.

Fortin, J. G., Anctil, F., Parent, L. E, Bolinder, M. A. (2008). Comparison of empirical daily surface incoming solar radiation models. Agricultural and Forest Meteorology, Vol 148, pp. 1332-1340.

Fröhlich, C., and Brusa, R.W. (1981). Solar radiation and its variation in time. Solar Physics, Vol. 74, pp. 209-215.

Fröhlich, C. (2006). Solar irradiance variability since 1978. Space Science Reviews, Vol 125, Issue 1, pp. 53-65.

Fujibe, F. (1988). Diurnal variations in the frequency of heavy precipitation in Japan. Journal of the Meteorological society of Japan, Vol 77, pp.1137-1149.

Fujibe, F. (2003). Long-term surface wind changes in the Tokyo Metropolitan area in the afternoon of sunny days in warm season. Journal of the Meteorological Society of Japan, Vol 81, No. 1, pp. 141-149.

Fujimori, Y., Hayashi Y., and Moriwaki, R. (2010). Characteristics of urban heat island phenomenon in Matsuyama plain. Annual journal of Hydraulic Engineering, JSCE, Vol. 54, pp. 313-318 (In Japanese).

Fujimoto, M., Watanabe, K., and Moriwaki, R. (2012). The characters of spatio-and temporal-variation of rainfall in Matsuyama plane. Journal of Hydroscience and Hydraulic Engineering, Vol. 30, No. 2, pp. 39-47.

Gansler, R. A., Klein, S. A., and Beckman, W. A. (1995). Investigation of minute solar radiation data. Solar Energy, Vol. 55, Issue. 1, pp. 21-27.

Gautier, C., Diak, G., and Masse, S. (1980). A simple physical model to estimate incident solar radiation at the surface from GOES satellite data. Journal of Applied Meteorology, Vol. 19, pp. 1005-1012.

Ghan, S. J., & Easter, R. C. (1992). Computationally efficient approximations to stariform cloud microphysics parameterization. Monthly Weather Review, Vol. 120, pp. 1572-1512.

Goodman, A. H. and Henderson-Seller, A. (1988). Cloud detection analysis: A review of recent program. Atmospheric Research, Vol. 21, pp. 203-228.

Green, M. A., Emery, K., Hishikawa, Y., Warta, W., and Dunlop, E. D. (2015). Solar cell efficiency tables (version 45) progress in Photovoltaics: Research and Application, Vol. 23, pp. 1-9. DOI: 10.1002/pip.2573.

Gueymard, C. A. (2004). The Sun's Total and Spectral Irradiance for Solar Energy, Applications and Solar Radiation Models. Solar Energy, Vol. 76, pp. 423-453.

Gueymard, C. A. (2012). Clear-sky irradiance predictions for solar resource mapping and large-scale applications: Improved validation, methodology and detailed performance analysis of 18 broadband radiative models. Solar Energy, Vol. 86, pp. 2145-2169.

Guichard, F., Parsons, D. B., Dudhia, J., and Bresch, J. (2003). Evaluating mesoscale model predictions of clouds and radiation with SGP ARM data over a seasonal timescale. Monthly Weather Review, Vol. 131, pp. 926-944.

Gulbrandsen, A. (1978). On the use of pyranometers in the study of spectral solar radiation and atmospheric aerosols. Journal of Applied Meteorology, Vol. 17, pp. 899-904.

Hahn, C. J., Warren, S. G, London, J., Chervin, R. M., and Jenne, R. L. (1990). Atlas of simultaneous occurrence of different cloud types over land. NCAR Technical Note TN-241+STR, Boulder, CO, pp. 21 + 188 maps.

Halthore, R. N., and Schwartz, S. E. (2000). Comparison of model-estimated and measured diffuse downward irradiance at surface in cloud-free skies, Journal of Geophysical Research, Vol 105, No. D12, pp. 20,165-21,077.

Heinle, A., Macke, A., and Srivastav, A. (2010). Automatic cloud classification of whole sky images. Atmospheric Measurement Techniques, Vol 3., pp. 557-567. doi:10.5194/amt-3-557-2010.

Houng, H. T. L., and Pathirana, A. (2013). Urbanization and climate change impacts on future urban flooding in Can tho city, Vietnam. Hydrology and Earth System Sciences, Vol. 17, pp. 379-394. doi:10.5194/hess-17-379-2013.

Inoue, T. (1987). A cloud type classification with NOAA 7 split-window measurement. Journal of Geophysical Research, Vol. 92, No. D4, pp. 3991-4000.

Inoue, T., and Kimura, F. (2004). Urban effects on low-level clouds around the Tokyo metropolitan area on clear summer days. Geophysical Research Letters, Vol. 31, Issue 5.

Iqbal, M. (1983). An Introduction to Solar Radiation, Academic press Canada, pp. 386.

ITACA. The sun as a source of Energy, Solar Photovoltaic. (http://www.itacanet.org/the-sun-as-a-source-of-energy/), Available online.

Jacovides, C. P., Tymviosa, F. S., Assimakopoulos, V. D., Kaltsounidesa, N. A. and Tymviosa, F. S. (2006). Comparative study of various correlations in estimating hourly diffuse fraction of global solar radiation. Renewable Energy, Vol 31, Issues 15, pp. 2492–2504.

Jarraud, M. (2008). Guide to Meteorological Instruments and Methods of Observation (WMO-No. 8). World Meteorological Organization: Geneva, Switzerland.

Ji, Q., and Tsay, S. C. (2000). On the dome effect of eppley pyrgeometers and pyranometers. Geophysical Research Letters, Vol. 27, No. 7, pp. 971-974.

Johnson, F. S. (1954). The solar constant. Journal of Meteorology, Vol. 11, No. 6, pp. 431-439.

Jong, R. D., and Steward, D. W. (1993). Estimating global solar radiation from common meteorological observation in western Canada. Canadian Journal of Plant Science, Vol. 73, pp. 509-518.

Kipp & Zonen. Instruction manual, CM-21 precision pyranometer, Manual version: 1004.

Kipp & Zonen (2006). Instruction manual, CMA series (albedo meter) and CMP series (pyranometer), Manual version: 0806.

Kipp & Zonen (2015). Instruction manual, SMP series & smart pyranometer, V1501.

Kitada, T., Okamura, K., & Tanaka S. (1998). Effects of Topography and Urbanization on Local Winds and Thermal Environment in the Nohbi Plain, Coastal Region of Central Japan: A Numerical Analysis by Mesoscale Meteorological Model with a k-ϵ Turbulence Model. Journal of Applied Meteorology, Vol. 37, No. 10, pp. 1026-1046.

Kliangsuwan, T., and Heednacram, A. (2015). Features extraction techniques for ground-based cloud type classification. Expert Systems with Applications, Vol. 42, pp. 8294-8303.

Kusaka, H., Kimura, F., Hirakuchi, H., and Mizutori, M. (2000). The effects of land-use alteration on the sea breeze and daytime heat in the Tokyo Metropolitan area. Journal of the Meteorological Society of Japan, Vol. 78, No. 4, pp. 405-420.

Lam, J. C., and Li, D. H. W. (1996). Correlation between global solar radiation and its direct and diffuse components. Building and Environment, Vol 31, Issue. 6, pp. 527–535.

Lecture notes/ JMA Training workshop (2013). Regional Instrument Centre (RIC) Tsukuba, RA-II(Asia), Meteorology Instrument Centre, Japan Meteorological Agency.

Leontyeva, E., and Stamnes, K. (1994). Estimation of cloud optical thickness from ground-based measurement of incoming solar radiation in the artic. Journal of Climate, Vol. 7, pp. 566-578.

Lim, B.B.P. (1980). Solar Energy Application in the Tropics. Proceeding of a Regional Seminar and Workshop on the Utilization of Solar Energy in Hot Humid Urban Development, Singapore.

Liou, K. N. (2002). An Introduction to Atmospheric Radiation. International Geophysics Series, Elsevier Science (USA), Vol. 84, pp. 525.

Liu, L., Xuejin, S., Chen, F., Zhao, S., and Gao, T. (2011). Cloud classification based on structure features of infrared images. Journal of Atmospheric and Oceanic Technology, Vol. 28, pp. 410-417.

Long, C. N., and Ackerman, T. P. (2000). Identification of clear skies from broadband pyranometer measurement and calculation of down welling shortwave cloud effects. Journal of Geophysical Research, Vol. 105, No. D12, pp. 15,609-15,626.

Long, C. N., Sabburg, J. M., Calbó, J. and Pagès, D. (2006). Retrieving cloud characteristics from ground based daytime color all-sky images. Journal of Atmospheric and Oceanic Technology, Vol. 23, pp. 633-652.

Lutgens, F. K., and Tarbuck, E. J. (1992). The Atmosphere: An Introduction to Meteorology, Fifth Edition, Prentice-hall Inc, pp. 421.

Lutz, H. J., Inoue, T., and Schmetz, J. (2003). Comparison of a split-window and a multi-spectral cloud classification for MODIS observation. Journal of the Meteorological Society of Japan, Vol. 81, No. 3, pp. 623-631.

Martínez-Chico, M., Battles, F. J., and Bosch, J. L. (2011). Cloud classification in a Mediterranean location using radiation data and sky images. Energy, Vol. 36, pp. 4055-4062.

Martínez, M. A., Andújar, J. M., and Enrique, J. M. (2009). A new and inexpensive pyranometer for the visible spectral range. Sensors, Vol. 9, No. 6, pp. 4615-4634.

Matsumoto, J., and Takahashi, K., (1999). Regional differences of daily rainfall characteristics in East Asian summer monsoon season. Geographical Review of Japan, Series B, Vol. 72, No. 2, pp. 193-201.

Merten, J., and Andreu, J. (1998). Clear separation of seasonal effects on the performance of amorphous silicon solar modules by outdoor I/V-measurements. Solar Energy material and Solar Cells, Vol, 52, pp. 11-25.

Michalsky, J., Dutton, E., Rubes, M., Nelson, D., Stoffel, T., Wesley, M., Splitt, M., and DeLuisi, J. (1999). Optimal measurement of surface shortwave irradiance using current instrumentation. Journal of Atmospheric and Oceanic Technology, Vol. 16, pp. 55-69.

Michalsky, J. J., Harrison, L. C., and Berkheiser, W. E. (1995). Cosine response characteristics of some radiometric and photometric sensors. Solar Energy, Vol. 54, No. 6, pp. 397-402.

Morimoto, K., Yamamoto, T., Shigetani, Y., and Moriwaki, R. (2013). Effects of differences in land use on formation of clouds~ field observations of cloud base level and solar

radiation in Matsuyama plain~. Annual Journal of Hydraulic Engineering, JSCE, Vol. 69, No. 4, pp I_1747-I_1752.

Moriwaki, R., Watanabe, K., & Morimoto, K. (2013). Urban dry island phenomenon and its impact on cloud base level. Journal of JSCE, 1, 521-529.

Myers, D. R. (2013). Solar radiation: practical modeling for renewable energy applications. CRC Press.

Ohmura, A., Dutton, E. G., Forgan, B., Fröhlich, C., Gilgen, H., Hegner, H., Heimo, A., König-Langlo, G., McArthur, B., Müller, G., Philipona, R., Pinker, R., Whitlock, C. H., Dehne, K., and Wild, M. (1998). Baseline surface radiation network (BSRN/WCRP): New precision radiometry for climate research. Bulletin of the American Meteorological Society, Vol. 79, No. 10, pp. 2115-2136.

O'Malley, M. S., and Duchon, C. E. (1996). A daytime radiation and cloud climatology from time series of measured surface irradiance. Proceeding of Sixth Atmospheric Radiation Measurement Science Team Meeting, San Antonio, TX, U.S. Department of Energy, pp. 249-251.

Orville, H. D. (1968). Ambient wind effects on the initiation and development of cumulus clouds over mountains. Journal of the Atmospheric Sciences, Vol. 25, No. 3, pp. 385-403.

Otkin, J. A., and Greenwald, T. J. (2008). Comparison of WRF model-simulated and MODIS-derived cloud data. Monthly Weather Review, Vol. 136, pp. 1957-1970.

Padovan, A., and Col, D. D. (2010): Measurement and modeling of solar irradiance components on horizontal and tilted planes. Solar Energy, Vol 84, pp. 2068-2084.

Parretta, A., Sarno, A., and Vicari, L. R. (1998). Effects of solar irradiation conditions on the outdoor performance of photovoltaic modules. Optics Communications, Vol. 153, pp. 153-163.

Paulescu, M., Paulescu, E., Gravila, P., and Badescu, V. (2013). Weather Modeling and Forecasting of PV Systems Operation. Green Energy and Technology, Springer-Verlag London.

Perez, R., Ineichen, P., Moore, K., Kmiecik, M., Chain, C., George, R., Vignola, F. (2002). A new operational model for satellite-derived irradiances: Description and validation. Solar Energy, Vol. 73, No. 5, pp. 307-317.

Pfister, G., Mckenzie, R. L., Liley, J. B., and Thomas, A. (2003). Cloud coverage based on all-sky imaging and its impact on surface solar irradiance. Journal of Applied Meteorology, American Meteorological Society, Vol. 42, pp. 1421-1434.

Philipona, R. (2002). Underestimation of solar global and diffuse radiation measured at Earth's surface. Journal of Geophysical Research, Vol. 107, No. D22, pp. 15-1 – 15-8.

Pielke, R. A., Adegoke, J., Beltran-Przekura, A., Hiemstra, C. A., Lin, J., Nair, U. S., Niyogi, D., and Nobis, T. E. (2007). An overview of regional land-use and land-cover impacts on rainfall. Tellus B, Vol. 59, No. 3, pp. 587-601.

Rabin, R. M., Stadler, S., Wetzel, P. J., Stensrud, D. J., and Gregory, M. (1990). Observed effects of landscape variability on convective clouds. Bulletin American Meteorological Society, Vol. 71, No. 3, pp. 272-280.

Randall, J. F., and Jabot, J. (2003). Is AM1. 5 applicable in practice? Modelling eight photovoltaic materials with respect to light intensity and two spectra. Renewable Energy, Vol. 28 No. 12, pp. 1851-1864.

Rastogi, B., Williams, A.P., Fischer, D.T., Iacobellis, S. F., McEachern, K., Carvalho, L., Jones, C., Baguskas, S. A., and Still, C. J. (2016). Spatial and temporal patterns of cloud cover and fog inundation in coastal California: Ecological Implication. Earth Interactions, Vol. 20, pp. 1-19.

Reno, M. J., Hansen, C. W., and Stein, J. S. (2012). Global horizontal irradiance clear sky models: Implementation and analysis. Sandia Reports, Sandia National Laboratories.

Reno, M. J. and Stein, J. S. (2013). Using cloud classification to model solar variability. SOLAR Conference Proceedings; pp.1.

Sabburg, J. M., and Long, C. N. (2004). Improved sky imaging for studies if enhanced UV irradiance. Atmospheric Chemistry and Physics, Vol. 4, pp. 2546-2552.

Saito, H., Nakayama, D., and Matsuyama, H. (2010). Relationship between the initiation of a shallow landslide and rainfall intensity-duration thresholds in Japan. Geomorphology, Vol. 118, pp. 167-175.

Sakai, S., and Umetani, K. (2009). Development of urban thermal environment observation system. Tenki, Vol.56, pp 25-39. (In Japanese)

Sakakibara, Y., and Matsui, E. (2005). Relation between heat island intensity and city size indices/ urban canopy characteristics in settlements of Nagano Basin, Japan. Geographical Review of Japan, Vol. 78, No. 12, pp. 812-824.

Shah, A., Torres, P., Tscharner, R., Wyrsch, N., and Keppner, H. (1999). Photovoltaic technology: the case for thin-film solar cells. Science, Vol. 285, pp. 692-698.

Shepherd, J. M., Carter, M., Manyin, M., Messen, D., and Burian, S. (2010). The impact of urbanization on current and future coastal precipitation: a case study for Houston. Environment and Planning B: Planning and Design, Vol. 37, pp. 284-304.

Shimojū, R., Nakayoshi, N., and Kanda, M. (2010). Multi-case study of urban torrential rain in summer Kanto region in consideration of the urban factor. Hydraulic Engineering Proceedings, Vol. 54, pp. 349-354 (in Japanese).

Singh, M., & Glennen, M. (2005). Automated ground-based cloud recognition. Pattern analysis and Applications, Vol. 8, pp. 258-271.

Skamarock, W. C., Klemp, J. B, Dudhia, J., Gill, D. O., Barker, D. M., Duda, M. G., Huang, X. –Y., Wang, W., and Powers, J. G. (2008). A Description of the Advanced Research WRF Version 3. NCAR Tech. Note NCAR/TN-475+STR, 113 pp.

Spencer, J. W. (1971). Fourier series representation of the position of the sun. Search, Vol. 2, No. 5, pp. 172-172.

Souza-Echer, M. P., Pereira, E. B., Bins, L. S., and Andrade, M. A. R. (2006). A simple method for the assessment of the cloud cover state in high-latitude regions by a ground-based digital camera. Journal of Atmospheric and Oceanic Technology, Vol. 23, pp. 437-447.

Tarpley, J. D. (1979). Estimating incident solar radiation at the surface from geostationary satellite data. Journal of Applied Meteorology, Vol. 18, pp. 1172-1181.

Tokinaga, H., Tanimoto, Y., Xie, S. P., Sampe, T., Tomita, H., and Ichikaw, H. (2009). Ocean Frontal Effects on the Vertical Development of Clouds over the Western North Pacific: In Situ and Satellite Observations*. Journal of Climate, Vol. 22, No. 16, pp. 4241-4260.

Tovar, J., Olmo, F. J., Batlles, F. J., and Alados-Arboledas, L. (2001). Dependence of one-minute global irradiance probability density distributions on hourly irradiation. Energy, Vol. 26, pp. 659-668.

Thapa Chhetri, D., and Moriwaki, R. (2015). Analysis of cloud properties in the Matsuyama plain using downward solar radiation dataset from a geostationary satellite. 9th International Conference on Urban Climate, Available online.

Vijayakumar, G., Kummert, M., Klein, S. A., and Beckman, W A. (2005). Analysis of short-term solar radiation data. Solar Energy, Vol. 79, pp. 495-504.

Wang, F., Wu, Y. H., Yang, H., Tanida, Y., and Kamei, A. (2015). Preliminary investigation of the 20 August 2014 debris flows triggered by a severe rainstorm in Hiroshima city, Japan. Geo-environmental Disasters, pp. 4-16.

Watanabe, Y., Yamada, T., and Suseno, D. P. Y. (2013). The Cloud Climatology Over Southeastern Asian Regions by Using MTSAT Cloud Classification (Japanese Title: MTSATによる輝度温度情報から作成した東南アジアにおける雲の気候特性). Journal of Japan Society of Civil Engineers, Ser. B1 (Hydraulic Engineering), Vol 69, pp. I_301-I_306.

Weisberg, J. S. (1981). Meteorology: The Earth and Its Weather, Second Edition, Houghton Mifflin Company, Boston, pp. 419.

Williams, A. P., Schwartz, R. E., Iacobellis, S., Seager, R., Cook, B. I., Still, S. J., Husak, G., and Michaelsen, J. (2015). Urbanization causes increased cloud base height and decreased fog in coastal Southern California. Geophysical Research Letters, Vol. 42, pp. 1527-1536.

World Meteorological Organization (1975). International cloud atlas, Vol 1, WMO- No. 407.

Wu, Z., Xu, X., Xia, M., Ma, M., and Li, L. (2015). Ground-based vision cloud image classification based on extreme learning machine. The open Cybernetics & Systematics Journal, Vol. 9, pp. 2877-2885.

Xia, M., Lu, W., Yang, J., Ma, Y., Yao, W., & Zheng, Z. (2015). A hybrid method based on extreme learning machine and k-nearest neighbor for cloud classification of ground-based visible cloud image. Neurocomputing, Vol. 160, pp. 238-249.

Xu, K. M., and Krueger, S. K. (1991). Evaluation of cloudiness parameterization using a cumulus ensemble model, Monthly Weather Review, Vol. 119, pp. 342-367.

Xu, K.M., and Randall, D. A. (1996). A semi empirical cloudiness parameterization for use in climate models. Journal of Atmospheric Science, Vol. 53, pp. 3084-3102.

Xu, K. M., and Randall, D. A. (1996). Evaluation of statistically based cloudiness parametrizations used in climate models. Journal of Atmospheric Sciences, Vol 53, No. 21, pp. 3103-3119.

Yang, S. K., Hou, Y. T., Miller, A. J., and Campana, K. A. (1999). Evaluation of the earth radiation budget in NCEP-NCAR reanalysis with ERBE. Journal of Climate, Vol. 12, pp. 477-493.

Yoshida, S., Ueno, S., Kataoka, N., Takakura, H., and Minemoto, T. (2013). Estimation of global tilted irradiance and output energy using meteorological data and performance of photovoltaic modules. Solar Energy, Vol 93, pp. 90-99.